EBM Experimental Biology and Medicine

Volume 250 | Issue 8

Experimental Biology and Medicine

Editor-in-Chief

Nicola Conran
University of Campinas, Brazil

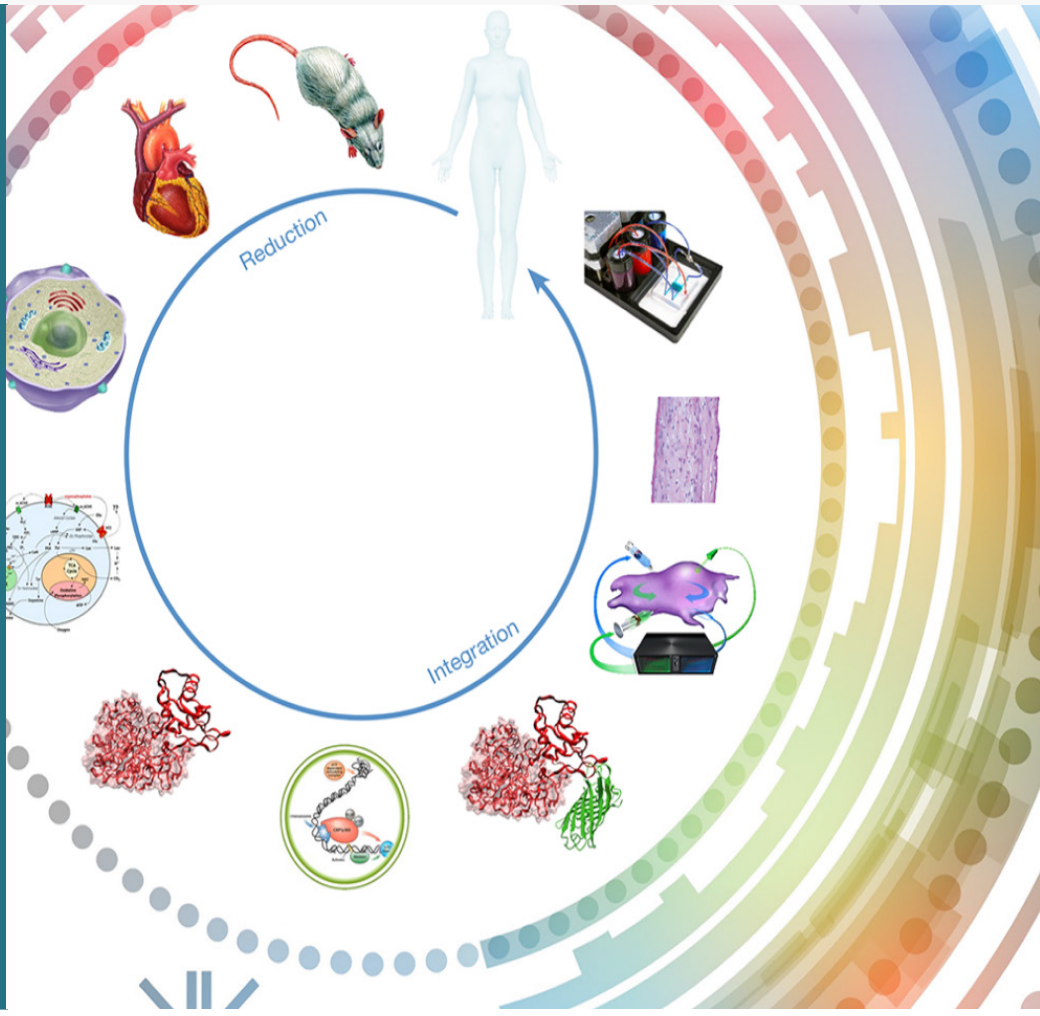

ISBN 978-2-8325-7023-4
DOI 10.3389/978-2-8325-7023-4

frontiers | Publishing Partnerships

Society for Experimental Biology and Medicine
3220 N Street NW, #179
Washington DC 20007, USA
Executive Director – ed@sebm.org

www.sebm.org

EBM Experimental Biology and Medicine

Editorial Board

ISSN 1535-3699
ISBN 978-2-8325-7023-4
DOI 10.3389/978-2-8325-7023-4

Generative AI statement
Any alternative text (Alt text) provided alongside figures in the articles in this ebook has been generated by Frontiers with the support of artificial intelligence and reasonable efforts have been made to ensure accuracy, including review by the authors wherever possible. If you identify any issues, please contact us.

EBM Experimental Biology and Medicine

2025 | Volume 250 | Issue 8 | ISSN 1535-3699

Table of contents

Physiology, Pathophysiology and Mechanisms of Disease

Population Health

Highlight

Population Health

EBM Experimental Biology and Medicine

TYPE Original Research
PUBLISHED 29 August 2025
DOI 10.3389/ebm.2025.10452

OPEN ACCESS

*CORRESPONDENCE
Lianhua Liu,
llh1979@163.com
Yuqing Chen,
chen_yuqing0229@163.com

†These authors have contributed equally to this work

RECEIVED 29 November 2024
ACCEPTED 06 August 2025
PUBLISHED 29 August 2025

CITATION
Zhao S, Zhang X, Miao Y, Gao X, Wan Q, Qiu W, Si H, Han Y, Du X, Feng Y, Liu L and Chen Y (2025) Integrated analysis of metabolome and microbiome in a mouse model of sodium valproate-induced autism.
Exp. Biol. Med. 250:10452.
doi: 10.3389/ebm.2025.10452

Integrated analysis of metabolome and microbiome in a mouse model of sodium valproate-induced autism

Shuzhen Zhao[1†], Xinyan Zhang[2†], Yanqiu Miao[3], Xueya Gao[4], Qiuhua Wan[5], Wei Qiu[6], Haixia Si[7], Yingjie Han[8], Xiao Du[1], Yuanyuan Feng[1], Lianhua Liu[9*] and Yuqing Chen[10*]

[1]Child Rehabilitation Center, Jining Maternal and Child Health Family Planning Service Center, Jining, China, [2]Department of Nursing, Jining Maternal and Child Health Family Planning Service Center, Jining, China, [3]Department of Child Health, Zoucheng People's Hospital, Zoucheng, China, [4]Department of Pediatrics, Jining Maternal and Child Health Family Planning Service Center, Jining, China, [5]Clinical Laboratory, Jining Maternal and Child Health Family Planning Service Center, Jining, China, [6]Shandong Yiyang Health Group Baodian Mining Hospital, Zoucheng, China, [7]Department of Obstetrics and Gynecology, Jining Maternal and Child Health Family Planning Service Center, Jining, China, [8]Department of Obstetrics, Jining No. 1 People's Hospital, Jining, China, [9]Department of Medical Administration, Jining Maternal and Child Health Family Planning Service Center, Jining, China, [10]Department of Health, Jining Maternal and Child Health Family Planning Service Center, Jining, China

Abstract

Sodium valproate (SV) has been shown to induce autism in animal models. In this study, the SV method was used to establish a mouse model of autism, and anxiety-like behaviours and learning memory performance were evaluated by behavioural tests. The effects of SV on metabolic profiles and gut microbiota were assessed by integrating gas chromatography-mass spectrometry and 16S ribosomal RNA gene sequencing. Correlations between metabolites and gut microbiota were determined using Spearman correlation coefficient. Behavioral tests, including the three-chambered social assay, repetitive behaviors, open field test, elevated plus-maze test, and novel object recognition test, demonstrated that SV treatment exacerbated anxiety-like behaviors and impeded spatial learning and memory in mice. SV disrupted metabolic pathways in hippocampus, cortex, intestine, and serum, affecting primarily valine, leucine and isoleucine biosynthesis, glycerophospholipid metabolism and glutathione metabolism and so on. SV also altered gut microbiota at the genus level, decreasing the abundances of *Dubosiella*, *Faecalibaculum*, *Clostridia_UCG-014*, *Bifidobacterium*, and *Alloprevotella*, while increase the abundances of *Lactobacillus*, *Alistipes*, and *Lachnospiraceae* in intestine. The results of correlation analysis showed that in hippocampus, *Bifidobacterium* was positively correlated with serine and glycine, while *Alistipes* was negatively correlated with them. These findings

suggested that SV may contribute to the development of autism progression by altering the gut microbiota abundances and metabolite profiles. This may provide new direction for the management of autism.

KEYWORDS

gas chromatography-mass spectrometry, 16S ribosomal RNA, gut microbiota, metabolite, autism

Impact statement

Sodium valproate (SV) has been shown to induce autism in animal models. In this study, we employed a gas chromatography-mass spectrometry (GC-MS)-based metabolomics approach, complemented by 16S ribosomal RNA (rRNA) sequencing, to elucidate potential associations between gut microbiota components and metabolic pathways following exposure to SV. SV disrupted metabolic pathways in hippocampus, cortex, intestine, and serum, affecting primarily valine, leucine and isoleucine biosynthesis, glycerophospholipid metabolism and glutathione metabolism and so on. SV also altered gut microbiota at the genus level, decreasing the abundances of *Dubosiella*, *Faecalibaculum*, *Clostridia_UCG-014*, *Bifidobacterium*, and *Alloprevotella*, while increase the abundances of *Lactobacillus*, *Alistipes*, and *Lachnospiraceae* in intestine. The results of correlation analysis showed that in hippocampus, *Bifidobacterium* was positively correlated with serine and glycine, while *Alistipes* was negatively correlated with them. These findings suggest that SV may induce neurotoxicity and promote autism progression by altering the gut microbiota abundances and brain metabolite profiles. Our study provides a more comprehensive understanding of the toxic effects induced by SV in a mouse model of autism.

Introduction

Autism spectrum disorder (ASD) is a neurodevelopmental disorder among children [1]. It is statistically that approximately 20 out of every 10,000 children suffer from ASD worldwide, especially for those as young as 1–3 years old [2]. The clinical symptoms of ASD generally include social communication difficulties, repetitive behaviors or even self-injurious behaviors [3]. In addition, patients with ASD may also suffer from epilepsy and mental retardation [4]. Currently, although the detailed causes of ASD are still unknown, multiple factors such as social influences, environmental insults and genetic aberrations can lead to the development of ASD [5, 6]. In some clinical reports, Purkinje cell integrity loss in the cerebellum, hyperserotonemia and oxidative stress damage are considered as the key pathological findings [7–9]. Additionally, some researches demonstrated that early life environmental factors such as chemical and drug exposure in the mother and prenatal viral infections may also increase the risk of ASD in the offspring [10, 11]. Some chemicals such as misoprostol, thalidomide, mercury and ethanol induce the generation of reactive oxygen species, leading to the development deficits of cerebellum and brain [12].

Sodium valproate (SV) is a well-known anti-epileptic drug since its first introduction in 1978 [13]. In 1995, it was approved by the Food and Drug Administration and became the mood-stabilizing agent of choice for use in stabilization of mania associated with bipolar disorder [14, 15]. Recently, SV has been also employed in migraine prophylaxis and control of neuropathic pain [4]. As the number of indications for SV usage increases, so does the incidence of both accidental and intentional exposures. It is reported that children exposed to SV *in utero* can cause fetal-valproate syndrome [16]. Fetal-valproate syndrome shows autism like symptoms such as repetitive behaviors, language and communication deficits, hyper excitability and global delays in behavioral development [17–19]. Bairy et al. and Hamza et al. uncovered the reproductive toxicity of SV in male rats, manifesting as the decrease of sperm count and sperm motility [20, 21]. Sivathanu et al. conducted a case report that a female infant presented with global developmental delay and infantile spasms [22]. She was then started on SV but developed encephalopathy after an initial improvement [22]. However, the symptoms of vomiting and seizures were reversal on withdrawal of SV [22]. Mei et al. reported a 42-year-old man received antiepileptic treatment with SV following meningioma surgery [23]. He was diagnosed as liver failure and eventually died [23]. SV was also reported to induce hematologic toxicity including bone marrow failure, macrocytosis, thrombocytopenia and neutropenia [24]. Additionally, SV was also used to induce autism in animal models due to its property of affecting brain neurodevelopment and synaptic integration disturbances [25]. These data indicated that SV-induced toxicity represents an increasing concern for toxicologists. Therefore, it is paramount to investigate the mechanisms responsible for SV-associated toxicity.

Humans and animals evolved in intimate association with microbial communities. Gut microbiota plays a crucial role in organ development, metabolism and immune system [26–28]. The microbiota-gut-brain-axis describes the physiological connection to exchange information among the microbiota, the gut and the brain [29]. Gut microbiota represents the greatest density and absolute abundance of microorganisms in the human body. A healthy microbial composition is important

to health, as dysbiosis is often observed in irritable bowel syndrome, inflammatory bowel disease, obesity, allergy, depression and of course in ASD [30–32]. Researches have demonstrated that gastrointestinal (GI) symptoms such as diarrhoea, constipation and vomiting in children with ASD are fourfold than those of healthy population [33, 34]. Additionally, lower diversities of bacterial communities are found in ASD children, which may be related to the severity of GI symptoms [35]. Meanwhile, the abundance of *Clostridia species (spp)* was relatively higher in autistic individuals, indicating that it is involved in the pathogenesis of ASD [35]. Interestingly, structural changes in the brain and less sociable behaviors are observed in germ-free mice, which suggests that there may be a functional connection between the microbiota and the brain [36, 37].

In this study, we employed an integrated gas chromatography-mass spectrometry (GC-MS)-based metabolomics approach along with 16S ribosomal RNA (rRNA) sequencing to elucidate potential associations between gut microbiota components and metabolic pathways following exposure to SV. Our findings provide a comprehensive understanding of the toxic effects induced by SV in autism mice model. This study provides a research basis for an in-depth investigation of the mechanisms of ASD caused by SV exposure.

Materials and methods

Chemicals and reagents

Sigma Aldrich (St. Louis, MO, USA) provided sodium valproate (SV), N, O-bis(trimethylsilyl)trifluoroacetamide (containing 1% trimethylchlorosilane) and O-methylhydroxylamine hydrochloride (purity ≥98%). Methanol (chromatographic grade), heptadecanoic acid (purity ≥98%) and pyridine were obtained from Macklin Biochemical (Shanghai, China).

Animals and experimental design

The C57BL/6 mice (10 females and 5 males) weighing between 20 and 25 g and aged 8 weeks were procured from Vital River Laboratory Animal Technology located in Pinghu, China. SV-induced autism mouse model was established as previously depicted [38]. In brief, mice were housed with free water and food under a 12 h light/dark cycle at 20–22°C in plastic cages for acclimatization. One week later, mice were kept in separate cages for mating, with one male and two females in each cage. Female mice were placed in a separate plastic cage when pregnant, and divided into two groups randomly. This day was defined as embryonic day 0 (E0). On the day of E13, one group of pregnant mice (n = 5) was administrated with SV (500 mg/kg dissolved in normal saline) via intraperitoneal injection, while the others (n = 5) were given the equivalent volume of saline. The delivery day was considered as postnatal day 0 (P0). Three weeks later (P21), all mice offspring were weaned and sex-grouped, with 5 mice a cage. Pups from SV-injected mothers were considered as the SV group, while those of mothers treated with saline were used as control mice. Each repeat was performed as a separate, independent observation. All experimental procedures conformed to the Guidelines for the Use of Laboratory Animals, and approved by the Ethical Committee for Animal Experimentation of Jining No.1 People's Hospital (Approval No. JNRM-2023-DW-034).

Behavioral tests

When the pups grew at the age of 8 weeks, they were used for behavioral tests. The social choice test was performed in mice using a three-chamber apparatus comprising a central compartment and two end chambers. A stimulus mouse was randomly introduced into one end chamber (designated as the social chamber), while the opposite chamber served as the non-social chamber [39, 40]. Two identical transparent plexiglass cylinders with perforations for air exchange were positioned in the end chambers. The experimental mouse was placed in the central compartment and permitted to freely explore all chambers for 10 min. Throughout the test session, the duration of time spent in each chamber was recorded, and baseline locomotor activity was quantified.

To detect repetitive behavior, the test mouse is individually placed in a clean environment with bedding, similar to a home cage. The mouse is first allowed to acclimate for 5 min, after which its activity is recorded for 10 min. The duration of repetitive behaviors (such as grooming or digging) is measured using a stopwatch.

For open field test, an open field box (45 × 45 × 30 cm) was used [41]. The 25 × 25 cm area in the center was defined as the central region. Mice were placed into this area and given 10 min for habituation. The distance moved, average speed and moving time of mice were recorded.

For elevated plus-maze test, an apparatus consisted of two closed arms (50 × 10 × 40 cm) and two open arms (50 × 10 cm) [42]. A 25 × 25 cm central platform connected the arms. The apparatus was raised to 50 cm above the floor. Mice were placed on the center platform for 5 min. The number of open/closed arm entries and the corresponding time spent time were recorded. Ethanol (70%) was used to clean the apparatus following each test.

A novel object recognition test is conducted on the mice. On the first day, the test mouse is individually placed in a white, opaque circular chamber for a 30-minute habituation session. On the second day, the mouse is allowed to freely explore two identical, symmetrically positioned objects in the chamber for

10 min. On the third day, one of the two objects is randomly replaced with a novel object that differs in shape and texture, and the test mouse is allowed to explore both objects freely for 10 min. During the test, Ethovision XT 10.1 (Noldus) is used to analyze and record the sniffing time of the mouse toward the novel object (N) and the familiar object (F). The experiment is conducted over three consecutive days.

Sample collection

After behavioral testing, mice were anesthetized with sodium pentobarbital (50 mg/kg), and blood was collected via orbital extraction. The blood samples were centrifuged at 4°C and 4000 rpm for 10 min and then stored at −80°C for further use. Subsequently, the mice were euthanized via cervical dislocation. The intestine, hippocampus, and cerebral cortex were collected, rapidly frozen in liquid nitrogen, and stored at −80°C for further experiments.

Sample preparation

For serum samples, 100 μL of each sample was mixed with 350 μL of heptadecanoic acid (100 μg/mL) and centrifuged at 14,000 rpm for 15 min at 4°C. The supernatant was then dried with liquid nitrogen at 37°C. Subsequently, O-methylhydroxylamine hydrochloride (15 mg/mL) was added, and the mixture was incubated at 70°C for 90 min. Then, 100 μL of N,O-bis(trimethylsilyl)trifluoroacetamide containing 1% trimethyl chlorosilane was added and incubated at 70°C for one hour. For tissue samples, 50 mg of each sample was homogenized in 1 mL of methanol, followed by the addition of 50 μL of heptadecanoic acid (1 mg/mL). The remaining steps were the same as those for the serum samples. A 10 μL aliquot from both the control and SV groups was pooled to serve as a quality control (QC) sample.

GC-MS analysis

GC-MS analysis was performed using a 7890B GC system and 7000C mass spectrometer (Agilent Technologies, USA) equipped with an HP-5MS fused silica capillary column. Helium was used as the carrier gas at a flow rate of 1 mL/min. A sample volume of 1 μL was injected into the GC-MS system with a split ratio of 50:1. The injection temperature, transfer line temperature, and ion source temperature were set to 280°C, 250°C, and 230°C respectively. Electron collision ionization was set to −70 EV with an acquisition frequency of 20 spectra/s. Mass spectrometry employed electrospray ionization in positive mode with a mass/charge (m/z) full scan range from 50 to 800.

Data processing and multivariate analysis

The raw data obtained from gas chromatography-mass spectrometry (GC-MS) analysis were processed using Agilent MassHunter software (version B.07.00). Metabolites in the quality control (QC) samples with a similarity score greater than 80% were identified using the GC-MS library of the National Institute of Standards and Technology (NIST 14). A reference library containing all QC samples was established for spectral matching of experimental sample metabolites. To minimize deconvolution errors during automated data processing and eliminate misidentifications, manual verification was performed.

The resulting comprehensive data matrix included peak indices (RT-m/z pairs), sample names, and corresponding peak areas. Data normalization was performed using the total peak area normalization method. Further data analysis was conducted using orthogonal partial least squares discriminant analysis (OPLS-DA) in SIMCA-P 14.0 software. A two-tailed Student's t-test was used to assess differences between the two groups. Compounds with a VIP score greater than 1.0 and a p-value less than 0.05 were considered potential differentially expressed metabolites. Heatmap clustering analysis and pathway enrichment were performed using MetaboAnalyst 5.0 software.

16S rRNA sequencing of gut microbiota

Microbial genomic DNA from colonic contents was extracted using the E.Z.N.A.® Soil DNA Kit and separated by 1% agarose gel electrophoresis, followed by PCR amplification of the V3-V4 region of the bacterial 16S rRNA gene. PCR products were purified and sequenced using the TruSeq™ DNA Sample Preparation Kit. Raw data were obtained following the RS_ReadsOfInsert1 protocol. High-quality sequences were processed using the QIIME software package (version 1.9.1). Operational taxonomic units (OTUs) were clustered at 97% similarity using UPARSE (version 7.1). Taxonomic classification analysis was conducted using the Silva 16S rRNA database with the ribosomal database project classifier and the Bayesian algorithm, applying a confidence threshold of 70%.

Results

Autistic-like social and repetitive behavioral deficits in SV-induced mice

In behavioral tests, SV-induced mice showed significantly reduced social interaction on the three-chamber social approach assay, showing diminished preference for investigating a social stimulus as compared to an object (Figures 1A,B, $P < 0.0001$). When allowed the opportunity for direct interaction with a novel

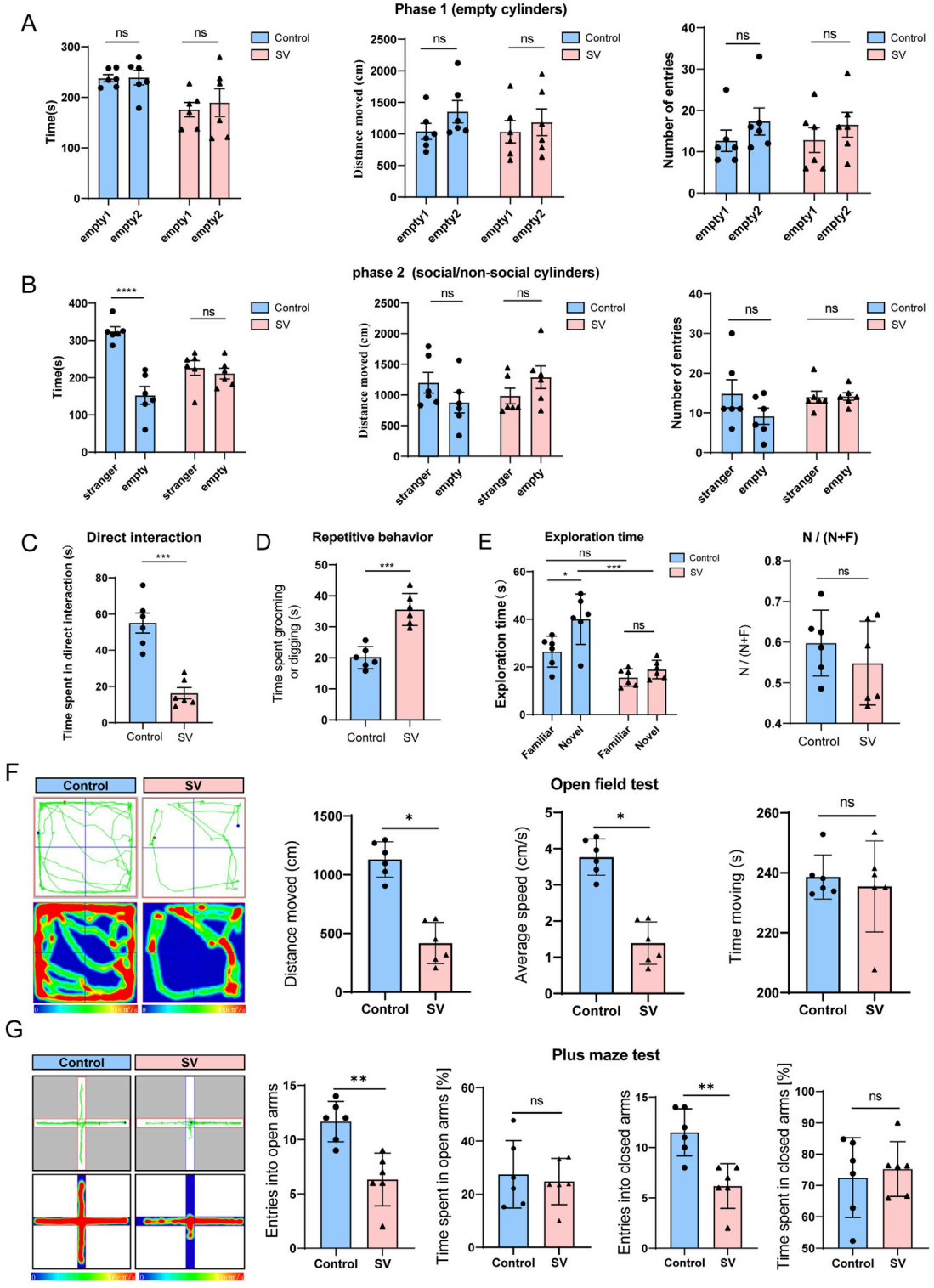

FIGURE 1
Autistic-like social and repetitive behavioral deficits in SV-induced mice. **(A–C)** The three-chambered social assay, **(D)** repetitive behaviors, **(E)** novel object recognition test, **(F)** open field test, and **(G)** elevated plus-maze test were performed to assess the anxiety like-behaviors and the learning and memory performance of mice. Error bars are Mean ± SEM. *p*-values from unpaired Student's t-tests, $^{*}P < 0.05$, $^{**}P < 0.01$, $^{***}P < 0.001$.

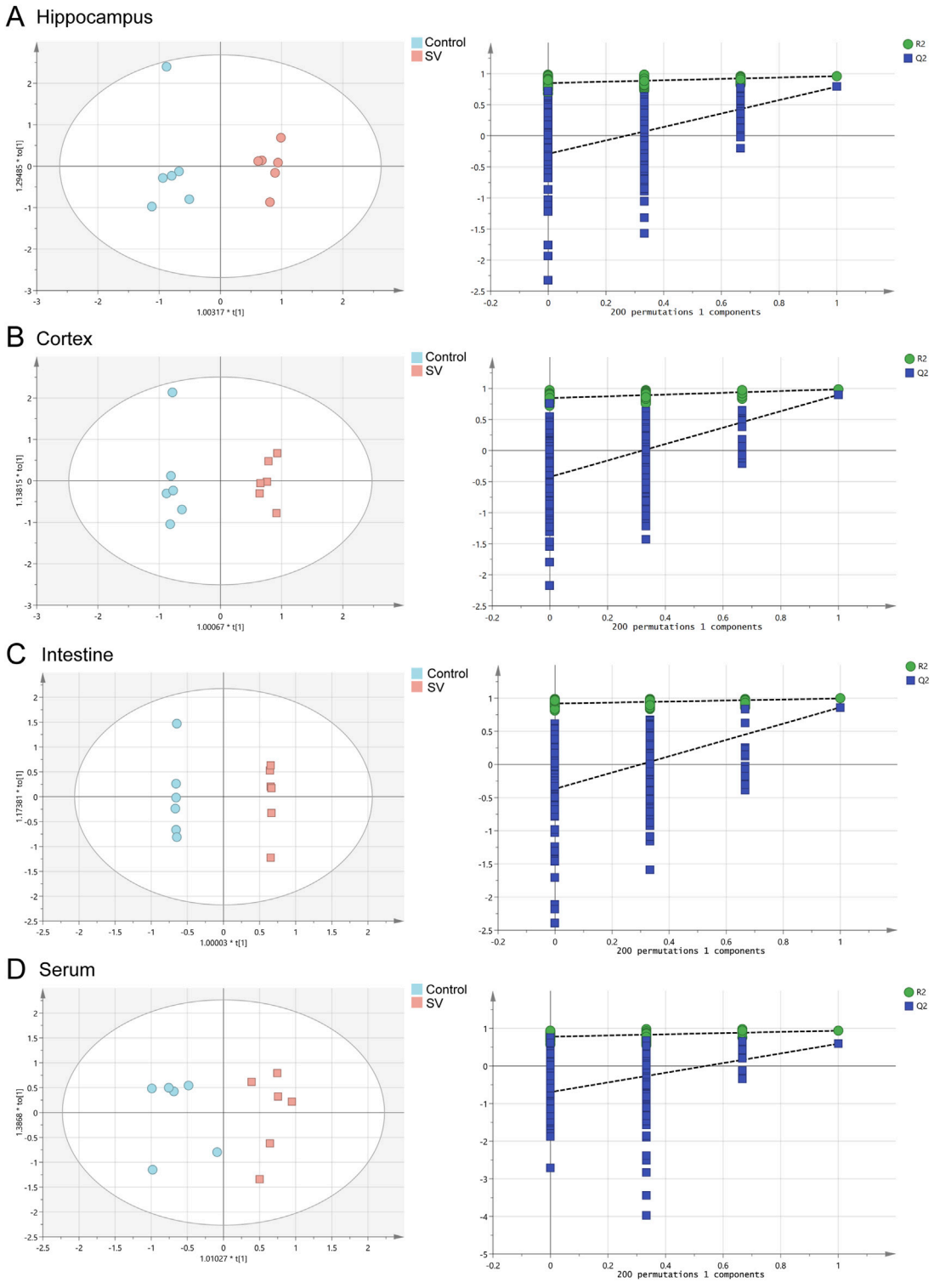

FIGURE 2
OPLS-DA score plots and 200 permutation tests. **(A)** Hippocampus, **(B)** cortex, **(C)** intestine and **(D)** serum.

TABLE 1 OPLS-DA parameter scores.

Tissues	R^2X (cum)	R^2Y (cum)	Q^2 (cum)
Hippocampus	0.616	0.961	0.791
Cortex	0.682	0.985	0.897
Intestine	0.572	0.995	0.861
Serum	0.715	0.939	0.590

R^2X: the explanation rate of the X matrices; R^2Y: the explanation rate of the Y matrices; Q^2: the prediction ability.

stimulus mouse, SV-induced mice also spent significantly less time initiating contact in comparison to wild-type controls (Figure 1C, $P < 0.001$). In a home-cage like environment, SV-induced mice showed significantly increased time engaging in repetitive behaviors such as grooming and digging (Figure 1D, $P < 0.001$). Additionally, SV-induced mice displayed enhanced recognition memory (novel object-recognition test) (Figure 1E, $P < 0.001$). Open field test demonstrated that the distance moved and average speed of mice in the SV group were significantly reduced compared to those of mice in the control group (Figure 1F, $P < 0.05$). But the time spent in the open field between the two groups seemed no significant differences. The elevated plus-maze test indicated that the numbers of open arm entries and closed arm entries of mice in the SV group were dramatically reduced relative to the control group (Figure 1G, $P < 0.05$), and there were no significant differences between the two groups on the time spent in open or closed arms. Therefore, SV-induced mice show strong autistic-like social and repetitive behavioral deficits.

Metabolomic profiles of SV-exposed mice by GC-MS

To determine the effects of SV on the metabolomic profiles of mice among hippocampus, cortex, intestine and serum, a GC-MS-based untargeted metabolomics approach was applied in this study. The representative GC-MS total ion chromatograms (TICs) of QC from hippocampus, cortex, intestine and serum were shown in Supplementary Figures S1A–D. The results indicated that there were significant differences in TICs among different QC samples. As illustrated in Figures 2A–D and Table 1, OPLS-DA models showed that clear differences were observed between the control and SV groups. In different tissues and serum, the proportion of variance explained by the OPLS-DA model (R^2X) was 61.6%, 68.2%, 57.2%, and 71.5%, respectively. Additionally, the intersection points between blue regression line (Q^2-point) and vertical axis were all negative values, indicating that the OPLS-DA models and the predication were reliable.

VIP value >1 and p-value < 0.05 were considered as the important criteria for potential metabolites. As manifested in Figures 3A–D, the cluster analysis of differentially-expressed metabolites of the control group and SV group were depicted. A total of 11 differential metabolites were identified in hippocampal tissues, including 1-monopalmitin (MG (16:0/0:0/0:0)), formamide, o-phosphoethanolamine, glycine, ethanolamine, gamma-aminobutyric acid, serine, L-threonine, pipecolic acid, glycerol, and myo-inositol, all of which were downregulated following SV treatment. In cortex, 7 downregulated metabolites including ethanolamine, glycine, 2-Aminobenzoic acid, serine, L-glutamic acid, o-phosphoethanolamine and adenosine were identified. Moreover, we observed SV treatment altered a total of 8 metabolites including creatinine, myristic acid, desmosterol, stearic acid, palmitelaidic acid, palmitic acid, pyroglutamic acid and scyllo-inositol in intestine tissues. Among these differentially-expressed metabolites, only creatinine was found to be downregulated after SV treatment. In the serum, 11 upregulated metabolites including pyroglutamic acid, palmitic acid, urea, citric acid, glycine, myo-inositol, L-valine, L-proline, ornithine, L-alanine and serine were identified following SV treatment. Next, the differentially-expressed metabolites were subjected to pathway analysis via Metaboanalyst 6.0 and KEGG database. As shown in Figure 4A and Table 2, we found that SV treatment mainly affected galactose metabolism, glycine, serine and threonine metabolism, and glycerophospholipid metabolism in hippocampus. In cortex, pathways of glutathione metabolism, porphyrin metabolism, and glyoxylate and dicarboxylate metabolism were altered following SV treatment. In intestine, only biosynthesis of unsaturated fatty acids and fatty acid biosynthesis were affected by SV treatment. Notably, SV treatment affected glutathione metabolism, arginine biosynthesis, and alanine, aspartate and glutamate metabolism in serum samples. The detailed metabolic network illustrated in Figure 4B highlights the significant impact of SV treatment. Our analysis revealed that SV-exposed disrupted not only various amino acid metabolic pathways but also glutathione metabolism, which plays a critical role in cellular antioxidant defense, and galactose metabolism, an essential pathway for carbohydrate processing.

The changes of gut microbiota induced by SV treatment

Gut microbiota at OTU level in SV-treated mice were determined. As shown in Figure 5A, a total of 232 OTUs

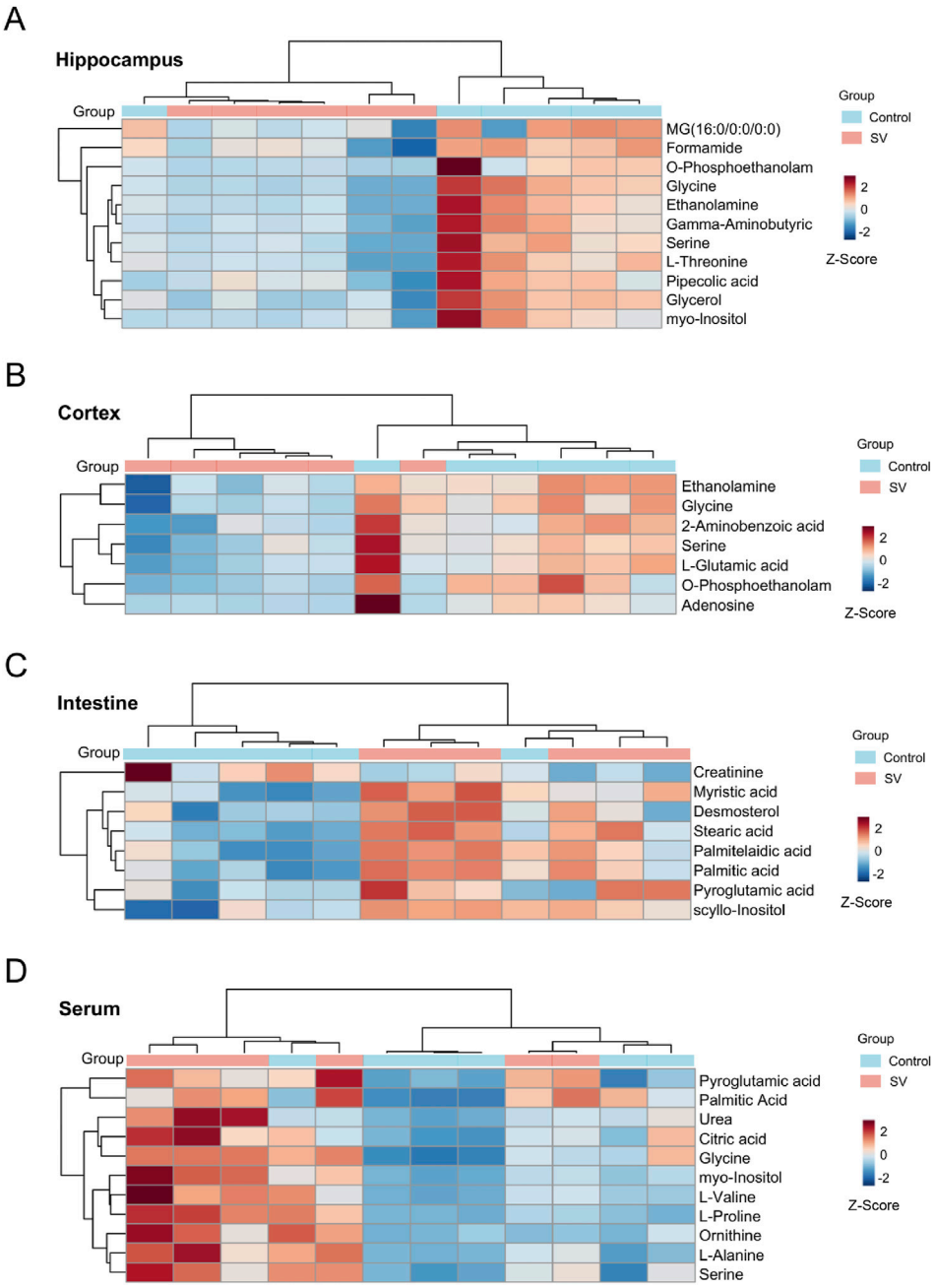

FIGURE 3
Heatmap of differential metabolites in **(A)** hippocampus, **(B)** cortex, **(C)** intestine and **(D)** serum in the SV groups compared with controls. "Control" represents untreated control mice and "SV" represents mice prenatally exposed to sodium valproate. Rows represent samples and columns represent metabolites. The color legend is located at the top right of the figure, where blue represents the control group and red represents the SV-treated group. Prior to unsupervised hierarchical clustering of the samples (rows), the relative abundance of the compounds was z-score normalized, thus making the down-regulated relative expression abundance appear in blue (–2 to 0) and the up-regulated relative expression abundance appear in red (0–2). Darker colors indicate more upregulated metabolite expression.

were shared in all the samples, and the results showed a species abundance of the control group > the SV group. Supplementary Figures S2A,B shows that community richness and diversity were altered after the SV-exposed (alpha-diversity indices Chao and Ace). The coverage index representing the sample coverage detected indicated that the sequencing depth was representative of the gut microbiome (Supplementary Figure S2C). Beta-diversity was analyzed using the principal

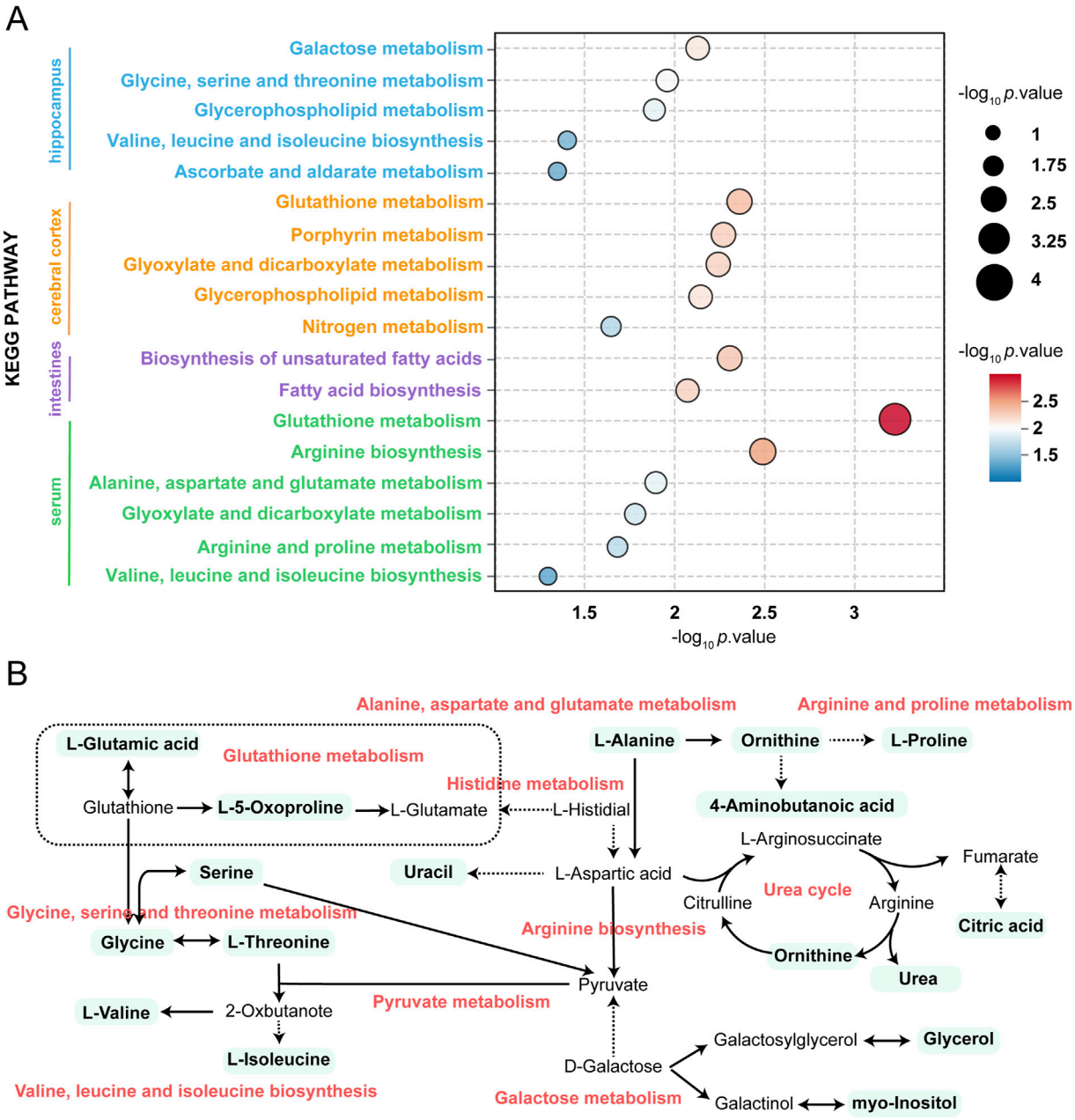

FIGURE 4
Summary of pathway analysis performed using MetaboAnalyst 6.0. **(A)** KEGG pathway enrichment analysis of differentially metabolites. **(B)** Schematic diagram of related metabolic pathways affected by SV in serum and major tissues.

coordinate analysis (PCoA) on OTU level showed a significant separation between the control group and the SV group (Figure 5B). The abscissa represents the first principal component and the ordinate is the second principal component. Furthermore, 66% is the contribution value of the first principal component to the sample difference, while 22.62% is the contribution value of the second principal component to the sample difference. The analyses of bacterial communities showed that at the phylum level, *Bacteroidota*, *Firmicutes*, *Actinobacteriota* were the major components of gut microbiota in the control group, while the abundances of *Patescibacteria* and *Verrucomicrobiota* were increased but *Proteobacteria* and *Desulfobacterota* were decreased following SV treatment (Figures 5C,D). At the genus level, the gut microbiota in the control group was mainly composed of *Muribaculaceae*, *Lactobacillus*, and *Alistipes*. After induced by

TABLE 2 Pathway analysis performed using MetaboAnalyst 5.0 software.

Samples	Pathway names	Raw p	-$\log_{10}$ p value
Hippocampus	Galactose metabolism	7.4E-3	2.128
	Glycine, serine and threonine metabolism	0.011	1.958
	Glycerophospholipid metabolism	0.013	1.884
	Valine, leucine and isoleucine biosynthesis	0.040	1.398
	Ascorbate and aldarate metabolism	0.045	1.348
Cortex	Glutathione metabolism	4.4E-3	2.359
	Porphyrin metabolism	5.4E-3	2.271
	Glyoxylate and dicarboxylate metabolism	5.7E-3	2.244
	Glycerophospholipid metabolism	7.2E-3	2.143
	Nitrogen metabolism	0.023	1.644
	Biosynthesis of unsaturated fatty acids	4.9E-3	2.313
	Fatty acid biosynthesis	8.2E-3	2.084
Intestine	Glutathione metabolism	5.6E-4	3.255
	Arginine biosynthesis	3.2E-3	2.499
Serum	Alanine, aspartate and glutamate metabolism	0.013	1.901
	Glyoxylate and dicarboxylate metabolism	0.016	1.789
	Arginine and proline metabolism	0.020	1.691
	Valine, leucine and isoleucine biosynthesis	0.0497	1.303
	Galactose metabolism	7.4E-3	2.128
	Glycine, serine and threonine metabolism	0.011	1.958

SV treatment, the abundances of *Dubosiella*, *Faecalibaculum*, and *Clostridia_UCG-014* were decreased, while the abundances of *Lactobacillus*, *Alistipes*, and *Lachnoclostridium* were increased (Figures 5E,F).

Relevance analysis between metabolites and gut microbiota

Spearman's correlation coefficient was used to assess the relationships between metabolites and gut microbiota at both the phylum and genus levels. At the phylum level, *Firmicutes* showed negative correlations with pipecolic acid, glycine, and ethanolamine in the hippocampus (Supplementary Figure S3A). *Patescibacteria* exhibited negative correlations with serine, O-phosphoethanolamine, L-threonine, gamma-aminobutyric acid, and formamide. *Proteobacteria* exhibited positive correlations with MG (16:0/0:0/0:0) and glycerol. In the cortex (Supplementary Figure S3B), *Campilobacterota*, *Cyanobacteria*, *Proteobacteria*, and *unclassified_Bacteria* were positively correlated with adenosine. *Proteobacteria* also showed positive correlations with L-glutamic acid, ethanolamine, and 2-aminobenzoic acid. In the intestine (Supplementary Figure S3C), *Cyanobacteria* exhibited negative correlations with scyllo-inositol, palmitic acid, palmitelaidic acid, and myristic acid, while *Patescibacteria* showed positive correlations with these metabolites. *Bacteroidota* exhibited negative correlations with palmitelaidic acid and myristic acid. In the serum (Supplementary Figure S3D), *Patescibacteria* showed positive correlations with several metabolites, including citric acid, glycine, and L-alanine. *Cyanobacteria* and *unclassified_Bacteria* exhibited negative correlations with serine, pyroglutamic acid, and L-alanine.

At the genus level, several bacterial genera, including *Alistipes*, *Alloprevotella*, *Bifidobacterium*, and *Candidatus Saccharimonas*, showed strong correlations with various metabolites in the hippocampus (Figure 6A). Specifically, *Alloprevotella*, *Bifidobacterium*, and *Muribaculum* exhibited positive correlations with metabolites such as serine, o-phosphoethanolamine, L-threonine, glycine, gamma-aminobutyric acid, formamide, and ethanolamine. In contrast, *Alistipes*, *Candidatus Saccharimonas*, and *Lachnospiraceae NK4A136 group* were negatively correlated with these same metabolites. In the cortex (Figure 6B), *Alloprevotella* showed

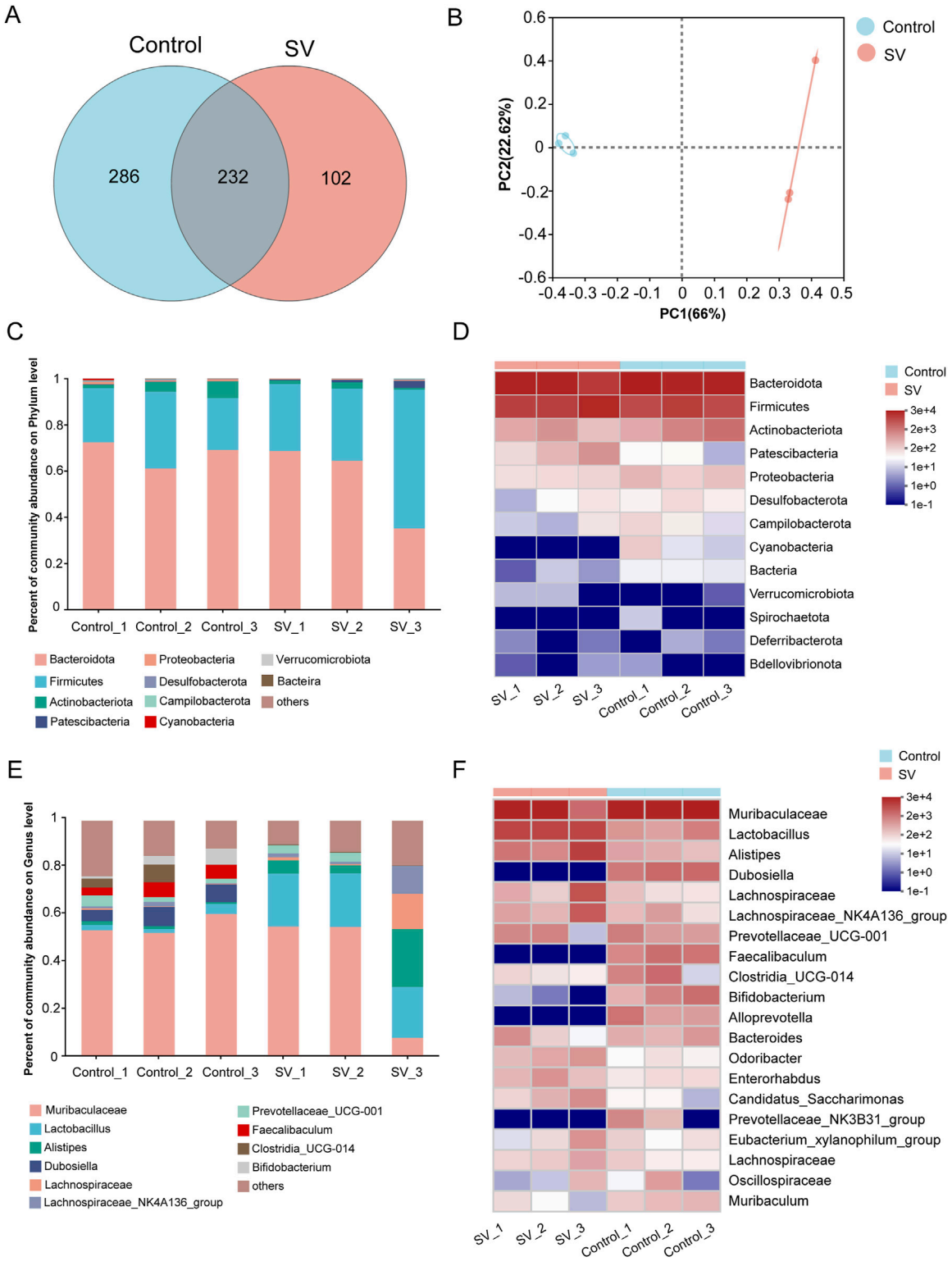

FIGURE 5
The changes of gut microbiota induced by SV treatment. **(A)** OTU distribution Venn diagram. **(B)** PCoA on OUT level between SV and control groups. **(C)** Histogram of gut microflora at the phylum level. **(D)** Heatmap of gut microflora at the phylum level. **(E)** Histogram of gut microflora at the genus level. **(F)** Heatmap of gut microflora at the genus level.

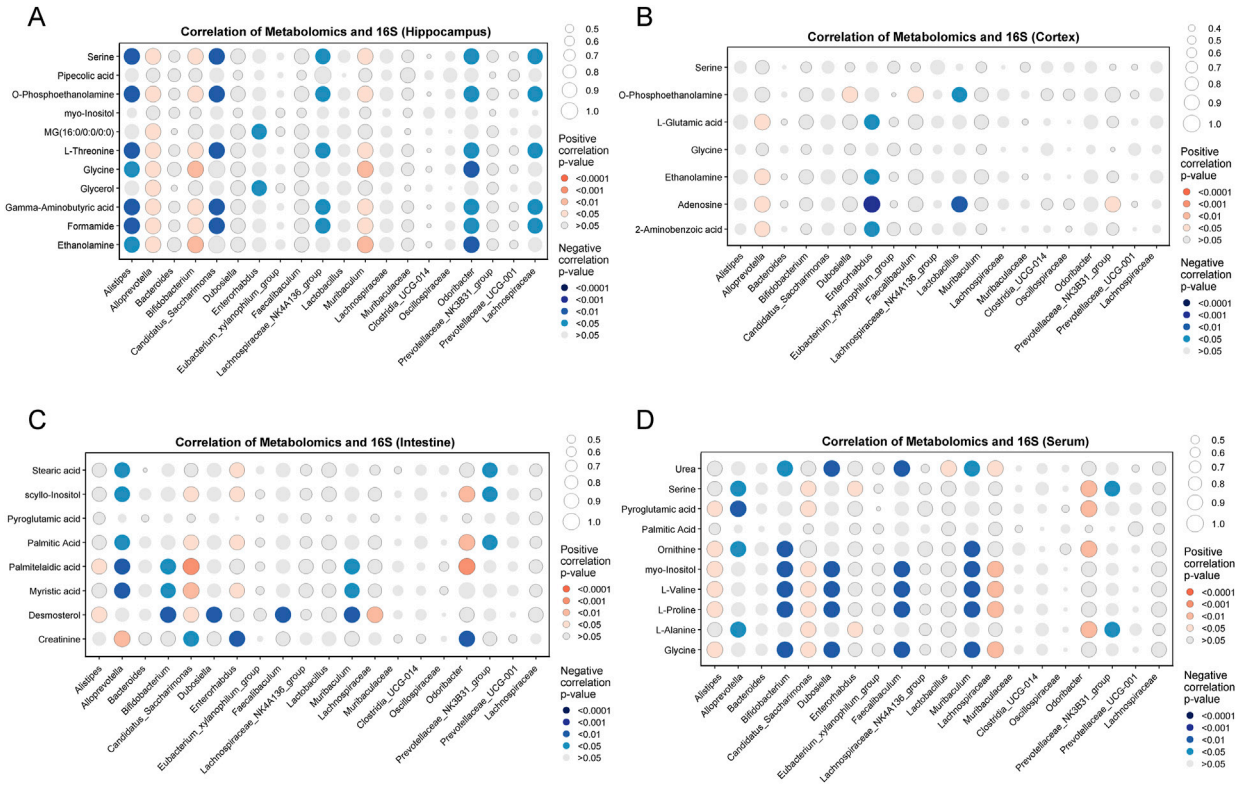

FIGURE 6
Spearman correlation analysis of metabolites and gut microbiota at the genus level. **(A)** Hippocampus, **(B)** cortex, **(C)** intestine, and **(D)** serum. Red: positive correlations, blue: negative correlations.

positive correlations with L-glutamic acid, glycine, adenosine, and 2-aminobenzoic acid, while *Enterorhabdus* exhibited negative correlations with these metabolites. Additionally, *Lactobacillus* was negatively correlated with adenosine, while the *Prevotellaceae NK3B31 group* showed a positive correlation. In the intestine (Figure 6C), *Alloprevotella*, *Bifidobacterium*, and *Muribaculum* were negatively correlated with palmitic acid and myristic acid, whereas *Candidatus Saccharimonas* was positively correlated with these metabolites. In the serum (Figure 6D), *Alistipes*, *Candidatus Saccharimonas*, and *Lachnoclostridium* were found to have positive correlations with several key metabolites, including glycine, L-proline, L-valine, and myo-inositol. Similarly, *Bifidobacterium*, *Dubosiella*, *Faecalibaculum*, and *Muribaculum* also exhibited positive correlations with these metabolites. Additionally, *Bifidobacterium*, *Dubosiella*, *Faecalibaculum*, and *Muribaculum* were negatively correlated with urea.

Discussion

SV is a widely used anticonvulsant drug that modulates γ-aminobutyric acid (GABA) [43–46]. Studies suggest that SV likely improves psychotic symptoms by inhibiting presynaptic GABA transaminase (the enzyme responsible for catalyzing the breakdown of GABA into succinic semialdehyde), stimulating glutamate decarboxylase (the enzyme that catalyzes the synthesis of GABA from glutamate), or indirectly increasing presynaptic GABA levels through negative feedback, thereby inducing its release [47, 48]. SV may also regulate the activity of dopamine, serotonin, and glutamate, thus playing a role in improving symptoms of schizophrenia and behavioral disorders. Although SV was historically regarded as a drug with minimal side effects and was extensively used in clinical practice [49–51], however, it has been shown that SV can induce hepatotoxicity, hematotoxicity and neurotoxicity [23, 24, 52]. For example, prenatal exposure to SV increases the risk of a range of fetal disorders, including anencephaly, developmental delay, cognitive impairment, autism, and neural tube defects such as spina bifida [53–55]. Studies in rodent models have demonstrated that prenatal SV exposure can result in core symptoms resembling those observed in individuals with autism spectrum disorder (ASD) [56, 57]. Additionally, several studies have reported cognitive impairments in SV-induced autism-like models [56–59]. However, studies investigating the specific mechanisms underlying SV-induced autism remain limited.

For example, Rahel Feleke et al. [60] found that a group of genes downregulated by valproic acid (VPA) were significantly enriched in pathways related to neurodevelopment and synaptic function, as well as in genetic traits associated with human intelligence, schizophrenia, and bipolar disorder. Park et al. [61] reported that in a VPA-induced ASD mouse model, upregulation of Rnf146 led to dysregulation of the Wnt/β-catenin signaling pathway, resulting in impaired social behaviors in mice. Hyo Sang Go et al. [62] demonstrated that VPA could activate the NF-κB signaling pathway and upregulate Bcl-XL, thereby inhibiting normal apoptosis of neural progenitor cells, which may contribute to the neurodevelopmental defects observed in fetal valproate syndrome. In our study, we used a mouse model of autism induced by SV exposure to further investigate the causes of SV-induced autism pathogenesis through untargeted metabolomics combined with gut microbial 16S RNA sequencing.

As researchers continue to focus on autism, the pathogenesis of autism is becoming clearer. Some studies have shown that autism is associated with abnormalities in the body's metabolism. A report conducted by Tărlungeanu et al. indicated that disrupted amino acid metabolism is a crucial cause of ASD [63]. A recent study has indicated an association between amino acid synthesis/metabolism and attention deficit/hyperactivity disorder or depression [64]. In a study linking polymorphisms for the risk of autism to protein interaction networks in cortex, amino acid synthesis/metabolism ranks the highest score among the biological pathways [65]. Similarly, Brister et al. also uncovered that the dysfunction of amino acid synthesis/metabolism is observed in participants with ASD, which is related to neurodevelopment and affects ASD-related symptoms [66]. We hypothesized that amino acid synthesis/metabolism might be affected by SV treatment. We found that glycine and serine were reduced in the hippocampus of SV-treated mice. Glycine is a well-known non-essential amino acid that possesses anti-inflammatory capability. Research has shown that as the inflammatory status is an important pathological feature in ASD progression, supplementation with glycine in diet may have therapeutic potential for patients with ASD [67]. Meanwhile, similar to gamma-Aminobutyric acid, glycine acts as an excitatory neurotransmitter to depolarize membrane potentials during the early development of central nervous system [68]. It must shift from excitatory to inhibitory neurotransmitter at birth and maturation, otherwise it may lead to the occurrence of ASD [69]. Serine, derived from glycine, is an effective coagonist of N-methyl-D-aspartate receptor in brain areas and its absence has been reported to be associated with the pathogenesis of neurological disorders [70, 71]. It has been demonstrated that the glycine/serine sites on the N-methyl-D-aspartate receptors can serve as a target for the treatment of ASD [72]. These public data uncovered the great importance of glycine and serine metabolism. These results implied that the decrease of glycine and serine caused by SV-exposed may be related to the development of ASD in mice.

Furthermore, our study suggests that disorders of lipid metabolism occur in autism. Lipids in the brain may influence emotional and perception behaviors, leading to depression and anxiety disorders [73]. The central nervous system (CNS) mainly consists of phospholipids (e.g., phosphatidylcholine), sphingolipids (e.g., ceramides), and sterols (e.g., cholesterol), while the content of neutral glycerides is relatively low under physiological conditions. However, some studies have indicated that certain neutral lipids may also be involved in the regulation of neurological diseases [74]. Neutral lipids can be incorporated into lipid droplets. Lipid droplets establish functional contact sites with other organelles such as mitochondria and the endoplasmic reticulum (ER), playing crucial roles in intracellular signaling and metabolism to promote metabolic cross-talk and regulation. Furthermore, although lipid droplets are typically scarce in a healthy CNS, substantial accumulation of lipid droplets has been observed predominantly in glial cells in the aging brain and in neurodegenerative diseases such as multiple sclerosis, Alzheimer's disease, Parkinson's disease, and Huntington's disease, due to imbalances in lipid uptake, synthesis, and mobilization [74]. This implies that disorders of lipid metabolism might be associated with the development of ASD. In our study, we performed KEGG pathway enrichment analysis of differential metabolites in different tissues of ASD mice, and the results showed that autism caused by SV exposure was associated with the biosynthesis of multiple fatty acids and the glycerophospholipid metabolic pathway. These results suggest that we believe that SV-induced disorders of lipid-phospholipid metabolism may be one of the major causes of ASD development.

The *Firmicutes* phylum and *Bacteroidota* phylum are the major components of the gut microbiota. We found that both in the control and SV groups, *Firmicutes* phylum and *Bacteroidota* phylum were indeed the major components of gut microbiota. These indicated that SV had few effects on these two microbial communities. Notably, a recent study demonstrated that the abundances of *Cyanobacteria* were increased with age in typically developing individuals compared to the patients with ASD [75]. Interestingly, in patients with late-life depression, higher abundances of *Patescibacteria* and *Verrucomicrobiota* were observed [76]. We therefore speculated that there may be similar alterations in SV-induced autism mice. In this study, we found that the abundances of *Patescibacteria* and *Verrucomicrobiota* were increased but *Cyanobacteria* and *unclassified_Bacteria* were decreased following SV treatment. There results indicated that SV treatment could result in gut microbiota components changes at the phylum level. At the genus level, the mice treatment with SV showed more altered genera, including the decrease abundances of *Dubosiella*, *Faecalibaculum*, *Clostridia_UCG-014*, and *Bifidobacterium* and the increase abundances of *Lactobacillus*, *Alistipes*,

Lachnospiraceae, and *Lachnospiraceae_NK4A136*. Our results lend credence to some published findings suggesting that the decrease abundances of the *Dubosiella* and *Bifidobacterium* were associated with the development of ASD [75, 77]. Several microorganisms can mediate gut–brain signaling through inducing host production of neurotransmitters and metabolites, and generating some neuroactive compounds themselves [78]. For instance, *Bifidobacterium* and *Parabacteroides* can produce gamma-Aminobutyric acid, a key neurotransmitter in the brain system [79]. We therefore believed that SV treatment may mediate microbiota-gut-brain-axis to induce neurotoxicity in autism mice through decreasing the abundance of *Bifidobacterium* in intestine tissues.

Since microorganisms can affect host production of metabolites, we then explored the relationship between gut microbes and metabolic changes in mice with ASD. Currently, numerous studies have demonstrated correlations between changes in the gut microbiome and metabolome. For instance, Wu et al. [80] reported that blood metabolites associated with impaired glycemic control were linked to alterations in the gut microbiota. Fu et al. [81] found that the gut microbiota could influence the development of inflammatory bowel disease (IBD) by modulating bile acid metabolism. Liu et al. [82] also demonstrated a relationship between the gut microbiota and lipid metabolism. Moreover, several studies have shown that alterations in the gut microbiota can impact brain metabolism and subsequently regulate the development of various diseases. For example, Wang et al. [83] found that the gut microbiota regulated insomnia-like behaviors via the gut-brain metabolic axis. Similarly, Xiao et al. [84] demonstrated that fecal microbiota transplantation (FMT) could ameliorate gut dysbiosis, cognitive decline, and depression-like behaviors induced by bilateral common carotid artery occlusion (BCCAO), possibly by increasing the relative abundance of short-chain fatty acid (SCFA)-producing bacteria and enhancing SCFA levels, thereby alleviating chronic cerebral hypoperfusion (CCH) injury.

The results of the analysis show that in hippocampus, *Bifidobacterium* was positively correlated with serine and glycine, while *Alistipes* was negatively correlated with them. Meanwhile, in cortex, similar patterns were observed in spite of no significant differences. These results implied that SV challenge may affect glycine, serine and threonine metabolism and further influence the abundances of *Bifidobacterium* and *Alistipes* via gut-brain-axis, eventually leading to the development of ASD. Additionally, gut microbiota may have direct or indirect effects on drug metabolism, such as providing a series of additional reactions and modulating drug metabolism in host [85]. Although it has been confirmed that there are some interactions between the microbiota-gut-brain-axis and brain disorders including ASD [86, 87], the potential association between gut microbiome changes and the brain metabolic alterations influenced by SV remains unclear.

Although this study, through multi-omics integration, revealed associations between gut microbiota-metabolite alterations and autism-like behaviors induced by SV exposure, certain limitations remain. While our findings suggest that SV exposure leads to dysbiosis of gut microbiota in mice, further studies utilizing fecal microbiota transplantation or germ-free animal models are necessary to validate the underlying mechanisms. Furthermore, KEGG pathway analysis indicated a potential association between lipid metabolism and the pathogenesis of autism. In future studies, we plan to quantify free fatty acids in intestinal tissues and employ techniques such as Oil Red O staining, intestinal electron microscopy, and targeted lipidomic profiling to investigate impairments in lipid absorption and storage induced by SV exposure. In addition, we intend to extend our research to clinical settings by comparing metabolomic profiles of autism patients with those of SV-induced autism mouse models. By analyzing the shared and distinct metabolic alterations between human patients and animal models, we aim to achieve a more comprehensive understanding of the metabolic disturbances and underlying mechanisms involved in autism spectrum disorder.

Finally, although this study highlights the potential involvement of gut microbiota-metabolite associations in SV-induced autism, it only provides preliminary insights into possible mechanisms underlying SV-induced autism, and does not constitute clinical validation. Therefore, these preclinical findings should not be used to encourage dietary or probiotic interventions without medical supervision.

Conclusion

SV exposure led to toxicity associated with gut microbiota and metabolomic pathways changes in autism mice. SV treatment mainly disrupted lipid metabolism and amino acid synthesis/metabolism in hippocampus and cortex, and more importantly, disturbed glycine, serine and threonine metabolism in hippocampus. Additionally, SV decreased the abundances of *Bifidobacterium*, and increased *Alistipes* abundance. These may be an important regulatory mechanism for SV-caused ASD.

Author contributions

Conceptualization, LL and YC; Methodology, YM, XG, QW, WQ, HS, YH, XD, YF; Software, YM, XG, QW, WQ, HS, YH, XD, YF; Validation, LL and YC; Investigation, SZ and XZ; Writing-Original Draft Preparation, SZ and XZ; Writing-Review and Editing, all authors; Visualization, SZ and XZ; Supervision, LL and YC. All authors contributed to the article and approved the submitted version.

Data availability

The datasets presented in this study can be found in online repositories. The names of the repository/repositories and accession number(s) can be found in the article/ Supplementary Material. The metabolomics data presented in the study are deposited in the metabolights repository, accession number MTBLS10013. The 16S rRNA data presented in the study are deposited in the NCBI BioProject repository, accession number PRJNA1103334.

Ethics statement

The animal study was approved by Ethical Committee for Animal Experimentation of Jining No. 1 People's Hospital. The study was conducted in accordance with the local legislation and institutional requirements. Ethics approval number: JNRM-2023-DW-034.

Funding

The author(s) declare that financial support was received for the research and/or publication of this article. The experiments in this study were completed with the support of internal institutional funding.

Acknowledgments

We acknowledge the strong support of Jining Maternal and Child Health Family Planning Service Center, Zoucheng People's Hospital, Shandong Yiyang Health Group Baodian Mining Hospital and Jining No.1 People's Hospital.

Conflict of interest

The author(s) declared no potential conflicts of interest with respect to the research, authorship, and/or publication of this article.

Generative AI statement

The author(s) declare that no Generative AI was used in the creation of this manuscript.

Supplementary material

The Supplementary Material for this article can be found online at: https://www.ebm-journal.org/articles/10.3389/ebm.2025.10452/full#supplementary-material

SUPPLEMENTARY FIGURE 1
Representative GC–MS TICs of QC from **(A)** hippocampus, **(B)** cortex, **(C)** intestine and **(D)** serum.

SUPPLEMENTARY FIGURE 2
Alpha-diversity was investigated using the **(A)** Ace, **(B)** Chao, and **(C)** coverage indexes.

SUPPLEMENTARY FIGURE 3
Spearman correlation analysis of metabolites and gut microbiota at the phylum level. **(A)** Hippocampus, **(B)** cortex, **(C)** intestine, and **(D)** serum. Red: positive correlations, blue: negative correlations.

References

1. Hyman SL, Levy SE, Myers SM, Council On Children With Disabilities SOD, Behavioral P. Identification, evaluation, and management of children with autism spectrum disorder. *Pediatrics* (2020) 145. doi:10.1542/peds.2019-3447

2. Fakhoury M. Autistic spectrum disorders: a review of clinical features, theories and diagnosis. *Int J Developmental Neurosci* (2015) **43**:70–7. doi:10.1016/j.ijdevneu.2015.04.003

3. Nazeer A, Ghaziuddin M. Autism spectrum disorders: clinical features and diagnosis. *Pediatr Clin North America* (2012) **59**:19–25. ix. doi:10.1016/j.pcl.2011.10.007

4. Arafat EA, Shabaan DA. The possible neuroprotective role of grape seed extract on the histopathological changes of the cerebellar cortex of rats prenatally exposed to valproic acid: animal model of autism. *Acta Histochem* (2019) **121**:841–51. doi:10.1016/j.acthis.2019.08.002

5. Bernard S, Enayati A, Redwood L, Roger H, Binstock T. Autism: a novel form of mercury poisoning. *Med Hypotheses* (2001) **56**:462–71. doi:10.1054/mehy.2000.1281

6. Chaste P, Leboyer M. Autism risk factors: genes, environment, and gene-environment interactions. *Dialogues Clin Neurosci* (2012) **14**:281–92. doi:10.31887/dcns.2012.14.3/pchaste

7. Kelly E, Meng F, Fujita H, Morgado F, Kazemi Y, Rice LC, et al. Regulation of autism-relevant behaviors by cerebellar-prefrontal cortical circuits. *Nat Neurosci* (2020) **23**:1102–10. doi:10.1038/s41593-020-0665-z

8. Hranilović D, Bujas-Petković Z, Tomičić M, Bordukalo-Nikšić T, Blažević S, Čičin-Šain L. Hyperserotonemia in autism: activity of 5HT-associated platelet proteins. *J Neural Transm (Vienna)* (2009) **116**:493–501. doi:10.1007/s00702-009-0192-2

9. Kern JK, Jones AM. Evidence of toxicity, oxidative stress, and neuronal insult in autism. *J Toxicol Environ Health B* (2006) **9**:485–99. doi:10.1080/10937400600882079

10. Dai YC, Zhang HF, Schon M, Bockers TM, Han SP, Han JS, et al. Neonatal oxytocin treatment ameliorates autistic-like behaviors and oxytocin deficiency in valproic acid-induced rat model of autism. *Front Cell Neurosci* (2018) **12**:355. doi:10.3389/fncel.2018.00355

11. Pham C, Symeonides C, O'Hely M, Sly PD, Knibbs LD, Thomson S, et al. Early life environmental factors associated with autism spectrum disorder symptoms in children at age 2 years: a birth cohort study. *Autism* (2022) **26**:1864–81. doi:10.1177/13623613211068223

12. Pragnya B, Kameshwari JS, Veeresh B. Ameliorating effect of piperine on behavioral abnormalities and oxidative markers in sodium valproate induced autism in BALB/C mice. *Behav Brain Res* (2014) **270**:86–94. doi:10.1016/j.bbr.2014.04.045

13. Pinkston R, Walker LA. Multiorgan system failure caused by valproic acid toxicity. *The Am J Emerg Med* (1997) **15**:504–6. doi:10.1016/s0735-6757(97)90195-9

14. Davis LL, Ryan W, Adinoff B, Petty F. Comprehensive review of the psychiatric uses of valproate. *J Clin Psychopharmacol* (2000) **20**:1S–17S. doi:10.1097/00004714-200002001-00001

15. Nemeroff CB. An ever-increasing pharmacopoeia for the management of patients with bipolar disorder. *J Clin Psychiatry* (2000) **61 Supp 13**(Suppl. 13):19–25.

16. Santos de Oliveira R, Lajeunie E, Arnaud E, Renier D. Fetal exposure to sodium valproate associated with baller-gerold syndrome: case report and review of the literature. *Childs Nerv Syst* (2006) **22**:90–4. doi:10.1007/s00381-004-1089-x

17. Markram K, Rinaldi T, Mendola DL, Sandi C, Markram H. Abnormal fear conditioning and amygdala processing in an animal model of autism. *Neuropsychopharmacology* (2008) **33**:901–12. doi:10.1038/sj.npp.1301453

18. Schneider T, Przewłocki R. Behavioral alterations in rats prenatally exposed to valproic acid: animal model of autism. *Neuropsychopharmacology* (2005) **30**:80–9. doi:10.1038/sj.npp.1300518

19. Schneider T, Labuz D, Przewłocki R. Nociceptive changes in rats after prenatal exposure to valproic acid. *Pol J Pharmacol* (2001) **53**:531–4.

20. Bairy L, Paul V, Rao Y. Reproductive toxicity of sodium valproate in male rats. *Indian J Pharmacol* (2010) **42**:90–4. doi:10.4103/0253-7613.64503

21. Hamza AA, Amin A. Apium graveolens modulates sodium valproate-induced reproductive toxicity in rats. *J Exp Zoolog A: Ecol Genet Physiol* (2007) **307A**: 199–206. doi:10.1002/jez.357

22. Sivathanu S, Sampath S, Veerasamy M, Sunderkumar S. Encephalopathy in an infant with infantile spasms: possible role of valproate toxicity. *BMJ Case Rep* (2014) **2014**:bcr2013200895. doi:10.1136/bcr-2013-200895

23. Mei X, Wu HC, Ruan M, Cai LR. Acute liver failure with thrombotic microangiopathy due to sodium valproate toxicity: a case report. *World J Clin Cases* (2021) **9**:4310–7. doi:10.12998/wjcc.v9.i17.4310

24. Acharya S, Bussel JB. Hematologic toxicity of sodium valproate. *J Pediatr Hematology/Oncology* (2000) **22**:62–5. doi:10.1097/00043426-200001000-00012

25. Rinaldi T, Kulangara K, Antoniello K, Markram H. Elevated NMDA receptor levels and enhanced postsynaptic long-term potentiation induced by prenatal exposure to valproic acid. *Proc Natl Acad Sci U S A* (2007) **104**:13501–6. doi:10.1073/pnas.0704391104

26. Collins J, Borojevic R, Verdu EF, Huizinga JD, Ratcliffe EM. Intestinal microbiota influence the early postnatal development of the enteric nervous system. *Neurogastroenterology & Motil* (2014) **26**:98–107. doi:10.1111/nmo.12236

27. Dabke K, Hendrick G, Devkota S. The gut microbiome and metabolic syndrome. *J Clin Invest* (2019) **129**:4050–7. doi:10.1172/jci129194

28. Zheng D, Liwinski T, Elinav E. Interaction between microbiota and immunity in health and disease. *Cell Res* (2020) **30**:492–506. doi:10.1038/s41422-020-0332-7

29. Santocchi E, Guiducci L, Fulceri F, Billeci L, Buzzigoli E, Apicella F, et al. Gut to brain interaction in autism spectrum disorders: a randomized controlled trial on the role of probiotics on clinical, biochemical and neurophysiological parameters. *BMC Psychiatry* (2016) **16**:183. doi:10.1186/s12888-016-0887-5

30. Dinan TG, Cryan JF. The microbiome-gut-brain axis in health and disease. *Gastroenterol Clin North America* (2017) **46**:77–89. doi:10.1016/j.gtc.2016.09.007

31. Muszer M, Noszczyńska M, Kasperkiewicz K, Skurnik M. Human microbiome: when a friend becomes an enemy. *Arch Immunol Ther Exp (Warsz)* (2015) **63**:287–98. doi:10.1007/s00005-015-0332-3

32. Petra AI, Panagiotidou S, Hatziagelaki E, Stewart JM, Conti P, Theoharides TC. Gut-microbiota-brain axis and its effect on neuropsychiatric disorders with suspected immune dysregulation. *Clin Ther* (2015) **37**:984–95. doi:10.1016/j.clinthera.2015.04.002

33. Fulceri F, Morelli M, Santocchi E, Cena H, Del Bianco T, Narzisi A, et al. Gastrointestinal symptoms and behavioral problems in preschoolers with autism spectrum disorder. *Dig Liver Dis* (2016) **48**:248–54. doi:10.1016/j.dld.2015.11.026

34. Iovene MR, Bombace F, Maresca R, Sapone A, Iardino P, Picardi A, et al. Intestinal dysbiosis and yeast isolation in stool of subjects with autism spectrum disorders. *Mycopathologia* (2017) **182**:349–63. doi:10.1007/s11046-016-0068-6

35. Kang DW, Park JG, Ilhan ZE, Wallstrom G, Labaer J, Adams JB, et al. Reduced incidence of prevotella and other fermenters in intestinal microflora of autistic children. *PLoS One* (2013) **8**:e68322. doi:10.1371/journal.pone.0068322

36. Dinan TG, Cryan JF. Gut instincts: microbiota as a key regulator of brain development, ageing and neurodegeneration. *The J Physiol* (2017) **595**:489–503. doi:10.1113/jp273106

37. Vuong HE, Yano JM, Fung TC, Hsiao EY. The microbiome and host behavior. *Annu Rev Neurosci* (2017) **40**:21–49. doi:10.1146/annurev-neuro-072116-031347

38. Eissa N, Azimullah S, Jayaprakash P, Jayaraj RL, Reiner D, Ojha SK, et al. The dual-active histamine H3 receptor antagonist and acetylcholine esterase inhibitor E100 ameliorates stereotyped repetitive behavior and neuroinflammmation in sodium valproate induced autism in mice. *Chemico-Biological Interactions* (2019) **312**:108775. doi:10.1016/j.cbi.2019.108775

39. Fairless AH, Katz JM, Vijayvargiya N, Dow HC, Kreibich AS, Berrettini WH, et al. Development of home cage social behaviors in BALB/cJ vs. C57BL/6J mice. *Behav Brain Res* (2013) **237**:338–47. doi:10.1016/j.bbr.2012.08.051

40. Sankoorikal GM, Kaercher KA, Boon CJ, Lee JK, Brodkin ES. A mouse model system for genetic analysis of sociability: C57BL/6J *versus* BALB/cJ inbred mouse strains. *Biol Psychiatry* (2006) **59**:415–23. doi:10.1016/j.biopsych.2005.07.026

41. Lucchina L, Depino AM. Altered peripheral and central inflammatory responses in a mouse model of autism. *Autism Res* (2014) **7**:273–89. doi:10.1002/aur.1338

42. Fatemi I, Delrobaee F, Bahmani M, Shamsizadeh A, Allahtavakoli M. The effect of the anti-diabetic drug metformin on behavioral manifestations associated with ovariectomy in mice. *Neurosci Lett* (2019) **690**:95–8. doi:10.1016/j.neulet.2018.10.024

43. Fukuchi M, Nii T, Ishimaru N, Minamino A, Hara D, Takasaki I, et al. Valproic acid induces up- or down-regulation of gene expression responsible for the neuronal excitation and inhibition in rat cortical neurons through its epigenetic actions. *Neurosci Res* (2009) **65**:35–43. doi:10.1016/j.neures.2009.05.002

44. Janszky J, Tényi D, Bóné B. Valproate in the treatment of epilepsy and status epilepticus. *Ideggyogy Sz* (2017) **70**:258–64. doi:10.18071/isz.70.0258

45. Gagnon DJ, Fontaine GV, Riker RR, Fraser GL. Repurposing valproate, enteral clonidine, and phenobarbital for comfort in adult ICU patients: a literature review with practical considerations. *Pharmacotherapy* (2017) **37**:1309–21. doi:10.1002/phar.2017

46. Quinn NJ, Hohlfelder B, Wanek MR, Duggal A, Torbic H. Prescribing practices of valproic acid for agitation and delirium in the intensive care unit. *Ann Pharmacother* (2021) **55**:311–7. doi:10.1177/1060028020947173

47. Löscher W. Basic pharmacology of valproate: a review after 35 years of clinical use for the treatment of epilepsy. *CNS Drugs* (2002) **16**:669–94. doi:10.2165/00023210-200216100-00003

48. Löscher W. Valproate: a reappraisal of its pharmacodynamic properties and mechanisms of action. *Prog Neurobiol* (1999) **58**:31–59. doi:10.1016/s0301-0082(98)00075-6

49. Rakitin A, Eglit T, Kõks S, Lember M, Haldre S. Comparison of the metabolic syndrome risk in valproate-treated patients with epilepsy and the general population in Estonia. *PLoS One* (2014) **9**:e103856. doi:10.1371/journal.pone.0103856

50. Rakitin A, Kõks S, Reimann E, Prans E, Haldre S. Changes in the peripheral blood gene expression profile induced by 3 months of valproate treatment in patients with newly diagnosed epilepsy. *Front Neurol* (2015) **6**:188. doi:10.3389/fneur.2015.00188

51. Rakitin A, Kõks S, Haldre S. Metabolic syndrome and anticonvulsants: a comparative study of valproic acid and carbamazepine. *Seizure* (2016) **38**:11–6. doi:10.1016/j.seizure.2016.03.008

52. Triyasakorn K, Ubah UDB, Roan B, Conlin M, Aho K, Awale PS. The antiepileptic drug and toxic teratogen valproic acid alters microglia in an environmental mouse model of autism. *Toxics* (2022) **10**:379. doi:10.3390/toxics10070379

53. Rasalam AD, Hailey H, Williams JH, Moore SJ, Turnpenny PD, Lloyd DJ, et al. Characteristics of fetal anticonvulsant syndrome associated autistic disorder. *Dev Med Child Neurol* (2005) **47**:551–5. doi:10.1017/s0012162205001076

54. Koren G, Nava-Ocampo AA, Moretti ME, Sussman R, Nulman I. Major malformations with valproic acid. *Can Fam Physician* (2006) **52**:441–7.

55. Christensen J, Grønborg TK, Sørensen MJ, Schendel D, Parner ET, Pedersen LH, et al. Prenatal valproate exposure and risk of autism spectrum disorders and childhood autism. *Jama* (2013) **309**:1696–703. doi:10.1001/jama.2013.2270

56. Nicolini C, Fahnestock M. The valproic acid-induced rodent model of autism. *Exp Neurol* (2018) **299**:217–27. doi:10.1016/j.expneurol.2017.04.017

57. Manzo J, Hernández-Aguilar ME, Toledo-Cárdenas MR, Herrera-Covarrubias D, Coria-Avila GA. Dysregulation of neural tube vascular development as an aetiological factor in autism spectrum disorder: insights from valproic acid exposure. *The J Physiol* (2025). doi:10.1113/jp286899

58. Zohny SM, Habib MZ, Mohamad MI, Elayat WM, Elhossiny RM, El-Salam MFA, et al. Memantine/aripiprazole combination alleviates cognitive dysfunction in valproic acid rat model of autism: hippocampal CREB/BDNF signaling and glutamate homeostasis. *Neurotherapeutics* (2023) **20**:464–83. doi:10.1007/s13311-023-01360-w

59. Taheri F, Joushi S, Esmaeilpour K, Ebrahimi MN, Taherizadeh Z, Taheri P, et al. Transmission of behavioral and cognitive impairments across generations in rats subjected to prenatal valproic acid exposure. *Birth Defects Res* (2024) **116**: e2309. doi:10.1002/bdr2.2309

60. Feleke R, Jazayeri D, Abouzeid M, Powell KL, Srivastava PK, O'Brien TJ, et al. Integrative genomics reveals pathogenic mediator of valproate-induced neurodevelopmental disability. *Brain* (2022) **145**:3832–42. doi:10.1093/brain/awac296

61. Park G, Jang WE, Kim S, Gonzales EL, Ji J, Choi S, et al. Dysregulation of the Wnt/β-catenin signaling pathway via Rnf146 upregulation in a VPA-induced mouse model of autism spectrum disorder. *Exp Mol Med* (2023) **55**:1783–94. doi:10.1038/s12276-023-01065-2

62. Go HS, Seo JE, Kim KC, Han SM, Kim P, Kang YS, et al. Valproic acid inhibits neural progenitor cell death by activation of NF-κB signaling pathway and up-regulation of Bcl-XL. *J Biomed Sci* (2011) **18**:48. doi:10.1186/1423-0127-18-48

63. Tărlungeanu DC, Deliu E, Dotter CP, Kara M, Janiesch PC, Scalise M, et al. Impaired amino acid transport at the blood brain barrier is a cause of autism spectrum disorder. *Cell* (2016) **167**:1481–94.e18. doi:10.1016/j.cell.2016.11.013

64. Yang J, Yan B, Zhao B, Fan Y, He X, Yang L, et al. Assessing the causal effects of human serum metabolites on 5 major psychiatric disorders. *Schizophrenia Bull* (2020) **46**:804–13. doi:10.1093/schbul/sbz138

65. Golovina E, Fadason T, Lints TJ, Walker C, Vickers MH, O'Sullivan JM. Understanding the impact of SNPs associated with autism spectrum disorder on biological pathways in the human fetal and adult cortex. *Sci Rep* (2021) **11**:15867. doi:10.1038/s41598-021-95447-z

66. Brister D, Rose S, Delhey L, Tippett M, Jin Y, Gu H, et al. Metabolomic signatures of autism spectrum disorder. *J Personalized Med* (2022) **12**:1727. doi:10.3390/jpm12101727

67. van Sadelhoff JHJ, Perez Pardo P, Wu J, Garssen J, van Bergenhenegouwen J, Hogenkamp A, et al. The gut-immune-brain axis in autism spectrum disorders; A focus on amino acids. *Front Endocrinol (Lausanne)* (2019) **10**:247. doi:10.3389/fendo.2019.00247

68. Kaila K, Price TJ, Payne JA, Puskarjov M, Voipio J. Cation-chloride cotransporters in neuronal development, plasticity and disease. *Nat Rev Neurosci* (2014) **15**:637–54. doi:10.1038/nrn3819

69. Zheng HF, Wang WQ, Li XM, Rauw G, Baker GB. Body fluid levels of neuroactive amino acids in autism spectrum disorders: a review of the literature. *Amino Acids* (2017) **49**:57–65. doi:10.1007/s00726-016-2332-y

70. Ozeki Y, Sekine M, Fujii K, Watanabe T, Okayasu H, Takano Y, et al. Phosphoserine phosphatase activity is elevated and correlates negatively with plasma d-serine concentration in patients with schizophrenia. *Psychiatry Res* (2016) **237**:344–50. doi:10.1016/j.psychres.2016.01.010

71. Deutschenbaur L, Beck J, Kiyhankhadiv A, Muhlhauser M, Borgwardt S, Walter M, et al. Role of calcium, glutamate and NMDA in major depression and therapeutic application. *Prog Neuro-Psychopharmacology Biol Psychiatry* (2016) **64**:325–33. doi:10.1016/j.pnpbp.2015.02.015

72. Basu AC, Tsai GE, Ma CL, Ehmsen JT, Mustafa AK, Han L, et al. Targeted disruption of serine racemase affects glutamatergic neurotransmission and behavior. *Mol Psychiatry* (2009) **14**:719–27. doi:10.1038/mp.2008.130

73. Bozek K, Wei Y, Yan Z, Liu X, Xiong J, Sugimoto M, et al. Organization and evolution of brain lipidome revealed by large-scale analysis of human, chimpanzee, macaque, and mouse tissues. *Neuron* (2015) **85**:695–702. doi:10.1016/j.neuron.2015.01.003

74. Vanherle S, Loix M, Miron VE, Hendriks JJA, Bogie JFJ. Lipid metabolism, remodelling and intercellular transfer in the CNS. *Nat Rev Neurosci* (2025) **26**:214–31. doi:10.1038/s41583-025-00908-3

75. Dan Z, Mao X, Liu Q, Guo M, Zhuang Y, Liu Z, et al. Altered gut microbial profile is associated with abnormal metabolism activity of Autism Spectrum disorder. *Gut Microbes* (2020) **11**:1246–67. doi:10.1080/19490976.2020.1747329

76. Tsai CF, Chuang CH, Wang YP, Lin YB, Tu PC, Liu PY, et al. Differences in gut microbiota correlate with symptoms and regional brain volumes in patients with late-life depression. *Front Aging Neurosci* (2022) **14**:885393. doi:10.3389/fnagi.2022.885393

77. Strati F, Cavalieri D, Albanese D, De Felice C, Donati C, Hayek J, et al. New evidences on the altered gut microbiota in autism spectrum disorders. *Microbiome* (2017) **5**:24. doi:10.1186/s40168-017-0242-1

78. Morais LH, Schreiber HL, Mazmanian SK. The gut microbiota-brain axis in behaviour and brain disorders. *Nat Rev Microbiol* (2021) **19**:241–55. doi:10.1038/s41579-020-00460-0

79. Buckley MM, O'Brien R, Brosnan E, Ross RP, Stanton C, Buckley JM, et al. Glucagon-like Peptide-1 secreting L-Cells coupled to sensory nerves translate microbial signals to the host rat nervous system. *Front Cell Neurosci* (2020) **14**:95. doi:10.3389/fncel.2020.00095

80. Wu H, Lv B, Zhi L, Shao Y, Liu X, Mitteregger M, et al. Microbiome-metabolome dynamics associated with impaired glucose control and responses to lifestyle changes. *Nat Med* (2025) **31**:2222–31. doi:10.1038/s41591-025-03642-6

81. Fu Y, Guzior DV, Okros M, Bridges C, Rosset SL, González CT, et al. Balance between bile acid conjugation and hydrolysis activity can alter outcomes of gut inflammation. *Nat Commun* (2025) **16**:3434. doi:10.1038/s41467-025-58649-x

82. Liu Y, Liu J, Ren R, Xin Z, Luo Y, Chen Y, et al. Short-term and long-term high-fat diet promote metabolic disorder through reprogramming mRNA m(6)A in white adipose tissue by gut microbiota. *Microbiome* (2025) **13**:75. doi:10.1186/s40168-025-02047-4

83. Wang Z, Wang Z, Lu T, Yuan G, Chen W, Jin J, et al. Gut microbiota regulate insomnia-like behaviors via gut-brain metabolic axis. *Mol Psychiatry* (2024) **30**:2597–611. doi:10.1038/s41380-024-02867-0

84. Xiao W, Su J, Gao X, Yang H, Weng R, Ni W, et al. The microbiota-gut-brain axis participates in chronic cerebral hypoperfusion by disrupting the metabolism of short-chain fatty acids. *Microbiome* (2022) **10**:62. doi:10.1186/s40168-022-01255-6

85. Wilson ID, Nicholson JK. Gut microbiome interactions with drug metabolism, efficacy, and toxicity. *Translational Res* (2017) **179**:204–22. doi:10.1016/j.trsl.2016.08.002

86. Maiuolo J, Gliozzi M, Musolino V, Carresi C, Scarano F, Nucera S, et al. The contribution of gut microbiota-brain axis in the development of brain disorders. *Front Neurosci* (2021) **15**:616883. doi:10.3389/fnins.2021.616883

87. Srikantha P, Mohajeri MH. The possible role of the microbiota-gut-brain-axis in autism spectrum disorder. *Int J Mol Sci* (2019) **20**:2115. doi:10.3390/ijms20092115

EBM Experimental Biology and Medicine

TYPE Original Research
PUBLISHED 29 August 2025
DOI 10.3389/ebm.2025.10430

OPEN ACCESS

*CORRESPONDENCE
Fengli Gao,
gaofl2594@163.com

†These authors have contributed equally to this work

RECEIVED 12 November 2024
ACCEPTED 19 August 2025
PUBLISHED 29 August 2025

CITATION
Miao Y, Wang L, Zhao G, Gou W, Chen S, Ding C, Li Z and Gao F (2025) RNA binding proteins potentially regulate alternative splicing of immune-related genes during the progression of coronary artery disease.
Exp. Biol. Med. 250:10430.
doi: 10.3389/ebm.2025.10430

RNA binding proteins potentially regulate alternative splicing of immune-related genes during the progression of coronary artery disease

Yulin Miao[1†], Lei Wang[1†], Gang Zhao[1], Wei Gou[1], Shan Chen[1], Chao Ding[1], Zongxin Li[2] and Fengli Gao[1*]

[1]Department of Vascular Surgery, General Hospital of Ningxia Medical University, Yinchuan, Ningxia, China, [2]The First Clinical Medical College, Ningxia Medical University, Yinchuan, Ningxia, China

Abstract

RNA-binding proteins (RBPs) are crucial in disease as they regulate the biological functions of RNA. However, their role in coronary artery disease (CAD) progression remains unclear. RNA-seq from peripheral blood of CAD patients and no-CAD controls was analyzed to compare differentially expressed genes (DEGs) and explore their potential functions. The distribution of immune cells was assessed by CIBERSORT algorithm. Alternative splicing (AS) pattern was quantified by SUVA. Immune-related AS events (ASEs) were screened via ImmPort database. Co-expression network of ASEs, differentially expressed RBPs (DERBPs), mitochondrion and apoptosis genes, and immune cells was constructed to clarify their potential functions. A total of 1521 DEGs were detected, including 99 DERBPs, which were mainly downregulated and enriched in mRNA processing, RNA splicing, mRNA transport, and innate immune response pathways in CAD. Seven DERBPs (ANG, C4BPA, DDX60, IFIH1, IPO7, MATR3, OTUD4) were associated with immune function. Analysis of the immune cell fraction demonstrated significant increase in macrophage M0 and CD8 T cells and decrease in resting dendritic cells and activated memory CD4 T cells. Immune-related ASEs correlated with atherosclerotic stenosis were mainly the complex "alt3p/alt5p" splicing types. DERBP-AS's co-expression identified a key A5′SS event of CTSB gene. Co-expression of this event with TST and SYNCRIP may lead to a change in the proportion of macrophage M0 and CD8 T cells, respectively. The mitochondrion and apoptosis genes were also dysregulated in CAD and correlated with four DERBPs. In conclusion, RBPs have potential regulatory role in the progression of CAD by regulating the ASEs of immune-related genes and mediating immune cells composition. These findings highlight RBPs as potential therapeutic targets for CAD.

KEYWORDS

RNA-binding proteins, coronary artery disease, alternative splicing, co-expression, immune cells

Impact statement

RNA-binding proteins (RBPs) play important functions in diseases because they regulate the biological function of RNA. However, their role in the pathogenesis of coronary artery disease remains unclear. By analyzing peripheral blood RNA sequencing data of CAD patients and healthy controls, this study found dysregulated RBPs expression in CAD patients, and constructed a potential regulatory network of dysregulated RBPs, immune cells and alternative splicing events. Further analysis suggests that RBPs may influence immune microenvironment remodeling by modulating the alternative splicing pattern of immune genes, thereby promoting the progression of CAD. This study illustrates the important function of RBPs in the pathogenesis of CAD and provides potential targets for CAD treatment in future.

Introduction

Coronary artery disease (CAD) is a group of cardiovascular diseases (CVDs) that lead to myocardial ischemia, hypoxia, necrosis and dysfunction due to insufficient blood supply or blockage of coronary arteries [1]. Despite the continuous development of medicine, CAD is widely diagnosed worldwide, and is recognized as one of the primary causes of mortality and disease burden related to CVD [2]. Atherosclerosis is a major cause of CAD, and atherosclerotic stenosis is an inflammatory phenomenon caused by the accumulation of lipid particles and enrichment of inflammatory cytokines, resulting in structural abnormalities in the vessel lumen [3]. In patients with CAD, lipid plaques form in the lining of the coronary arteries, leading to narrowing of the vessel lumen, preventing normal blood supply to the heart muscle. Over time, lipid plaques gradually increase in size and may rupture, forming thrombi that further block the coronary arteries and cause acute ischemia [4]. As bioinformatics technology develops, studies continue to uncover the underlying mechanisms that mediate the development of CAD, which may lead to new approaches to treating CAD. Immune responses mediate homeostasis and damage repair in cardiac physiology and contribute to metabolism and tissue clearance in the healthy heart. However, long-term immune responses that are not controlled can result in adverse cardiac remodeling and further deterioration of cardiac function [5]. In CAD, each immune cell response may play a crucial role. However, the molecular mechanisms of immune cells involved in developing CAD are not yet fully understood and the exact causes remain unclear.

It has been reported that innate immune cells (such as neutrophils, monocytes, and macrophages) and adaptive immune cells (such as T and B cells) interact closely in the pathogenesis and development of atherosclerosis [3]. Macrophages and lymphocytes exist at all stages of plaque formation and promote CAD progression. A significant increase in inflammatory macrophages can lead to a larger area of atherosclerotic plaque [6]. In CAD patients, the $CD8^+$ T lymphocytes in the peripheral blood is significantly increased, leading to increased production of interferon γ, which exacerbates the atherosclerotic process [7]. In addition, immune cells can accelerate the development of atherosclerosis by regulating the production and circulation of monocytes [8]. Meanwhile, it is not determined how the immune cells are regulated during the development of CAD.

RNA binding proteins (RBPs) can regulate transcription, splicing, modification, translation, localization and transport by binding to target RNAs [9]. RBPs mediate RNA regulation and control translation, which are crucial in angiogenesis [10]. RBPs have critical functions in the initiation, progression and rupture of atherosclerotic plaques by regulating endothelial and vascular structure, immune cell infiltration, and lipid accumulation [11]. Alternative splicing (AS) is one molecular process by which precursor mRNAs (pre-mRNAs) of the same gene can be spliced differently to produce multiple mature mRNAs [12]. Abnormal alternative splicing can result in protein dysfunction, which can lead to various diseases [13]. RBPs are currently a major focus in the study to explore the molecular mechanisms of CAD, and the AS of RBPs and pre-mRNAs has emerged as a key regulator of CAD and is considered to be potential therapeutic targets. The differential expression of RBPs not only affects the tissue-specific splicing pattern, but also affects the alternative splicing transcript of CAD prognostic risk [14]. Further in-depth research is required to investigate how RBPs regulate AS in CAD progression, as there are limited studies on this topic.

In this study, we analyzed transcriptome sequencing data (RNA-seq) from peripheral blood of patients with high coronary artery stenosis (CAD) and healthy controls without coronary artery disease (no-CAD), and focused our attention on the dysregulated RBPs and their potential regulatory functions on the immune cell fractions and alternative splicing pattern within these two groups. We found that the expression of RBPs is dysregulated in the CAD group and may influence the remodeling of the immune microenvironment by regulating alternative splicing of immune-related genes, which expands our understanding of the pathogenesis of CAD.

Materials and methods

Retrieval and process of public data

The published RNA-seq dataset (GSE202625) was downloaded from the Sequence Read Archive (SRA) database with SRA run files, which were then converted to fastq files by NCBI SRA Tool fastq-dump (v.2.8.0). The low-quality bases of raw sequencing reads were trimmed using the FASTX-Toolkit (v.0.0.13;[1]). The removal criteria were the base with terminal mass less than

1 http://hannonlab.cshl.edu/fastx_toolkit/

20 and 30% of the reads whose base quality was less than 20. Then we used to the FastQC[2] check the quality of filtered reads.

RNA-seq alignment and differentially expressed gene (DEG) analysis

The quality-filtered reads were then aligned to the human GRCh38 genome via HISAT2 software (v.2.2.1) [15]. Uniquely aligned reads were used to calculate the reads count located on each gene. The normalized expression level of each gene was evaluated using fragments per kilobase of exon per million fragments (FPKM). The DESeq2 (v.1.30.1) software [16], which analyzes the differential expression between samples, was used to perform differential gene expression analysis using the reads count file, and obtain the DEGs with the fold change (FC ≥2 or ≤0.5) and false discovery rate (FDR ≤0.05).

Extraction of differentially expressed RBPs

Then we extracted the differentially expressed RBPs from all the DEG set according a catalog of 2,141 RBPs that were retrieved from three previous reports [17–19].

Alternative splicing identification and dysregulation analysis

According to the alignment of RNA-seq dataset, the alternative splicing events (ASEs) were identified and quantified by splicing ratios using the SUVA (v2.0) software [20]. The different splicing pattern of each group was analyzed. Reads proportion of SUVA AS event (pSAR) of each AS events were calculated to identify the differential ASEs.

Analysis on immune-related genes

To analyzed the expression pattern of immune-related genes, we retrieved 1793 immune-related genes from the ImmPort database[3] to identify their expression pattern and make an overlap analysis with DEGs in this study.

Analysis on mitochondria-related genes

We also analyzed the expression pattern of 1136 mitochondria-related genes that were extracted from the Human MitoCarta3.0 database [21].

Analysis on apoptosis-related genes

The 87 apoptosis-related genes were obtained from Molecular Signatures database (GSEA | MSigDB).

Cell-type quantification

We used the CIBERSORT algorithm (v1.03) [22] to estimate immune cell fractions with the default parameter. The FPKM values of each expressed gene were used as input. We identified the fractions of 22 human immune cell phenotypes in the study, which have been detailed described in the results part. The fraction difference of each immune cell type were also calculated between CAD and normal groups.

Co-expression analysis

The co-expression analysis of RBP and immune cells was constructed by calculating the Pearson's correlation coefficient between RBP and immune cells. We finally screened out the RBP and immune cell correlation pairs with absolute correlation coefficient ≥0.6 and *P*-value ≤0.01.

The co-expression analysis was performed for immune-related ASEs and RBPs co-expressed with immune cells. Meanwhile, Pearson's correlation coefficient among them was calculated. Immune-related ASE and RBP co-expressed with immune cells pairs with absolute correlation coefficient ≥0.6 and *P*-value ≤0.01 were screened.

Functional enrichment analysis

The enriched Gene Ontology (GO) pathways for selected gene sets were identified using KOBAS 2.0 [23] by calculating p-value using Hypergeometric test and Benjamini-Hochberg FDR controlling procedure to define the significance of each pathway.

Statistical analysis

Principal component analysis (PCA) for expressed genes was performed by R package factoextra[4] to show the clustering of CAD and non-CAD samples with the first two components. The in house-script sogen was used to visualize the genomic distribution and structure of aligned reads for selected genes by normalizing their expression using TPM (Tags Per Million).

2 http://www.bioinformatics.babraham.ac.uk/projects/fastqc

3 https://www.immport.org/shared/genelists

4 https://cloud.r-project.org/package=factoextra

The pheatmap package[5] in R was used to perform gene expression clustering based on Euclidean distance. Student's *t*-test was used for statistical comparison between two groups. The Venn diagram for overlapping analysis is produced using jvenn website (Venn Diagrams-jvenn) [24].

Results

RNA-seq analysis of peripheral blood cells from patients with CAD and no-CAD donors revealed DERBPs

The RNA-seq data for GSE202625 were downloaded and re-analyzed from the GEO database and consisted of 27 CAD patients and 25 no-CAD controls. All CAD patients had confirmed severe coronary atherosclerosis (>70% stenosis in at least one vessel) by coronary computed tomography angiography (CCTA), whereas no-CAD controls had no atherosclerosis. Samples with correlation coefficients ≥0.9 or higher were first extracted, and then outlier samples were excluded; 11 CAD patients and 7 no-CAD controls were finally included in our study. First, we calculated the correlation coefficients for all the samples to evaluate the expression similarity of all samples and their comparability (Figure 1A). The results indicated that the samples within the group were highly correlated and suitable for further analyses. Then, we identified 1521 differentially expressed genes (DEGs) between CAD vs. no-CAD groups. Of these, 784 genes were upregulated and 737 genes were downregulated in the CAD group (Figure 1B). The GO analysis of up-regulated DEGs demonstrated that they were significantly enriched in pathways related to immune response, while the down-regulated DEGs were mainly enriched in cell division, cell cycle, DNA repair, and mRNA processing pathways (Supplementary Figures S1A,B). To validate the classification results based on DEGs, PCA was performed in this study. The two groups were clearly separated by the first or top component (Figure 1C), suggesting that the DEGs are of research significance.

Among the detected DEGs, we found 99 DERBPs (Figure 1D). The expression distribution of DERBPs showed obvious difference between the CAD and no-CAD groups, and most of these DERBPs were down-regulated in CAD (Figure 1E). GO analysis demonstrated that these DERBPs were enriched in biological pathways including mRNA processing, RNA splicing, mRNA transport and innate immune response (Figure 1F). DERBPs are primarily associated with RNA post-transcriptional regulation, and some are also involved in immune response biology. We selected seven immune-related DERBPs, including *ANG, C4BPA, DDX60, IFIH1, IPO7, MATR3*, and *OTUD4*, and found they were significantly differentially expressed between CAD vs. no-CAD groups (Figure 1G). To sum up, there results demonstrate that DERBPs may influence CAD development by mediating immune responses and their potential downstream target genes.

Dynamic changes of DERBP were associated with immune microenvironment regulation in coronary artery disease group

To further investigate the composition differences of immune cells in the CAD patients, we used CIBERSORT immune cell infiltration method to analyze the scores of different immune cells between CAD vs. no-CAD samples for the 15 immune cell types (Supplementary Figure S2A). Immune cell type analysis was performed on samples from both groups, and we found the significant difference ($P < 0.05$) for the proportions of macrophage M0, CD8 T cells, resting dendritic cells, and activated memory CD4 T cells between the CAD and no-CAD groups (Figure 2A). The PCA plot showed the variability in the percentage of immune cells between the two groups, which is sufficient to show that there is substantial variability in the proportion of immune cells in the peripheral blood of CAD patients (Figure 2B). Based on the ratio of the relative proportions of different immune cells, we found an increase in macrophage M0 and CD8 T cells and a decrease in resting dendritic cells and activated memory CD4 T cells in the CAD group (Figure 2C). The proportion difference of CD8 T cells, CD4 T cells, macrophage M0 and resting dendritic cells was significant ($P < 0.05$), and we further demonstrated the distribution of these four immune cell types between the two groups (Figure 2D). The changes in immune cells indirectly suggest that the development of CAD may be related to the immune cell microenvironment.

To investigate how DERBPs associated with the immune cell microenvironment in CAD, we performed co-expression analysis between immune cells and DERBPs. It was found that 36 DERBPs were associated with CD8 T cells, macrophage M0 was correlated with 5 DERBPs, and resting dendritic cells were correlated with 39 DERBPs ($|correlation| \geq 0.6$, $p \leq 0.01$) (Figure 2E). In addition, neutrophils, out B cells and activated NK cells were similarly co-expressed with a small number of DERBPs (Supplementary Figure S2B). We found that some of these DERBPs co-expressed with immune cells are directly related to the innate immune response, such as MATR3 and IFIH1 co-expressed with CD8 T cells, and IPO7, DDX60, OTUD4 and MATR3 co-expressed with the resting dendritic cells. From the above co-expression relationships, we demonstrate that the expression changes of DERBPs can modulate the proportion of immune cells, and that a series of changes may contribute to the development of CAD.

5 https://cran.r-project.org/web/packages/pheatmap/index.html

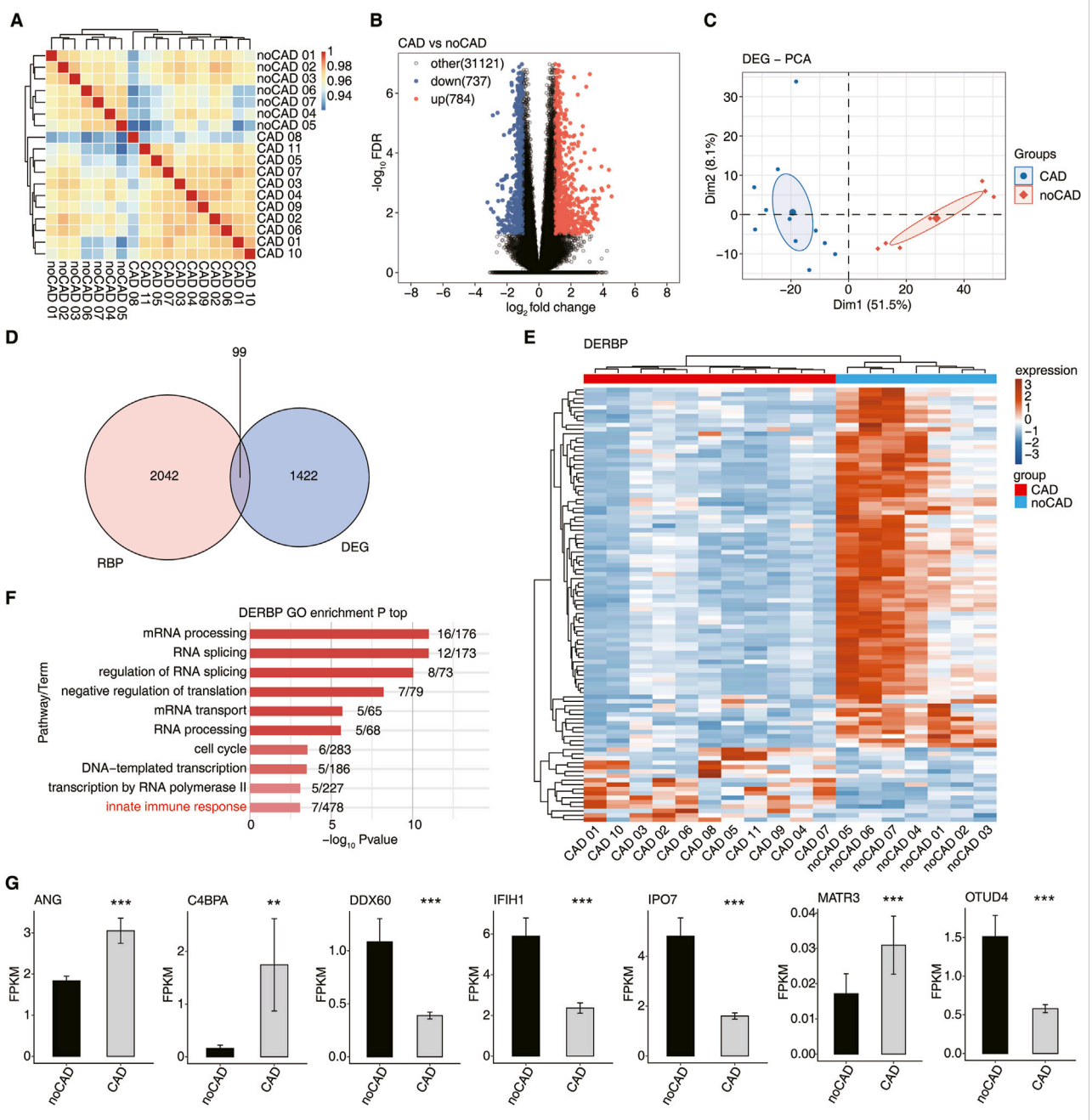

FIGURE 1
Expression profile analysis of differentially expressed RBPs in coronary artery disease. **(A)** Hierarchical clustering heatmap showing correlation between CAD and no-CAD samples based on the normalized values of all genes. **(B)** Volcano plots presenting differential pattern of all DEGs between CAD and no-CAD samples. **(C)** PCA result based on FPKM value of all DEGs. The ellipse represents for the confidence ellipse. **(D)** Venn diagram showing overlapped genes of DEGs and RBPs. **(E)** The heatmap diagram showing the expression profile of DERBP. **(F)** Bar plot showing the top enriched GO biological process results of DERBP. **(G)** The bar plot showing the FPKM values of 7 DERBPs. *: *P*-value ≤0.05, **: *P*-value ≤0.01, ***: *P*-value ≤0.001.

Co-disturbed regulatory network of immune-related RBPs and ASE was constructed in CAD

We have identified the 99 DERBPs existed between the CAD and no-CAD groups, and the expression of some DERBPs showed significant correlation with the proportion of immune cells, but how DERBPs affect peripheral blood immune cell changes in CAD patients is still unclear. RBPs are known to regulate pre-mRNA alternative splicing. Next, we focus on the co-expression relationship among DERBP, immune cells, and differentially expressed immune-related

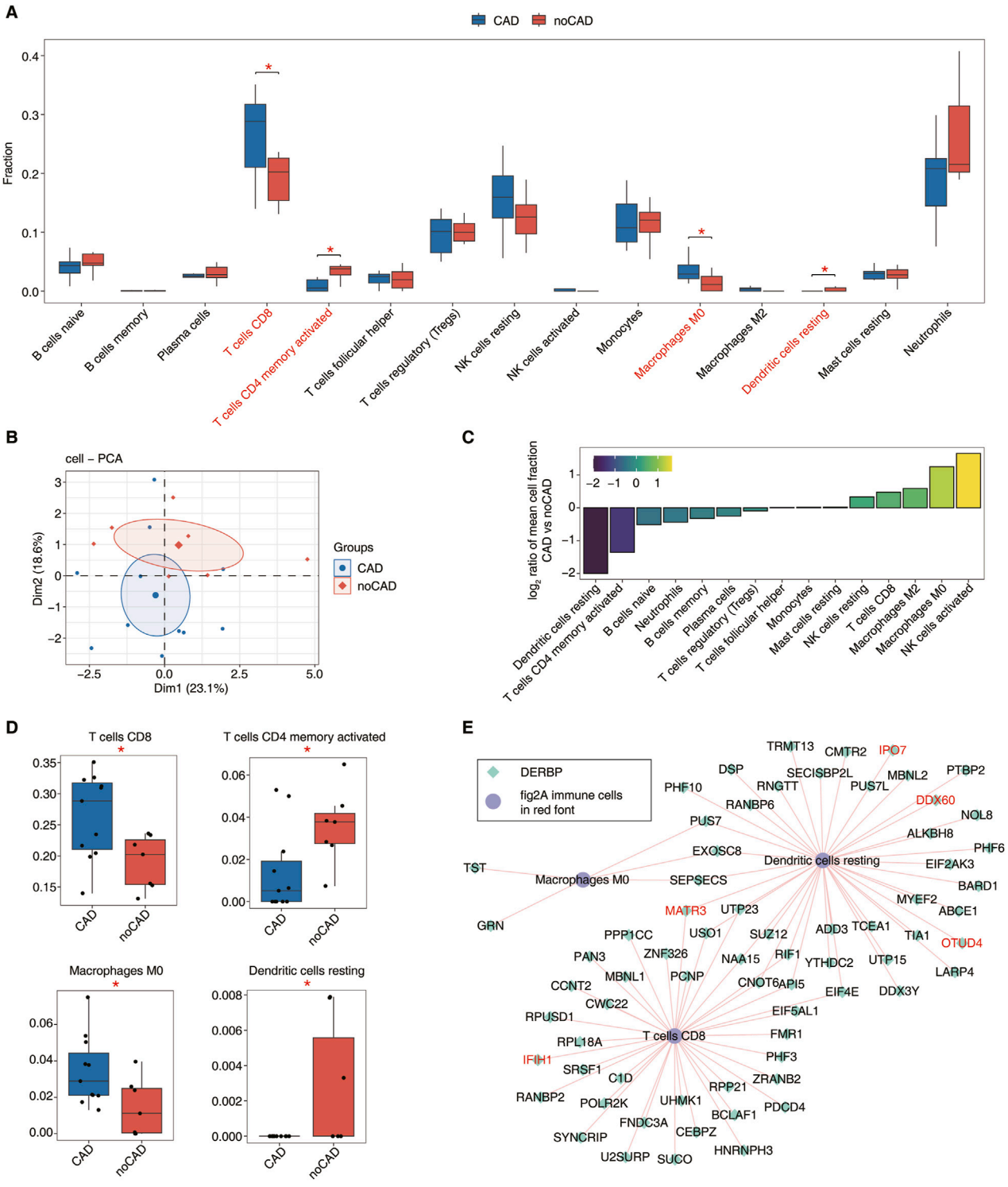

FIGURE 2
Dynamic changes of DERBP related to immune microenvironment regulation in coronary artery disease samples. **(A)** Boxplot showing percentage of immune cell types in CAD and no-CAG groups. The statistical difference between CAD and no-CAD samples was calculated by the Student's *t*-test. *: *P*-value ≤0.05, **: *P*-value ≤0.01, ***: *P*-value ≤0.001. **(B)** PCA result based on percentage of immune cell types. The ellipse for each group is the confidence ellipse. **(C)** Bar plot showing the relative frequency ratio at CAD vs. no-CAD based on decreasing values of ratio. **(D)** Boxplot showing the percentage of 4 significant immune cells. **(E)** Co-expression analysis of DERBP and Panle **A** immune cells in red font. The network showing the Co-expression of DERBP and immune cells in red font.

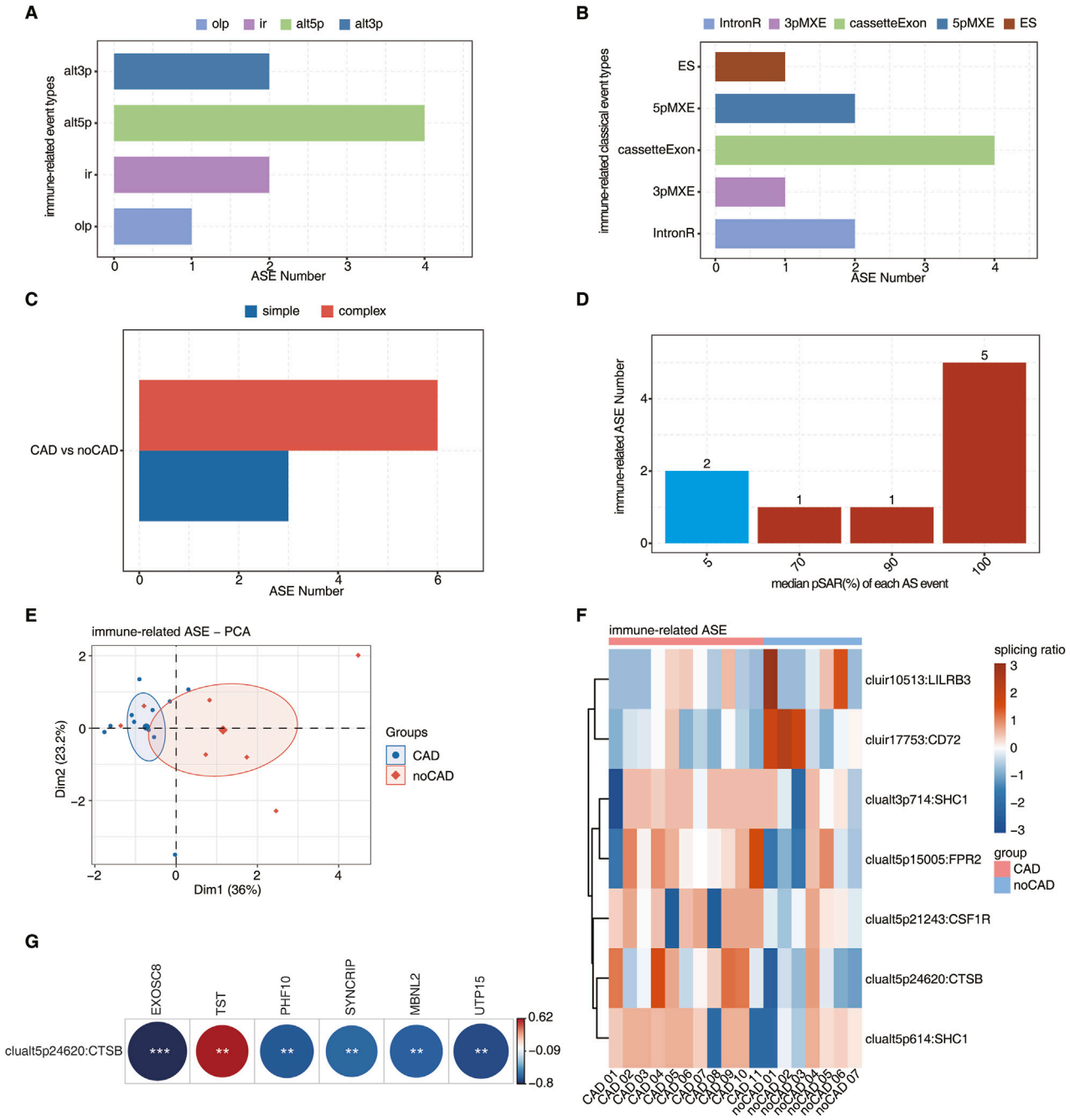

FIGURE 3
Analysis of immune-related SUVA in coronary artery disease and its co-expression of DERBP associated with immune microenvironment regulation. **(A)** Bar plot showing the number of immune-related regulatory AS detected by SUVA. **(B)** Splice junction constituting immune-related AS events detected by SUVA was annotated to classical AS event types. And the number of each classical AS event types were showed with bar plot. **(C)** Bar plot showing the number of simple and complex splicing events in immune-related AS events. **(D)** Bar plot showing immune-related ASE with different pSAR. ASE which pSAR (Reads proportion of SUVA AS event) ≥50% were labeled. **(E)** Principal component analysis (PCA) based on immune-related ASE of pSAR ≥50%. The ellipse for each group is the confidence ellipse. **(F)** The Heatmap showing the splicing ratio of immune-related AS events (PSAR ≥50%) in the CAD vs. no-CAD group. **(G)** The heatmap diagram showing co-expression analysis of immune-related AS events, RBP co-expressed with immune cells. Cutoffs of p value ≤0.01 and Pearson coefficient ≥0.6 or ≤−0.6 were applied to identify the co-expression pairs.

ASEs, to identify the alternative splicing of immune genes that may be regulated by DERBPs and further clarify the potential regulatory relationship between RBPs and immune-related ASEs in CAD.

We first analyzed all ASEs (Supplementary Figures S3A–F) that occurred in the CAD and no-CAD groups using the SUVA method, and then screened for immune gene-related ASEs by ImmPort database. The major differential immune-related ASEs identified by SUVA were 'alt3p/alt5p' event types (Figure 3A). The immune-related ASEs identified by SUVA were then matched with classical splicing events, which were mainly cassetteExon and 5pMXE types (Figure 3B). Meanwhile, the immune-associated ASEs in CAD were predominantly complex splicing events (Figure 3C), illustrating the complexity of CAD-related splicing in modulating the immune response.

One ASE contains at least two RNA isoforms, and one isoform may only account for a small part of the total RNA molecules of this gene, so we would like to find the dominant transcript. The splicing rate pSAR (proportion of SUVA AS event Reads) was used to calculate the proportion of each isoform in which the ASE is located and compared to the total isoform levels of the entire gene; a lower pSAR indicates that the two transcripts involved in splicing account for a smaller proportion of gene expression. Figure 3D showed the number distribution of ASEs that account for different proportions of all reads in the region, with a significant proportion of ASEs accounting for only a small proportion. We selected 7 immune-related ASEs that were the predominant transcripts (pSAR >= 50%) for subsequent analyses, and a small number of immune-related ASEs played a major role in CAD disease by performing PCA using their splicing ratios (Figure 3E). The ASEs of key transcripts in immune-related ASEs were shown by heatmap, showing a significant difference in the splicing ratio of immune-related ASEs between CAD and no-CAD groups (Figure 3F).

To identify immune-related ASEs that may be regulated by DERBPs in CAD patients, we performed co-expression analyses between immune-related ASEs and immune cell-associated DERBPs and found that the A5′SS event of the CTSB gene (clualt5p24620:CTSB) was co-expressed with 6 DERBPs that were worthy of attention (|correlation| ≥0.6, $p \leq 0.01$) (Figure 3G). Where the distribution of reads of splicing events on CTSB showed that the splicing ratio was significantly higher in CAD (Supplementary Figure S3G), suggesting that this ASE may be important for CAD formation. Considering that these 6 DERBPs were also co-expressed with immune cells, in particular TST and SYNCRIP co-expressed with macrophage M0 and CD8 T cells, respectively (Figure 2E). Therefore, we hypothesized that the TST-CTSB and SYNCRIP-CTSB co-expression pairs may affect the peripheral blood macrophage M0 and CD8 T cell ratios in CAD patients, respectively.

DERBPs potentially regulate expression of mitochondrial and apoptotic genes

Mitochondria are important regulatory centers of apoptosis, for mitochondrial dysfunction activates the apoptotic signaling pathway and promotes apoptosis in various cell types. Next, we explored the expression pattern of all apoptosis-related genes and mitochondrial-related genes in CAD and noCAD patients, and found they showed obvious difference between CAD and noCAD samples (Figures 4A,B). The overlap analysis results demonstrated that there were 4 apoptosis-related genes, and 53 mitochondrial-related genes were DEGs (Figure 4C). As an important regulatory factor in cardiovascular diseases, we also analyzed the expression of HIF-1α signaling pathway, and found HIF1A was downregulated in CAD samples (Figure 4D). Although both SIRT1 and SIRT6 are inhibitors of HIF-1α, their expression changes are opposite (Figure 4D), which implies the complex role of HIF-1α signaling in CAD. To clarify whether the function of immune-related DERBPs in CAD is associated with mitochondrial dysfunction, we constructed a co-expression regulatory network by analyzing the correlations between the seven immune-related DERBPs and these DEGs. The results indicated that HIF-1α signaling might mediate the regulation of mitochondrial-related genes by OTUD4, IPO7, DDX60, and MATR3 (Figure 4E). What's more interesting, all these correlated genes were downregulated in CAD.

Discussion

With changing lifestyles, the incidence of CAD with high mortality is increasing every year and has become one of the most serious public health problems. Atherosclerosis is an inflammation-associated disease with immune properties, driven by an innate immune response via monocytes and macrophages, with the resulting chronic inflammatory response attracting various immune cells, including innate and adaptive immune systems, to the atherosclerotic plaques [25, 26]. In this study, we performed bioinformatics analysis to focus on characterizing the immune microenvironment in CAD by analyzing RNA-seq data from GSE202625. The potential regulatory relationship between RBPs and immune-related alternative splicing during CAD progression was explored by analyzing DEGs and differential ASEs occurring in peripheral blood samples from CAD and no-CAD patients to shed light on possible pathogenic mechanisms in CAD. Through comprehensive exploration of this dataset, we found that a large number of genes were altered between the CAD vs. no-CAD groups, and further analysis revealed 99 DERBPs. GO analysis suggested that some DERBPs were associated with immune response effects in CAD, consistent with the conclusion of a previous report on the involvement of RBPs

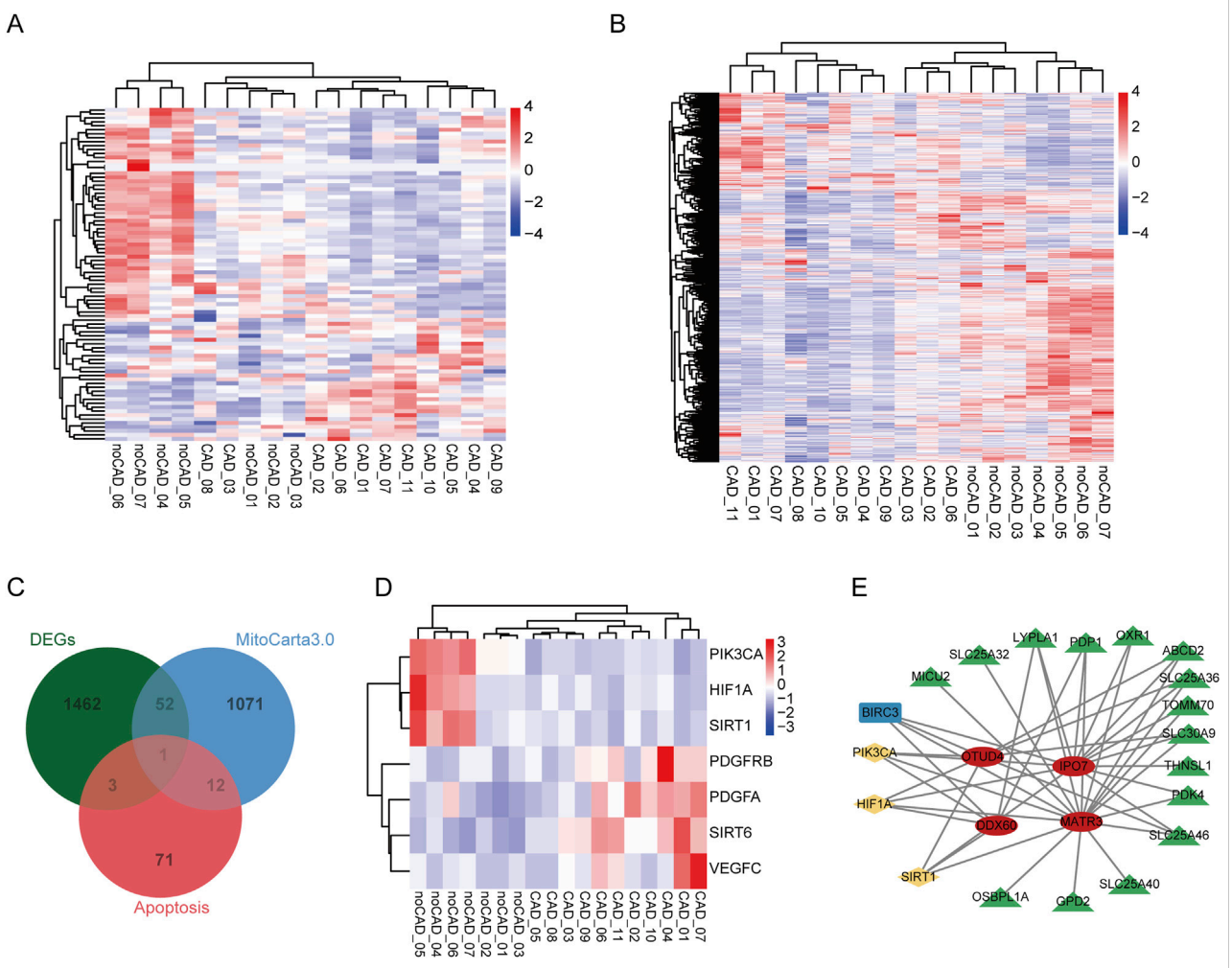

FIGURE 4
Analysis of mitochondrial dysfunction in CAD and its co-expression of seven immune-related DERBPs. **(A)** The heatmap of all apoptosis-related genes in the CAD vs. no-CAD group. **(B)** The heatmap of all mitochondria-related genes in the CAD vs. no-CAD group. **(C)** Venn diagram showing the overlap of DEGs, apoptosis- and mitochondria-related genes. **(D)** The heatmap of HIF-1α signaling related genes in the CAD vs. no-CAD group. **(E)** The mitochondrial dysfunction regulatory network of immune-related DERBPs. Red ovals represent immune-related DERBPs, green triangles represent mitochondrial-related genes, blue rectangle represents apoptosis-related genes, yellow rhombuses represent HIF-1α signaling related genes.

in immune cell regulation of atherosclerotic plaques [11]. Notably, we identified seven immune related DERBPs (*ANG*, *C4BPA*, *DDX60*, *IFIH1*, *IPO7*, *MATR3*, *OTUD4*) in the innate immune response and HIF1-α pathways that may be involved in the pathogenic process of CAD by modulating the immune cell changes.

The proteins encoded by ANG are potent mediators of neovascularization and are therefore often referred to as angiopoietins [27]. Members of the ANG family all play important roles in atherosclerosis, with ANG II thought to have pro-atherogenic effects [28]. Atherosclerotic plaque rupture can induce the acute coronary syndromes, and ANG II induces macrophage apoptosis by inducing the expression of monocyte chemotactic proteins, ultimately leading to the formation of vulnerable atherosclerotic plaques [29]. ANG II type 1 receptor blockade was found to be associated with a reduction in carotid atherosclerosis by studying the effects of valsartan on carotid artery atherosclerosis [30]. ANG II plays an important role in cardiovascular disease and can be used as therapeutic targets in cardiovascular pathologies [31, 32]. C4BPA (Complement C4b-binding protein alpha chain) is a protein associated with the immune system that has a regulatory role in the complement system and plays an important role in the immune response [33]. The role and mechanism of C4BPA in atherosclerosis have not been elucidated, but one study has shown that C4BPA expression is a promising biomarker to

predict clopidogrel resistance during the treatment of atherosclerosis [34, 35], and clopidogrel is mainly used to prevent and treat diseases related to atherosclerosis and thrombosis. In addition, C4BPA can affect the activity of the complement system [36, 37], which may influence the pathogenesis and development of atherosclerosis by modulating the activity of the complement system and the inflammatory response. MATR3 (Matrin 3) is a nuclear RNA/DNA-binding protein and extensively regulates gene expression pattern, which is involved in cardiac development and exists in endothelial cells and arterial smooth muscle cells of cardiac arteries and veins [38]. While endothelial cell and smooth muscle cell dysfunction have essential function in the occurrence and development of atherosclerosis, indicating the potential regulatory role of MATR3 in atherosclerosis development.

IFIH1 encodes a protein known as MDA5 (melanoma differentiation-associated protein 5) and is an important immune-related gene involved in the process of virus infections [39]. IFIH1 was found to be an immune-related hub gene of atherosclerosis and may be a potential target for patients with atherosclerosis [40]. DDX60 is a member of the DEAD-box family and was originally thought to be an antiviral protein involved in the regulation of cellular immune responses to viral infection [41, 42]. DDX60 has antiviral effects, and certain viral infections are also considered a risk factor for atherosclerosis [43]. IPO7 (Importin 7) is an important nuclear transporter protein gene that encodes a protein involved in the transport of substances within the nucleus and between the cytoplasm of cells, and plays an important role in many biological processes [44, 45]. OTUD4 (OUT deubiquitinase 4) is a protein with deubiquitinase activity that is involved in regulating the deubiquitination modification of intracellular proteins, thereby affecting protein stability and function [46, 47]. The immune response plays a key role in the pathogenesis of atherosclerosis [48]. All of these immune-related RBP genes that we have identified can potentially regulate the immune system and are directly or indirectly involved in the immune response that ultimately affects the progression of atherosclerosis. Taken together, these DERBPs are enriched in the innate immune response pathway, and may have important functions in CAD disease by modulating immune responses in different ways, which needs to be further validated in future studies.

By analyzing the distribution of immune cells, we found a significant increase in M0 macrophage and CD8 T cells and a significant decrease in activated memory CD4 T cells and resting dendritic cells in the CAD group. Current research suggests that CD8 T cells are emerging as a key cell population in atherosclerosis [49]. Studies have shown the increased proportion of CD8 T cells in the cellular distribution of atherosclerotic plaques in mice and humans [50, 51]. M0 macrophages have not been activated or polarized, and studies have shown a significant increase in M0 macrophages in CAD patients [52]. CD4 T cells can differentiate into different TH or Treg cell subtypes, which can modulate the response of other immune cells and exert direct pro- or anti-inflammatory effects, making the diverse roles of CD4 T cells in atherosclerosis. Among these cell subtypes, Treg cells have anti-atherosclerotic effects, and depletion of Treg cells accelerates atherosclerosis [53]. In addition, the distribution of resting dendritic cells was significantly downregulated in patients with myocardial infarction [54]. These studies further suggest that the distribution of immune cells correlates with the progression of CAD. Co-expression analysis of immune cells and DERBPs was performed and found that CD8 T, macrophage M0 and resting dendritic cells all correlated with some DERBPs. It suggests that the DERBPs can cause changes in the proportion of immune cells in the peripheral blood of CAD patients, indirectly suggesting that the development of CAD may be related to the microenvironment of immune cells. We also realized that our results were based on peripheral blood samples, which have been used in exploring the gene expression profile during infection with bacterial meningitis [55]. This approach can globally detect gene expression of immune cells in peripheral blood, but further studies focusing on plaque samples are also necessary to identify the infiltrated immune cells during CAD progression.

We then constructed a co-expression network of immune-related ASEs and immune-cell-related DERBPs and finally identified that the A5′SS event of the CTSB gene correlates with six DERBPs (MBNL2, UTP15, PHF10, TST, EXOSC8, and SYNCRIP) in CAD patients. CTSB (Cathepsin B) belongs to the lysosomal cathepsin family of proteases and regulates the quantity of lysosomes and autophagosomes in cells [56, 57]. CTSB has been involved in the progression of apoptosis, autophagy, and certain types of cancer [58, 59]. CTSB is also involved in the development of several cardiovascular diseases, such as atherosclerosis, heart failure, myocardial infarction and so on [60]. Additionally, it has been found that genetic variation in the CTSB promoter may affect the development of dilated cardiomyopathy [61]. These studies have shown that CTSB plays a crucial role in regulating cardiac remodeling. Therefore, CTSB is also considered a potential therapeutic target for heart failure. CTSB is involved in extracellular matrix decomposition processes, such as fibronectin, elastin, and collagen IV, which can lead to the destruction of collagen fibers in plaques and decreased plaque stability [62]. CTSB appears to play a role in autophagy at later stages of carotid atherosclerotic plaque compared to early stages [63]. Therefore, CTSB is a potential therapeutic target for atherosclerosis and is expected to provide new ideas and methods for the treatment of this disease. Based on the result that TST and SYNCRIP were co-expressed with macrophage M0 and CD8 T cells, respectively, we

hypothesize that the TST-CTSB splicing event co-expression pair may affect changes in the peripheral blood macrophage M0 cell ratio in CAD patients, and that the SYNCRIP-CTSB splicing event co-expression pair may affect changes in the peripheral blood CD8 T-cell ratio in CAD patients, which may potentially exacerbate the occurrence of CAD disease.

Conclusion

In this study, our analysis of RNA-seq data from peripheral blood of CAD patients and no-CAD controls revealed the dysregulation of RBPs expression in CAD patients, and constructed the potential regulatory network between dysregulated RBPs and immune cells, as well as the ASEs. Further analyses suggest that RBPs may contribute to the progression of CAD by influencing the remodeling of the immune microenvironment through the regulation of alternative splicing of immune-related genes. Our results indicate the important roles of RBPs in CAD progression, and suggest that these RBPs as well as their potential targets are targets for CAD treatment in future.

Author contributions

YM, LW, and FG designed the study, wrote and edited the initial draft of the manuscript. GZ, WG, SC, CD, and ZL analyzed the RNA sequencing data and edited the images. All authors contributed to the article and approved the submitted version.

Data availability

The original contributions presented in the study are included in the article/Supplementary Material, further inquiries can be directed to the corresponding author.

Ethics statement

Ethical approval was not required for the study involving humans in accordance with the local legislation and institutional requirements. Written informed consent to participate in this study was not required from the participants or the participants' legal guardians/next of kin in accordance with the national legislation and the institutional requirements.

Funding

The author(s) declare that financial support was received for the research and/or publication of this article. This study was supported by the Ningxia Hui Autonomous Region's science and technology benefiting the people program (2022CMG03042) and the Natural Science Foundation of Ningxia Hui Autonomous Region (2024AAC03658).

Conflict of interest

The author(s) declared no potential conflicts of interest with respect to the research, authorship, and/or publication of this article.

Generative AI statement

The author(s) declare that no Generative AI was used in the creation of this manuscript.

Supplementary material

The Supplementary Material for this article can be found online at: https://www.ebm-journal.org/articles/10.3389/ebm.2025.10430/full#supplementary-material

References

1. Iaconelli A, Pellicori P, Dolce P, Busti M, Ruggio A, Aspromonte N, et al. Coronary revascularization for heart failure with coronary artery disease: a systematic review and meta-analysis of randomized trials. *Eur J Heart Fail* (2023) **25**:1094–104. doi:10.1002/ejhf.2911

2. Vos T, Lim SS, Abbafati C, Abbas KM, Abbasi M, Abbasifard M, et al. Global burden of 369 diseases and injuries in 204 countries and territories, 1990-2019: a systematic analysis for the Global Burden of Disease Study 2019. *The Lancet* (2020) **396**:1204–22. doi:10.1016/s0140-6736(20)30925-9

3. Neupane R, Jin X, Sasaki T, Li X, Murohara T, Cheng XW. Immune disorder in atherosclerotic cardiovascular disease - clinical implications of using circulating T-cell subsets as biomarkers. *Circ J* (2019) **83**:1431–8. doi:10.1253/circj.cj-19-0114

4. Libby P. The changing landscape of atherosclerosis. *Nature* (2021) **592**:524–33. doi:10.1038/s41586-021-03392-8

5. Swirski FK, Nahrendorf M. Cardioimmunology: the immune system in cardiac homeostasis and disease. *Nat Rev Immunol* (2018) **18**:733–44. doi:10.1038/s41577-018-0065-8

6. Kott KA, Vernon ST, Hansen T, De Dreu M, Das SK, Powell J, et al. Single-cell immune profiling in coronary artery disease: the role of state-of-the-art immunophenotyping with mass cytometry in the diagnosis of atherosclerosis. *J Am Heart Assoc* (2020) **9**:e017759. doi:10.1161/jaha.120.017759

7. Bergstrom I, Backteman K, Lundberg A, Ernerudh J, Jonasson L. Persistent accumulation of interferon-gamma-producing CD8+CD56+ T cells in blood from patients with coronary artery disease. *Atherosclerosis* (2012) **224**:515–20. doi:10.1016/j.atherosclerosis.2012.07.033

8. Cochain C, Koch M, Chaudhari SM, Busch M, Pelisek J, Boon L, et al. CD8+ T cells regulate monopoiesis and circulating Ly6C-high monocyte levels in atherosclerosis in mice. *Circ Res* (2015) **117**:244–53. doi:10.1161/circresaha.117.304611

9. Hentze MW, Castello A, Schwarzl T, Preiss T. A brave new world of RNA-binding proteins. *Nat Rev Mol Cell Biol* (2018) **19**:327–41. doi:10.1038/nrm.2017.130

10. Smith MR, Costa G. RNA-binding proteins and translation control in angiogenesis. *The FEBS J* (2022) **289**:7788–809. doi:10.1111/febs.16286

11. Sachse M, Tual-Chalot S, Ciliberti G, Amponsah-Offeh M, Stamatelopoulos K, Gatsiou A, et al. RNA-binding proteins in vascular inflammation and atherosclerosis. *Atherosclerosis* (2023) **374**:55–73. doi:10.1016/j.atherosclerosis.2023.01.008

12. Marasco LE, Kornblihtt AR. The physiology of alternative splicing. *Nat Rev Mol Cell Biol* (2023) **24**:242–54. doi:10.1038/s41580-022-00545-z

13. Liu J, Lin CX, Zhang X, Li Z, Huang W, Liu J, et al. Computational approaches for detecting disease-associated alternative splicing events. *Brief Bioinform* (2023) **24**:bbad106. doi:10.1093/bib/bbad106

14. De Bruin RG, Rabelink TJ, Van Zonneveld AJ, Van Der Veer EP. Emerging roles for RNA-binding proteins as effectors and regulators of cardiovascular disease. *Eur Heart J* (2017) **38**:1380–8. doi:10.1093/eurheartj/ehw567

15. Kim D, Paggi JM, Park C, Bennett C, Salzberg SL. Graph-based genome alignment and genotyping with HISAT2 and HISAT-genotype. *Nat Biotechnol* (2019) **37**:907–15. doi:10.1038/s41587-019-0201-4

16. Love MI, Huber W, Anders S. Moderated estimation of fold change and dispersion for RNA-seq data with DESeq2. *Genome Biol* (2014) **15**:550. doi:10.1186/s13059-014-0550-8

17. Castello A, Fischer B, Eichelbaum K, Horos R, Beckmann BM, Strein C, et al. Insights into RNA biology from an atlas of mammalian mRNA-binding proteins. *Cell* (2012) **149**:1393–406. doi:10.1016/j.cell.2012.04.031

18. Gerstberger S, Hafner M, Tuschl T. A census of human RNA-binding proteins. *Nat Rev Genet* (2014) **15**:829–45. doi:10.1038/nrg3813

19. Castello A, Fischer B, Frese CK, Horos R, Alleaume AM, Foehr S, et al. Comprehensive identification of RNA-binding domains in human cells. *Mol Cell* (2016) **63**:696–710. doi:10.1016/j.molcel.2016.06.029

20. Cheng C, Liu L, Bao Y, Yi J, Quan W, Xue Y, et al. SUVA: splicing site usage variation analysis from RNA-seq data reveals highly conserved complex splicing biomarkers in liver cancer. *RNA Biol* (2021) **18**:157–71. doi:10.1080/15476286.2021.1940037

21. Rath S, Sharma R, Gupta R, Ast T, Chan C, Durham TJ, et al. MitoCarta3.0: an updated mitochondrial proteome now with sub-organelle localization and pathway annotations. *Nucleic Acids Res* (2021) **49**:D1541–d1547. doi:10.1093/nar/gkaa1011

22. Newman AM, Liu CL, Green MR, Gentles AJ, Feng W, Xu Y, et al. Robust enumeration of cell subsets from tissue expression profiles. *Nat Methods* (2015) **12**:453–7. doi:10.1038/nmeth.3337

23. Xie C, Mao X, Huang J, Ding Y, Wu J, Dong S, et al. KOBAS 2.0: a web server for annotation and identification of enriched pathways and diseases. *Nucleic Acids Res* (2011) **39**:W316–322. doi:10.1093/nar/gkr483

24. Bardou P, Mariette J, Escudié F, Djemiel C, Klopp C. jvenn: an interactive Venn diagram viewer. *BMC Bioinformatics* (2014) **15**:293. doi:10.1186/1471-2105-15-293

25. Wolf D, Ley K. Immunity and inflammation in atherosclerosis. *Circ Res* (2019) **124**:315–27. doi:10.1161/circresaha.118.313591

26. He C, Kim HI, Park J, Guo J, Huang W. The role of immune cells in different stages of atherosclerosis. *Int J Med Sci* (2024) **21**:1129–43. doi:10.7150/ijms.94570

27. Roy P, Orecchioni M, Ley K. How the immune system shapes atherosclerosis: roles of innate and adaptive immunity. *Nat Rev Immunol* (2022) **22**:251–65. doi:10.1038/s41577-021-00584-1

28. Silva GM, Franca-Falcao MS, Calzerra NTM, Luz MS, Gadelha DDA, Balarini CM, et al. Role of renin-angiotensin system components in atherosclerosis: focus on ang-II, ACE2, and ang-1-7. *Front Physiol* (2020) **11**:1067. doi:10.3389/fphys.2020.01067

29. Shu S, Zhang Y, Li W, Wang L, Wu Y, Yuan Z, et al. The role of monocyte chemotactic protein-induced protein 1 (MCPIP1) in angiotensin II-induced macrophage apoptosis and vulnerable plaque formation. *Biochem Biophysical Res Commun* (2019) **515**:378–85. doi:10.1016/j.bbrc.2019.05.145

30. Ramadan R, Dhawan SS, Binongo JN, Alkhoder A, Jones DP, Oshinski JN, et al. Effect of angiotensin II type I receptor blockade with valsartan on carotid artery atherosclerosis: a double blind randomized clinical trial comparing valsartan and placebo (EFFERVESCENT). *Am Heart J* (2016) **174**:68–79. doi:10.1016/j.ahj.2015.12.021

31. Montezano AC, Nguyen Dinh Cat A, Rios FJ, Touyz RM. Angiotensin II and vascular injury. *Curr Hypertens Rep* (2014) **16**:431. doi:10.1007/s11906-014-0431-2

32. Civieri G, Iop L, Tona F. Antibodies against angiotensin II type 1 and Endothelin 1 type A receptors in cardiovascular pathologies. *Int J Mol Sci* (2022) **23**:927. doi:10.3390/ijms23020927

33. Cagliani R, Forni D, Filippi G, Mozzi A, De Gioia L, Pontremoli C, et al. The mammalian complement system as an epitome of host–pathogen genetic conflicts. *Mol Ecol* (2016) **25**:1324–39. doi:10.1111/mec.13558

34. Liu X, Jiang C, Yang P. Association of single nucleotide polymorphisms in the 5' upstream region of the C4BPA gene with essential hypertension in a northeastern Han Chinese population. *Mol Med Rep* (2017) **16**:1289–97. doi:10.3892/mmr.2017.6736

35. Xie HG, Jiang LP, Tai T, Ji JZ, Mi QY. The complement system and C4b-binding protein: a focus on the promise of C4BPα as a biomarker to predict clopidogrel resistance. *Mol Diagn Ther* (2024) **28**:189–99. doi:10.1007/s40291-023-00691-w

36. Sjoberg AP, Trouw LA, Blom AM. Complement activation and inhibition: a delicate balance. *Trends Immunol* (2009) **30**:83–90. doi:10.1016/j.it.2008.11.003

37. Zhang J, Zhu W, Yang S, Liu J, Tang F, Li Y. Identification and validation of a novel prognostic signature of gastric cancer based on seven complement system-related genes: an integrated analysis. *Crit Rev Eukaryot Gene Expr* (2025) **35**:1–22. doi:10.1615/critreveukaryotgeneexpr.2024057000

38. Quintero-Rivera F, Xi QJ, Keppler-Noreuil KM, Lee JH, Higgins AW, Anchan RM, et al. MATR3 disruption in human and mouse associated with bicuspid aortic valve, aortic coarctation and patent ductus arteriosus. *Hum Mol Genet* (2015) **24**:2375–89. doi:10.1093/hmg/ddv004

39. Rice GI, Park S, Gavazzi F, Adang LA, Ayuk LA, Van Eyck L, et al. Genetic and phenotypic spectrum associated with IFIH1 gain-of-function. *Hum Mutat* (2020) **41**:837–49. doi:10.1002/humu.23975

40. Dong R, Jiang G, Tian Y, Shi X. Identification of immune-related biomarkers and construction of regulatory network in patients with atherosclerosis. *BMC Med Genomics* (2022) **15**:245. doi:10.1186/s12920-022-01397-4

41. Schoggins JW, Wilson SJ, Panis M, Murphy MY, Jones CT, Bieniasz P, et al. A diverse range of gene products are effectors of the type I interferon antiviral response. *Nature* (2011) **472**:481–5. doi:10.1038/nature09907

42. Tapescu I, Cherry S. DDX RNA helicases: key players in cellular homeostasis and innate antiviral immunity. *J Virol* (2024) **98**:e00040-24. doi:10.1128/jvi.00040-24

43. Peretz A, Azrad M, Blum A. Influenza virus and atherosclerosis. *QJM: An Int J Med* (2019) **112**:749–55. doi:10.1093/qjmed/hcy305

44. Freedman ND, Yamamoto KR. Importin 7 and importin α/importin β are nuclear import receptors for the glucocorticoid receptor. *Mol Biol Cell* (2004) **15**:2276–86. doi:10.1091/mbc.e03-11-0839

45. Itoh Y, Miyamoto Y, Tokunaga M, Suzuki T, Takada A, Ninomiya A, et al. Importin-7-dependent nuclear translocation of the Flavivirus core protein is required for infectious virus production. *Plos Pathog* (2024) **20**:e1012409. doi:10.1371/journal.ppat.1012409

46. Zhao Y, Majid MC, Soll JM, Brickner JR, Dango S, Mosammaparast N. Noncanonical regulation of alkylation damage resistance by the OTUD4 deubiquitinase. *The EMBO J* (2015) **34**:1687–703. doi:10.15252/embj.201490497

47. Ci M, Zhao G, Li C, Liu R, Hu X, Pan J, et al. OTUD4 promotes the progression of glioblastoma by deubiquitinating CDK1 and activating MAPK signaling pathway. *Cell Death Dis* (2024) **15**:179. doi:10.1038/s41419-024-06569-x

48. Wan Q, Liu Z, Yang M, Wu J. Acceleratory effects of ambient fine particulate matter on the development and progression of atherosclerosis in apolipoprotein E knockout mice by down-regulating CD4(+)CD25(+)Foxp3(+) regulatory T cells. *Toxicol Lett* (2019) **316**:27–34. doi:10.1016/j.toxlet.2019.09.005

49. Schafer S, Zernecke A. CD8(+) T cells in atherosclerosis. *Cells* (2020) **10**:37. doi:10.3390/cells10010037

50. Cochain C, Vafadarnejad E, Arampatzi P, Pelisek J, Winkels H, Ley K, et al. Single-cell RNA-seq reveals the transcriptional landscape and heterogeneity of aortic macrophages in murine atherosclerosis. *Circ Res* (2018) **122**:1661–74. doi:10.1161/circresaha.117.312509

51. Winkels H, Ehinger E, Vassallo M, Buscher K, Dinh HQ, Kobiyama K, et al. Atlas of the immune cell repertoire in mouse atherosclerosis defined by single-cell RNA-sequencing and mass cytometry. *Circ Res* (2018) **122**:1675–88. doi:10.1161/circresaha.117.312513

52. Deng Y, Wang X, Liu Z, Lv X, Ma B, Nie Q, et al. *In silico* identification of key genes and immune infiltration characteristics in epicardial adipose tissue from patients with coronary artery disease. *Biomed Res Int* (2022) **2022**:5610317. doi:10.1155/2022/5610317

53. Saigusa R, Winkels H, Ley K. T cell subsets and functions in atherosclerosis. *Nat Rev Cardiol* (2020) **17**:387–401. doi:10.1038/s41569-020-0352-5

54. Lai L, Zhang A, Yang B, Charles EJ, Kron IL, Yang Z. Plasmacytoid dendritic cells mediate myocardial ischemia/reperfusion injury by secreting type I interferons. *J Am Heart Assoc* (2021) **10**:e020754. doi:10.1161/jaha.121.020754

55. Lill M, Kõks S, Soomets U, Schalkwyk LC, Fernandes C, Lutsar I, et al. Peripheral blood RNA gene expression profiling in patients with bacterial meningitis. *Front Neurosci* (2013) **7**:33. doi:10.3389/fnins.2013.00033

56. Man SM, Kanneganti TD. Regulation of lysosomal dynamics and autophagy by CTSB/cathepsin B. *Autophagy* (2016) **12**:2504–5. doi:10.1080/15548627.2016.1239679

57. Li C, Sun S, Zhuang Y, Luo Z, Ji G, Liu Z. CTSB nuclear translocation facilitates DNA damage and lysosomal stress to promote retinoblastoma cell death. *Mol Biotechnol* (2024) **66**:2583–94. doi:10.1007/s12033-023-01042-0

58. Wang Y, Yuan T, He L, Huang J, Wilfred N, Yang W, et al. Melittin treatment suppressed malignant NSCLC progression through enhancing CTSB-mediated hyperautophagy. *Biomed & Pharmacother* (2024) **180**:117573. doi:10.1016/j.biopha.2024.117573

59. Zhao K, Sun Y, Zhong S, Luo JL. The multifaceted roles of cathepsins in immune and inflammatory responses: implications for cancer therapy, autoimmune diseases, and infectious diseases. *Biomark Res* (2024) **12**:165. doi:10.1186/s40364-024-00711-9

60. Cai Z, Xu S, Liu C. Cathepsin B in cardiovascular disease: underlying mechanisms and therapeutic strategies. *J Cell Mol Med* (2024) **28**:e70064. doi:10.1111/jcmm.70064

61. Zhou Y, Gao S, Ding L, Yan H, Pang S, Yan B. Correlation analysis of CTSB promoter polymorphism and function in patients with dilated cardiomyopathy. *DNA Cell Biol* (2023) **42**:203–11. doi:10.1089/dna.2022.0525

62. Wu H, Du Q, Dai Q, Ge J, Cheng X. Cysteine protease cathepsins in atherosclerotic cardiovascular diseases. *J Atheroscler Thromb* (2018) **25**:111–23. doi:10.5551/jat.rv17016

63. Dai J, Zhang Q, Wan C, Liu J, Zhang Q, Yu Y, et al. Significances of viable synergistic autophagy-associated cathepsin B and cathepsin D (CTSB/CTSD) as potential biomarkers for sudden cardiac death. *BMC Cardiovasc Disord* (2021) **21**:233. doi:10.1186/s12872-021-02040-3

EBM Experimental Biology and Medicine

TYPE Original Research
PUBLISHED 01 October 2025
DOI 10.3389/ebm.2025.10599

OPEN ACCESS

*CORRESPONDENCE
Hai Gao,
GaoHai417@163.com

RECEIVED 25 March 2025
ACCEPTED 03 September 2025
PUBLISHED 01 October 2025

CITATION
Gao H, Wu T, Xue J, Liu J, Wen D and Huang G (2025) Unveiling the dual role of CD3G: a diagnostic biomarker for depression and its oncogenic implications.
Exp. Biol. Med. 250:10599.
doi: 10.3389/ebm.2025.10599

Unveiling the dual role of CD3G: a diagnostic biomarker for depression and its oncogenic implications

Hai Gao[1,2,3,4,5]*, Ting Wu[6], Jihui Xue[1,3,4,5,7], Jing Liu[2,3,4,5], Dongmei Wen[2,3,4,5] and Guanwei Huang[8]

[1]Nutrition Department, Xiamen Xianyue Hospital, Xiamen, Fujian, China, [2]Hospital Infection Control Department, Xiamen Xianyue Hospital, Xiamen, Fujian, China, [3]Xianyue Hospital Affiliated with Xiamen Medical College, Xiamen, Fujian, China, [4]Fujian Psychiatric Center, Xiamen, Fujian, China, [5]Fujian Clinical Research Center for Mental Disorders, Xiamen, Fujian, China, [6]Department of Infectious Diseases, The First Affiliated Hospital of Xiamen University, Xiamen, Fujian, China, [7]Public health Department, Xiamen Xianyue Hospital, Xiamen, Fujian, China, [8]Operation Management Department, Xiamen Maternnal and Child Health Hospital, Xiamen, Fujian, China

Abstract

Depression has been increasingly associated with immune system dysregulation. This study investigates the potential of CD3 Gamma Subunit of T-Cell Receptor Complex (CD3G) as a diagnostic marker for depression, while also examining its role across various cancer types. Comparative analyses of immune cell infiltration and pathway activities were conducted using single-sample Gene Set Enrichment Analysis (ssGSEA) on datasets GSE98793. Depression patients were defined based on clinical diagnoses and compared to healthy controls (HC) without any psychiatric disorders. Differentially expressed genes (DEGs) were identified, followed by weighted gene co-expression network analysis (WGCNA), least absolute shrinkage and selection operator (LASSO) and logistic regression to pinpoint independent diagnostic markers. Functional enrichment analyses were performed to explore the biological implications of CD3G expression in depression. Pan-cancer analyses were also conducted to investigate CD3G's role in cancer. Depression patients exhibited significant decreases in CD8 T cells, cytotoxic cells, T cells, T helper cells, Tgd, and Th2 cells, with increased levels of dendritic cells and neutrophils compared to HC. Immune pathway activities showed increased antimicrobial, chemokine, cytokine, and TNF family member activities, with decreased TCR signaling activity in depression patients. CD3G was identified as a key immune-related gene and independent diagnostic marker for depression, validated by GSE76826 dataset. Low CD3G expression in depression was associated with enhanced immune response and inflammatory pathways. In pan-cancer analysis, CD3G was upregulated in numerous cancers and correlated with immune cell infiltration and oncogenic pathways. The study highlights significant dysregulation in immune cell infiltration and pathway activities in depression, with CD3G emerging as a critical immune-related gene and potential diagnostic marker.

CD3G's role in immune modulation and cancer underscores its relevance in both depression and oncology, suggesting potential therapeutic targets and prognostic indicators.

KEYWORDS

depression, immune dysregulation, CD3G, diagnostic marker, inflammatory pathways

Impact statement

The findings of this study are expected to enhance our understanding of the immune mechanisms underlying depression and identify CD3G as a critical biomarker for diagnosis. Moreover, the dual role of CD3G in both depression and cancer underscores its potential as a therapeutic target, offering new insights into the intersection of neuroimmune and oncogenic pathways. This research not only provides a novel perspective on the pathophysiology of depression but also paves the way for innovative diagnostic and therapeutic approaches.

Introduction

Depression is a debilitating mental health disorder that affects millions of people worldwide, contributing significantly to global morbidity and disability [1, 2]. Traditionally, depression has been primarily understood through a neurochemical lens, focusing on imbalances in neurotransmitters such as serotonin, dopamine, and norepinephrine [3, 4]. However, emerging evidence suggests that depression is also closely linked to immune system dysregulation, indicating a more complex pathophysiology involving neuroimmune interactions [5].

Recent studies have highlighted the role of immune cells and inflammatory pathways in the development and progression of depression [6, 7]. Immune cell infiltration and the activation of specific immune pathways have been observed in patients with depression, suggesting that immune dysregulation may contribute to the onset and maintenance of depressive symptoms [8, 9]. This paradigm shift opens new avenues for identifying novel biomarkers and therapeutic targets, potentially leading to more effective diagnosis and treatment strategies. One such promising biomarker is CD3G, a gene encoding the gamma chain of the CD3 complex, which is crucial for T cell receptor signaling and T cell function [10–12]. Previous research has implicated CD3G in various immune-related processes, and its dysregulation has been observed in several diseases, including autoimmune disorders and cancers [13–15]. However, its specific role in depression remains largely unexplored.

This study aims to investigate the potential of CD3G as a diagnostic marker for depression by analyzing immune cell infiltration and pathway activities in depression patients compared to healthy controls (HC). We conducted comprehensive bioinformatics analyses using ssGSEA on publicly available datasets (GSE98793) to identify key immune-related pathways. Additionally, Weighted Gene Co-expression Network Analysis (WGCNA), Least Absolute Shrinkage and Selection Operator (LASSO) regression, and logistic regression were employed to pinpoint independent diagnostic markers. Functional enrichment analyses were performed to elucidate the biological implications of CD3G expression in depression. Furthermore, we extended our investigation to a pan-cancer analysis to examine CD3G's role across various cancer types, given its known involvement in immune modulation.

The findings of this study are expected to enhance our understanding of the immune mechanisms underlying depression and identify CD3G as a critical biomarker for diagnosis. Moreover, the dual role of CD3G in both depression and cancer underscores its potential as a therapeutic target, offering new insights into the intersection of neuroimmune and oncogenic pathways. This research not only provides a novel perspective on the pathophysiology of depression but also paves the way for innovative diagnostic and therapeutic approaches.

Materials and methods

Depression-related dataset acquisition

The depression-associated dataset was acquired from the NCBI GEO database (https://www.ncbi.nlm.nih.gov/geo/) [16]. Using the search term "depression" on the GEO homepage, the dataset was filtered based on specific criteria: 1) inclusion of blood samples from both healthy individuals and individuals with depression; 2) availability of raw data in the dataset; and 3) a minimum sample size of 10. Two datasets, GSE98793 and GSE76826, were ultimately chosen (Table 1). GSE98793 includes 64 healthy controls and 128 individuals with depression, while GSE76826 includes 12 healthy controls and 20 individuals with depression. A sample size calculation was not explicitly performed; however, the selected datasets met the predefined criteria to ensure sufficient statistical power for downstream analysis. Microarray data and platform annotation files were retrieved using the GEOquery package (v.2.76.0) in R software. Gene ID conversion was conducted on the downloaded matrix files according to the annotation files, removing probes with missing or duplicate annotations. Data analysis was performed using the limma package (v.3.64.0) in R

TABLE 1 Information on depression-related datasets used in the current study.

GEO ID	Platform	Healthy controls	Depression	Source	Application
GSE98793	GPL570	64	128	Blood	Analysis
GSE76826	GPL17077	12	20	Blood	Validation

software, with microarray data normalization carried out using the normalizeBetweenArrays function within the limma package (v.3.64.0).

Evaluation of immune microenvironment

To evaluate the differential abundance of immune cell subsets and immune response pathways between the healthy control (HC) and depression cohorts, we implemented single-sample Gene Set Enrichment Analysis (ssGSEA). The gene sets employed for the quantification of various immune cell populations were derived from established literature [17]. The xCell algorithm was utilized to assess the immune score levels between the HC and depression groups. Concurrently, we retrieved genomic datasets pertinent to immune response pathways from the ImmPort repository (http://www.immport.org) [18]. Immune pathways-related genes (IPGs) were also obtained from the ImmPort database. Pearson correlation analysis was conducted to determine the relationship between CD3G expression and the composition of immune cell subsets, as well as immune response pathways.

Utilizing WGCNA to identify immune-related significant modules

Co-expression networks were established using the WGCNA package (v.1.6.0) in R software [19]. The determination of an appropriate soft threshold β with a correlation coefficient $R^2 > 0.9$ was conducted based on GSE98793 expression profiles. Subsequently, the adjacency matrix of the GSE98793 microarray expression profile was constructed following weighted calculation, and then converted to a topological overlap matrix using the TOM overlap calculation formula. The correlation between each gene module and the sample phenotype was calculated, leading to the identification of the gene module exhibiting the strongest correlation with the immune score as the pivotal module.

Identification of signature gene for depression

We employed the limma package (v.3.64.0) to identify differentially expressed genes (DEGs) between the HC and depression cohorts, defining DEGs as genes with an adjusted p-value <0.05. Utilizing the Venn tool, we generated a Venn diagram to depict the overlap of genes from DEGs, IPGs, and significant modules identified via WGCNA. These overlapping genes were denoted as pivotal immune-related genes. LASSO regression was then conducted to unveil signature genes from the pivotal immune-related gene set, which were further refined through Cox regression analysis.

Analysis of the potential biological functions of the CD3G gene

Depression samples in the GSE98793 dataset were stratified into CD3G-low and CD3G-high cohorts based on the median CD3G expression levels. Differentially expressed genes (DEGs) between the CD3G-low and CD3G-high cohorts were determined using the limma package (v.3.64.0), with an adjusted p-value threshold of <0.05. Visualization of DEGs was accomplished through the ComplexHeatmap package (v.2.24.0). Gene Ontology (GO) and Kyoto Encyclopedia of Genes and Genomes (KEGG) enrichment analyses were conducted using the clusterProfiler R package (v.4.16.0), with the results illustrated via the ggplot2 package (v.3.4.4). Additionally, the ggplot2 package facilitated the visualization of variations in immune infiltrate levels and immune pathways between the CD3G-low and CD3G-high cohorts.

Pan-cancer analysis of CD3G

The gene expression data for CD3G across 33 types of cancer were obtained from The Cancer Genome Atlas (TCGA) database (https://portal.gdc.cancer.gov/) [20]. This dataset includes normalized RNA-Seq data for various tumor and adjacent normal tissues. Clinical data, including overall survival information, were also retrieved to assess prognostic significance. Box plots were generated to compare the expression levels of CD3G between tumor and normal tissues for each cancer type. Statistical significance was determined using the Wilcoxon rank-sum test, with a p-value threshold of <0.05 considered significant. The prognostic value of CD3G expression in different cancers was evaluated using univariate Cox regression analysis. Forest plots were used to visualize the hazard ratios (HR) and 95% confidence intervals (CI) for overall survival across the 33 cancer types. The relationship between

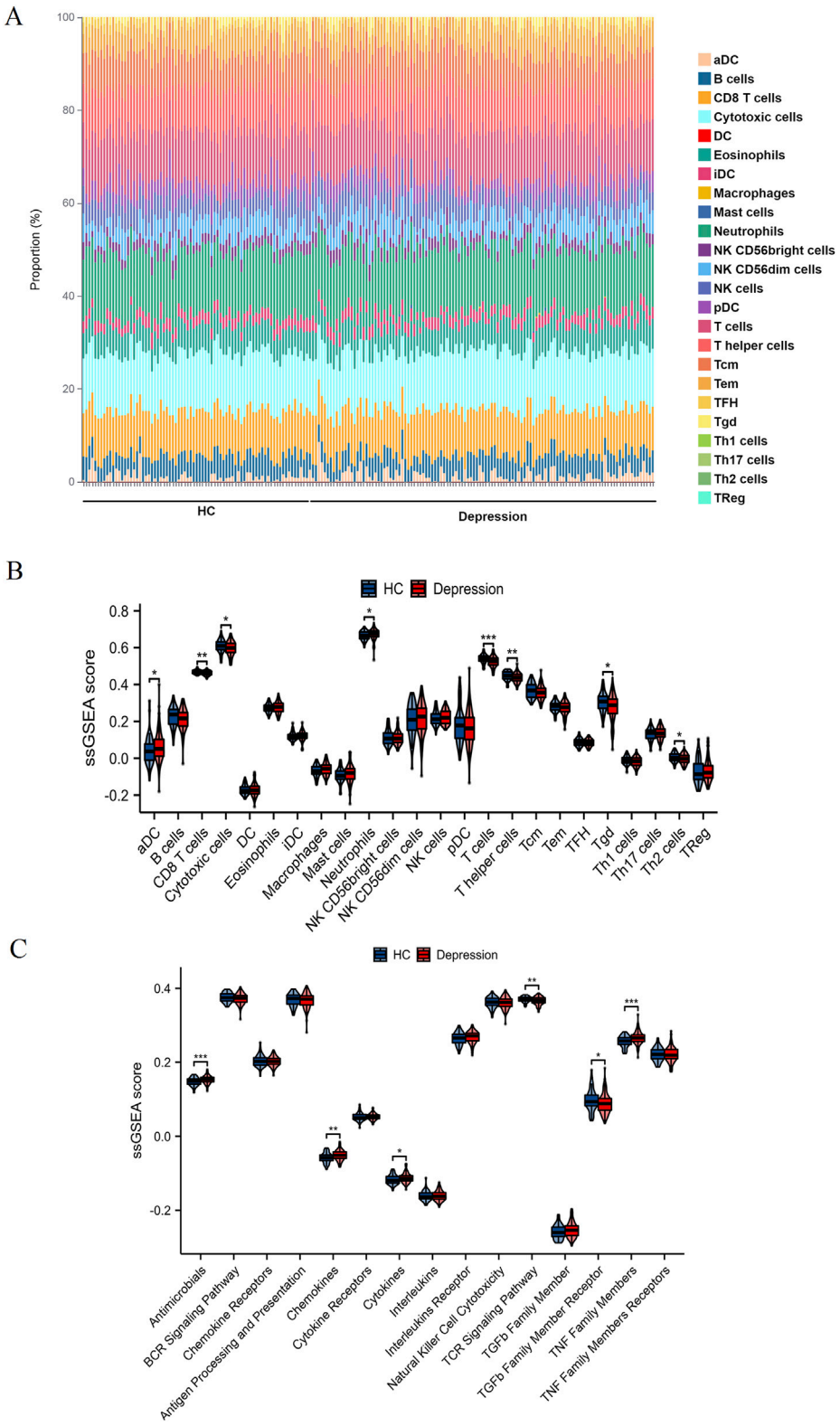

FIGURE 1
Comparative analysis of immune cell infiltration and immune pathway activity. **(A)** Proportional distribution of various immune cell types in HC and depression patients. Each bar represents a single sample, with different colors indicating different immune cell subsets. **(B)** ssGSEA scores illustrating the differences in the infiltration of specific immune cell types between HC (blue) and depression patients (red). **(C)** ssGSEA scores
(*Continued*)

FIGURE 1 (Continued)
showing the activity levels of various immune-related pathways in HC (blue) and depression patients (red). Statistically significant differences are marked with asterisks (*P < 0.05, **P < 0.01, ***P < 0.001).

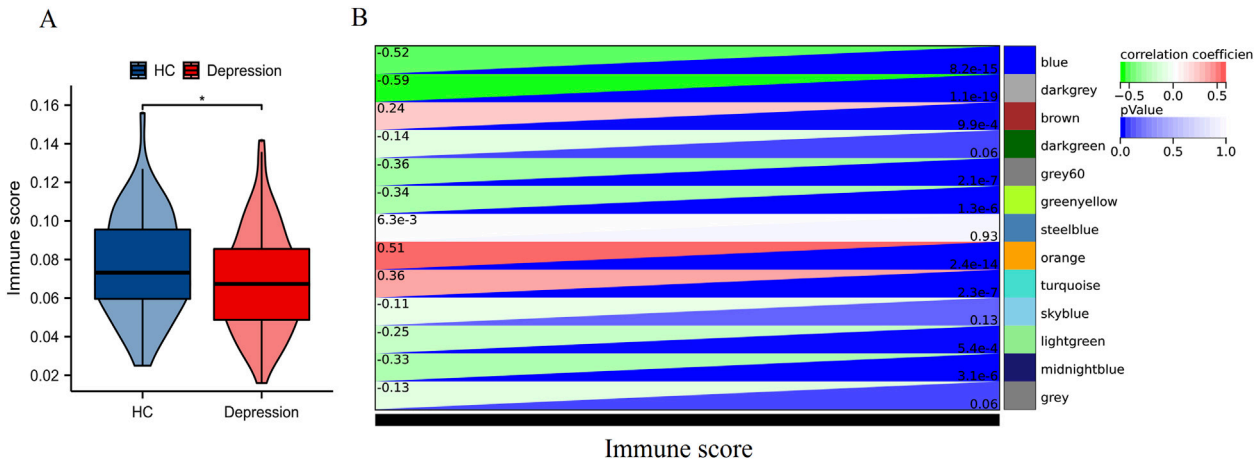

FIGURE 2
WGCNA based on immune scores. **(A)** Distribution of immune scores between HC and depression patients. *P < 0.05. **(B)** Heatmap of module-trait relationships displaying the correlation between module eigengenes and immune scores.

CD3G expression and immune cell infiltration was analyzed using the single-sample Gene Set Enrichment Analysis (ssGSEA) algorithm (v.1.44.5). The ssGSEA scores for various immune cell types were computed for each tumor sample. Correlation coefficients between CD3G expression and immune cell infiltration scores were calculated using Spearman correlation test. A heatmap was constructed to display the correlation coefficients. Box plots and forest plots were generated using the ggplot2 package (v.3.4.4), while heatmaps were created using the ComplexHeatmap package (v.2.24.0).

Gene set variation analysis (GSVA)

The z-score algorithm in the R-package GSVA (v.1.44.5) was utilized to integrate CD3G gene expression as a reflection of pathway activity across 14 functional state gene sets. Z-scores were computed individually for each gene set, followed by calculating the Pearson correlation analysis to assess the statistical correlation between genes and each gene set z-score [21, 22].

Drug sensitivity analysis

The association between CD3G gene expression in the GDSC1 and GDSC2 databases and the IC50 of chemotherapeutic drugs was assessed through Spearman correlation analysis [23]. A negative correlation indicates that higher gene expression corresponds to increased drug sensitivity in the cell line, while a positive correlation suggests that elevated gene expression leads to greater drug resistance.

Statistical analysis

All statistical analyses were conducted in the R programming environment (version 4.2.1). Wilcoxon rank-sum tests compared CD3G expression between disease and normal groups. Univariate Cox regression evaluated prognostic significance. Spearman correlation analysis linked CD3G expression to immune infiltration.

Results

Secondary outcome: immune cell infiltration patterns and pathway activity in depression

Comparative analysis of immune cell infiltration and pathway activity

Figures 1A,B reveals distinct immune cell distribution patterns between HC and depression patients. Notably, the

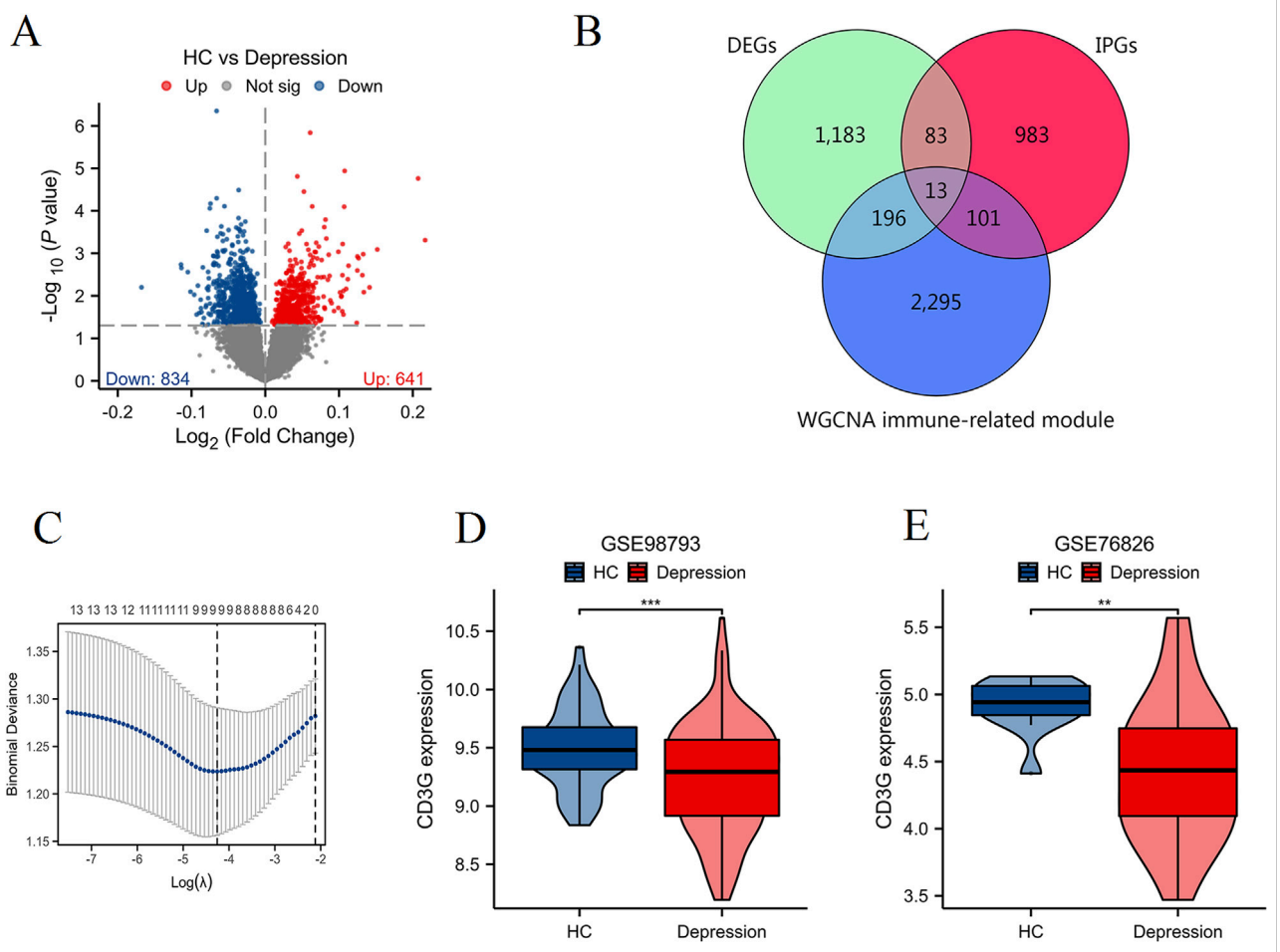

FIGURE 3
Identification and validation of key immune-related gene CD3G in depression. **(A)** Volcano plot showing DEGs between HC and depression patients. **(B)** Venn diagram illustrating the intersection of DEGs, IPGs, and genes from significant WGCNA modules. **(C)** LASSO regression analysis for feature selection. Expression levels of CD3G in the GSE98793 dataset **(D)** and GSE76826 dataset **(E)**. ***P < 0.001, **P < 0.01.

TABLE 2 The results of Logistic analysis.

Characteristics	Total(N)	Univariate analysis		Multivariate analysis	
		Odds ratio (95% CI)	P value	Odds ratio (95% CI)	P value
VEGFC	192	4.447 (1.698–11.649)	**0.002**	2.710 (0.906–8.109)	0.075
CD3G	192	0.262 (0.121–0.566)	**<0.001**	0.385 (0.156–0.949)	**0.038**
PRKCQ	192	0.467 (0.199–1.098)	0.081	2.939 (0.820–10.537)	0.098
CXCR6	192	0.440 (0.232–0.834)	**0.012**	0.508 (0.238–1.088)	0.081
TNFSF13	192	2.920 (1.381–6.177)	**0.005**	2.304 (0.890–5.963)	0.085
S100B	192	0.519 (0.312–0.864)	**0.012**	0.709 (0.399–1.260)	0.241
S100P	192	1.316 (1.023–1.694)	**0.032**	1.215 (0.910–1.623)	0.187
TRAV12-2	192	0.265 (0.107–0.654)	**0.004**	0.521 (0.185–1.467)	0.217
TRGJ1	192	0.378 (0.165–0.866)	**0.022**	0.537 (0.203–1.423)	0.211

Bold type indicates a p-value less than 0.05.

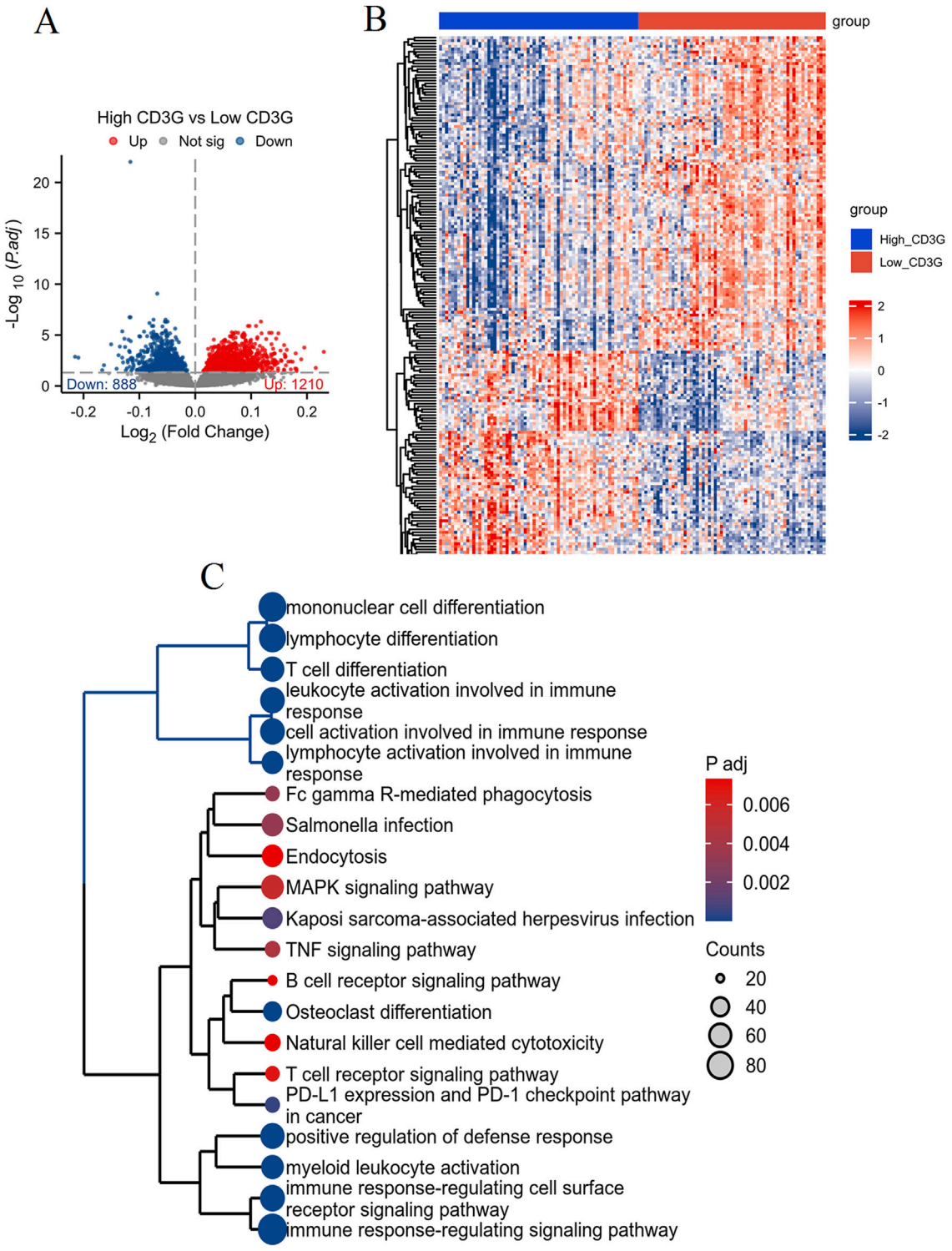

FIGURE 4
Differential expression and enrichment analysis based on CD3G expression levels in depression. **(A)** Volcano plot showing DEGs between high CD3G and low CD3G depression subgroups. **(B)** Heatmap of hierarchical clustering analysis of DEGs between high CD3G and low CD3G expression groups. **(C)** Functional enrichment tree plot displaying the significantly enriched pathways and processes associated with DEGs between high and low CD3G depression subgroups.

depression group exhibited marked reductions in CD8 T cells, cytotoxic cells, T cells, T helper cells, Tgd, and Th2 cells compared to HC (all $P < 0.05$), while dendritic cells (aDC) and neutrophils were significantly elevated ($P < 0.05$). Consistent with these cellular changes, ssGSEA analysis (Figure 1C) demonstrated divergent pathway activity profiles: antimicrobials, chemokine, cytokine, and TNF family members showed pronounced upregulation in depression ($P < 0.05$), whereas TCR signaling and TGFb family member receptor activities were substantially suppressed ($P < 0.05$). Collectively, these findings underscore systemic immune dysregulation in depression, characterized by altered cellular infiltration and pathway activation.

Primary outcome: immune score-associated gene modules and CD3G as a diagnostic biomarker

WGCNA reveals immune score-associated gene modules

As illustrated in Figure 2A, immune scores were significantly diminished in depression patients versus HC ($P < 0.05$). WGCNA identified three critical modules (Figure 2B) correlated with immune scores: the blue and darkgrey modules showed strong negative correlations ($r = -0.52$ and -0.59, respectively), whereas the orange module displayed robust positive correlation ($r = 0.51$). These results implicate immune-related gene network dysregulation as a potential contributor to depression pathogenesis.

CD3G as a diagnostic biomarker for depression

Volcano plot analysis (Figure 3A) identified 1,475 DEGs (834 downregulated, 641 upregulated) in depression. Intersection of DEGs, immune pathway genes (IPGs), and WGCNA module genes (Figure 3B) yielded 13 immune-related hub genes. LASSO regression (Figure 3C) and subsequent logistic regression uniquely identified CD3G as an independent diagnostic marker ($P < 0.038$) (Table 2). Consistent downregulation of CD3G was validated in both discovery (GSE98793, Figure 3D, $P < 0.001$) and replication cohorts (GSE76826, Figure 3E, $P < 0.01$), solidifying its role as a robust diagnostic indicator.

Exploratory outcomes: CD3G expression subgroups and pan-cancer implications

CD3G expression subgroups reveal immune pathway divergence

Comparative transcriptomic profiling (Figures 4A,B) between high- and low-CD3G depression subgroups identified 2,098 DEGs (888 downregulated, 1,210 upregulated). Functional enrichment analysis (Figure 4C) highlighted the enriched immune pathways: mononuclear cell differentiation, lymphocyte differentiation, T cell differentiation, leukocyte activation, and several immune response-related pathways such as the T cell receptor signaling pathways, natural killer cell mediated cytotoxicity, and PD-L1 expression and PD-1 checkpoint pathway in cancer. GSEA/GSVA (Figures 5A–C) further confirmed elevated inflammatory signatures (NFKB/STAT3 signaling, hypoxia, oxidative stress) in the low-CD3G subgroup ($P < 0.05$), with CD3G expression inversely correlating with chemokine production and leukocyte migration pathways.

Immune microenvironment differences by CD3G status

ssGSEA profiling (Figures 6A,C) revealed contrasting immune cell infiltration patterns: the high-CD3G subgroup had abundant adaptive immune cells (B/T cells, Th1/Th2 subsets), whereas the low-CD3G group showed dominance of innate immune populations (neutrophils, macrophages, mast cells) ($P < 0.05$). Correlation heatmaps (Figures 6B,D) strengthened these associations, with CD3G expression positively linked to TCR signaling but negatively associated with cytokine/TNF pathways, suggesting CD3G as a master regulator of immune polarization in depression.

Pan-cancer implications of CD3G dysregulation

Cross-cancer analysis (Figure 7A) demonstrated widespread CD3G upregulation in 20 malignancies (e.g., BRCA, LUAD; $P < 0.001$) but downregulation in ACC ($P < 0.05$). Figure 7B shows the association of CD3G expression with overall survival (OS) across different types of cancer. CD3G expression was associated with the OS in BRCA ($P = 0.0392$), CESC ($P = 0.0184$), HNSC ($P = 0.0045$), LGG ($P < 0.001$), LIHC ($P = 0.028$), LUAD ($P = 0.0077$), OV ($P = 0.0011$), SKCM ($P < 0.001$), UCEC ($P = 0.0033$), and UVM ($P = 0.0031$). CD3G expression positively correlated with infiltration levels of most of immune cells, such as B cells, CD8 T cells, cytotoxic cells, neutrophils, Th1 cells ($P < 0.05$), across multiple cancers, positioning it as a pan-cancer immune modulator (Figure 7C).

CD3G links oncogenesis and drug sensitivity

As shown in Figure 8, significant positive correlations were observed between CD3G expression and several oncogenic processes, including: Angiogenesis ($R = 0.31$, $P < 2.2e-16$), Apoptosis ($R = 0.44$, $P < 2.2e-16$), Differentiation ($R = 0.53$, $P < 2.2e-16$), DNA Damage ($R = 0.21$, $P < 2.2e-16$), EMT (Epithelial-Mesenchymal Transition) ($R = 0.31$, $P < 2.2e-16$), Hypoxia ($R = 0.15$, $P < 2.2e-16$), Inflammation ($R = 0.58$, $P < 2.2e-16$), Invasion ($R = 0.29$, $P < 2.2e-16$), Metastasis ($R = 0.4$, $P < 2.2e-16$), Proliferation ($R = 0.6$, $P < 2.2e-16$), Quiescence ($R = 0.59$, $P < 2.2e-16$), and Stemness ($R = 0.41$, $P < 2.2e-16$). These results demonstrate that high CD3G expression is strongly associated with the activation of many oncogenic pathways, reflecting its potential role in promoting cancer progression.

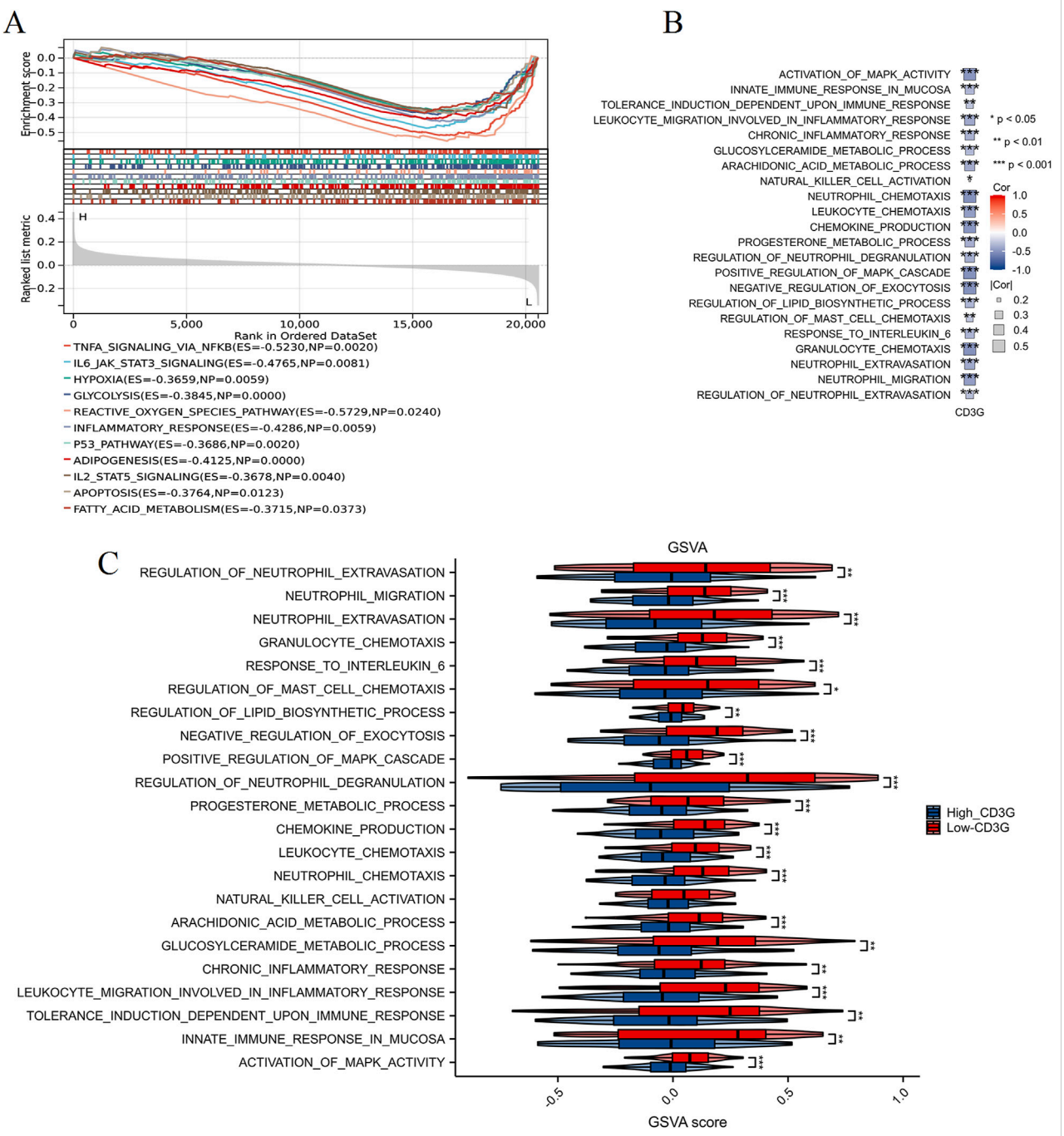

FIGURE 5
Enrichment analysis of high and low CD3G expression subgroups in depression. **(A)** GSEA plot comparing high CD3G and low CD3G expression subgroups. **(B)** Heatmap showing the correlation between CD3G expression and pathway activity based on GSVA. **(C)** GSVA scores comparing pathway activity between high and low CD3G expression subgroups. ***P < 0.001, **P < 0.01, *P < 0.05.

In addition, Figure 9A shows the Spearman correlation analysis of CD3G gene expression with the half-maximal inhibitory concentration (IC50) of various antagonists in the GDSC1 database. Notably, CD3G expression was negatively correlated with the IC50 values for multiple drugs, including PIK-93, THZ-2-49, NG-25, TL-1-85, AR-42, etc (all P < 0.001), indicating that higher CD3G expression is associated with increased sensitivity to these drugs. Figure 9B depicts the

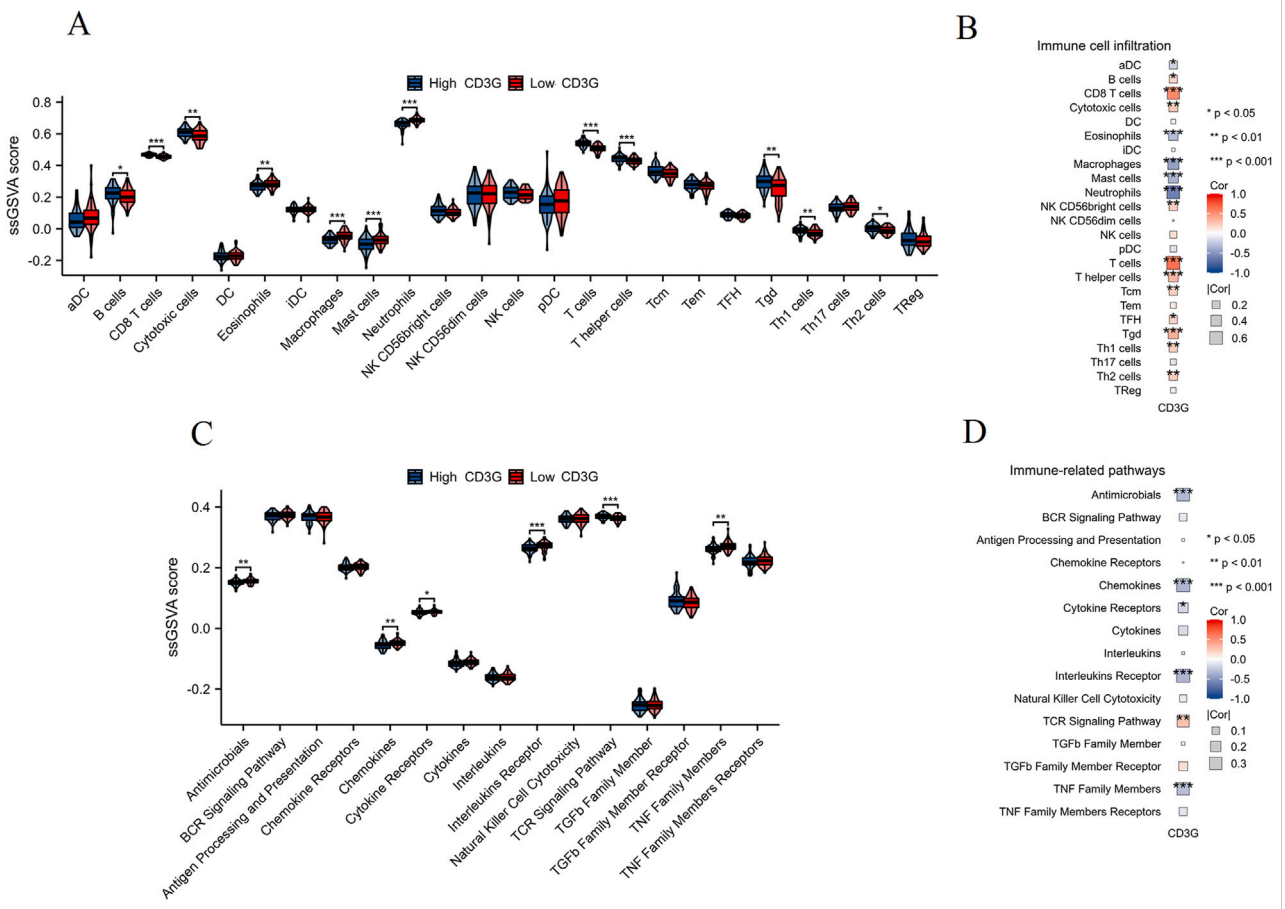

FIGURE 6
Immune cell infiltration and immune pathway activity analysis in CD3G-related subgroups. **(A)** ssGSEA scores comparing the infiltration levels of various immune cell types between high CD3G (blue) and low CD3G (red) expression subgroups. **(B)** Heatmap showing the correlation between CD3G expression and immune cell infiltration. **(C)** ssGSEA scores comparing the activity of immune-related pathways between high CD3G (blue) and low CD3G (red) expression subgroups. **(D)** Heatmap depicting the correlation between CD3G expression and the activity of immune-related pathways. ***P < 0.001, **P < 0.01, *P < 0.05.

Spearman correlation analysis of CD3G gene expression with the IC50 values in the GDSC2 database. The analysis includes 30 different drugs, with significant negative correlations for CD3G expression observed for drugs such as Vincristine, Venetoclax, Nilotinib, NU7441, I-BET-762, etc (all P < 0.001). These results suggest that elevated CD3G expression levels increase the sensitivity of cancer cell lines to these anticancer agents.

Discussion

In this study, we explored the dual role of CD3G as a potential diagnostic biomarker for depression and its oncogenic implications across various cancer types. Our findings reveal significant dysregulation of immune cell infiltration and pathway activities in patients with depression, with CD3G emerging as a critical immune-related gene.

In recent years, a growing body of research has underscored the significance of immune processes in the onset of depressive disorder [24]. Our results confirm and extend previous studies that have linked depression with immune system dysregulation. For instance, the observed decrease in CD8 T cells, cytotoxic cells, and various T cell subsets (T helper cells, Tgd, Th2) alongside an increase in dendritic cells and neutrophils is consistent with earlier research indicating altered immune profiles in depression [25, 26]. The increased activities of antimicrobial, chemokine, cytokine, and TNF family member pathways, coupled with decreased TCR signaling pathway, further underscore the complex interplay between immune response and depressive disorders. These findings align with the concept of inflammation and immune activation playing a crucial role in the pathophysiology of depression [27, 28].

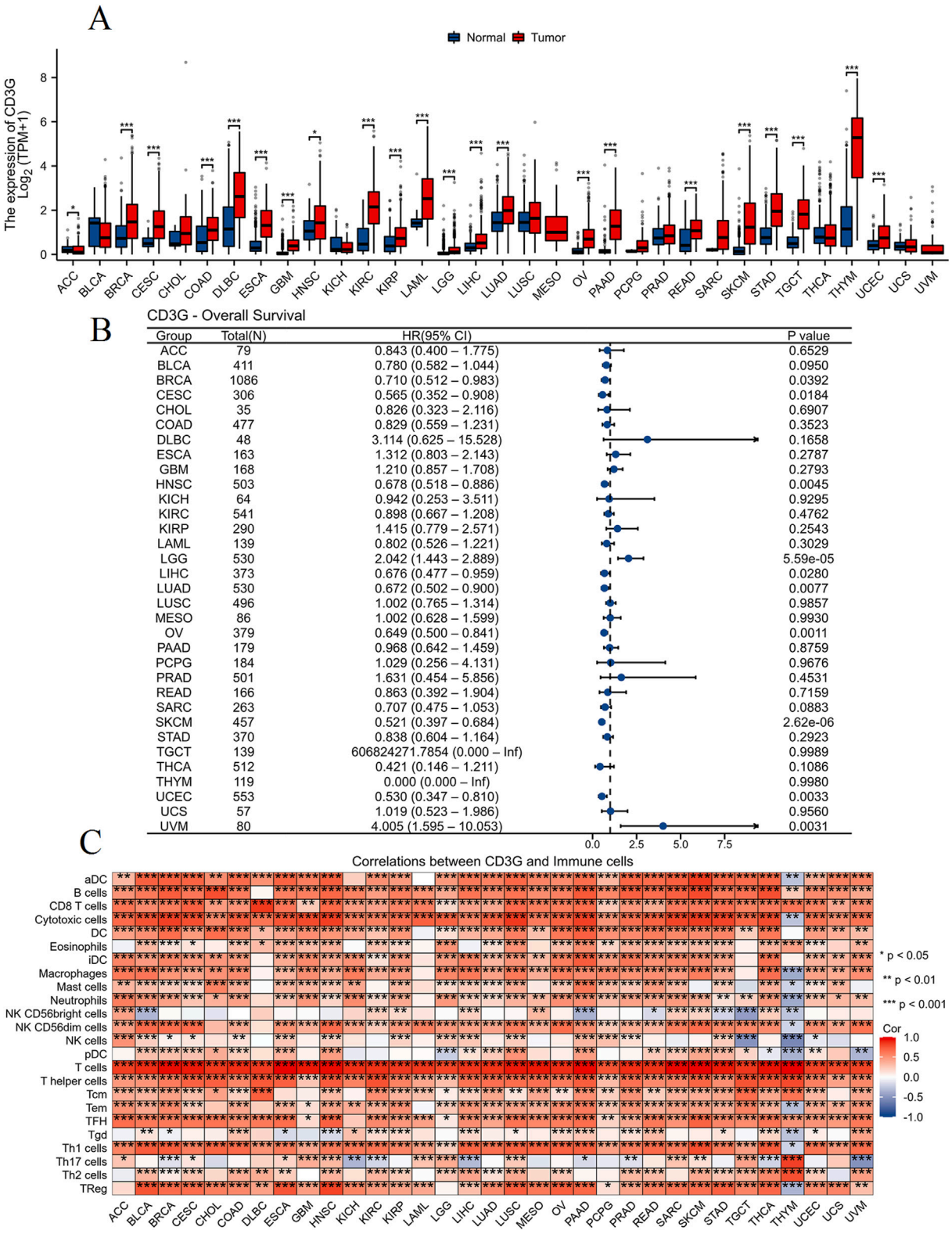

FIGURE 7
Pan-cancer analysis of CD3G. **(A)** Box plot comparing CD3G expression levels between normal (blue) and tumor (red) tissues across various types of cancer. **(B)** Forest plot displaying the hazard ratios (HR) with 95% confidence intervals (CI) and P-values for overall
(*Continued*)

FIGURE 7 (Continued)
survival (OS) associated with CD3G expression in different cancer types. **(C)** Heatmap showing the correlation between CD3G expression and infiltration levels of various immune cells across multiple cancer types.

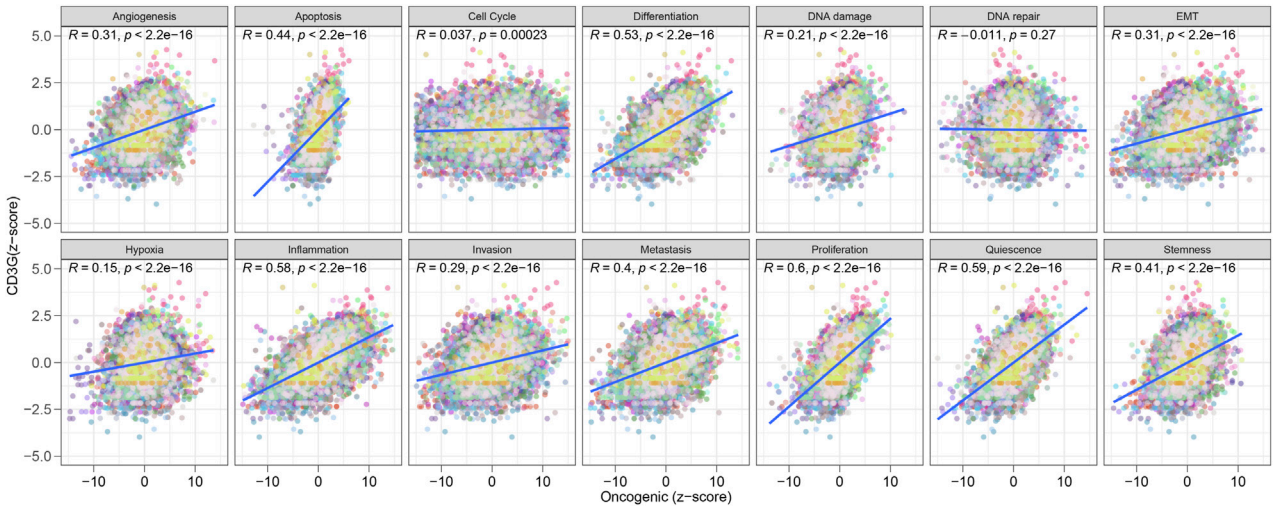

FIGURE 8
Correlation between CD3G expression and oncogenic pathways.

Building upon the identification of CD3G as an independent diagnostic marker for depression, it is essential to delve deeper into the mechanistic underpinnings of its association with immune infiltration and inflammatory pathways. Our analyses revealed that lower expression levels of CD3G correlate with an upregulation of immune response and inflammatory pathways. This observation aligns with the growing body of evidence suggesting that immune dysregulation plays a pivotal role in the pathophysiology of depression. The role of CD3G in TCR signaling is well-documented, with CD3G being a critical component of the CD3 complex essential for T-cell activation and immune response modulation [29]. Its reduced expression, as observed in our study, may lead to impaired T-cell function, thereby triggering compensatory mechanisms that enhance systemic inflammation. This is supported by studies indicating that T-cell dysfunction can result in a skewed cytokine production profile, favoring pro-inflammatory states [26]. Furthermore, the association between low CD3G expression and increased immune response in depression might be indicative of an underlying chronic inflammatory state. Chronic inflammation has been implicated in the pathogenesis of depression, with elevated levels of inflammatory markers such as interleukin-6 and tumor necrosis factor-alpha frequently reported in depressed individuals [25]. Our findings suggest that CD3G could serve as a bridge linking immune system dysregulation to the development and persistence of depressive symptoms. Previous studies have not extensively explored CD3G in the context of depression, making this a pioneering discovery.

In the realm of oncology, our pan-cancer analysis reveals that CD3G is upregulated in numerous cancers and is correlated with immune cell infiltration and oncogenic pathways. This finding is consistent with literature suggesting that CD3G, as a component of the T-cell receptor complex, plays a role in T-cell activation and cancer immune surveillance [30]. The upregulation of CD3G in various cancers may indicate its involvement in tumor immune evasion mechanisms. Moreover, the correlation between CD3G expression and immune infiltration across cancers supports the hypothesis that CD3G could serve as a prognostic marker and a potential target for immunotherapy [14].

The dual focus on CD3G in both depression and cancer is a novel aspect of our study. Previous research has typically examined the role of immune genes in either psychiatric disorders or oncology separately. By integrating these fields, our study underscores the importance of immune modulation in both depression and cancer, suggesting potential therapeutic targets that could be leveraged across these conditions. This

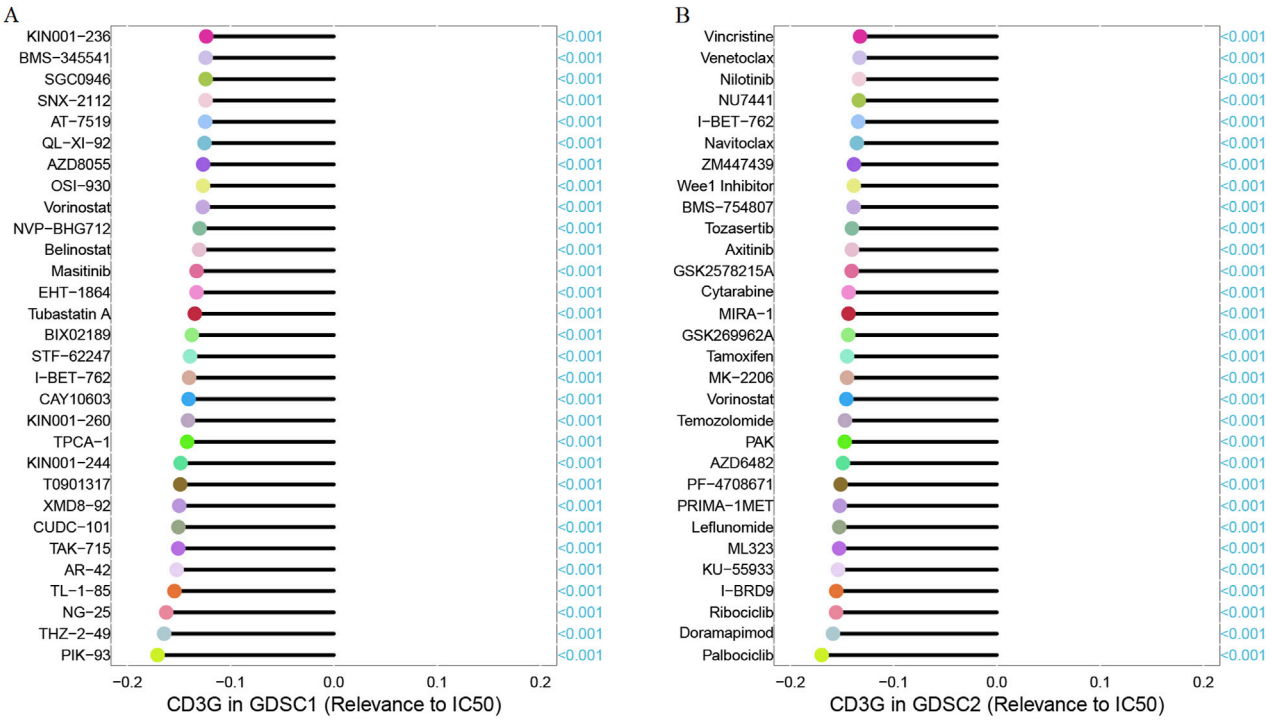

FIGURE 9
Correlation between CD3G expression and drug sensitivity (IC50) in GDSC1 **(A)** and GDSC2 **(B)** databases.

integrative approach highlights the interconnected nature of immune-related diseases and underscores the importance of holistic biomedical research.

Despite these promising findings, our study has several limitations that should be acknowledged. First, the use of publicly available datasets, while providing a robust sample size, may introduce variability due to differences in data collection methods and patient populations. Second, the cross-sectional nature of the data limits our ability to infer causal relationships between CD3G expression and disease states. Longitudinal studies would be necessary to establish causality and understand the temporal dynamics of immune dysregulation in depression and cancer. Third, while our study identifies CD3G as a potential diagnostic marker, further validation using independent cohorts and prospective clinical trials is essential to confirm its clinical utility. Additionally, the mechanistic insights proposed are based on bioinformatic analyses and require experimental validation to elucidate the precise biological pathways involved.

Conclusion

In conclusion, our study provides compelling evidence for the role of CD3G as a diagnostic marker for depression and its oncogenic implications. The significant dysregulation in immune cell infiltration and pathway activities highlighted in our findings underscores the critical importance of CD3G in the pathophysiology of both depression and cancer. These insights not only deepen our understanding of the biological underpinnings of these conditions but also open promising new avenues for therapeutic intervention. Targeting CD3G could potentially revolutionize the approach to diagnosing and treating depression and various cancers, offering hope for more effective and personalized medical strategies.

Author contributions

HG was responsible for writing the manuscript and developing the study concepts and design. JX and JL conducted the literature research. DW and GH were in charge of data analysis and figure production. TW provided review and editing services for the manuscript. All authors contributed to the article and approved the submitted version.

Data availability

The data utilized in this study were sourced from the GEO database, accessible at https://www.ncbi.nlm.nih.gov/geo/.

Funding

The author(s) declare that financial support was received for the research and/or publication of this article. This study was supported by the Natural Science Foundation of Xiamen (3502Z202372102).

Conflict of interest

The author(s) declared no potential conflicts of interest with respect to the research, authorship, and/or publication of this article.

Generative AI statement

The author(s) declare that no Generative AI was used in the creation of this manuscript.

Any alternative text (alt text) provided alongside figures in this article has been generated by Frontiers with the support of artificial intelligence and reasonable efforts have been made to ensure accuracy, including review by the authors wherever possible. If you identify any issues, please contact us.

References

1. Monroe SM, Harkness KL. Major depression and its recurrences: life course matters. *Annu Rev Clin Psychol* (2022) **18**:329–57. doi:10.1146/annurev-clinpsy-072220-021440

2. Ménard C, Hodes GE, Russo SJ. Pathogenesis of depression: insights from human and rodent studies. *Neuroscience* (2016) **321**:138–62. doi:10.1016/j.neuroscience.2015.05.053

3. Nemeroff CB. Recent advances in the neurobiology of depression. *Psychopharmacol Bull* (2002) **36**(Suppl. 2):6–23.

4. Krishnan V, Nestler EJ. The molecular neurobiology of depression. *Nature* (2008) **455**:894–902. doi:10.1038/nature07455

5. Tubbs JD, Ding J, Baum L, Sham PC. Immune dysregulation in depression: evidence from genome-wide association. *Brain Behav and Immun - Health* (2020) **7**:100108. doi:10.1016/j.bbih.2020.100108

6. Anderson G, Maes M. Oxidative/nitrosative stress and immuno-inflammatory pathways in depression: treatment implications. *Curr Pharm Des* (2014) **20**:3812–47. doi:10.2174/13816128113196660738

7. Maes M. Depression is an inflammatory disease, but cell-mediated immune activation is the key component of depression. *Prog Neuro-Psychopharmacology Biol Psychiatry* (2011) **35**:664–75. doi:10.1016/j.pnpbp.2010.06.014

8. Wohleb ES, Franklin T, Iwata M, Duman RS. Integrating neuroimmune systems in the neurobiology of depression. *Nat Rev Neurosci* (2016) **17**:497–511. doi:10.1038/nrn.2016.69

9. Leonard BE. Inflammation and depression: a causal or coincidental link to the pathophysiology? *Acta Neuropsychiatr* (2018) **30**:1–16. doi:10.1017/neu.2016.69

10. Smith-Garvin JE, Koretzky GA, Jordan MS. T cell activation. *Annu Rev Immunol* (2009) **27**:591–619. doi:10.1146/annurev.immunol.021908.132706

11. Wan YY. Multi-tasking of helper T cells. *Immunology* (2010) **130**:166–71. doi:10.1111/j.1365-2567.2010.03289.x

12. Garcillán B, Fuentes P, Marin AV, Megino RF, Chacon-Arguedas D, Mazariegos MS, et al. CD3G or CD3D knockdown in mature, but not immature, T lymphocytes similarly cripples the human TCRαβ complex. *Front Cell Dev Biol* (2021) **9**:608490. doi:10.3389/fcell.2021.608490

13. Wang Z, He Y, Cun Y, Li Q, Zhao Y, Luo Z. Identification of potential key genes for immune infiltration in childhood asthma by data mining and biological validation. *Front Genet* (2022) **13**:957030. doi:10.3389/fgene.2022.957030

14. Wang J, Gu X, Cao L, Ouyang Y, Qi X, Wang Z, et al. A novel prognostic biomarker CD3G that correlates with the tumor microenvironment in cervical cancer. *Front Oncol* (2022) **12**:979226. doi:10.3389/fonc.2022.979226

15. Jiang L, Xu J, Ni J, Gao X, Zhu Z, Dong D, et al. A functional insertion/deletion polymorphism in the proximal promoter of CD3G is associated with susceptibility for hepatocellular carcinoma in Chinese population. *DNA Cell Biol* (2012) **31**:1480–5. doi:10.1089/dna.2012.1706

16. Clough E, Barrett T, Wilhite SE, Ledoux P, Evangelista C, Kim IF, et al. NCBI GEO: archive for gene expression and epigenomics data sets: 23-Year update. *Nucleic Acids Res* (2024) **52**:D138–d144. doi:10.1093/nar/gkad965

17. Dai J, Xia K, Huai D, Li S, Zhou L, Wang S, et al. Identification of diagnostic signature, molecular subtypes, and potential drugs in allergic rhinitis based on an inflammatory response gene set. *Front Immunol* (2024) **15**:1348391. doi:10.3389/fimmu.2024.1348391

18. Bhattacharya S, Andorf S, Gomes L, Dunn P, Schaefer H, Pontius J, et al. ImmPort: disseminating data to the public for the future of immunology. *Immunol Res* (2014) **58**:234–9. doi:10.1007/s12026-014-8516-1

19. Langfelder P, Horvath S. WGCNA: an R package for weighted correlation network analysis. *BMC Bioinformatics* (2008) **9**:559. doi:10.1186/1471-2105-9-559

20. Wang Z, Jensen MA, Zenklusen JC. A practical guide to the cancer genome atlas (TCGA). *Methods Mol Biol* (2016) **1418**:111–41. doi:10.1007/978-1-4939-3578-9_6

21. Yuan H, Yan M, Zhang G, Liu W, Deng C, Liao G, et al. CancerSEA: a cancer single-cell state atlas. *Nucleic Acids Res* (2019) **47**:D900–d908. doi:10.1093/nar/gky939

22. Lee E, Chuang HY, Kim JW, Ideker T, Lee D. Inferring pathway activity toward precise disease classification. *Plos Comput Biol* (2008) **4**:e1000217. doi:10.1371/journal.pcbi.1000217

23. Yang W, Soares J, Greninger P, Edelman EJ, Lightfoot H, Forbes S, et al. Genomics of drug sensitivity in cancer (GDSC): a resource for therapeutic biomarker discovery in cancer cells. *Nucleic Acids Res* (2012) **41**:D955–61. doi:10.1093/nar/gks1111

24. Drevets WC, Wittenberg GM, Bullmore ET, Manji HK. Immune targets for therapeutic development in depression: towards precision medicine. *Nat Rev Drug Discov* (2022) **21**:224–44. doi:10.1038/s41573-021-00368-1

25. Dantzer R, O'Connor JC, Freund GG, Johnson RW, Kelley KW. From inflammation to sickness and depression: when the immune system subjugates the brain. *Nat Rev Neurosci* (2008) **9**:46–56. doi:10.1038/nrn2297

26. Miller AH, Raison CL. The role of inflammation in depression: from evolutionary imperative to modern treatment target. *Nat Rev Immunol* (2016) **16**:22–34. doi:10.1038/nri.2015.5

27. Colasanto M, Madigan S, Korczak DJ. Depression and inflammation among children and adolescents: a meta-analysis. *J Affective Disord* (2020) **277**:940–8. doi:10.1016/j.jad.2020.09.025

28. Beurel E, Toups M, Nemeroff CB. The bidirectional relationship of depression and inflammation: double trouble. *Neuron* (2020) **107**:234–56. doi:10.1016/j.neuron.2020.06.002

29. van der Merwe PA, Dushek O. Mechanisms for T cell receptor triggering. *Nat Rev Immunol* (2011) **11**:47–55. doi:10.1038/nri2887

30. Asghari Alashti F, Minuchehr Z. MiRNAs which target CD3 subunits could be potential biomarkers for cancers. *PLoS One* (2013) **8**:e78790. doi:10.1371/journal.pone.0078790

EBM Experimental Biology and Medicine

TYPE Review
PUBLISHED 03 September 2025
DOI 10.3389/ebm.2025.10604

OPEN ACCESS

*CORRESPONDENCE
Dhirendra Singh,
dhirendra.singh246@gmail.com
Abidemi James Akindele,
jakindele@unilag.edu.ng

RECEIVED 28 March 2025
ACCEPTED 13 August 2025
PUBLISHED 03 September 2025

CITATION
Singh D, Oladimeji-Salami JA and Akindele AJ (2025) Unraveling the pharmacological and therapeutic potential of Ranolazine beyond antianginal drug use: a new insight. *Exp. Biol. Med.* 250:10604. doi: 10.3389/ebm.2025.10604

Unraveling the pharmacological and therapeutic potential of Ranolazine beyond antianginal drug use: a new insight

Dhirendra Singh[1]*, Joy Awulika Oladimeji-Salami[2] and Abidemi James Akindele[3]*

[1]Department of Pharmacology, M.M College of Pharmacy, Maharishi Markandeshwar (Deemed to be University), Mullana, Ambala, Haryana, India, [2]Special Duties Department, National Biotechnology Development Agency, Abuja, Nigeria, [3]Department of Pharmacology, Therapeutics and Toxicology, Faculty of Basic Medical Sciences, College of Medicine, University of Lagos, Lagos, Nigeria

Abstract

Ranolazine (RAN) is an acetanilide and piperazine derivative that selectively blocks the late sodium current in cardiac cells and is prescribed in adults as an add-on medication for the symptomatic management of patients with stable angina pectoris who are insufficiently managed or intolerant of first-line antianginal treatments. RAN was first approved by the U.S. Food and Drug Administration (FDA) in 2006 and the European Medicine Agency in 2008 for the treatment of chronic stable angina. RAN has no substantial effect on hemodynamic indicators, including heart rate and blood pressure. RAN also slows fatty acid oxidation, which increases glucose oxidation, lowers lactic acid generation, and optimizes heart performance. Besides its antianginal effect, RAN has recently revealed additional pharmacological properties such as neuroprotective, hepatoprotective, renal protective, cardioprotective, and antidiabetic effects and other beneficial pharmacological activities. We choose to write this current review paper to address the many hidden pharmacological and therapeutic potentials of RAN beyond its antianginal activity.

KEYWORDS

anticancer, cardioprotective, renalprotective, neuroprotective, hepatoprotective

Impact statement

Drug re-purposing, finding new therapeutic applications for old or existing drugs, provides the avenue to increase the therapeutic options for the treatment of disease conditions with the possible benefit of enhanced efficacy and safety profile. Beyond its antianginal action, Ranolazine exhibits a variety of pharmacological actions which can be explored for therapeutic benefits. This review extensively sheds light on a number of these pharmacological actions to broaden knowledge and spheres of potential therapeutic applications of Ranolazine.

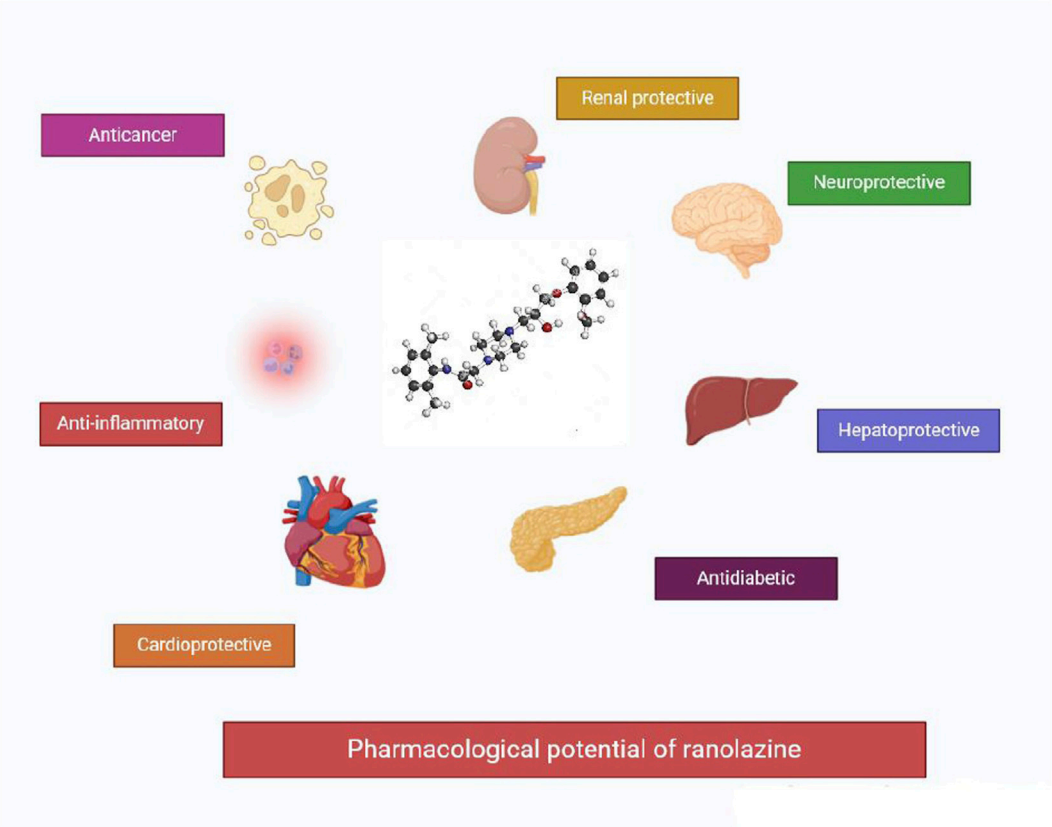

GRAPHICAL ABSTRACT
Pharmacological potential of ranolazine.

Introduction

Ranolazine (RAN) is N-(2, 6-dimethyl phenyl)-4(2-hydroxy-3-[2-methoxyphenoxy] - propyl)-1-piperazine acetamide dihydrochloride. It is an active piperazine whose anti-ischemic effect was originally attributed to the selective inhibition of fatty acid oxidation with a consequent shift of metabolism to more energy-efficient glucose oxidation [1]. An alternative mechanism of action proposed in the past for RAN was the inhibition of β_1 and β_2 adrenoceptors [2]. However, this mechanism (which is associated with sympathetic nervous system regulation of heart rate and contractility) is less prominent compared to RAN's primary action on cardiac ion channels. It is a less significant involvement at the therapeutic concentration of RAN for the treatment of angina, with the main mechanism being linked to inhibition of the late sodium current in cardiac myocytes. This effect reduces intracellular calcium overload and improves myocardial relaxation and oxygen efficiency. At the clinical level, RAN decreases the current of sodium and potassium ion channels. It has been well studied that inhibition of the late phase of the inward sodium current occurs during cardiac repolarization [3]. In pathological conditions, a rise in calcium ion concentrations contributes to increased sodium-calcium interaction, which induces an increase in the cytosolic calcium concentration [4]. Calcium overload is thought to be the factor that induces reduced left ventricular relaxation during moderate ischemia as well as reperfusion. Increased left ventricular diastolic wall stress compromises myocardial tension circulation, which continues to rise still. Moreover, calcium overload has harmful impacts on myocardial electrical activity, predisposing to ventricular tachycardia [5]. Although this mechanism has been well studied mainly in rodents, the anti-ischemic activity of RAN due to late Na-channel suppression of myocardial perfusion lacks evidence to support this mechanism in patients with ischemic heart disorders. RAN slows the delayed rectifying K^+ current at therapeutic doses and enhances the Q-T interval [6]. The total effect of RAN on the action potential period is equilibrium between the combined effects of rectifier potassium current as well as late sodium current suppression, which prolongs the QT interval by 2–6 ms [7]. Figure 1 shows the mechanism of action of RAN.

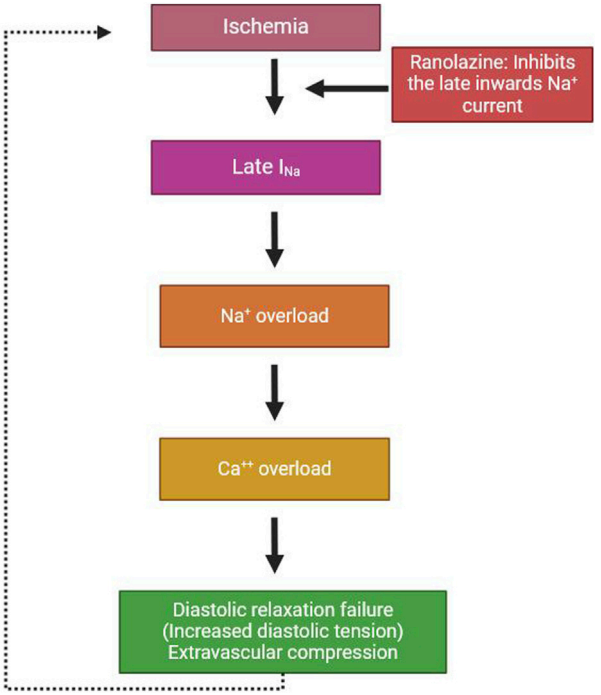

FIGURE 1
Mechanism of action of ranolazine.

The pharmacologically induced attenuation of the late sodium current enhances cardiac diastolic relaxation by decreasing diastolic wall stress. This ultimately results in an improvement of segmental myocardial ischemia.

RAN was first used in therapeutic settings over 25 years ago. It is widely used to treat some disorders and is safe and effective in many cases. Many preclinical and clinical experiments show that RAN may exert cellular protective effects by specifically suppressing the late sodium inward current (late iNa). In the past few years, RAN has been associated with numerous positive properties, such as anticancer, renoprotective, hepatoprotective, neuroprotective, cardioprotective, analgesic, and anti-inflammatory activity, and other benefits independent of its antianginal function.

RAN modulates several cellular pathways like TNF-α, NF-κB, Capase-3, IL-1β, IL-6, PPAR-γ, Bax bcl-2, Notch2/Hes1, AKT-eNOS, COX-2, and ERK, which is activity independent of its cardiac protective mechanism.

Search strategies

The literature search was done on multiple electronic databases. These include Web of Science, PubMed, Scopus, and Google Scholar. Appropriate search terms and combinations were used, including ranolazine, pharmacokinetics, neuroprotective, hepatoprotective, renoprotective, cardioprotective, and antidiabetic effects.

Pharmacokinetics

RAN is available as an oral tablet for therapeutic use and as an intravenous formulation for experimental application. Initially, oral RAN was evaluated as an instant release (IR) formulation. RAN IR has an overall terminal removal half-life of 1.4–1.9 h and a 10-fold peak-trough gap of 240–400 mg three times per day [8]. RAN is now commonly available as a sustained-release (SR) formulation with a more extended absorption phase, with a maximal plasma concentration (Cmax) usually seen 4–6 h after oral administration and an estimated apparent total elimination half-life of 7 h after steady state. The peak-trough difference at 500–1000 mg twice/day is only 1.6-fold, which is much improved over that of the IR formulation [9–11]. The steady state is usually reached within 3 days of twice-daily dosing. RAN plasma amounts that are clinically beneficial for chronic angina range from 2 to 6 μmol/L [12, 13]. The oral bioavailability of RAN is 30%–55% and is not influenced by food. RAN is approximately 65% bound to serum protein, mainly α1-acid glycoprotein [14]. RAN is mainly cleared by the liver metabolic enzyme cytochrome P450 (CYP) 3A4 (70–85%) and is a substrate of P-glycoprotein. Additional processes include CYP2D6 metabolism (10–15 percent), glucuronidation (<5 percent), and renal excretion of unchanged RAN (<5 percent) [8].

Anticancer effects

Driffort et al. found that RAN repressed the pro-invasive shape of human breast cancer MDA-MB-231 cells and decreased the localized extracellular matrix degradation activity [15]. Qiu et al. and Lee et al. validated similar findings and discovered that the anti-invasive action might occur independently of proliferation [16, 17]. Qiu and his group found that RAN's anti-invasive activity was dose-related, with concentrations as low as 2.5 μM during hypoxia [16]. Guzel et al. found that, in human colorectal cancer cells, (i) hypoxia markedly increased Matrigel invasion and (ii) therapeutic dosages of RAN decreased invasiveness without compromising proliferative ability or cell survival [18].

Rizaner and colleagues demonstrated that for robust metastatic rat prostate cancer Mat-LyLu cells, RAN (i) hindered Matrigel migration under both normoxic and hypoxic circumstances and (ii) decreased the proportion of cells in the lung metastases showing Nav1.7 [19]. Pemmireddy and team examined the anticancer action of RAN on 1,2-Dimethyl hydrazine (DMH)-induced colon cancer in mice and found that RAZ substantially reduced colon cancer in

mice, most likely because of cancer cell growth deregulations [20]. Using the Dunning model of rat prostate cancer, Bugan and coworkers demonstrated in double-blind tests that gavage administration of 2.5–5 μM RAN inhibited lung metastasis by as much as 63% [21]. Guth et al. demonstrated that RAN (i) inhibited tumor development and (ii) boosted anti-cancer immunity, as shown by reduced tumor $CD8^+$ T-cells Tim3 content, enhanced macrophages, and lowered blood myeloid immunosuppressive monocytes in the TRAMPC1 genetic mice model of prostate cancer [22]. Lastly, Lasheras-Otero et al. demonstrated that RAN inhibited liver metastases in a mouse model of melanoma [23].

Cardioprotective effects

Tocchetti et al. revealed that RAN could avert doxorubicin-induced cardiac failure in mice and HL-1 cardiomyocytes via lowering ROS production [24]. Furthermore, RAN has been shown to mitigate cardiac dysfunction induced by trastuzumab, which is believed to mediate its activity by inhibiting the generation of ROS [25]. De Lorenzo and teammates found that RAN mitigated not just the cardiotoxic adverse effects of trastuzumab but also of pertuzumab and trastuzumab-emtansine (TDM1) when employed in combinatorial therapies both *in vitro* and *in vivo* [26]. Cappetta et al. conducted an experiment using RAN and stated that it could protect cardiomyocytes from doxorubicin-caused oxidative damage [27]. RAN could attenuate MTX-caused oxidative damage in H9c2 cardiomyocytes by reducing MDA, LOOH, AOPPs, and XO activity, maintaining T-SH, CAT, and TAC levels, and prohibiting the HIF-1α inflammatory cascade [28]. Jiang et al. reported that therapy with RAN in Phospholamban (PLN) knockout hiPSCs-CMs could significantly repair Ca^{2+} handling abnormalities and cellular energy metabolism, thus alleviating the PLN knockout phenotype of HF [29].

In high glucose-treated cardiac fibroblasts, RAN decreased pyroptosis, prevented collagen deposition, and enhanced heart function via enhancing miR-135b expression [30]. Furthermore, RAN protected against diabetic cardiomyopathy-induced apoptosis in rats via activation of the NOTCH1/NRG1 signaling cascade [31]. Tawfik and team showed that RAN administration ameliorated the isoprenaline-mediated myocardial damage in both nondiabetic and diabetic rats by improving histopathological scores, reducing apoptotic markers, and modulating AMPK activity [32]. Le DE and his team proved that RAN increased both resting and stress-induced cardiac adenosine levels and caused small-vessel vasodilation, which improved ischemia in dogs [33]. RAN also showed a positive effect on cardiomyocytes subjected to ischemia/reperfusion, but only when used during ischemia, and this effect is accomplished through improving calcium regulation during ischemia [34].

Tantray et al confirmed that RAN had a protective role in myocardial infarction, similar to ischemic preconditioning facilitators, via promoting myocardial Nitric oxide, Adenosine, Bradykinin, and K^+ATPase levels in an isolated heart [35]. In anaesthetized rabbits subjected to ischemia and reperfusion, RAN lowered infarct size and raised salvage area index, activating a process similar to PreC and PostC that required activation of the RISK axis [36]. Feng and co-workers demonstrated that chronic RAN treatment effectively reduced the increased concentrations of NE and BNP-45 caused by CHF and improved LV function in CHF rats [37]. RAN increased cardiac function and decreased the level of heart injury in rats with congestive heart failure, which is likely due to the activation of AKT phosphorylation [38]. RAN attenuates pressure overload-mediated cardiac hypertrophy and systolic and diastolic activity by restoring Na^+ and Ca^{2+} handling, preventing downstream hypertrophic pathways, and reducing ER stress [39].

In an animal model of heart failure, RAN ameliorated cardiac remodeling and improved systolic and diastolic performance by normalizing Ca^{2+} storage [40]. Coppini and colleagues showed that acute RAN treatment lowered intracellular Na^+ and Ca^{2+} levels as well as CaMKII activity, which contributed to the decrease in hypertrophic cardiomyopathy-associated cardiac remodeling and myocardial dysfunction [41]. Moreover, RAN treatment decreased oxidative stress and alleviated diastolic dysfunction in rats fed a high-salt diet to develop hypertension [42].

Williams and co-workers demonstrated that RAN was efficient in lowering diastolic dysfunction in spontaneously hypertensive rats, and its mechanism of action was associated with suppression of the enhanced late sodium current in the SHR, resulting in decreased Ca^{2+} overload [43]. Le et al. proposed that RAN elevated adenosine concentrations in coronary veins in anaesthetized dogs, both at rest and during dobutamine-caused myocardial ischemia, mostly via enhancing the function of the cytosolic-5′-nucleotidase enzyme [33].

In individuals with CCS, RAN has been proposed as a way to increase myocardial perfusion and lessen mechanical compression of coronary microcirculation [44]. RAN enhanced coronary flow reserve in 58 patients with angina and myocardial ischemia but no obstructive coronary artery disease. This was likely because it improved abnormal coronary autoregulation, which decreased the baseline diastolic coronary flow rate and elevated the hyperemic diastolic coronary flow rate [45]. Furthermore, angina was found to improve when RAN was given in comparison to a placebo in a small trial involving women who had angina, signs of myocardial ischemia, but no obstructive coronary artery disease (CAD). There was also a trend towards improvement in the anomalies of myocardial perfusion detected by cardiac magnetic resonance imaging (CMR imaging). Additionally, compared to women with CFR >3.0, those with CFR ≤3.0 had a markedly

increased myocardial perfusion reserve index (MPRI) while using RAN versus placebo [46]. RAN therapy also increases arginine plasma values and reduces oxidative stress in a randomized controlled study of 20 patients with unstable angina pectoris and acute cardiac ischemia [47].

Chou and colleagues discovered that RAN notably reduced action potential time, Cai transient time, and Cai decay duration, improved conduction inhomogeneity, and repressed arrhythmogenic alternans induction in db/db mouse hearts with acute IR damage [48]. Wolfes et al. studied the impact of RAN paired with various selective NCX-blockers in an isolated whole-heart model of AF in rabbits and discovered that both combinations extended aERP and aPRR and thereby reduced the development of AF [49]. In levosimendan-produced atrial fibrillation, RAN has a prominent antiarrhythmic effect, and the primary mechanism is a slight delay in repolarization and refractory period, which preserves the atrial myocardium against premature excitement and atrial fibrillation in rabbits [50]. Additionally, RAN appeared to have a dose-dependent antiarrhythmic impact on pacing-induced reentrant ventricular arrhythmias during the late phase of myocardial infarction in anaesthetized rabbits [51].

Markandeya et al. revealed that RAN inhibited late INa, which shortened APD and abolished triggered activity in Lmna (N195K/N195K) ventricular myocytes [52]. RAN has been found to enhance redox balance and mitochondrial activity in the atrium of rats suffering from acetylcholine-$CaCl_2$-mediated atrial fibrillation [53]. RAN reduced delayed repolarization, aberrant electrical activity, and greater late sodium currents in elderly rats continuously exposed to low testosterone, all of which encouraged maladaptive electrical remodeling in ventricular myocytes [54].

Mustroph and colleagues investigated the beneficial effect of RAN on ethanol-induced atrial fibrillation and discovered that it efficiently suppressed atrial fibrillation by altering the activity of the CaMKII-dependent NaV1.5 channel [55]. RAN also inhibited electrical remodeling, causing atrial fibrillation in HL-1 atrial myocytes through modification of the PI3K/Akt signaling axis [56]. Opacic and his group emphasized that RAN effectively lengthened the atrial effective refractory time and lowered the atrial conduction rate at baseline and after 2 days of AF in a goat model of lone AF [57]. RAN was also compared with vernakalant for cardioversion of acutely produced AF in 15 rabbit hearts. AF was produced with atrial burst pacing and acetylcholine/isoproterenol. RAN besides vernakalant showed equal efficacy in preventing AF [58].

Similarly, recent research in horses found that, in comparison with single medications, the combination of dofetilide and RAN improved the antiarrhythmic effects on acutely generated AF, influencing cardioversion time, susceptibility at AF, and AF latency [59]. The combination of RAN and ivabradine has been evaluated in AF in pigs and the combined effect of these two drugs reduced ventricular rate via decreasing conduction at the AV node (increased A-H period) and minimizing the dominant AF frequency [60].

RAN was tested to assess its effects in a canine model of heart disease. It blocks atrial fibrillation in animals by lengthening the atrial refractory duration and atrial conduction time. No pro-arrhythmic influence was apparent on the ventricle [61]. Also, RAN administration avoided VT in the porcine model of catecholaminergic polymorphic ventricular tachycardia and decreased the T-wave length [62]. RAN has also been found to be non-inferior to lidocaine and sotalol in avoiding ischemia-reperfusion-induced ventricular tachycardia in a rat model [63]. Malavaki and team examined the vasorelaxant action of RAN and nicardipine on the rabbit aorta. Researchers found that RAN has a synergistic interaction with nicardipine to trigger vaso-relaxation in rabbit aortas [64]. RAN inhibited the occurrence and minimized the duration of action potentials in HL-1 cells, resulting in an antiarrhythmic response [65].

In another study, RAN reduced HOCl-LDL-associated alterations in cardiac contractility and electrophysiology, including arrhythmias in primary cardiomyocytes [66]. Del-Canto et al. found that RAN ameliorated the electrophysiological effects responsible for the stretch-induced modification of HL-1 cell fibrillatory activation patterns by altering the rise in activation rate and preserving the magnitude of activation [67]. RAN modified the ECG abnormalities, diminished Ca^{2+} sparks and abnormal waves, lowered the *in vitro* events and the frequency of arrhythmias noticed in isolated cardiomyocytes of hypothyroid mice [68]. Two preclinical studies of RAN demonstrate promise in preventing long QT syndrome in rats. RAN suppressed QT prolongation, prevented early after depolarizations, and reduced the duration of torsades de pointes [69, 70].

RAN showed antiarrhythmic efficacy against AT (Atrial Tachycardia) elicited by rapid burst stimulation in anaesthetized rabbits [71]. Nunoi and his team examined the anti-atrial fibrillatory effect and pharmacological safety characteristics of RAN in halothane-anesthetized dogs. Researchers found that RAN had little effect on ventricular early repolarization *in vivo*, but it did extend late repolarization with no danger of re-entrant arrhythmias [72].

Wolfes and colleagues evaluated the impact of RAN in combination with several specific NCX-blockers in an isolated whole-heart AF model. Both combinations increased the atrial effective refractory time while decreasing the frequency of AF episodes [49]. Aidonidis et al. investigated whether co-treatment of RAN-AMIO would show additive antiarrhythmic effects. RAN notably improved the propagation duration of fast atrial depolarizations and enhanced the AMIO-mediated mild elevations in aPRR [73]. Miranda and co-workers explored the influence of RAN on healthy cardiomyocytes as well as a cellular model of type 3 long QT syndromes (LQT3). RAN had a small effect on sarcomere shortening in healthy ENDO and EPI cells, and it reduced arrhythmias caused by INaL to the same rate as ENDO and EPI cells [74].

Eleclazine and RAN reduced the AF window and AF burden in association with the inhibition of both endogenous and enhanced atrial late INa with half maximal inhibitory concentrations (IC50) of 1.14 and 9.78 μM and 0.94 and 8.31 μM, respectively [75]. RAN normalized AV-conduction in Scn5a1798insD/+ mice by preventing the mutation-induced increase in intracellular sodium ($[Na^+]i$) and calcium ($[Ca^{2+}]i$) concentrations [76]. RAN also inhibited TASK-1 channels, and inhibition of TASK-1 may contribute to the observed antiarrhythmic effects of RAN [3]. RAN suppressed CaT alternans and decreased the Ca^{2+}-voltage coupling gain in a dog HF model, reducing arrhythmogenic cardiac alternans [77]. RAN has continued to yield amazing outcomes, such as the cessation of acutely caused AF in horses via cardioversion [78]. RAN partially prevented action potential and QT interval prolongation in 4-week-old $Scn5a^{+/\Delta QKP}$ mice and suppressed arrhythmias [79].

Ke and colleagues examined how Ca^{2+} homeostasis was affected in CKD mice and discovered that RAN, by controlling CaMKII, PLB, and late Na^+ current, reduced the length of the QT interval and the development of cardiac arrhythmogenesis [80]. Huang et al. investigated the role of FGF23 in activating the INa-Late, resulting in calcium imbalance and increasing PV arrhythmogenesis, and found that RAN-reduced FGF23 enhanced beating rates, calcium fluctuations, and mitochondrial ROS in PV cardiomyocytes [81].

In human atrial myocytes, RAN alone or when combined with low-dose dronedarone prolonged APD, increased cellular hyperpolarization, and decreased SR Ca (2+) leakage [82]. RAN has been observed to possess a similar effect to mexiletine in terms of action potential period shortening, with less paradoxical action potential duration prolongation in LQT3 mutant cells [83]. In the rabbit heart model, RAN perfusion substantially decreased the number of breakthrough-type excitations (BEs) in the ischemic border zone (BZ) and mitigated ischemia-caused shortening of action potentials in the BZ without influencing conduction velocity, most likely because of IKr repression [84]. RAN also decreased VT load and implanted cardioverter-defibrillator (ICD) shocks in 11/12 individuals receiving drug-refractory shocks [85]. RAN also proved to be effective, well-tolerated, and safe in reducing ventricular arrhythmia episodes and ICD interventions in patients with recurrent antiarrhythmic drug-refractory events [86]. After analyzing a group of AF patients on RAN, Black-Maier et al. discovered that the medication is linked to decreased AF DF but not altered organization index or fibrillatory wave amplitude [87]. RAN, a late I (Na) blocker, appeared to possess antiarrhythmic effects, according to continuous ECG monitoring of patients admitted for acute coronary syndrome within the first week [88].

RAN was tested in patients having coronary artery disorder and paroxysmal AF who used to have a double chamber pacemaker able to detect AF. RAN 375 mg twice each day compared with placebo shortened average AF duration and mean AF length. There was no substantial variation in QTc. The 500 mg and 750 mg arms combined showed a reduction in AF recurrence with borderline statistical significance [89]. RAN has also been demonstrated to result in a greater conversion rate of AF to normal sinus rhythm when administered in combination with amiodarone than amiodarone alone in randomized clinical research including 121 patients [90]. Tsanaxidis et al. found that a single 1000 mg daily treatment of RAN when given with amiodarone leads to a faster recovery to sinus rhythm and a better sinus conversion rate than amiodarone alone. The addition of RAN had no detrimental effect on left ventricular activity [91]. The additive value of RAN to amiodarone in AF has been confirmed by two meta-analyses. The use of RAN accelerates the time for AF cardioversion. It also helps avoid new-onset AF in people with disabilities rhythm of sinus [92, 93].

The HARMONY study demonstrated that combining moderate dosages of oral RAN with decreased doses of dronedarone effectively ameliorated the AF burden in individuals with paroxysmal AF and was tolerated satisfactorily [94]. Many other small trials have found that RAN decreases conversion time from atrial fibrillation to sinus rhythm. It also increases heart function following coronary artery bypass grafting (CABG) [95–98]. Another clinical study explored the impact of RAN on AF in postoperative atrial fibrillation (POAF). Patients having heart valve and/or heart bypass surgery have been involved. The addition of RAN to normal treatment markedly decreased the frequency of POAF. There was no effect on the stay in the intensive care facility or cardiovascular death, but the rate of cardiovascular readmission decreased by 30 days [99].

In patients experiencing acute coronary syndrome without ST-segment acceleration, RAN has been found to minimize the rate of non-sustained ventricular tachycardias and atrial fibrillation (AF) [100]. In another small study of eight patients with long QT syndrome type 3 (LQTS3), RAN was demonstrated to successfully decrease the QT period, hence reducing the frequency of ventricular arrhythmias [101]. Figure 2 shows the therapeutic efficacy of RAN in heart dysfunction. RAN inhibits TNF-α, IL-1β, NF-κB, Caspase-3, Bax, ROS, and Ca^{2+} levels and activates Notch, AMPK, and miR-135b Bcl-2, resulting in improved outcomes for cardiac arrhythmia, cardiac fibrosis, cardiac injury, and myocardial infarction.

Cempaka Putri et al. [102] conducted a systematic review and meta-analysis on the efficacy of using RAN to improve diastolic performance and exercise capacity in heart failure with preserved ejection fraction. It was established that RAN was significantly efficacious in improving diastolic performance in heart failure patients with preserved ejection fraction, with no significant effect on blood pressure, heart rate, and ventricular repolarization rate (shortening of the QT interval).

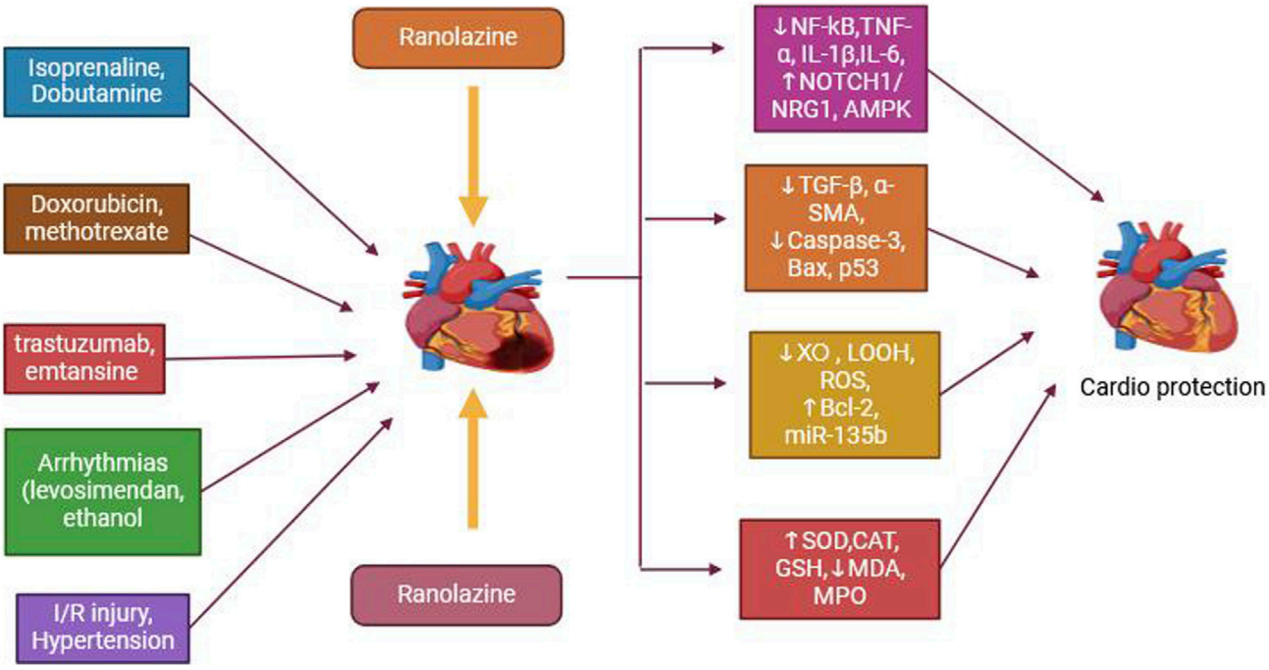

FIGURE 2
Therapeutic efficacy of ranolazine in heart dysfunction.

Neuroprotective effects

Piano and colleagues investigated the protective effect of RAN on microglia cells stimulated by LPS and found that RAN counteracts the neurotoxic effect of LPS-activated microglia on 661W neuronal cells [103]. RAN dramatically enhanced cell survival and growth in cultured astrocytes at any tested dose while decreasing LDH loss, Smac/Diablo activity, and Caspase-3 action, demonstrating a decreased rate of cell death [104].

Akgul and co-workers examined the beneficial effect of RAN in a brain I/R model of rats and concluded that RAN helped in cerebral recovery by increasing Bcl-2 and NA levels and decreasing AChE, TNF-α, and ACP levels [105]. Kahlig and team studied the antiepileptic action of RAN in hippocampus neurons and discovered that at therapeutic doses, RAN lowered the action potential firing rate of hippocampal neurons in response to recurrent depolarizing current injections by stabilizing the inactivated states of Na^+ channels [106]. Peters et al. investigated the possibility of RAN as an anticonvulsant and found that RAN affected Nav1.2 channels, lowering macroscopic currents and slowing the recovery of rapid and slow inactivation of the Nav1.2 channel in hamster ovary cells stably expressing the rat Nav1.2 channel [107].

In a rat model of DOX-induced neurotoxicity, RAN reduced brain inflammation, improved BBB integrity, alleviated brain mitochondrial dysfunction, inhibited apoptosis, and preserved microglial structure and hippocampal plasticity [108]. Samir et al. revealed that RAN has a unique neuroprotective function against scopolamine-caused dementia in rats via antioxidative, anti-inflammatory, and anti-apoptotic actions as well as regulation of GFAP, BDNF, and Tau protein levels [109]. In diabetic neuropathy rats, RAN and pioglitazone have separately altered evoked-pain activity, lowered sciatic TNF-α and 1L-1β levels, decreased levels of Nav1.7 channels, and enhanced expression of the spinal PPAR-γ gene [110]. Chandrashekhar and colleagues conducted an open-label dose-ascending trial of RAN in 14 people with amyotrophic lateral sclerosis, examining muscular cramp symptoms. It was discovered that RAN improved cramp occurrence and severity, which supports its study into muscular cramps [111]. Figure 3 shows promising therapeutic applications of RAN in neuronal injury.

RAN primarily activates anti-apoptotic and neuronal survival pathways such as Bcl-2. It also suppresses Caspase-3, TNF-α, IL-1β, IL-6, ROS, and other factors that promote neuronal death.

Renal protective effects

RAN substantially reduces renal ischemia-reperfusion damage in rats, which was accomplished by modulating the

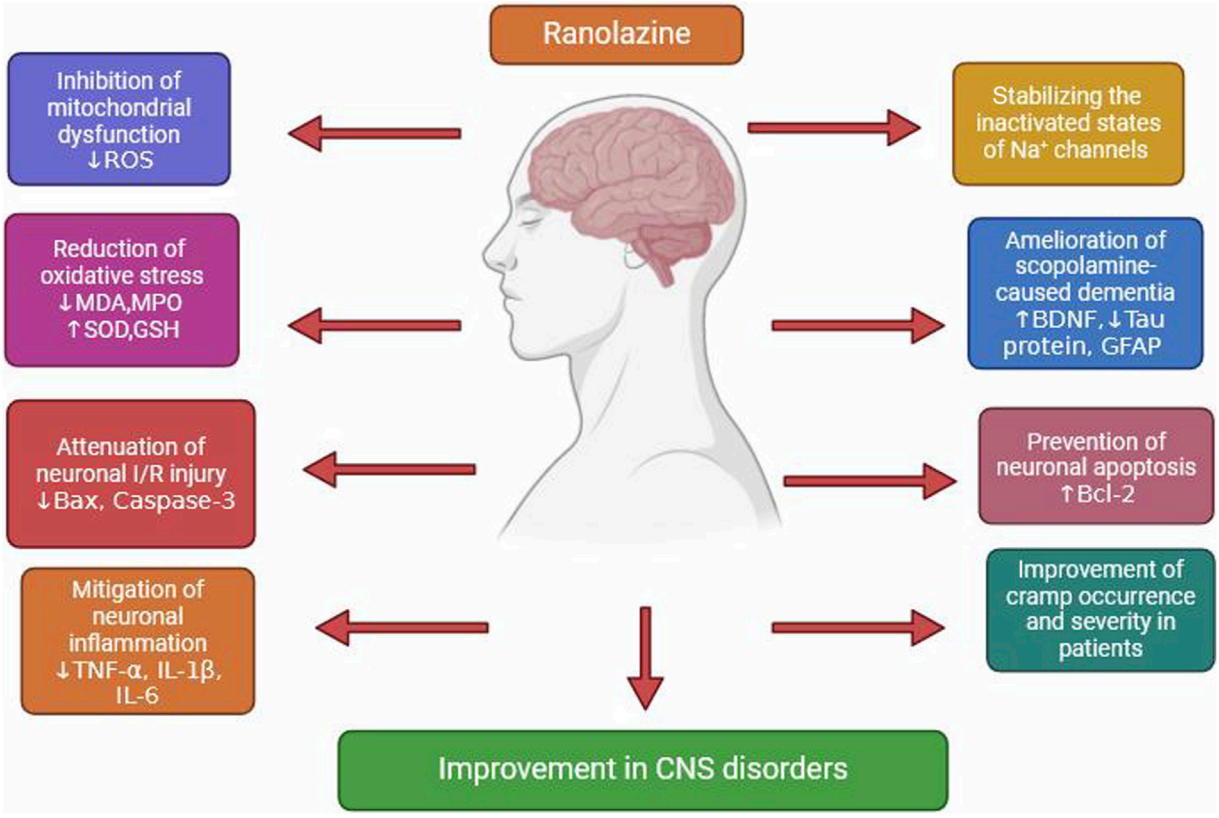

FIGURE 3
Promising therapeutic applications of ranolazine in neuronal injury.

inflammatory reactions via a noteworthy drop in renal tissue level of HMG box1, IL-1ß, downregulation of the Notch2/Hes1 signaling pathway, and anti-oxidant action [112]. According to Abbas and teammates, RAN dramatically reduces renal ischemia-reperfusion damage in rats by increasing Bcl2 protein levels, decreasing Bax and TNF-alpha levels, and inhibiting the oxidative stress biomarker F2-isoprostane and Notch2/Hes1 signaling cascade [113]. Nayaka and Vaish revealed that RAN therapy dramatically lowered blood glucose levels, preserved renal functions, and maintained near-normal renal structure due to its glycemic management and anti-inflammatory and anti-oxidative effects against STZ-caused diabetic nephropathy in rats [114]. Ma and associates investigated the protective effect of RAN in contrast-induced acute renal injury (CI-ARI). Pre-treatment of RAN in CI-ARI mice showed no effect on total blood pressure but significantly enhanced renal perfusion, decreased contrast-associated microcirculation disruption, accelerated renal capillary thickness, and ameliorated renal vascular permeation [115]. Yusuf et al. investigated administering RAN as a preventative for patients with low renal failure having PCI and discovered that it might prevent the development of CIN [116].

Pain and inflammation

RAN inhibited DRG neuron hyperexcitability by interfering with inactivated Na (+) channels, and these activities could lead to its anti-allodynic action in animal models of neuropathic pain [117]. Furthermore, at a dose routinely employed in clinical settings, RAN was discovered to be efficacious in preventing the fast firing of DRG neurons with WT Nav1.7 channels, reducing neuropathic and inflammatory pain [118].

RAN has been demonstrated to attenuate pain behavior in animal models of acquired neurotic pain; however, the drug's effects on cold-induced pain were more potent than mechanical allodynia, and the reduction in pain was only temporary, lasting only 30–90 min based on oral or *i.p* delivery [119]. Casey et al. assessed the analgesic efficacy of RAN in complete Freund's adjuvant-mediated inflammatory pain in rats. They found that RAN exhibited a dose-dependent analgesic effect [120]. According to Gould et al. RAN at 30 mg/kg efficiently ameliorated the painful mechanical allodynia related to demyelination injury, which was induced by the administration of doxorubicin [121].

Naveena and colleagues investigated the anti-inflammatory efficacy of RAN in acute and sub-acute inflammation models in rats and found that RAN substantially lowered paw oedema volume and histological sections revealed a reduction in granulation tissue development [122]. Lenz and coworkers claimed that Na^+ suppression by RAN resulted in lower expression of adhesion molecules and pro-inflammatory cytokines as well as reduced adherence of leukocytes to activated endothelium *in vitro* and *in vivo* [123].

Antidiabetic activity

Jordá et al. found that RAN improved insulin consequences in primary culture astrocytes by increasing anti-inflammatory facilitators like PPAR-γ, decreasing pro-inflammatory agents like COX-2, and boosting the action of Mn-SOD and components of the AKT-eNOS and ERK signaling cascade [124]. Bashir and colleagues investigated the antidiabetic efficacy of RAN against STZ-caused diabetes in rats. It was observed that RAN improved plasma fasting glucose levels and also exhibited a positive effect on the lipid profile [125].

Non-clinical investigations showed that RAN reduced fasting and non-fasting glucose levels and preserved pancreatic β-cells in STZ-induced diabetic mice [126]. In animal models of diabetes, RAN lowered postprandial and basal glucagon concentrations, resulting in a drop in hyperglycemia, demonstrating that RAN's glucose-lowering actions might be achieved via the blocking of sodium channels in pancreatic alpha cells [127]. Guerra-Ojeda explored the potential beneficial effects of RN on insulin activity in the rabbit aorta. They discovered that RAN improved vascular sensitivity to insulin, reducing tissue resistance to the hormone by raising the activities of p-eNOS/eNOS and pAKT/AKT [128]. Cassano et al. assessed the effects of RAN on glucose metabolism and cognitive performance in a T2DM model of Wistar rats and concluded that RAN improved glucose metabolism, enhanced learning and long-term memory, and modified the pro-inflammatory characteristics of diabetic mice [129]. Another study revealed the protective impact of RAN on hippocampal neurodegeneration and astrocyte activation in an STZ T2DM rat model and found that RAN reduced T2DM-induced neuronal injury and loss [130].

A post-hoc examination of the MERLIN-TIMI 36 trials indicated a 0.64 percent drop in HbA1c in diabetic patients who took RAN relative to those who did not. Fasting plasma glucose was also notably decreased by an average of 25.7 mg/dL [131]. Pettus et al. recently verified the MERLIN-TIMI 36 trial results. They investigated the use of high-dose RAN for glycemic control in addition to glimepiride background treatment (4 mg/day) in type 2 diabetes patients with an average baseline HbA1c level of 8.1% [132].

The CARISA research showed that RAN is effective at reducing HbA1c levels in patients with unstable angina. In this assay, HbA1c was not a given result, and further stratification of results based on insulin or oral antihyperglycemic use was not possible [133]. A later randomized analysis of 465 T2D patients with an average HbA1c~8 controlled by lifestyle alone at the start indicated that RAN resulted in higher declines in HbA1c than placebo at 24 weeks (mean difference = 0.56, $p < 0.0001$) [134]. In addition to its anti-ischemic and antianginal properties, RAN demonstrated the capacity to reduce HbA1c in individuals with coronary artery disease and T2DM in two clinical investigations [135]. In a group of patients with T2D and CCS, RAN, in addition to usual anti-ischemic and glucose-lowering medication, also showed effectiveness in restoring endothelial function and glycemic status, as measured by Hb1Ac and short-term GV indices [136].

Muscle disorder

When 10 μM RAN was applied for treating C2C12 myoblasts throughout cell growth, transformation, and the development of new myotubes, it increased the levels of myogenic regulator factors (Myf5 and MyoD), suppressed cell progression factor, decreased ROS, and preserved mitochondrial homeostasis [137]. Tomczyk and colleagues evaluated the positive effects of RAN on skeletal muscle function and metabolism in dyslipidemic rats. They learned that RAN-mediated suppression of FFA oxidation in ApoE/LDLR −/− mice resulted in reduced exercise performance and total adenine nucleotide pool [138].

Torcinaro et al. explored the efficacy of RAN in preventing skeletal muscle dysfunctions associated with aging and discovered that RAN administration dramatically enhanced the muscular strength of elderly mice via up-regulating antioxidant and mitochondrial genes, and by increasing NADH-dehydrogenase function [139]. Novak and collaborators revealed that RAN improved muscle functioning compared to mexiletine without major side effects in a mouse model of myotonia congenita [140]. An open treatment study with RAN at a dose of 2 × 500 mg in 13 patients with chloride channel myotonia showed a significantly reduced EMG myotonia, and according to patient reports, significantly reduced muscle stiffness, and, to a lesser extent, a reduction in muscle weakness and reduced myotonia in clinical tests [141].

Lorusso et al. recently investigated the efficacy of RAN in an open-label trial of 10 patients having paramyotonia congenita and concluded that RAN dramatically reduced both subjective symptoms and clinical myotonia [142]. A phase 2 study is underway to assess the efficacy of RAN in MC, paramyotonia congenita, and Type 1 myotonic dystrophy. Patients with the above conditions were randomized to receive RAN 500 mg twice daily for 2 weeks followed by 1000 mg two times daily for 2 more weeks, compared to placebo. Primary outcomes are quality of life measurements for health and neuromuscular

disease, and EMG to assess for changes in muscle potentials and performance. It is a phase 2 trial to mainly assess the safety profile of the drug in these neuromuscular conditions (NCT02251457).

Pulmonary hypertension

Lee and colleagues investigated the preventive function of RAN against monocrotaline-caused PAH in rat models and found that RAN attenuated ventricular hypertrophy, B-type natriuretic peptide values, fibrosis activation, and cardiovascular mortality [143]. Rocchetti et al. have established that RAN inhibited constitutive elevation of the late sodium current, thereby delaying the development of myocardial remodeling in an experimental rat model of PAH induced by monocrotaline [144]. Teixeira-Fonseca et al. proved that RAN attenuated right ventricular hypertrophy while improving P wavelength and QT period in a monocrotaline-caused PH rat model [145]. In an *in vivo* study, acute treatment of RAN dramatically decreased isoproterenol-caused ventricular tachycardia/ventricular fibrillation and related cardiovascular mortality in rats with pre-existing pulmonary arterial hypertension (PAH) and heart remodeling [146]. Furthermore, a pilot experiment at a single center revealed that 8 of the 11 recruited patients completed all the research exams. The WHO FC, RV function, and exercise tolerance findings revealed improvement without any changes to the invasive hemodynamic measures, and the RV size in PAH patients was decreased after 3 months of RAN medication [147].

A recent double-blind, randomized, placebo-controlled RAN trial (n = 9 RAN, n = 6 placebo) revealed that RAN therapy enhanced RV ejection fraction but not 6-min wall distance (6MWD), N-terminal pro-brain natriuretic peptide, or quality-of-life expectancy measures in patients having precapillary pulmonary hypertension [148]. Finch and colleagues observed that the approved antianginal drug RAN improved cardiopulmonary hemodynamics, functional status, and exercise tolerance in both short-term and long-term (average time on drug approximately 2 years) plans in a cohort of patients with PH-HFpEF [149]. A Phase Ib investigation including 12 PAH patients showed no statistical significance in terms of adverse events between the control and RAN groups after a 12-week follow-up period. This outcome demonstrated the safety of the RAN therapy but did not accomplish the therapeutic aim, partly because the study medication did not reach a therapeutic serum level [150].

Peripheral arterial disease

An animal model demonstrated that injecting RAN into the femoral artery causes a long-lasting dilatation of the artery, equivalent to that produced by nitroglycerin. This outcome might be attributed to α1-adrenergic receptor inhibition, which does not affect heart rate and systemic blood pressure [151]. In a pilot research study including 45 patients with irregular claudication, RAN 1000 mg BID elicited an improvement in peak walking time in comparison with placebo. Though RAN did not ameliorate the ankle-brachial index at rest, patients with extremely irregular claudication had approximately 40 percent improvement in walking time relative to placebo compared to cilostazol [152].

Hepatoprotective effects

Saed and his colleagues assessed the efficacy of RAN in attenuating obesity-induced NAFLD and hyperglycemia and concluded that RAN therapy enhanced glucose tolerance and lowered hepatic triacylglycerol levels in obese mice through increasing the activity of mRNA, which plays a role in modulating lipogenesis [153]. Al Batran stated that in a mouse model of nonalcoholic fatty liver disease, RAN significantly improved glucose oxidation via increasing PDH function [154]. Pzolat and colleagues investigated the preventive effects of RAN against MTX-induced liver injury in rats and found that RAN could attenuate MTX toxicity by reducing MDA and MPO values, enhancing SOD, CAT, and GSH levels, and improving mononuclear inflammation, vascular congestion, and fibrosis [155].

Testicular injury

Bilge et al. evaluated the protective effect of RAN in a testis torsion rat model induced by I/R and demonstrated that RAN protected against testicular damage by reducing MDA levels and improving histopathological scores [156].

Other activities

A recent study revealed that prolonged RAN treatment enhanced energy metabolism by enhancing muscle ATP content and slowing muscular strength reduction in a mouse model of amyotrophic lateral sclerosis (ALS) [157]. Marchio et al. studied the impact of RAN on vascular function and adrenergic response in human saphenous veins. They observed that RAN reduced adrenergic vasoconstriction by acting as an α_1 antagonist and enhancing the huge conductance Ca^{2+}activated K^+ channel [158].

Molecular mechanisms of non-cardiac effects of Ranolazine

The non-cardiac effects of RAN have been associated with various molecular mechanisms. These include ion channel (late

sodium and calcium) modulation, adrenergic receptor antagonism, and metabolic effects, which collectively result in improved cellular ion homeostasis, reduced oxidative stress, and mild vasodilation in non-cardiac tissues [159]. RAN selectively inhibits the late phase of the inward sodium current and elicits a mild blocking effect on L-type calcium channels. The impacts of these effects include a reduction in intracellular sodium, consequent decrease in calcium overload via the sodium–calcium exchanger (stabilization of cellular ion homeostasis and reduction of cellular stress in tissues), and weak vasodilatory properties with consequences on vascular smooth muscle tone and peripheral circulation [159, 160]. RAN elicits antagonistic action at alpha-1 and beta-1 adrenergic receptors present in vascular, nervous, and other tissues. This antagonistic action contributes to the modulation of vascular tone and sympathetic nervous system effects, devoid of significant changes in heart rate or blood pressure [160].

RAN invokes inhibition of delayed rectifier potassium current, which, beyond cardiac tissue, could influence electrophysiological properties in other excitable tissues [160]. RAN partially inhibits fatty acid oxidation at higher concentrations, leading to alteration of metabolic processes in non-cardiac tissues; this may lead to improvement of cellular energy efficiency under stress conditions [161].

Conclusion

RAN is a well-known selective INa,L inhibitor and the most commonly utilized antianginal agent. This amazing substance is mostly used to treat chronic angina (chest pain). RAN is an add-on medicine for the relief of symptoms of individuals suffering from stable angina pectoris and those who are poorly controlled or intolerant to first-line antianginal therapy. However, an exciting surge of interest is rising around the possibility of RAN being repurposed for a varied array of health conditions. This review article investigates RAN's varied pharmacological actions, shedding light on its prospective possibilities outside the field of antianginal drugs. The review demonstrates its promise in treating an astounding variety of illnesses, from anticancer activity and neuroprotection to renal and liver protection, renal antidiabetic advantages, and anti-inflammatory capabilities.

The repurposing of RAN offers clinical promise in various health conditions, including pulmonary hypertension, arrhythmia, heart failure, metabolic disease, and oncology, in view of its unique ion channel modulation, metabolic effects, and anti-inflammatory properties. These benefits of RAN, coupled with its safety profile, offer translational opportunities for diverse therapeutic benefits.

Future perspective

RAN exhibits pleiotropic properties, demonstrating several mechanisms of action and protective benefits against various disease models already established. Given that inflammation and oxidative stress are the fundamental contributors to almost all human diseases, medications that might impede these processes are expected to be beneficial in various medical conditions. The review focuses on the many pharmacological properties of RAN, as it has been demonstrated to produce these effects.

Author contributions

All authors listed have made a substantial, direct, and intellectual contribution to the work and approved it for publication.

Funding

The author(s) declare that no financial support was received for the research and/or publication of this article.

Conflict of interest

The author(s) declared no potential conflicts of interest with respect to the research, authorship, and/or publication of this article.

Generative AI statement

The author(s) declare that no Generative AI was used in the creation of this manuscript.

References

1. McCormack JG, Barr RL, Wolff AA, Lopaschuk GD. Ranolazine stimulates glucose oxidation in normoxic, ischemic, and reperfused ischemic rat hearts. *Circulation* (1996) **93**(1):135–42. doi:10.1161/01.cir.93.1.135

2. Létienne R, Vié B, Puech A, Vieu S, Le Grand B, John GW. Evidence that ranolazine behaves as a weak beta1-and beta2-adrenoceptor antagonist in the rat [correction of cat] cardiovascular system. *Naunyn Schmiedebergs Arch Pharmacol* (2001) **363**(4):464–71. doi:10.1007/s002100000378

3. Ratte A, Wiedmann F, Kraft M, Katus HA, Schmidt C. Antiarrhythmic properties of ranolazine: inhibition of atrial fibrillation associated TASK-1 potassium channels. *Front Pharmacol* (2019) **10**:1367. doi:10.3389/fphar.2019.01367

4. Tani M, Neely JR. Role of intracellular Na^+ in Ca^{2+} overload and depressed recovery of ventricular function of reperfused ischemic rat hearts. Possible involvement of H^+-Na^+ and Na^+-Ca^{2+} exchange. *Circ Res* (1989) **65**(4):1045–56. doi:10.1161/01.res.65.4.1045

5. Belardinelli L, Shryock JC, Fraser H. Inhibition of the late sodium current as a potential cardioprotective principle: effects of the late sodium current inhibitor ranolazine. *Heart* (2006) **92**(Suppl. 4):iv6–iv14. doi:10.1136/hrt.2005.078790

6. Gupta T, Khera S, Kolte D, Aronow WS, Iwai S. Antiarrhythmic properties of ranolazine: a review of the current evidence. *Int J Cardiol* (2015) **187**:66–74. doi:10.1016/j.ijcard.2015.03.324

7. Chaitman BR. Ranolazine for the treatment of chronic angina and potential use in other cardiovascular conditions. *Circulation* (2006) **113**(20):2462–72. doi:10.1161/CIRCULATIONAHA.105.597500

8. Cocco G, Rousseau MF, Bouvy T, Cheron P, Williams G, Detry JM, et al. Effects of a new metabolic modulator, ranolazine, on exercise tolerance in angina pectoris patients treated with beta-blocker or diltiazem. *J Cardiovasc Pharmacol* (1992) **20**(1):131–8. doi:10.1097/00005344-199207000-00017

9. Jerling M, Huan BL, Leung K, Chu N, Abdallah H, Hussein Z. Studies to investigate the pharmacokinetic interactions between ranolazine and ketoconazole, diltiazem, or simvastatin during combined administration in healthy subjects. *The J Clin Pharmacol* (2005) **45**(4):422–33. doi:10.1177/0091270004273992

10. Jerling M, Abdallah H. Effect of renal impairment on multiple-dose pharmacokinetics of extended-release ranolazine. *Clin Pharmacol & Ther* (2005) **78**(3):288–97. doi:10.1016/j.clpt.2005.05.004

11. Gordon M. *Medical review of safety (ranolazine)*. Rockville, MD: U.S. Food and Drug Administration (2003). Available online at: http://www.fda.gov/ohrms/dockets/ac/03/briefing/4012B2_02_Division%20Dir%20%20Memo.htm (Accessed August 22, 2023).

12. Chaitman BR, Skettino SL, Parker JO, Hanley P, Meluzin J, Kuch J, et al. Antiischemic effects and long-term survival during ranolazine monotherapy in patients with chronic severe angina. *J Am Coll Cardiol* (2004) **43**(8):1375–82. doi:10.1016/j.jacc.2003.11.045

13. Chaitman BR, Pepine CJ, Parker JO, Skopal J, Chumakova G, Kuch J, et al. Effects of ranolazine with atenolol, amlodipine, or diltiazem on exercise tolerance and angina frequency in patients with severe chronic angina: a randomized controlled trial. *JAMA* (2004) **291**(3):309–16. doi:10.1001/jama.291.3.309

14. Chaitman BR. Efficacy and safety of a metabolic modulator drug in chronic stable angina: review of evidence from clinical trials. *J Cardiovasc Pharmacol Ther* (2004) **9**(Suppl. 1):S47–64. doi:10.1177/107424840400900105

15. Driffort V, Gillet L, Bon E, Marionneau-Lambot S, Oullier T, Joulin V, et al. Ranolazine inhibits NaV1.5-mediated breast cancer cell invasiveness and lung colonization. *Mol Cancer* (2014) **13**:264. doi:10.1186/1476-4598-13-264

16. Qiu S, Fraser SP, Pires W, Djamgoz MBA. Anti-invasive effects of minoxidil on human breast cancer cells: combination with ranolazine. *Clin Exp Metastasis* (2022) **39**(4):679–89. doi:10.1007/s10585-022-10166-7

17. Lee A, Fraser SP, Djamgoz MBA. Propranolol inhibits neonatal Nav1.5 activity and invasiveness of MDA-MB-231 breast cancer cells: effects of combination with ranolazine. *J Cell Physiol* (2019) **234**(12):23066–81. doi:10.1002/jcp.28868

18. Guzel RM, Ogmen K, Ilieva KM, Fraser SP, Djamgoz MBA. Colorectal cancer invasiveness *in vitro:* predominant contribution of neonatal Nav1.5 under normoxia and hypoxia. *J Cell Physiol* (2019) **234**(5):6582–93. doi:10.1002/jcp.27399

19. Rizaner N, Uzun S, Fraser SP, Djamgoz MBA, Altun S. Riluzole: anti-invasive effects on rat prostate cancer cells under normoxic and hypoxic conditions. *Basic & Clin Pharmacol & Toxicol* (2020) **127**(4):254–64. doi:10.1111/bcpt.13417

20. Pemmireddy R, Alvala R, Sama V, Sriramoju A. Effect of ranolazine on 1, 2 - dimethyl hydrazine induced colon cancer in mice. *Asian J Pharm Pharmacol* (2019) **5**(6):1183–90. doi:10.31024/ajpp.2019.5.6.15

21. Bugan I, Kucuk S, Karagoz Z, Fraser SP, Kaya H, Dodson A, et al. Anti-metastatic effect of ranolazine in an *in vivo* rat model of prostate cancer, and expression of voltage-gated sodium channel protein in human prostate. *Prostate Cancer Prostatic Dis* (2019) **22**(4):569–79. doi:10.1038/s41391-019-0128-3

22. Guth A, Monk E, Agarwal R, Bergman BC, Zemski-Berry KA, Minic A, et al. Targeting fat oxidation in mouse prostate cancer decreases tumor growth and stimulates anti-cancer immunity. *Int J Mol Sci* (2020) **21**(24):9660. doi:10.3390/ijms21249660

23. Lasheras-Otero I, Feliu I, Maillo A, Moreno H, Redondo-Muñoz M, Aldaz P, et al. The regulators of peroxisomal acyl-carnitine shuttle CROT and CRAT promote metastasis in melanoma. *J Invest Dermatol* (2023) **143**(2):305–16.e5. doi:10.1016/j.jid.2022.08.038

24. Tocchetti CG, Carpi A, Coppola C, Quintavalle C, Rea D, Campesan M, et al. Ranolazine protects from doxorubicin-induced oxidative stress and cardiac dysfunction. *Eur J Heart Fail* (2014) **16**(4):358–66. doi:10.1002/ejhf.50

25. Riccio G, Antonucci S, Coppola C, D'Avino C, Piscopo G, Fiore D, et al. Ranolazine attenuates trastuzumab-induced heart dysfunction by modulating ROS production. *Front Physiol* (2018) **9**:38. doi:10.3389/fphys.2018.00038

26. De Lorenzo C, Paciello R, Riccio G, Rea D, Barbieri A, Coppola C, et al. Cardiotoxic effects of the novel approved anti-ErbB2 agents and reverse cardioprotective effects of ranolazine. *OncoTargets Ther* (2018) **11**:2241–50. doi:10.2147/OTT.S157294

27. Cappetta D, Esposito G, Coppini R, Piegari E, Russo R, Ciuffreda LP, et al. Effects of ranolazine in a model of doxorubicin-induced left ventricle diastolic dysfunction. *Br J Pharmacol* (2017) **174**(21):3696–712. doi:10.1111/bph.13791

28. Dogan Z, Durmus S, Ergun DD, Gelisgen R, Uzun H. Ranolazine exhibits anti-inflammatory and antioxidant activities in H9c2 cardiomyocytes. *Eur Rev Med Pharmacol Sci* (2023) **27**(7):2953–63. doi:10.26355/eurrev_202304_31927

29. Jiang Y, Li X, Guo T, Lu WJ, Ma S, Chang Y, et al. Ranolazine rescues the heart failure phenotype of PLN-deficient human pluripotent stem cell-derived cardiomyocytes. *Stem Cell Rep* (2022) **17**(4):804–19. doi:10.1016/j.stemcr.2022.02.016

30. Ren L, Chen X, Nie B, Qu H, Ju J, Bai Y. Ranolazine inhibits pyroptosis *via* regulation of miR-135b in the treatment of diabetic cardiac fibrosis. *Front Mol Biosci* (2022) **9**:806966. doi:10.3389/fmolb.2022.806966

31. Chen X, Ren L, Liu X, Sun X, Dong C, Jiang Y, et al. Ranolazine protects against diabetic cardiomyopathy by activating the NOTCH1/NRG1 pathway. *Life Sci* (2020) **261**:118306. doi:10.1016/j.lfs.2020.118306

32. Tawfik MK, Ameen AM. Cardioprotective effect of ranolazine in nondiabetic and diabetic male rats subjected to isoprenaline-induced acute myocardial infarction involves modulation of AMPK and inhibition of apoptosis. *Can J Physiol Pharmacol* (2019) **97**(7):661–74. doi:10.1139/cjpp-2018-0571

33. Le DE, Davis CM, Wei K, Zhao Y, Cao Z, Nugent M, et al. Ranolazine may exert its beneficial effects by increasing myocardial adenosine levels. *Am J Physiology-Heart Circulatory Physiol* (2020) **318**(1):H189–H202. doi:10.1152/ajpheart.00217.2019

34. Calderón-Sánchez EM, Domínguez-Rodríguez A, López-Haldón J, Jiménez-Navarro MF, Gómez AM, Smani T, et al. Cardioprotective effect of ranolazine in the process of ischemia-reperfusion in adult rat cardiomyocytes. *Revista Española de Cardiología (English Edition)* (2016) **69**(1):45–53. doi:10.1016/j.rec.2015.02.027

35. Tantray J, Sharma AK, Singh S, Zaid M, Bhat M, Gill K, et al. Ranolazine exert its beneficial effects in myocardial infarction like ischemic preconditioning mediators by increasing myocardial nitric oxide, adenosine, Bradykinin and K^+ATPase Levels. *Res Square* (2024). doi:10.21203/rs.3.rs-3825042/v1

36. Efentakis P, Andreadou I, Bibli SI, Vasileiou S, Dagres N, Zoga A, et al. Ranolazine triggers pharmacological preconditioning and postconditioning in anesthetized rabbits through activation of RISK pathway. *Eur J Pharmacol* (2016) **789**:431–8. doi:10.1016/j.ejphar.2016.08.001

37. Feng G, Yang Y, Chen J, Wu Z, Zheng Y, Li W, et al. Ranolazine attenuated heightened plasma norepinephrine and B-Type natriuretic peptide-45 in improving cardiac function in rats with chronic ischemic heart failure. *Am J Transl Res* (2016) **8**(2):1295–301.

38. Wang GT, Li H, Yu ZQ, He XN. Effects of ranolazine on cardiac function in rats with heart failure. *Eur Rev Med Pharmacol Sci* (2019) **23**(21):9625–32. doi:10.26355/eurrev_201911_19456

39. Nie J, Duan Q, He M, Li X, Wang B, Zhou C, et al. Ranolazine prevents pressure overload-induced cardiac hypertrophy and heart failure by restoring aberrant Na^+ and Ca^{2+} handling. *J Cell Physiol* (2019) **234**(7):11587–601. doi:10.1002/jcp.27791

40. Teng S, Ren Z, Zhao K. Vagal stimulation facilitates improving effects of ranolazine on cardiac function in rats with chronic ischemic heart failure. *Curr Mol Med* (2018) **18**(1):36–43. doi:10.2174/1566524018666180608085330

41. Coppini R, Mazzoni L, Ferrantini C, Gentile F, Pioner JM, Laurino A, et al. Ranolazine prevents phenotype development in a mouse model of hypertrophic cardiomyopathy. *Circ Heart Fail* (2017) **10**(3):e003565. doi:10.1161/CIRCHEARTFAILURE.116.003565

42. De Angelis A, Cappetta D, Piegari E, Rinaldi B, Ciuffreda LP, Esposito G, et al. Long-term administration of ranolazine attenuates diastolic dysfunction and adverse myocardial remodeling in a model of heart failure with preserved ejection fraction. *Int J Cardiol* (2016) **217**:69–79. doi:10.1016/j.ijcard.2016.04.168

43. Williams S, Pourrier M, McAfee D, Lin S, Fedida D. Ranolazine improves diastolic function in spontaneously hypertensive rats. *Am J Physiology-Heart Circulatory Physiol* (2014) **306**(6):H867–81. doi:10.1152/ajpheart.00704.2013

44. Venkataraman R, Belardinelli L, Blackburn B, Heo J, Iskandrian AE. A study of the effects of ranolazine using automated quantitative analysis of serial myocardial perfusion images. *JACC: Cardiovasc Imaging* (2009) **2**(11):1301–9. doi:10.1016/j.jcmg.2009.09.006

45. Tagliamonte E, Rigo F, Cirillo T, Astarita C, Quaranta G, Marinelli U, et al. Effects of ranolazine on noninvasive coronary flow reserve in patients with myocardial ischemia but without obstructive coronary artery disease. *Echocardiography* (2015) **32**(3):516–21. doi:10.1111/echo.12674

46. Mehta PK, Goykhman P, Thomson LE, Shufelt C, Wei J, Yang Y, et al. Ranolazine improves angina in women with evidence of myocardial ischemia but no obstructive coronary artery disease. *JACC: Cardiovasc Imaging* (2011) **4**(5): 514–22. doi:10.1016/j.jcmg.2011.03.007

47. Schwemer TF, Deutscher N, Diermann N, Böger R, Schwedhelm E, Blankenberg S, et al. Effect of ranolazine on plasma arginine derivatives and urinary isoprostane 8-iso-$PGF_{2\alpha}$ in patients with myocardial infarction in the randomized RIMINI-trial. *Sci Rep* (2019) **9**(1):5708. doi:10.1038/s41598-019-42239-1

48. Chou CC, Lee HL, Chang GJ, Wo HT, Yen TH, Wen MS, et al. Mechanisms of ranolazine pretreatment in preventing ventricular tachyarrhythmias in diabetic db/db mice with acute regional ischemia-reperfusion injury. *Sci Rep* (2020) **10**(1): 20032. doi:10.1038/s41598-020-77014-0

49. Wolfes J, Ellermann C, Broer N, Rath B, Willy K, Leitz PR, et al. Antiarrhythmic effect of ranolazine in combination with selective NCX-inhibition in an experimental model of atrial fibrillation. *Pharmaceuticals (Basel).* (2020) **13**(10):321. doi:10.3390/ph13100321

50. Ellermann C, Kohnke A, Dechering DG, Kochhäuser S, Reinke F, Fehr M, et al. Ranolazine prevents levosimendan-induced atrial fibrillation. *Pharmacology* (2018) **102**(3-4):138–41. doi:10.1159/000490572

51. Moschovidis V, Simopoulos V, Stravela S, Dipla K, Hatziefthimiou A, Stamatiou R, et al. Dose-dependent effects of ranolazine on reentrant ventricular arrhythmias induced after subacute myocardial infarction in rabbits. *J Cardiovasc Pharmacol Ther* (2020) **25**(1):65–71. doi:10.1177/1074248419858113

52. Markandeya YS, Tsubouchi T, Hacker TA, Wolff MR, Belardinelli L, Balijepalli RC. Inhibition of late sodium current attenuates ionic arrhythmia mechanism in ventricular myocytes expressing LaminA-N195K mutation. *Heart Rhythm* (2016) **13**(11):2228–36. doi:10.1016/j.hrthm.2016.08.007

53. Zou D, Geng N, Chen Y, Ren L, Liu X, Wan J, et al. Ranolazine improves oxidative stress and mitochondrial function in the atrium of acetylcholine-CaCl2 induced atrial fibrillation rats. *Life Sci* (2016) **156**:7–14. doi:10.1016/j.lfs.2016.05.026

54. Banga S, Mishra M, Heinze-Milne SD, Jansen HJ, Rose RA, Howlett SE. Chronic testosterone deficiency increases late inward sodium current and promotes triggered activity in ventricular myocytes from aging male mice. *Am J Physiology-Heart Circulatory Physiol* (2023) **325**(2):H264–H277. doi:10.1152/ajpheart.00505.2022

55. Mustroph J, Baier MJ, Unsin D, Provaznik Z, Kozakov K, Lebek S, et al. Ethanol-Induced atrial fibrillation results from late I_{Na} and can be prevented by ranolazine. *Circulation* (2023) **148**(8):698–700. doi:10.1161/CIRCULATIONAHA.123.064561

56. Ko TH, Jeong D, Yu B, Song JE, Le QA, Woo SH, et al. Inhibition of late sodium current *via* PI3K/Akt signaling prevents cellular remodeling in tachypacing-induced HL-1 atrial myocytes. *Pflügers Archiv - Eur J Physiol* (2023) **475**(2):217–31. doi:10.1007/s00424-022-02754-z

57. Opačić D, van Hunnik A, Zeemering S, Dhalla A, Belardinelli L, Schotten U, et al. Electrophysiological effects of ranolazine in a goat model of lone atrial fibrillation. *Heart Rhythm* (2021) **18**(4):615–22. doi:10.1016/j.hrthm.2020.11.021

58. Frommeyer G, Sterneberg M, Dechering DG, Kochhäuser S, Bögeholz N, Fehr M, et al. Comparison of vernakalant and ranolazine in atrial fibrillation. *J Cardiovasc Med* (2017) **18**(9):663–8. doi:10.2459/JCM.0000000000000545

59. Carstensen H, Kjær L, Haugaard MM, Flethøj M, Hesselkilde EZ, Kanters JK, et al. Antiarrhythmic effects of combining dofetilide and ranolazine in a model of acutely induced atrial fibrillation in horses. *J Cardiovasc Pharmacol* (2018) **71**(1): 26–35. doi:10.1097/FJC.0000000000000541

60. Daniels JD, Hill JA. Funny and late: targeting currents governing heart rate in atrial fibrillation. *J Cardiovasc Electrophysiol* (2015) **26**(3):336–8. doi:10.1111/jce.12597

61. Burashnikov A, Di Diego JM, Barajas-Martínez H, Hu D, Zygmunt AC, Cordeiro JM, et al. Ranolazine effectively suppresses atrial fibrillation in the setting of heart failure. *Circ Heart Fail* (2014) **7**(4):627–33. doi:10.1161/CIRCHEARTFAILURE.114.001129

62. Alves Bento AS, Bacic D, Saran Carneiro J, Nearing BD, Fuller H, Justo FA, et al. Selective late INa inhibition by GS-458967 exerts parallel suppression of catecholamine-induced hemodynamically significant ventricular tachycardia and T-wave alternans in an intact porcine model. *Heart Rhythm* (2015) **12**(12):2508–14. doi:10.1016/j.hrthm.2015.07.025

63. Kloner RA, Dow JS, Bhandari A. First direct comparison of the late sodium current blocker ranolazine to established antiarrhythmic agents in an ischemia/reperfusion model. *J Cardiovasc Pharmacol Ther* (2011) **16**(2):192–6. doi:10.1177/1074248410386485

64. Malavaki C, Hatziefthimiou A, Daskalopoulou SS, Stefanidis I, Karatzaferi C, Aidonidis I. Ranolazine enhances nicardipine-induced relaxation of alpha1-adrenoceptor-mediated contraction on isolated rabbit aorta. *Acta Cardiol* (2015) **70**(2):157–62. doi:10.1080/ac.70.2.3073506

65. Strege P, Beyder A, Bernard C, Crespo-Diaz R, Behfar A, Terzic A, et al. Ranolazine inhibits shear sensitivity of endogenous Na^+ current and spontaneous action potentials in HL-1 cells. *Channels (Austin)* (2012) **6**(6):457–62. doi:10.4161/chan.22017

66. Koyani CN, Scheruebel S, Jin G, Kolesnik E, Zorn-Pauly K, Mächler H, et al. Hypochlorite-modified LDL induces arrhythmia and contractile dysfunction in cardiomyocytes. *Antioxidants (Basel)* (2021) **11**(1):25. doi:10.3390/antiox11010025

67. Del-Canto I, Gómez-Cid L, Hernández-Romero I, Guillem MS, Fernández-Santos ME, Atienza F, et al. Ranolazine-mediated attenuation of mechanoelectric feedback in atrial myocyte monolayers. *Front Physiol* (2020) **11**:922. doi:10.3389/fphys.2020.00922

68. Souza DS, Marques LP, Costa AD, Cruz JS, Rhana P, Santos-Miranda A, et al. Experimental hypothyroidism induces cardiac arrhythmias and ranolazine reverts and prevents the phenotype. *Life Sci* (2022) **308**:120945. doi:10.1016/j.lfs.2022.120945

69. Wu L, Shryock JC, Song Y, Li Y, Antzelevitch C, Belardinelli L. Antiarrhythmic effects of ranolazine in a Guinea pig *in vitro* model of long-QT syndrome. *The J Pharmacol Exp Ther* (2004) **310**(2):599–605. doi:10.1124/jpet.104.066100

70. Parikh A, Mantravadi R, Kozhevnikov D, Roche MA, Ye Y, Owen LJ, et al. Ranolazine stabilizes cardiac ryanodine receptors: a novel mechanism for the suppression of early afterdepolarization and torsades de pointes in long QT type 2. *Heart Rhythm* (2012) **9**(6):953–60. doi:10.1016/j.hrthm.2012.01.010

71. Aidonidis I, Simopoulos V, Dipla K, Hatziefthimiou A, Stamatiou R, Skoularigis I, et al. Effects of ranolazine and its combination with amiodarone on rapid pacing-induced reentrant atrial tachycardia in rabbits. *J Innov Card Rhythm Management* (2021) **12**(3):4421–7. doi:10.19102/icrm.2021.120304

72. Nunoi Y, Kambayashi R, Goto A, Hagiwara-Nagasawa M, Chiba K, Izumi-Nakaseko H, et al. *In vivo* characterization of anti-atrial fibrillatory potential and pharmacological safety profile of $I_{Na,\ L}$ plus I_{Kr} inhibitor ranolazine using the halothane-anesthetized dogs. *Heart Vessels* (2021) **36**(7):1088–97. doi:10.1007/s00380-021-01830-1

73. Aidonidis I, Simopoulos V, Stravela S, Dipla K, Stamatiou R, Hatziefthimiou A, et al. Ranolazine depresses conduction of rapid atrial depolarizations in a beating rabbit heart model. *J Interv Card Electrophysiol* (2021) **62**(1):153–9. doi:10.1007/s10840-020-00865-0

74. Miranda VM, Beserra SS, Campos DR. Inotropic and antiarrhythmic transmural actions of ranolazine in a cellular model of type 3 long QT syndrome. *Arq Bras Cardiol* (2020) **114**(4):732–5. doi:10.36660/abc.20190220

75. Chu Y, Yang Q, Ren L, Yu S, Liu Z, Chen Y, et al. Late sodium current in atrial cardiomyocytes contributes to the induced and spontaneous atrial fibrillation in rabbit hearts. *J Cardiovasc Pharmacol* (2020) **76**(4):437–44. doi:10.1097/FJC.0000000000000883

76. Rivaud MR, Marchal GA, Wolswinkel R, Jansen JA, van der Made I, Beekman L, et al. Functional modulation of atrioventricular conduction by enhanced late sodium current and calcium-dependent mechanisms in Scn5a1798insD/+ mice. *EP Europace* (2020) **22**(10):1579–89. doi:10.1093/europace/euaa127

77. Fukaya H, Plummer BN, Piktel JS, Wan X, Rosenbaum DS, Laurita KR, et al. Arrhythmogenic cardiac alternans in heart failure is suppressed by late sodium current blockade by ranolazine. *Heart Rhythm* (2019) **16**(2):281–9. doi:10.1016/j.hrthm.2018.08.033

78. Carstensen H, Hesselkilde EZ, Haugaard MM, Flethøj M, Carlson J, Pehrson S, et al. Effects of dofetilide and ranolazine on atrial fibrillatory rate in a horse model of acutely induced atrial fibrillation. *J Cardiovasc Electrophysiol* (2019) **30**(4): 596–606. doi:10.1111/jce.13849

79. Montnach J, Chizelle FF, Belbachir N, Castro C, Li L, Loussouarn G, et al. Arrhythmias precede cardiomyopathy and remodelling of Ca^{2+} handling proteins in a novel model of long QT syndrome. *J Mol Cell Cardiol* (2018) **123**:13–25. doi:10.1016/j.yjmcc.2018.08.019

80. Ke HY, Chin LH, Tsai CS, Lin FZ, Chen YH, Chang YL, et al. Cardiac calcium dysregulation in mice with chronic kidney disease. *J Cell Mol Med* (2020) **24**(6): 3669–77. doi:10.1111/jcmm.15066

81. Huang SY, Chen YC, Kao YH, Hsieh MH, Lin YK, Chung CC, et al. Fibroblast growth factor 23 dysregulates late sodium current and calcium homeostasis with enhanced arrhythmogenesis in pulmonary vein cardiomyocytes. *Oncotarget* (2016) **7**(43):69231–42. doi:10.18632/oncotarget.12470

82. Hartmann N, Mason FE, Braun I, Pabel S, Voigt N, Schotola H, et al. The combined effects of ranolazine and dronedarone on human atrial and ventricular electrophysiology. *J Mol Cell Cardiol* (2016) **94**:95–106. doi:10.1016/j.yjmcc.2016.03.012

83. Paci M, Passini E, Severi S, Hyttinen J, Rodriguez B. Phenotypic variability in LQT3 human induced pluripotent stem cell-derived cardiomyocytes and their

response to antiarrhythmic pharmacologic therapy: an *in silico* approach. *Heart Rhythm* (2017) **14**(11):1704–12. doi:10.1016/j.hrthm.2017.07.026

84. Ogawa T, Honjo H, Yamazaki M, Kushiyama Y, Sakuma I, Kodama I, et al. Ranolazine facilitates termination of ventricular tachyarrhythmia associated with acute myocardial ischemia through suppression of late I_{Na}-Mediated focal activity. *Circ J* (2017) **81**(10):1411–28. doi:10.1253/circj.CJ-17-0128

85. Bunch TJ, Mahapatra S, Murdock D, Molden J, Weiss JP, May HT, et al. Ranolazine reduces ventricular tachycardia burden and ICD shocks in patients with drug-refractory ICD shocks. *Pacing Clin Electrophysiol* (2011) **34**(12):1600–6. doi:10.1111/j.1540-8159.2011.03208.x

86. Curnis A, Salghetti F, Cerini M, Vizzardi E, Sciatti E, Vassanelli F, et al. Ranolazine therapy in drug-refractory ventricular arrhythmias. *J Cardiovasc Med* (2017) **18**(7):534–8. doi:10.2459/JCM.0000000000000521

87. Black-Maier EW, Pokorney SD, Barnett AS, Liu P, Shrader P, Ng J, et al. Ranolazine reduces atrial fibrillatory wave frequency. *Europace* (2017) **19**(7): 1096–100. doi:10.1093/europace/euw200

88. Scirica BM, Morrow DA, Hod H, Murphy SA, Belardinelli L, Hedgepeth CM, et al. Effect of ranolazine, an antianginal agent with novel electrophysiological properties, on the incidence of arrhythmias in patients with non ST-segment elevation acute coronary syndrome: results from the metabolic efficiency with ranolazine for less ischemia in non ST-Elevation acute coronary syndrome thrombolysis in myocardial infarction 36 (MERLIN-TIMI 36) randomized controlled trial. *Circulation* (2007) **116**(15):1647–52. doi:10.1161/CIRCULATIONAHA.107.724880

89. Leftheriotis D, Flevari P, Theodorakis G, Rigopoulos A, Ikonomidis I, Panou F, et al. The effects of ranolazine on paroxysmal atrial fibrillation in patients with coronary artery disease: a preliminary observational study. *J Atr Fibrillation* (2014) **6**(5):940. doi:10.4022/jafib.940

90. Koskinas KC, Fragakis N, Katritsis D, Skeberis V, Vassilikos V. Ranolazine enhances the efficacy of amiodarone for conversion of recent-onset atrial fibrillation. *Europace* (2014) **16**(7):973–9. doi:10.1093/europace/eut407

91. Tsanaxidis N, Aidonidis I, Hatziefthimiou A, Daskalopoulou SS, Giamouzis G, Triposkiadis F, et al. Ranolazine added to amiodarone facilitates earlier conversion of atrial fibrillation compared to amiodarone-only therapy. *Pacing Clin Electrophysiol* (2017) **40**(4):372–8. doi:10.1111/pace.13048

92. De Vecchis R, Ariano C, Giasi A, Cioppa C. Antiarrhythmic effects of ranolazine used both alone for prevention of atrial fibrillation and as an add-on to intravenous amiodarone for its pharmacological cardioversion: a meta-analysis. *Minerva cardioangiologica* (2018) **66**(3):349–59. doi:10.23736/S0026-4725.17.04349-3

93. Guerra F, Romandini A, Barbarossa A, Belardinelli L, Capucci A. Ranolazine for rhythm control in atrial fibrillation: a systematic review and meta-analysis. *Int J Cardiol* (2017) **227**:284–91. doi:10.1016/j.ijcard.2016.11.103

94. Reiffel JA, Camm AJ, Belardinelli L, Zeng D, Karwatowska-Prokopczuk E, Olmsted A, et al. The HARMONY trial: combined ranolazine and dronedarone in the management of paroxysmal atrial fibrillation: mechanistic and therapeutic synergism. *Circ Arrhythmia Electrophysiol* (2015) **8**(5):1048–56. doi:10.1161/CIRCEP.115.002856

95. Simopoulos V, Tagarakis GI, Daskalopoulou SS, Daskalopoulos ME, Lenos A, Chryssagis K, et al. Ranolazine enhances the antiarrhythmic activity of amiodarone by accelerating conversion of new-onset atrial fibrillation after cardiac surgery. *Angiology* (2014) **65**(4):294–7. doi:10.1177/0003319713477911

96. Miles RH, Passman R, Murdock DK. Comparison of effectiveness and safety of ranolazine versus amiodarone for preventing atrial fibrillation after coronary artery bypass grafting. *The Am J Cardiol* (2011) **108**(5):673–6. doi:10.1016/j.amjcard.2011.04.017

97. Burashnikov A, Antzelevitch C. Ranolazine *versus* amiodarone for prevention of postoperative atrial fibrillation. *Future Cardiol* (2011) **7**(6):733–7. doi:10.2217/fca.11.67

98. Tagarakis GI, Aidonidis I, Daskalopoulou SS, Simopoulos V, Liouras V, Daskalopoulos ME, et al. Effect of ranolazine in preventing postoperative atrial fibrillation in patients undergoing coronary revascularization surgery. *Curr Vasc Pharmacol* (2014) **11**(6):988–91. doi:10.2174/15701611106140128123506

99. Hammond DA, Smotherman C, Jankowski CA, Tan S, Osian O, Kraemer D, et al. Short-course of ranolazine prevents postoperative atrial fibrillation following coronary artery bypass grafting and valve surgeries. *Clin Res Cardiol* (2015) **104**(5): 410–7. doi:10.1007/s00392-014-0796-x

100. Gong M, Zhang Z, Fragakis N, Korantzopoulos P, Letsas KP, Li G, et al. Role of ranolazine in the prevention and treatment of atrial fibrillation: a meta-analysis of randomized clinical trials. *Heart Rhythm* (2017) **14**(1):3–11. doi:10.1016/j.hrthm.2016.10.008

101. Chorin E, Hu D, Antzelevitch C, Hochstadt A, Belardinelli L, Zeltser D, et al. Ranolazine for congenital Long-QT syndrome type III: experimental and long-term clinical data. *Circ Arrhythmia Electrophysiol* (2016) **9**(10):e004370. doi:10.1161/CIRCEP.116.004370

102. Putri DKSC, Andrianto A, Al-Farabi MJ, Saputra PBT, Nugraha RA. Efficacy of ranolazine to improve diastolic performance in heart failure with preserved ejection fraction: a systematic review and meta-analysis. *Eur Cardiol* (2023) **18**:e02. doi:10.15420/ecr.2022.10

103. Piano I, Votta A, Colucci P, Corsi F, Vitolo S, Cerri C, et al. Anti-inflammatory reprogramming of microglia cells by metabolic modulators to counteract neurodegeneration; a new role for ranolazine. *Sci Rep* (2023) **13**(1): 20138. doi:10.1038/s41598-023-47540-8

104. Aldasoro M, Guerra-Ojeda S, Aguirre-Rueda D, Mauricio MD, Vila JM, Marchio P, et al. Effects of ranolazine on astrocytes and neurons in primary culture. *PLoS One* (2016) **11**(3):e0150619. doi:10.1371/journal.pone.0150619

105. Akgul E, Gunduz MK, Parlar Aİ, Guner Y, Eroglu M, Ozhan A, et al. The anti-apoptotic effect of ranolazine on cerebral protection during cardiopulmonary bypass and carotid artery surgery. *Acta Cardiol Sin* (2024) **40**(1):77–86. doi:10.6515/ACS.202401_40(1).20230814C

106. Kahlig KM, Hirakawa R, Liu L, George ALJ, Belardinelli L, Rajamani S. Ranolazine reduces neuronal excitability by interacting with inactivated states of brain sodium channels. *Mol Pharmacol* (2014) **85**(1):162–74. doi:10.1124/mol.113.088492

107. Peters CH, Sokolov S, Rajamani S, Ruben PC. Effects of the antianginal drug, ranolazine, on the brain sodium channel Na(V)1.2 and its modulation by extracellular protons. *Br J Pharmacol* (2013) **169**(3):704–16. doi:10.1111/bph.12150

108. Chunchai T, Arinno A, Ongnok B, Pantiya P, Khuanjing T, Prathumsap N, et al. Ranolazine alleviated cardiac/brain dysfunction in doxorubicin-treated rats. *Exp Mol Pathol* (2022) **127**:104818. doi:10.1016/j.yexmp.2022.104818

109. Samir SM, Hassan HM, Elmowafy R, ElNashar EM, Alghamdi MA, AlSheikh MH, et al. Neuroprotective effect of ranolazine improves behavioral discrepancies in a rat model of scopolamine-induced dementia. *Front Neurosci* (2024) **17**:1267675. doi:10.3389/fnins.2023.1267675

110. Elkholy SE, Elaidy SM, El-Sherbeeny NA, Toraih EA, El-Gawly HW. Neuroprotective effects of ranolazine versus pioglitazone in experimental diabetic neuropathy: targeting Nav1.7 channels and PPAR-γ. *Life Sci* (2020) **250**:117557. doi:10.1016/j.lfs.2020.117557

111. Chandrashekhar S, Hamasaki AC, Clay R, McCalley A, Herbelin L, Pasnoor M, et al. Open-label pilot study of ranolazine for cramps in amyotrophic lateral sclerosis. *Muscle & Nerve* (2022) **66**(1):71–5. doi:10.1002/mus.27560

112. Abbas LM, Al-Mudhafar RH, Al-Mudhafar DH, Hadi NR. Ranolazine protects the kidney from ischemia/reperfusion injury in adult male rats by modulation of inflammatory and oxidative pathways and suppression of Notch2/Hes1 signalling pathway. *Syst Rev Pharm* (2021) **12**(1):12. doi:10.31838/srp.2021.1.72

113. Abbas LM, Hameed AMA, Abbas WJ, Abdulsatar M, Hadi NR. The anti-apoptotic, anti-inflammatory and anti-oxidant effects of ranolazine on renal ischemia-reperfusion injury in adult Male rats. *Int J Pharm Res* (2021) **13**(01). doi:10.31838/ijpr/2021.13.01.658

114. Nayaka R, Vaish R. Renoprotective potential of ranolazine in ameliorating diabetic nephropathy in a rat model of streptozotocin-induced diabetes. *J Pharm Negative Results* (2022) **13**:1599–605. doi:10.47750/pnr.2022.13.S02.251

115. Ma C, Chen T, Ti Y, Yang Y, Qi Y, Zhang C, et al. Ranolazine alleviates contrast-associated acute kidney injury through modulation of calcium-independent oxidative stress and apoptosis. *Life Sci* (2021) **267**:118920. doi:10.1016/j.lfs.2020.118920

116. Yusuf J, Prakash G, Safal S, Mehta V, Mukhopadhyay S. Efficacy of nicorandil and ranolazine in prevention of contrast-induced nephropathy in patients with mild-to-moderate renal dysfunction: a randomized controlled trial. *Coron Artery Dis* (2024) **35**(3):186–92. doi:10.1097/MCA.0000000000001347

117. Hirakawa R, El-Bizri N, Shryock JC, Belardinelli L, Rajamani S. Block of Na^+ currents and suppression of action potentials in embryonic rat dorsal root ganglion neurons by ranolazine. *Neuropharmacology* (2012) **62**(7):2251–60. doi:10.1016/j.neuropharm.2012.01.021

118. Estacion M, Waxman SG, Dib-Hajj SD. Effects of ranolazine on wild-type and mutant hNav1.7 channels and on DRG neuron excitability. *Mol Pain* (2010) **6**: 35. doi:10.1186/1744-8069-6-35

119. Gould HJ, Garrett C, Donahue RR, Paul D, Diamond I, Taylor BK. Ranolazine attenuates behavioral signs of neuropathic pain. *Behav Pharmacol* (2009) **20**(8):755–8. doi:10.1097/FBP.0b013e3283323c90

120. Casey GP, Roberts JS, Paul D, Diamond I, Gould HJ, 3rd. Ranolazine attenuation of CFA-induced mechanical hyperalgesia. *Pain Med* (2010) **11**(1): 119–26. doi:10.1111/j.1526-4637.2009.00763.x

121. Gould HJ, Soignier RD, Cho SR, Hernandez C, Diamond I, Taylor BK, et al. Ranolazine attenuates mechanical allodynia associated with demyelination injury. *Pain Med* (2014) **15**(10):1771–80. doi:10.1111/pme.12516

122. Naveena R, Hashilkar NK, Davangeri R, Majagi SI. Effect of anti-inflammatory activity of ranolazine in rat model of inflammation. *Indian J Med Res* (2018) **148**(6):743–7. doi:10.4103/ijmr.IJMR_1504_16

123. Lenz M, Salzmann M, Ciotu CI, Kaun C, Krychtiuk KA, Rehberger Likozar A, et al. Pharmacologic modulation of intracellular Na^+ concentration with ranolazine impacts inflammatory response in humans and mice. *Proc Natl Acad Sci USA* (2022) **119**(29):e2207020119. doi:10.1073/pnas.2207020119

124. Jordá A, Aldasoro M, Campo-Palacio I, Vila JM, Aldasoro C, Campos-Campos J, et al. Facilitation of insulin effects by ranolazine in astrocytes in primary culture. *Int J Mol Sci* (2022) **23**(19):11969. doi:10.3390/ijms231911969

125. Bashir S, Kalabharathi HL. Ranolazine improves glucose and lipid homoestasis in streptozotocin induced diabetes mellitus in albino wistar rats. *Int J Basic Clin Pharmacol* (2016) 1477–80. doi:10.18203/2319-2003.ijbcp20162456

126. Ning Y, Zhen W, Fu Z, Jiang J, Liu D, Belardinelli L, et al. Ranolazine increases β-cell survival and improves glucose homeostasis in low-dose streptozotocin-induced diabetes in mice. *The J Pharmacol Exp Ther* (2011) **337**(1):50–8. doi:10.1124/jpet.110.176396

127. Dhalla AK, Yang M, Ning Y, Kahlig KM, Krause M, Rajamani S, et al. Blockade of Na^+ channels in pancreatic α-cells has antidiabetic effects. *Diabetes* (2014) **63**(10):3545–56. doi:10.2337/db13-1562

128. Guerra-Ojeda S, Jorda A, Aldasoro C, Vila JM, Valles SL, Arias-Mutis OJ, et al. Improvement of vascular insulin sensitivity by ranolazine. *Int J Mol Sci* (2023) **24**(17):13532. doi:10.3390/ijms241713532

129. Cassano V, Leo A, Tallarico M, Nesci V, Cimellaro A, Fiorentino TV, et al. Metabolic and cognitive effects of ranolazine in type 2 diabetes mellitus: data from an *in vivo* model. *Nutrients* (2020) **12**(2):382. doi:10.3390/nu12020382

130. Cassano V, Tallarico M, Armentaro G, De Sarro C, Iannone M, Leo A, et al. Ranolazine attenuates brain inflammation in a rat model of type 2 diabetes. *Int J Mol Sci* (2022) **23**(24):16160. doi:10.3390/ijms232416160

131. Morrow DA, Scirica BM, Chaitman BR, McGuire DK, Murphy SA, Karwatowska-Prokopczuk E, et al. Evaluation of the glycometabolic effects of ranolazine in patients with and without diabetes mellitus in the MERLIN-TIMI 36 randomized controlled trial. *Circulation* (2009) **119**(15):2032–9. doi:10.1161/CIRCULATIONAHA.107.763912

132. Pettus J, McNabb B, Eckel RH, Skyler JS, Dhalla A, Guan S, et al. Effect of ranolazine on glycaemic control in patients with type 2 diabetes treated with either glimepiride or metformin. *Diabetes Obes Metab* (2016) **18**(5):463–74. doi:10.1111/dom.12629

133. Chisholm JW, Goldfine AB, Dhalla AK, Braunwald E, Morrow DA, Karwatowska-Prokopczuk E, et al. Effect of ranolazine on A1C and glucose levels in hyperglycemic patients with non-ST elevation acute coronary syndrome. *Diabetes Care* (2010) **33**(6):1163–8. doi:10.2337/dc09-2334

134. Eckel RH, Henry RR, Yue P, Dhalla A, Wong P, Jochelson P, et al. Effect of ranolazine monotherapy on glycemic control in subjects with type 2 diabetes. *Diabetes Care* (2015) **38**(7):1189–96. doi:10.2337/dc14-2629

135. Kosiborod M, Arnold SV, Spertus JA, McGuire DK, Li Y, Yue P, et al. Evaluation of ranolazine in patients with type 2 diabetes mellitus and chronic stable angina: results from the TERISA randomized clinical trial (type 2 diabetes evaluation of ranolazine in subjects with chronic stable angina). *J Am Coll Cardiol* (2013) **61**(20):2038–45. doi:10.1016/j.jacc.2013.02.011

136. Nusca A, Bernardini F, Mangiacapra F, Maddaloni E, Melfi R, Ricottini E, et al. Ranolazine improves glycemic variability and endothelial function in patients with diabetes and chronic coronary syndromes: results from an experimental study. *J Diabetes Res* (2021) **2021**:1–9. doi:10.1155/2021/4952447

137. Ileana T, Anna M, Pamela S, Fernanda V, Stefano B, Livio L. Ranolazine promotes muscle differentiation and reduces oxidative stress in C2C12 skeletal muscle cells. *Endocrine* (2017) **58**(1):33–45. doi:10.1007/s12020-016-1181-5

138. Tomczyk M, Braczko A, Jablonska P, Mika A, Przyborowski K, Jedrzejewska A, et al. Enhanced muscle strength in dyslipidemic mice and its relation to increased capacity for fatty acid oxidation. *Int J Mol Sci* (2021) **22**(22):12251. doi:10.3390/ijms222212251

139. Torcinaro A, Cappetta D, De Santa F, Telesca M, Leigheb M, Berrino L, et al. Ranolazine counteracts strength impairment and oxidative stress in aged sarcopenic mice. *Metabolites* (2022) **12**(7):663. doi:10.3390/metabo12070663

140. Novak KR, Norman J, Mitchell JR, Pinter MJ, Rich MM. Sodium channel slow inactivation as a therapeutic target for myotonia congenita. *Ann Neurol* (2015) **77**(2):320–32. doi:10.1002/ana.24331

141. Arnold WD, Kline D, Sanderson A, Hawash AA, Bartlett A, Novak KR, et al. Open-label trial of ranolazine for the treatment of myotonia congenita. *Neurology* (2017) **89**(7):710–3. doi:10.1212/WNL.0000000000004229

142. Lorusso S, Kline D, Bartlett A, Freimer M, Agriesti J, Hawash AA, et al. Open-label trial of ranolazine for the treatment of paramyotonia congenita. *Muscle & Nerve* (2019) **59**(2):240–3. doi:10.1002/mus.26372

143. Lee JC, Kim KC, Choe SY, Hong YM. Reduced immunoreactivities of B-type natriuretic peptide in pulmonary arterial hypertension rats after ranolazine treatment. *Anat Cell Biol* (2016) **49**(1):7–14. doi:10.5115/acb.2016.49.1.7

144. Rocchetti M, Sala L, Rizzetto R, Staszewsky LI, Alemanni M, Zambelli V, et al. Ranolazine prevents INaL enhancement and blunts myocardial remodelling in a model of pulmonary hypertension. *Cardiovasc Res* (2014) **104**(1):37–48. doi:10.1093/cvr/cvu188

145. Teixeira-Fonseca JL, de Lima Conceição MR, Leal-Silva P, Roman-Campos D. Ranolazine exerts atrial antiarrhythmic effects in a rat model of monocrotaline-induced pulmonary hypertension. *Basic & Clin Pharmacol & Toxicol* (2023) **132**(5):359–68. doi:10.1111/bcpt.13845

146. Liles JT, Hoyer K, Oliver J, Chi L, Dhalla AK, Belardinelli L. Ranolazine reduces remodeling of the right ventricle and provoked arrhythmias in rats with pulmonary hypertension. *The J Pharmacol Exp Ther* (2015) **353**(3):480–9. doi:10.1124/jpet.114.221861

147. Khan SS, Cuttica MJ, Beussink-Nelson L, Kozyleva A, Sanchez C, Mkrdichian H, et al. Effects of ranolazine on exercise capacity, right ventricular indices, and hemodynamic characteristics in pulmonary arterial hypertension: a pilot study. *Pulm Circ* (2015) **5**(3):547–56. doi:10.1086/682427

148. Han Y, Forfia P, Vaidya A, Mazurek JA, Park MH, Ramani G, et al. Ranolazine improves right ventricular function in patients with precapillary pulmonary hypertension: results from a double-blind, randomized, placebo-controlled trial. *J Card Fail* (2021) **27**(2):253–7. doi:10.1016/j.cardfail.2020.10.006

149. Finch KT, Stratton EA, Farber HW. Ranolazine for the treatment of pulmonary hypertension associated with heart failure with preserved ejection fraction: a pilot study. *The J Heart Lung Transplant* (2016) **35**(11):1370–3. doi:10.1016/j.healun.2016.07.015

150. Gomberg-Maitland M, Schilz R, Mediratta A, Addetia K, Coslet S, Thomeas V, et al. Phase I safety study of ranolazine in pulmonary arterial hypertension. *Pulm Circ* (2015) **5**(4):691–700. doi:10.1086/683813

151. Nieminen T, Tavares CA, Pegler JR, Belardinelli L, Verrier RL. Ranolazine injection into coronary or femoral arteries exerts marked, transient regional vasodilation without systemic hypotension in an intact porcine model. *Circ Cardiovasc Interventions* (2011) **4**(5):481–7. doi:10.1161/CIRCINTERVENTIONS.111.962852

152. Ma A, Garland WT, Smith WB, Skettino S, Navarro MT, Chan AQ, et al. A pilot study of ranolazine in patients with intermittent claudication. *Int Angiol* (2006) **25**(4):361–9.

153. Saed CT, Tabatabaei Dakhili SA, Greenwell AA, Chan JSF, Yang K, Gopal K, et al. The antianginal ranolazine fails to improve glycaemia in obese liver-specific pyruvate dehydrogenase deficient male mice. *Basic & Clin Pharmacol & Toxicol* (2023) **133**(2):194–201. doi:10.1111/bcpt.13906

154. Batran RA, Gopal K, Aburasayn H, Eshreif A, Almutairi M, Greenwell AA, et al. The antianginal ranolazine mitigates obesity-induced nonalcoholic fatty liver disease and increases hepatic pyruvate dehydrogenase activity. *JCI Insight* (2019) **4**(1):e124643. doi:10.1172/jci.insight.124643

155. Polat ME, Sarı E, Tanriverdi LH, Gunata M, Aladag M, Sahin AF, et al. A potential hepatoprotective effect of ranolazine against methotrexate-induced liver injury in rats. *Authorea* (2023). doi:10.22541/au.168490817.77526721/v1

156. Keseroglu BB, Ozer E, Karakan T, Ozgur BC, Surer H, Ogus E, et al. Protective effects of Ranolazine on testicular torsion and detorsion injury in rats. *Andrologia* (2020) **52**(7):e13616. doi:10.1111/and.13616

157. Scaricamazza S, Salvatori I, Giacovazzo G, Loeffler JP, Renè F, Rosina M, et al. Skeletal-muscle metabolic reprogramming in ALS-SOD1^{G93A} mice predates disease onset and is A promising therapeutic target. *iScience* (2020) **23**(5):101087. doi:10.1016/j.isci.2020.101087

158. Marchio P, Guerra-Ojeda S, Aldasoro M, Valles SL, Martín-Gonzalez I, Martínez-León JB, et al. Relaxant and antiadrenergic effects of ranolazine in human saphenous vein. *Eur J Cardio-Thoracic Surg* (2020) **58**(2):277–85. doi:10.1093/ejcts/ezaa034

159. Rouhana S, Virsolvy A, Fares N, Richard S, Thireau J. Ranolazine: an old drug with emerging potential; lessons from pre-clinical and clinical investigations for possible repositioning. *Pharmaceuticals (Basel)* (2021) **15**(1):31. doi:10.3390/ph15010031

160. Rayner-Hartley E, Sedlak T. Ranolazine: a contemporary review. *J Am Heart Assoc* (2016) **5**(3):e003196. doi:10.1161/JAHA.116.003196

161. Kaplan A, Amin G, Abidi E, Altara R, Booz GW, Zouein FA. Role of ranolazine in heart failure: from cellular to clinic perspective. *Eur J Pharmacol* (2022) **919**:174787. doi:10.1016/j.ejphar.2022.174787

EBM Experimental Biology and Medicine

TYPE Original Research
PUBLISHED 28 August 2025
DOI 10.3389/ebm.2025.10461

OPEN ACCESS

*CORRESPONDENCE
Nina D. Ullrich,
nina.ullrich@unibe.ch

RECEIVED 09 December 2024
ACCEPTED 11 August 2025
PUBLISHED 28 August 2025

CITATION
Fischer D, Sha'sha'a M, Schenz J, Tayan A, Mertens C, Decker SO, Gallenstein N, Dietrich M, Lajqi T, Hafner A, Weigand MA and Ullrich ND (2025) An approach to evaluate the effect of inflammatory microvesicles on Ca^{2+} handling in human-induced pluripotent stem cell-derived cardiomyocytes. *Exp. Biol. Med.* 250:10461. doi: 10.3389/ebm.2025.10461

An approach to evaluate the effect of inflammatory microvesicles on Ca^{2+} handling in human-induced pluripotent stem cell-derived cardiomyocytes

Dania Fischer[1,2], Mishkaat Sha'sha'a[1,3], Judith Schenz[1], Aycan Tayan[1], Christina Mertens[2,4], Sebastian O. Decker[1], Nadia Gallenstein[1], Maximilian Dietrich[1], Trim Lajqi[5], Anna Hafner[1], Markus A. Weigand[1] and Nina D. Ullrich[2,3,6]*

[1]Department of Anesthesiology, Medical Faculty Heidelberg, Heidelberg University, Heidelberg, Germany, [2]DZHK (German Centre for Cardiovascular Research), Partner Site Heidelberg, Heidelberg, Germany, [3]Department of Cardiovascular Physiology, Heidelberg University, Heidelberg, Germany, [4]Center for Translational Biomedical Iron Research, Department of Pediatric Oncology, Immunology, and Hematology, University of Heidelberg, Heidelberg, Germany, [5]Department of Neonatology, Heidelberg University Children's Hospital, Heidelberg, Germany, [6]Department of Physiology, University of Bern, Bern, Switzerland

Abstract

Microvesicles (MV) isolated from septic individuals were observed to impact systemic hemodynamics and cardiac function. The aim of this *in vitro* study was to analyze the effects of TNFα-induced endothelial MV (TMV) and MV from septic patients (SMV) on beating frequency and Ca^{2+} transient kinetics of human-induced pluripotent stem cell-derived cardiomyocytes (hiPSC-CM). MV were isolated from supernatants of TNFα-stimulated primary human pulmonary microvascular endothelial cells (HPMEC) and plasma from 20 sepsis patients by ultracentrifugation and quantified using flow cytometry. Spontaneous Ca^{2+} transients were measured in hiPSC-CM using the Ca^{2+}-sensitive ratiometric indicator fura-2 at different time points of incubation with different MV concentrations. At 16 h of incubation, higher MV concentrations showed significant differences, especially regarding decay and beating frequency. Despite high variability, at 10×10^6 MV/mL and 16 h of incubation, TMV significantly decreased frequency compared to control MV (CMV). SMV from septic patients did not reveal any significant effects on Ca^{2+} transients under these experimental settings. MV isolated from control or TNFα-treated HPMEC affected Ca^{2+} handling and spontaneous activity of hiPSC-CM, however, the measured effects were not consistent throughout the different conditions. Further refinement of the experiment conditions is needed to specify the exact conditions for crosstalk between endothelium-derived MV and cardiomyocytes.

KEYWORDS

cardiomyopathy, sepsis, cardiomyocytes, calcium transients, microvesicles

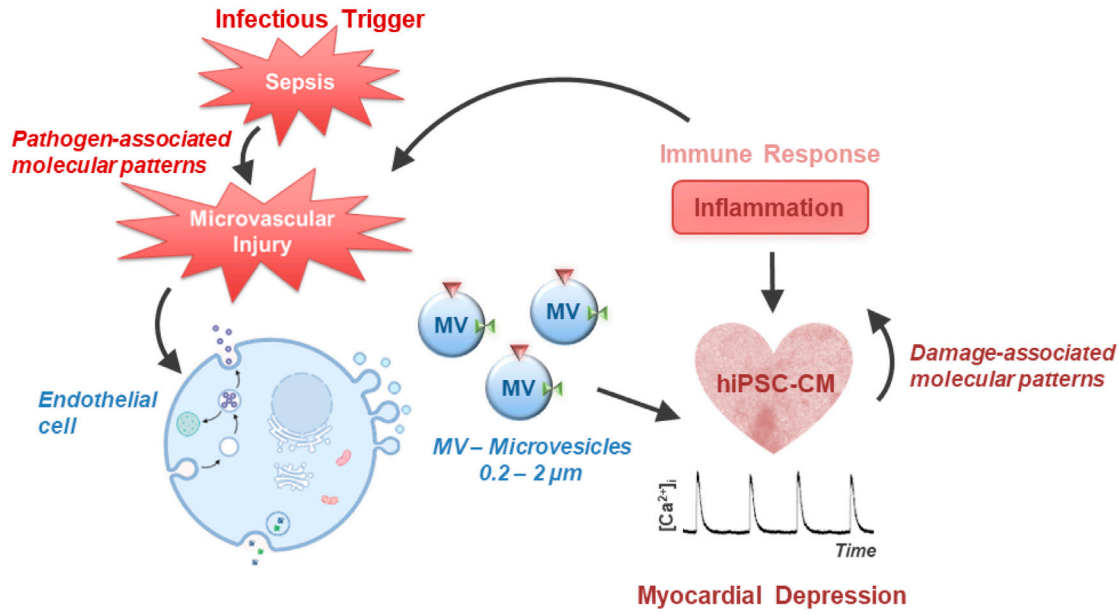

GRAPHICAL ABSTRACT

Impact statement

Given the established role of extracellular microvesicles in cellular communication and their potential impact on various physiological and pathological processes, we believe our findings are highly relevant to the scope of your journal. Our findings suggest that while microvesicles can modulate cardiac function, the precise conditions under which this crosstalk occurs require further refinement. This study offers valuable insights into the complex interactions between endothelium-derived microvesicles and cardiomyocytes, highlighting the need for more detailed investigation into the conditions that facilitate this interaction. This manuscript contributes to the growing body of knowledge in this field and spur further research into the therapeutic and diagnostic potential of microvesicles in sepsis and other cardiovascular conditions.

Introduction

Sepsis is a life-threatening clinical syndrome that arises from a severe disturbance in the body's reaction to infection. Parker et al. were the first to describe the association of newly developed myocardial dysfunction and its impact on mortality in patients with sepsis [1]. Since then, cardiac dysfunction has been recognized as a significant comorbidity in sepsis, termed septic cardiomyopathy. The prevalence and impact of septic cardiomyopathy can vary, but it is estimated that a significant proportion of patients with severe sepsis or septic shock develop cardiac dysfunction [2]. Septic cardiomyopathy is a complex condition, and there are still multiple aspects that are not fully understood [3]. Extracellular vesicles (EV) may participate in the pathogenesis of sepsis and septic cardiomyopathy in multiple ways. EV have been detected in the circulation of sepsis patients [4, 5]. EV are membrane vesicles released during cell activation, currently being considered as diagnostic biomarkers, mediators, or even therapeutic agents of sepsis [6, 7]. They are known to be active in cell-to-cell communication and can be differentiated by size and surface markers [8]. There are three types of EV, namely the submicron-size microvesicles (MV), the nanometer-size exosomes, and apoptotic bodies, which measure up to several micrometers in diameter [9].

Azevedo et al. reported that platelet-derived exosomes from septic shock patients induce myocardial dysfunction in isolated heart and papillary muscle preparations [10]. This negative inotropic effect was fully reversible upon withdrawal of exosomes. Mortaza et al. found that rats with sepsis induced by peritonitis exhibited a specific phenotype of MV derived from leukocytes. Inoculation of these MV in healthy rats reproduced hemodynamic, septic inflammatory patterns associated with oxidative and nitrosative stress [11]. Furthermore, Zhang et al. observed that H9c2 cells, derived from embryonic rat

cardiomyocytes, exhibited reduced cell viability and increased cell apoptosis and reactive oxygen species production when treated with EV derived from hypoxia/reoxygenation-treated human umbilical vein endothelial cells [12].

Sepsis-induced endothelial dysfunction and capillary leakage lead to impaired myocardial perfusion and tissue hypoxia, which further compromise cardiac function. Moreover, sepsis triggers an overwhelming release of pro-inflammatory cytokines. Tumor necrosis factor-α (TNFα) is one important pro-inflammatory cytokine upregulated in many inflammatory diseases and is a potent inducer of endothelial cell (EC)-derived MV formation [13]. These MV and ECs were shown to be involved in the pathophysiological mechanisms of sepsis and septic shock [14]. Moreover, exosomes from patients with septic shock convey miRNAs and mRNAs related to pathogenic pathways, including inflammatory response, oxidative stress, and cell cycle regulation [15]. It was also shown that miRNAs derived from neutrophil-derived EV play an important role in sepsis-associated cardiomyopathy. These miRNAs were shown to induce hypoxia inducible factor-1 (HIF-1) signaling to elicit development of septic cardiomyopathy in septic patients [16].

Based on the above mentioned clinical and experimental studies, we tested the hypothesis that MV isolated from septic patients affect cardiomyocyte contractility. To test this, we employed human-induced pluripotent stem cell-derived cardiomyocytes (hiPSC-CM) as our model system. Initially, we examined MV generated *in vitro* under stress conditions (induced by TNFα) by microvascular endothelial cells. These MV were applied directly to cardiomyocytes within a well-controlled experimental framework. We analyzed various MV concentrations and defined incubation times to assess their impact on cardiac Ca^{2+} handling. Since electromechanical coupling in cardiomyocytes is governed by intracellular Ca^{2+}, and Ca^{2+} transients are tightly regulated, even minor effects on contractility can be detected through changes in Ca^{2+} transient kinetics. Therefore, any alterations in Ca^{2+} homeostasis directly influences cardiomyocyte contractility. The goal of this *in vitro* study was to systematically investigate the effects of TNFα-induced endothelial MV and MV from septic patients on Ca^{2+} handling of hiPSC-CM.

Materials and methods

Cell culture

Endothelial cells

Primary human pulmonary microvascular endothelial cells (HPMEC) were commercially obtained from Promocell (C-12281, Heidelberg, Germany). Cells were cultivated under standard cell-culture conditions (37°C, 5% CO_2) in endothelial cell growth medium (MV2, C-22022) complemented with supplement-mix (C-39226). The medium was exchanged every two to 3 days. When cells reached 60%–70% confluency, they were split according to the manufacturer's instruction using the detach kit (C-41210, Promocell). Accordingly, cells were washed with HEPES (C-40010) and then detached using 0.04% Trypsin/0.03% EDTA (C-41010). After 3 min of centrifugation at 250 *g* and 37°C, the cell-pellet was resuspended. Cells were counted and 500,000 cells were added to a T75 flask prefilled with warm medium. Cells were expanded up to passage 7. At 90% confluency, cells were incubated with 100 ng/mL recombinant human TNFα (300-01A, PeproTech, Hamburg, Germany) for 24 h with a respective control of medium-only cells. Thereafter, supernatants were collected and snap-frozen for later MV isolation of TNFα-stimulated (TMV) and control MV (CMV).

Stem cell culture

Human-induced pluripotent stem cells (hiPSC) were provided by Dr. Cyganek, Stem Cell Unit Göttingen, University Medical Center Göttingen. Using the integration-free Sendai virus as described before by Rössler et al., the wild type hiPSC-line UMGi014-C clone 14 was generated from dermal fibroblasts [17]. Cells were seeded in StemFit Basic04 Complete Medium (Basic04CT, Nippon Genetics, Düren, Germany) containing the ROCK-inhibitor thiazovivin (1:1000, 72254, StemCell Technologies, Cologne, Germany) for 24 h. For maintenance of the culture, medium was changed every other day. At 70% confluency, cells were passaged. Standard cell culture plates were coated with 1:300 Matrigel (Corning, Berlin, Germany) in DMEM/F-12 (Gibco, Darmstadt, Germany) for at least 30 min (37°C, 5% CO_2). Cells were detached using 0.5 M EDTA (15575020, Thermo Fisher scientific, Darmstadt, Germany) for 7–10 min. After centrifugation at 25 *g* for 5 min, the cell pellet was resuspended in StemFit/thiazovivin medium and replated both in a 12-well plate for differentiation (1:20 to 1:40) and in a 6-well plate for maintenance (1:10 to 1:20).

Cardiac differentiation

The differentiation protocol is based on a Wnt/β-catenin signaling pathway modulation [18]. The procedure is described in Figure 1. At 95% confluency, the differentiation process was induced (day 0). hiPSC were treated with 5 μM CHIR99021 (72054, Stemcell Technologies) in RPMI 1640 (61870010, Life Technologies, Thermo Fisher Scientific) containing 11 mM glucose and B27 supplement without insulin (1:50, A18956, Gibco, Thermo Fisher Scientific). After 24 h, cells were maintained in diluted CHIR (2.5 μM) to improve the differentiation efficiency [18]. On day 3, medium was changed, and the Wnt pathway inhibitor IWP-4 (5 μM, 72552, StemCell Technology, Cologne, Germany) was added for 48 h, with a medium change on day 5. On day 7, the medium was switched to RPMI-B27+insulin (1:50, 17504, Gibco, Thermo Fisher Scientific) and changed every other day. Once contractions were detected, metabolic selection of cardiomyocytes was initiated by replacement of glucose with

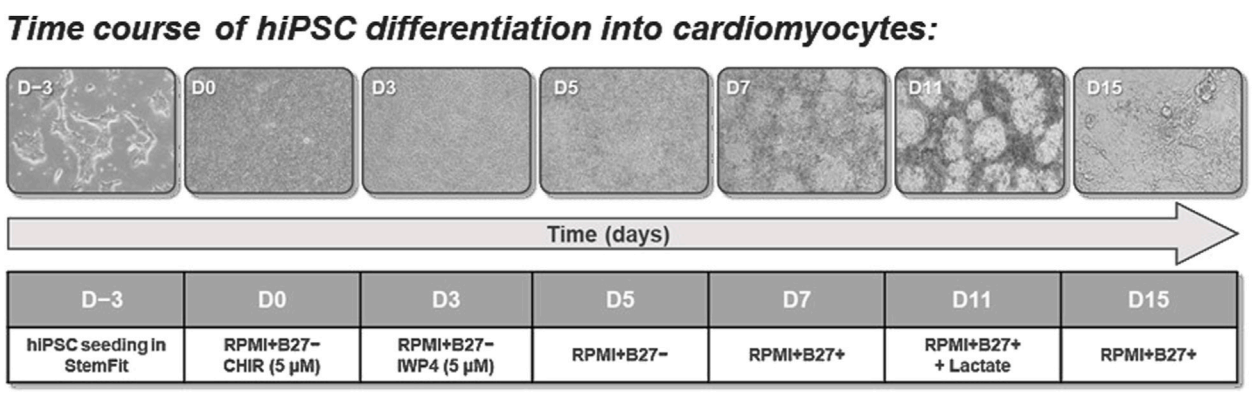

FIGURE 1
hiPSC differentiation to cardiomyocytes (hiPSC-CM). hiPSC were seeded three days before (D-3) start of differentiation (D0) and grown to colonies of about 70% confluency. Starting with D0, the Wnt signaling pathway was subsequently first activated (CHIR) and then inhibited (IWP4) to induce mesoderm and cardiogenic determination. From D9 onward, cells were beating and further metabolically selected using lactate. After selection, cells were kept in maintenance medium (RPMI+B27+) until further use.

sodium lactate (5 mM, L4263, Sigma-Aldrich, Merck) in RPMI 1640 + B27+insulin without glucose (11879020, Gibco). After 5 days of selection, hiPSC-CM were maintained in RPMI+B27+insulin.

Cardiomyocyte cell culture

Day 16 post differentiation, hiPSC-CM were seeded on glass bottom dishes (GBD, P35G-1.5-14-C, MatTEK, Life Sciences, Bratislava, Slovakia) for experimental purposes. Cells used for all experiments were differentiated from hiPSC passages 40-54. GBD were coated with Matrigel as described above. Splitting medium contained RPMI+B27+insulin without glucose (Life Technologies), 10% foetal bovine serum (Gibco), 0.1% thiazovivin (72254, StemCell Technology), and 1% penicillin/streptomycin (P4458, Sigma-Aldrich). Cells were rinsed twice with PBS (D8537, Sigma-Aldrich) and incubated with TrypLE Express (1-5x, 12605, Gibco). After 10 min of incubation (37°C, 5% CO_2), cells were gently detached. Cells were centrifuged at 6.2 *g* for 10 min, resuspended in splitting medium, counted, and seeded at 30,000 cells per dish on a GBD. Within 24 h, the medium was changed using RPMI+B27+insulin and changed every second day thereafter.

Sepsis and control plasma acquisition

Ethical approval for this study (reference number S-664/2020) was provided by the Ethical Committee of the Medical Faculty of Heidelberg University. The study was registered at the German Clinical Trial Register (DRKS00023301). Adult participants with abdominal, respiratory, or urinary tract sepsis were recruited within the first 24 h of sepsis onset. Inclusion criteria for patients with sepsis were applied according to Sepsis-3 criteria [19]: life-threatening organ dysfunction caused by a suspected or proven infection, an acute increase in total SOFA score of ≥2 points, onset <24 h, and age ≥18 years.

Whole blood was drawn on day 1 and centrifuged for 10 min at 2,000 *g* at room temperature. The plasma was further centrifuged for 15 min at 800 g and the supernatant was collected for isolation of septic MV (SMV). As a control for SMV, plasma was obtained from a plasmapheresis procedure, during which 12 freshly frozen plasmas from healthy donors were used for plasma exchange of a patient with ABO incompatibility before organ transplantation to gain CMV (Plasmapheresis CMV: (P)CMV). Both sepsis and plasmapheresis plasma were stored at −80°C.

MV preparation and incubation

Human primary microvascular endothelial cells (HPMEC) were cultured up to a maximum 7 passages to preserve the endothelial phenotype *in vitro*. Cells were incubated with TNFα (100 ng/mL). Unstimulated HPMEC served as control. After 24 h of incubation, medium was collected and MV were isolated and characterized as described below.

MV isolation

The following steps were conducted at 4°C. Defrosted plasma and cell culture supernatants were centrifuged for 15 min at 500 *g*. The supernatant was collected and centrifuged for 20 min at 4000 *g*. The supernatant of these samples was ultracentrifuged for 90 min at 100,000 *g*. Afterwards, the pellet was resuspended in PBS and centrifuged at 100,000 *g* for another 90 min. Finally, the MV pellet was collected and resuspended in PBS. All samples were quantified and stored at −70°C to preserve MV count.

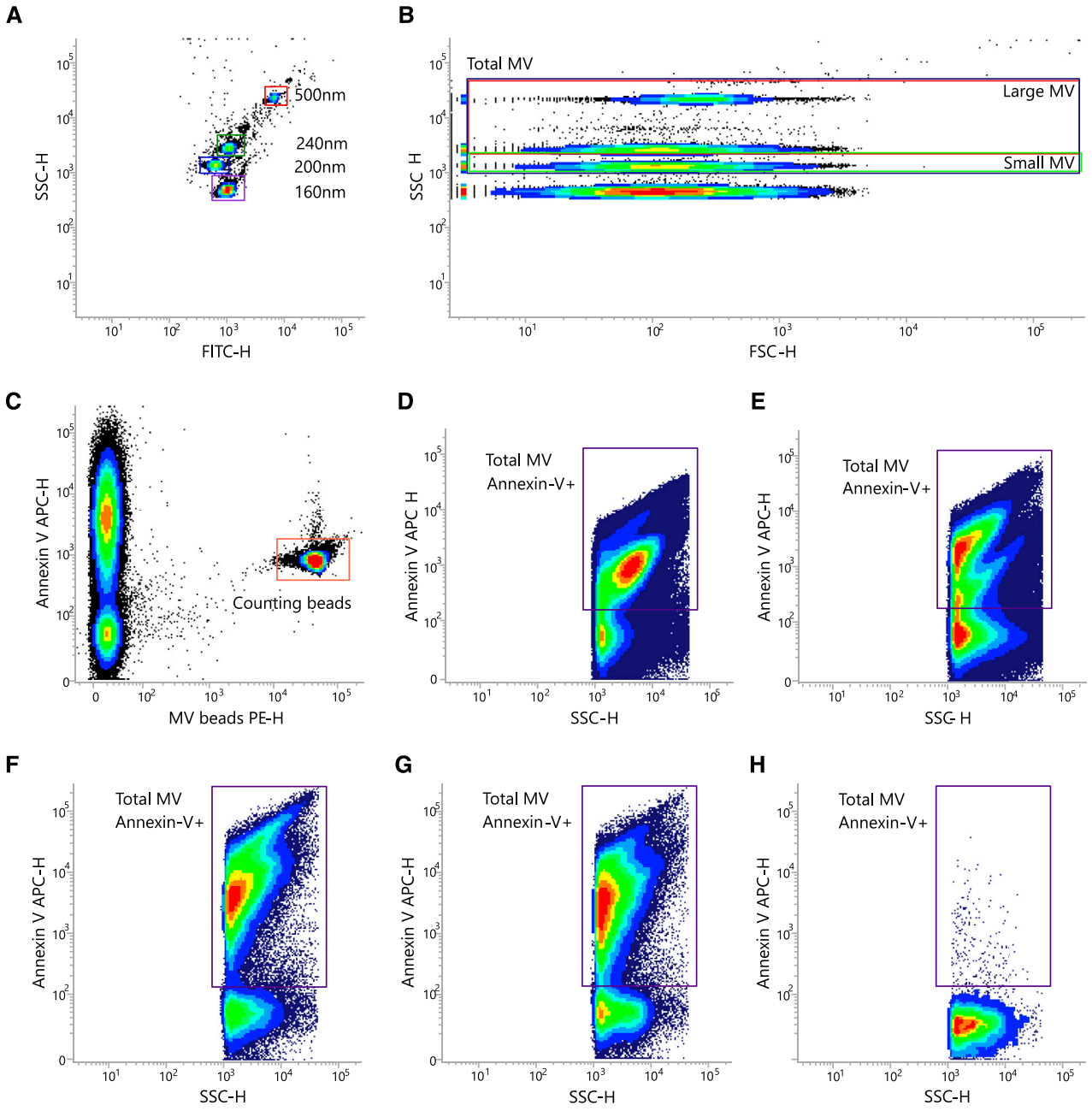

FIGURE 2
Representative gating strategy for quantification of MV. **(A–E)** Flow cytometer settings and gating strategy for MV quantification with Megamix-Plus SSC and MV-Counting Beads (0.3 µm sized PE fluorescent beads). Shown are density/dot blots from representative measurements. SSC-H vs. FITC-H **(A)** and SSC-H vs. FSC-H **(B)** density blot showing the location of the Megamix-Plus SSC beads. Beads were used to set up the SSCH, FITC-H, and FSC-H PMT voltage **(A,B)**, the MV gates **(B)**, and the SSC threshold for MV analysis. **(C)** Beads with a known concentration were spiked into all MV samples. Shown is a representative analysis of an MV isolate as SSC-H vs. FSC-H dot blots illustrating the Annexin V-stained MV within the prior defined (see **(B)**) MV gates. **(D-G)** Four examples of the gating strategy to characterize the MV population. **(H)** Negative control after addition of 20% Triton X-100.

MV characterisation and quantification

Flow cytometry was performed using the BD FACSLyric flow cytometer (BD Bioscience, Franklin Lakes, NJ, USA) with the accompanying BD FACSuite software.

All materials were filtered through a 0.22 µm sterile filter. Megamix-Plus SSC beads (7803, Biocytex, Marseille, France) were used to adjust the flow cytometer settings for standardized MV analysis according to the manufacturer's

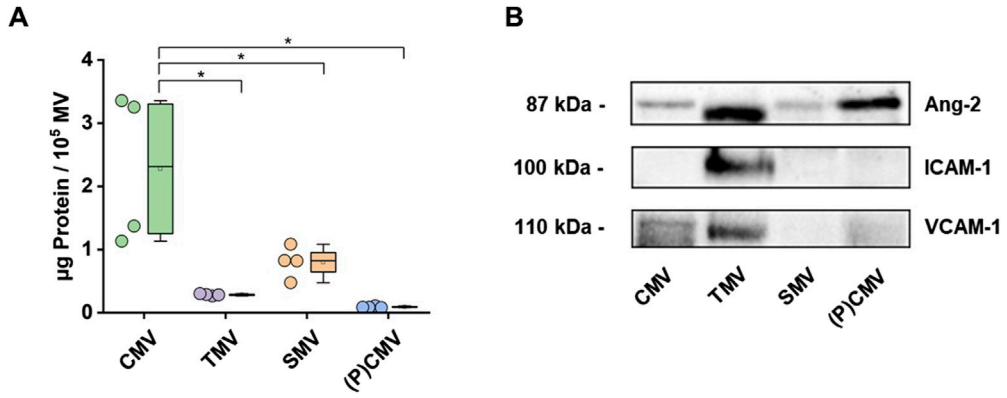

FIGURE 3
Characterization of MV. MV were isolated from the plasma of healthy volunteers (CMV), the supernatant of endothelial cell cultures stimulated with TNFα (100 ng/mL, 24 h; TMV), the plasma of septic patients (SMV), and a plasmapheresis procedure. **(A)** Protein concentration was determined using the Pierce™ 660 nm Protein Assay Kit. Data are shown as scatter dots and box plots indicating IQR range, mean, median, and whiskers extended to 1.5 IQR (n = 4 measurements). **(B)** MV preparations were analyzed by Western blot for Angiopoietin-2 (Ang-2), Intercellular Adhesion Molecule 1 (ICAM-1), and Vascular Cell Adhesion Molecule 1 (VCAM-1) protein content. Western blot images showing representative blots from two experiments.

instructions (Figure 2). MV were stained with Annexin-V APC (550474, BD Bioscience). MV were defined as Annexin-V positive events. MV-Counting Beads with a known concentration were spiked into each MV sample for quantification. The negative control was performed by adding Triton X-100.

Pierce protein assay for protein concentration

The protein concentration of MV lysates was determined using the Pierce 660 nm Protein Assay Kit (#22662, Thermo Fisher Scientific, Waltham, USA) according to the manufacturer's protocol, as described (Figure 3A) [20]. Standards, samples, and blanks were loaded into 96-well culture plates and combined with the provided protein reagent enhanced with the Ionic Detergent Compatible Reagent (IDCR, #22663, Thermo Fisher Scientific). Following a five-minute incubation at room temperature, absorbance was measured at 660 nm using an iMark microplate reader (Bio-Rad Laboratories, Hercules, USA). Protein concentrations were calculated by interpolation from the standard curve. Subsequently, 40 µg of total protein from each sample was loaded for SDS-PAGE and Western blot analysis.

SDS-PAGE Western blotting

MVs preparations were lysed using RIPA buffer supplemented with freshly prepared Pierce Protease and Phosphatase Inhibitor tablets (#A32959, Thermo Fisher Scientific) as described [20]. The lysates were vortexed and incubated on ice for 1 min to ensure complete EV disruption, followed by centrifugation at 12,000 × g for 30 min at 4°C. Supernatants were collected and combined with 5× Laemmli buffer, then heated at 95°C for 5 min to denature proteins and reduce disulfide bonds. Proteins were separated on a 10% SDS-PAGE gel and subsequently transferred onto a 0.45-µm PVDF membrane. To minimize nonspecific antibody binding, membranes were blocked with 1% bovine serum albumin (BSA) in TBS-T (Tris-buffered saline with 0.1% Tween-20) for 45 min at room temperature. Membranes were then incubated overnight at 4°C with primary antibodies. Primary antibodies were purchased from Santa Cruz Biotechnology, Inc. (Dallas, USA): Angiopoietin 2 (Ang-2; #sc-74403), ICAM-1 (#sc-107), and VCAM-1 (E10; #sc-13160). Anti-mouse secondary HRP-conjugated antibody (m-IgG1 BP-HRP; #sc-525408) was purchased from Santa Cruz Biotechnology, Inc. After washing with TBS-T to remove unbound antibodies, membranes were incubated with HRP-conjugated secondary antibodies for 1 h at room temperature. Following a final series of washes with TBS-T, protein bands were detected using enhanced chemiluminescence (ECL) reagents and imaged with the Chemi-Doc XRS+ system (Bio-Rad Laboratories, Figure 3B).

Cardiomyocyte treatment with MV

Human iPSC-CM were incubated with MV or PBS buffer (control) and experiments were then conducted. To assess different time points and concentrations, TMV (TNF-α-stimulated) and CMV (from unstimulated endothelial cells) were used. Initially 10^6 endothelial MV/mL were added for 1, 3, 6, 16, and 24 h independently to investigate the time course of MV effects. Then, 3, 6, and 10×10^6 endothelial MV/mL were added for 6 and 16 h to

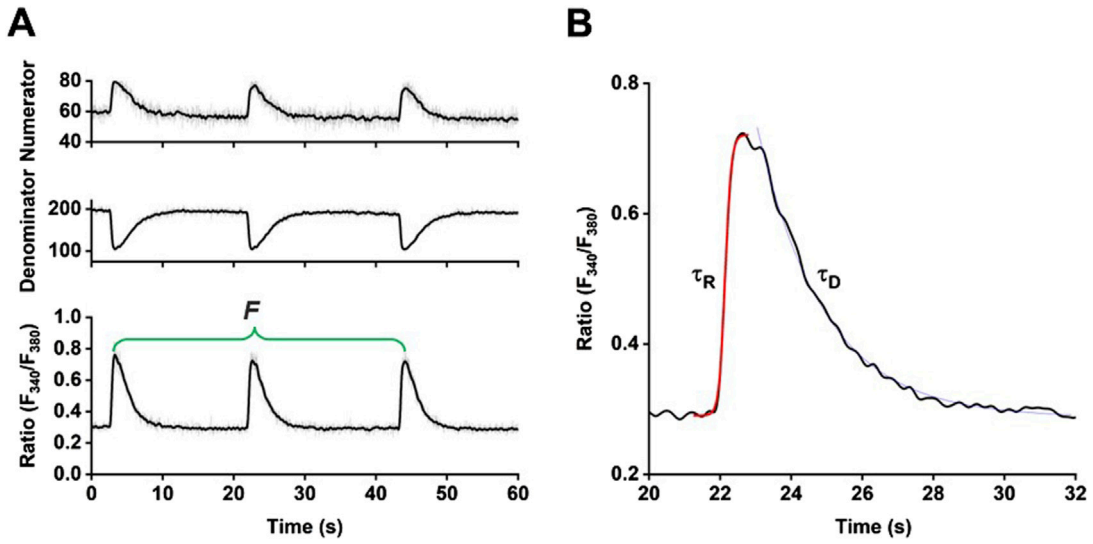

FIGURE 4
Functional analysis of spontaneous Ca^{2+} transients. **(A)** Sample traces of Ca^{2+} transients recorded using the ratiometric Ca^{2+}-sensitive indicator fura-2. **(B)** Enlargement of one Ca^{2+} transient and indication of the time constants τ_R and τ_D derived from sigmoidal and exponential decay fitting procedures, respectively.

analyze the effect of different MV concentrations. Finally, SMV (sepsis patients' MV) and (P)CMV were used and 10^7 plasma MV/mL from different patients were added separately for 16 h.

Functional analysis

Calcium transient acquisition

Spontaneous Ca^{2+} transients were measured using the ratiometric Ca^{2+}-sensitive fluorescent indicator fura-2. Human iPSC-CM were loaded with 0.75 µM fura-2-AM (F1221, Thermo Fisher Scientific) diluted in Tyrode's solution (pH 7.4, solution composition (in mM): NaCl 140, KCl 5.4, $CaCl_2$ 1.8, $MgCl_2$ 1.1, HEPES 10, and glucose 10) for 20 min at room temperature in the dark. After 10 min of de-esterification, spontaneous Ca^{2+} release activity was recorded using the IonOptix system (IonOptix, Dublin, Ireland). Cells were exposed to light emitted by a Xenon lamp passing through rapidly switching filters of 340 nm and 380 nm excitation wavelengths. The ratio of Ca^{2+}-bound (numerator) and unbound (denominator) fura-2 was determined and fluorescence emission was collected at 510 nm. Data were collected using the IonWizard software and are presented as fura-2 ratio (F_{340}/F_{380}).

Calcium transient analysis

For functional evaluation of spontaneous activity only regular beating hiPSC-CM were used. Three representative Ca^{2+} transients were analyzed at a steady state. To evaluate changes in Ca^{2+} release and reuptake activity in the different experimental groups, parameters were analyzed by assessing the time constants of Ca^{2+} rise (τ_R) and Ca^{2+} decay (τ_D) and the beating frequency using OriginPro® (Origin Lab Corporations, Northampton, MA, United States). τ_R was fitted with a sigmoidal function, whereas τ_D was fitted with an exponential decay function (Figure 4). Exclusion criteria for data analysis were set as Ca^{2+} peak below 0.4 F_{340}/F_{380}, Ca^{2+} baseline above 0.6 F_{340}/F_{380}, Time-To-Peak (TTP) above 2000 ms, τ_D above 4000 ms, and abnormal transient shapes.

Data and statistical analysis

Experiments were repeated in three rounds with three different stem cell passages for the HPMEC experiments. "n" denotes the number of individually analyzed cells (one data point), whereas "N" designates the analysis number of GBD, equivalent to three different hiPSC-CM passages for endothelial MV experiments and 16 different patients for the plasma MV experiment. Graphic design and statistical analysis were performed using OriginPro® (OriginLab software) and MV-count calculations using Excel. Normality was determined by a Shapiro-Wilk test and homoscedasticity by the Levens test. To evaluate the effect that MV may have on the Ca^{2+} transient parameters of hiPSC-CM based on the proposed hypothesis, the non-parametric Kruskal-Wallis test was conducted to test for differences between TMV or SMV-, CMV-, and PBS-treated

cardiomyocytes, followed by the Dunns post-hoc-test with a Bonferroni alpha error adjustment to compare two conditions to each other. Most of the data are illustrated as box plots representing each data point (dots), mean (black square), median (centre line), 25th −75th quantiles (box edges), and standard deviation (SD, whiskers). Data in the results are presented as mean ± SD. Statistical significance is indicated by * for $p < 0.05$.

Results

Stimulation of HPMECs with TNFα increased the concentration of MV in the supernatant by a factor of 5.8 (difference between means [stimulated vs. unstimulated] ± SEM: 79,097 ± 5 455; $p < 0.0001$; $n = 5$). The difference between TMV and CMV was 6.4-fold (difference between means [TMV–CMV] ± SEM: 251,676 ± 16,404; $p < 0.0001$; $n = 4$). Plasma from septic patients contained fewer MVs per µL than the supernatant from TNFα-stimulated HPMECs (difference between means [SMV–TMV] ± SEM: −169 034 ± 26,046; $p < 0.001$; $n = 4$). Protein content, on the other hand, was highest in CMV (Figure 3A). All MV preparations analyzed in this study consistently contained angiopoietin-2 (Ang-2) as part of their protein cargo, as confirmed by Western blot (Figure 3B; Supplementary Figure S3). MV from TNFα-stimulated HPMEC (TMV) also contained Intercellular Adhesion Molecule 1 (ICAM-1), whereas MV isolated from unstimulated HPMEC (CMV), septic patients, or healthy volunteers did not. Vascular Cell Adhesion Molecule 1 (VCAM-1) was found in all MV preparations except in MV from septic patients.

After differentiation and metabolic selection of hiPSC-CM, cells were incubated either with MV isolated from unstimulated HPMEC (CMV) or from TNFα-stimulated HPMEC (TMV). PBS-treated cells served as MV-negative control. In time-course experiments, different incubation times of MV on hiPSC-CM were evaluated, while in concentration-dependent experiments, different concentrations of MV were tested at two different time points. For the functional experiments, hiPSC-CM were loaded with fura-2 and Ca^{2+} transients were recorded over time. Since the rise and decay of the Ca^{2+} transients are sensitively regulated processes during the mechanism of excitation-contraction coupling, these parameters were evaluated, together with the spontaneous frequency of these transients, representative of the beating frequency. Details of the strategy to analyze Ca^{2+} transients are summarized in Figure 4 and indicate the time constants of τ_R and τ_D derived from curve fitting as well as the frequency (F).

In the first set of functional experiments, hiPSC-CM were incubated with 1×10^6 MV derived from either TNFα-stimulated or control HPMEC; PBS treatment served as MV-free control. The protocol of the time course experiment is outlined in Figure 5A. Ca^{2+} transients were evaluated at five different time points. Figure 5B shows the summary of the statistical evaluation of τ_R, τ_D, and F derived from the Ca^{2+} transients. Data were normalized to PBS control (raw data are summarized in Supplementary Figure S1). After 3 h of incubation, TMV-treated hiPSC-CM showed a faster rise in the Ca^{2+} transients compared to CMV-treated cells with reduced data variability. After 6 h of incubation, TMV-treated cells had even shorter τ_R than PBS controls (indicated by the orange background). While under these conditions, no difference was detected in the decay kinetics of the Ca^{2+} transients, and the frequency was significantly lower after 16 h of TMV-treatment compared to CMV and PBS (two-sample t-test: P = 0.0224).

To investigate the influence of different MV concentrations, hiPSC-CM were incubated with three distinct amounts of CMV or TMV, and the effect on Ca^{2+} transient kinetics were assessed at two different time points, namely after 6 and 16 h of incubation. Figure 6A summarizes the experimental strategy for the test of 3×10^6, 6×10^6, or 10×10^6 MV on Ca^{2+} transient function. The data for the statistical evaluation of τ_R, τ_D, and F derived from Ca^{2+} transients are given in Figure 6B (raw data are summarized in Supplementary Figure S2). Compared to PBS control, CMV- and TMV-treated hiPSC-CM had faster rises of Ca^{2+} transients at 3×10^6 MV at 6 (CMV and TMV) and 16 h (TMV only) of incubation. However, this effect was not present at higher MV concentrations. Longer incubation times had a significant effect on the decay of Ca^{2+} transients. Compared to PBS control after 16 h, CMV- and TMV-treated cells had a smaller τ_D, indicating faster return of $[Ca^{2+}]_i$ to baseline levels. Moreover, the frequency of spontaneous Ca^{2+} transients was also modified relative to PBS control, with a shift toward higher frequencies. At 10×10^6 MV and 16 h, TMV induced a significantly faster beating rate compared to CMV treatment.

In the last set of experiments, the effect of MV isolated from sepsis patients was studied. Septic patients were 66.4 ± 9.6 years of age and had a median SOFA score of 11 (6.8; 12). The data are summarized in Table 1. Figure 7A demonstrates the experimental flow. In this case, MV were isolated from plasmapheresis samples as negative control ((P)CMV) and from septic patients (SMV). hiPSC-CM were incubated with 10×10^6 MV for 16 h. Data were again normalized to PBS controls. The statistical evaluation of τ_R, τ_D, and F measured from Ca^{2+} transients did not reveal any significant differences after treatment of the cells with (P)CMV or SMV relative to control (Figure 7B).

Discussion

Our study aimed to investigate the potential impact of MV on the contractility of hiPSC-CM in a novel experimental model for septic cardiomyopathy. MV can contribute to apoptosis and inflammation of endothelial cells, which can cause the endothelial barrier to become leaky [20]. Moreover, as a result

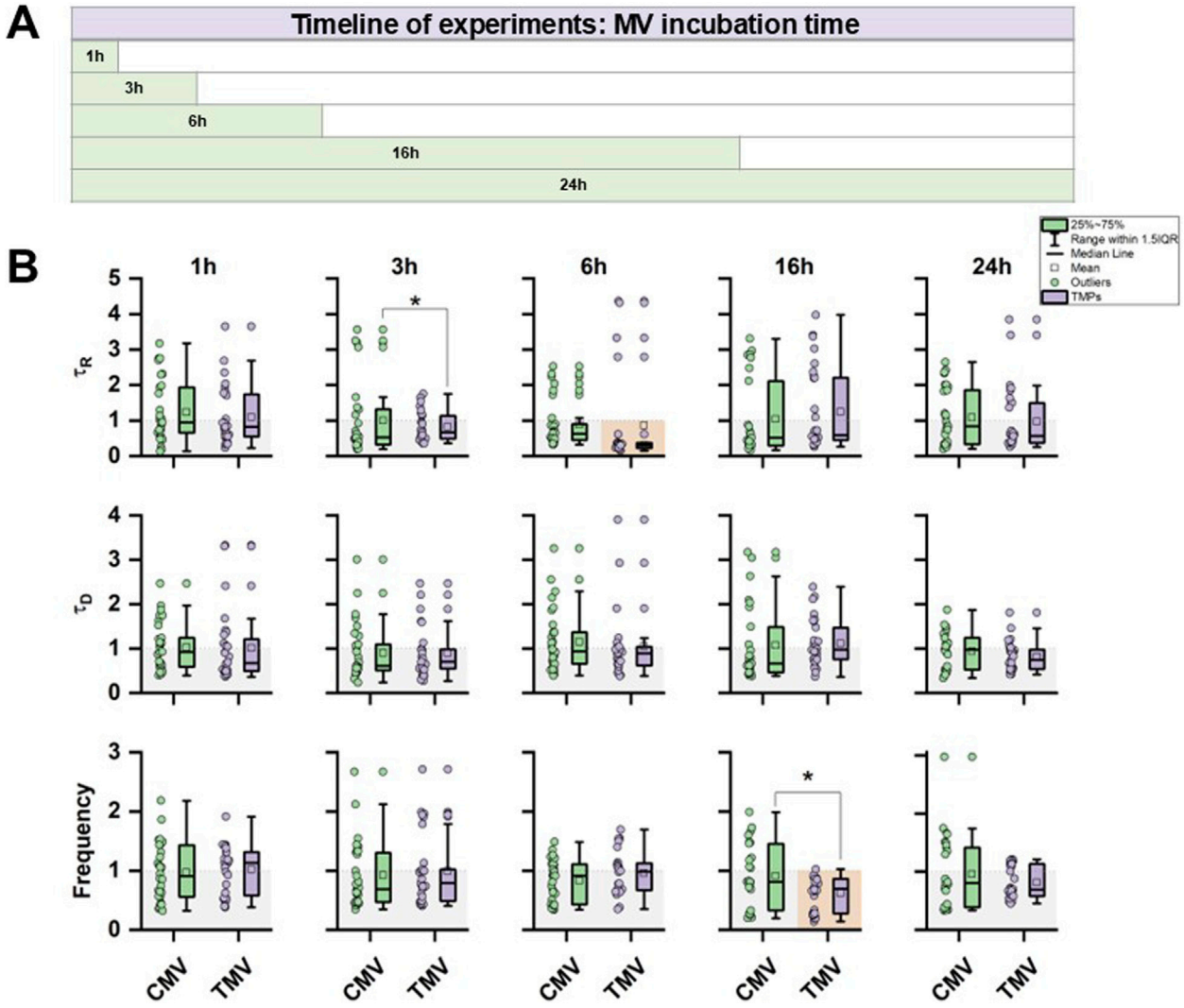

FIGURE 5
Time course of the effect of control (CMV) and TNFα-induced MV (TMV) from HPMEC on hiPSC-CM. **(A)** Protocol of the time course experiments indicating data collection after 1, 3, 6, 16, or 24 h of incubation. **(B)** Statistical summary of τ_R, τ_D, and *F* from hiPSC-CM Ca^{2+} transients from CMV and TMV treatment. Data are normalized to PBS control. Significances between CMV and TMV are indicated as * for $P < 0.05$; significances to PBS control are indicated as orange box. Experiments were repeated on three different hiPSC passages and differentiations. Each data point summarizes the average of 3 Ca^{2+} transients per cell, with a group size of 30 cells total per group.

of the systemic inflammatory response associated with sepsis, impaired endothelial function and myocardial dysfunction might arise, potentially mediated by MV.

Here, we focused on a specific subset of MV derived from HPMEC, a primary endothelial cell line that closely reflects cell function of the microvasculature. The study analyzed the effect of TNFα-derived TMV and SMV from septic patients on hiPSC-CM. As a functional readout, the temporal kinetics of Ca^{2+} transients were chosen. Ca^{2+}-induced Ca^{2+} release is the primary mechanism that bridges cardiomyocyte membrane activation (the action potential) to cell contraction [21, 22]. Therefore, influences that affect the contractility of cardiomyocytes can be reflected in changes in the release properties of this important intracellular messenger, Ca^{2+}. Particular attention was paid to the rise and decay kinetics of the Ca^{2+} transients and to the beating frequency of the cells. Despite isolated significant results in the presented data sets, the experiments revealed that TMV and SMV did not induce consistent responses in hiPSC-CM. These experiments demonstrate that MV have the potential to influence Ca^{2+} transient kinetics of hiPSC-CM, especially regarding the frequency of the Ca^{2+} release events. The upregulation of pro-apoptotic molecules and intercellular adhesion molecules were described in other cells after incubation

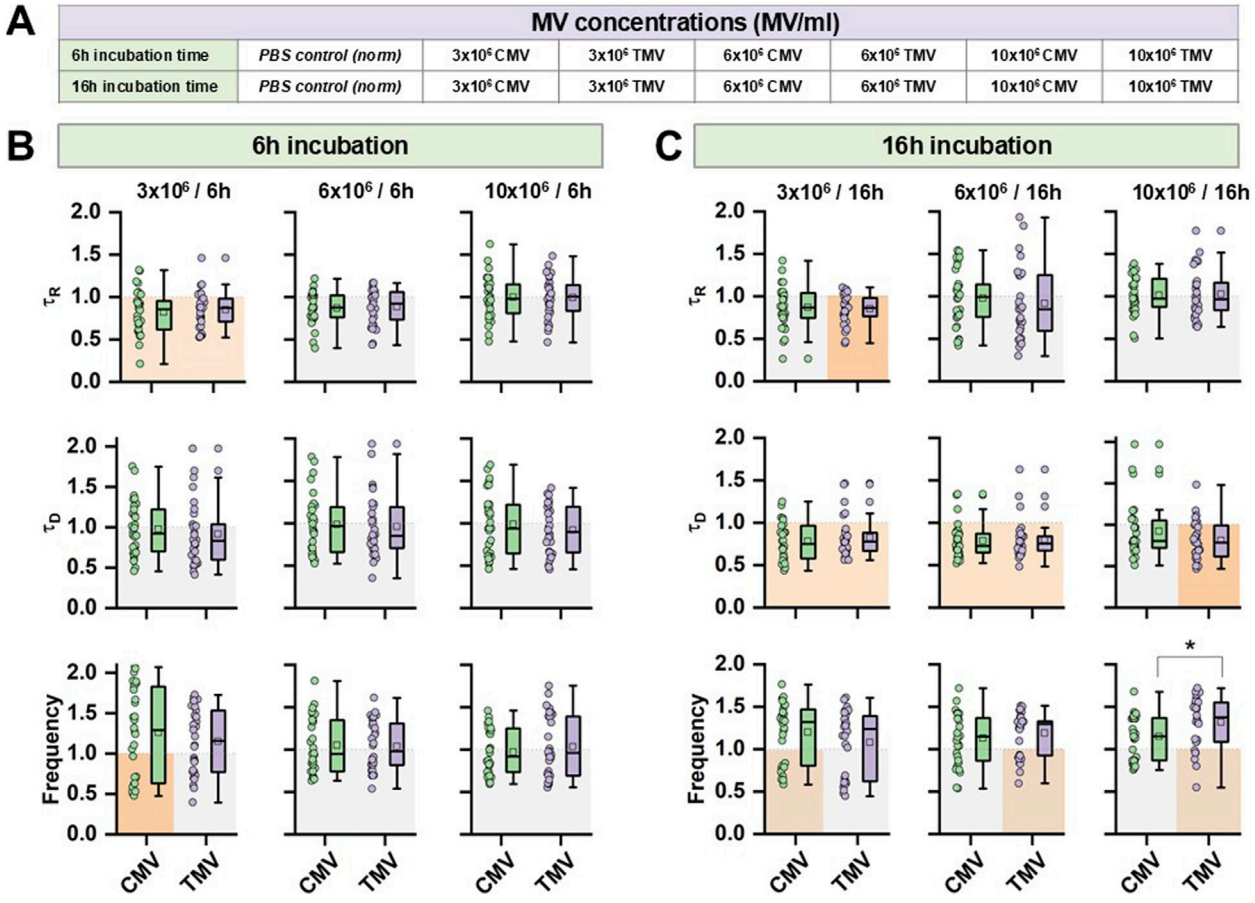

FIGURE 6
Concentration-dependence of the effect of CMV and TMV from HPMEC on hiPSC-CM relative to PBS. **(A)** Protocol of the dose-dependent experiments indicating data collection after 6 or 16 h of incubation. **(B,C)** Statistical summary of τ_R, τ_D, and *F* from hiPSC-CM Ca^{2+} transients from CMV and TMV treatment at two different time points, respectively. Data are normalized to PBS control. Significances between CMV and TMV are indicated as * for $P < 0.05$; significances to PBS control are indicated as orange box. Experiments were repeated on three different hiPSC passages and differentiations. Each data point summarizes the average of three Ca^{2+} transients per cell, with a group size of 30 cells total per group.

with TMV [21]. A similar effect might lie behind our findings. However, the high data variability, which is intrinsic to hiPSC-CM function, may mask stronger effects and impede the identification of significances.

Nevertheless, even subtle alterations in Ca^{2+} transient dynamics, such as changes in amplitude, rise time, or decay kinetics, can significantly impact EC-coupling in cardiomyocytes. Even minor changes may translate into impaired systolic contractility, delayed relaxation, and reduced Ca^{2+} reuptake efficiency, all of which are hallmarks of septic cardiomyopathy.

Moreover, disturbances in Ca^{2+} handling can promote arrhythmogenic conditions by destabilizing the membrane potential and increasing the susceptibility to afterdepolarizations. In the context of sepsis, where mitochondrial dysfunction, oxidative stress, and inflammatory mediators are abundant, such minor impairments may become functionally significant due to reduced cardiac reserve.

Another possible explanation for the high data variability could be attributed to the experimental limitations inherent in our model. While our *in vitro* model attempted to replicate constant physiological conditions, it is crucial to acknowledge that *in vitro* systems may not fully recapitulate the complex microenvironment present *in vivo*. Factors such as cell culture conditions, the purity and composition of MV preparation, and the specific characteristics of hiPSC-CM may influence the outcome of these experiments. Nevertheless, the variability in the effects of MV in the Ca^{2+} transient analyses likely reflect genuine biological heterogeneity, which is consistent with previously reported findings [23, 24].

Furthermore, the heterogeneity of the different MV populations and their diverse cargo contents add another layer of complexity to this study. Although MV used in these experiments were derived from one specific cell type, the HPMEC, future investigations may benefit from exploring

TABLE 1 The baseline characteristics of the patients.

Variable		Patients
n		16
Age, years		66.4 ± 9.6
Male sex, *n*		11
Sepsis focus	Lung	1
	Abdominal	11
	Urinary	1
Use of mechanical ventilation, *n* (%)		75
Duration of mechanical ventilation, days		4.4 ± 6.3
SOFA score D1		10.0 ± 3.4
APACHE II score D1		27.3 ± 8.0
ICU length of stay, days		5.1 ± 8.0
Hospital length of stay, days		20.7 ± 16.7
28-day hospital mortality, n (%)		12.5
MAP (mmHg)		78.2 ± 15.4
Lactate (mmol/L)		2.3 ± 1.3
PCT, ng/mL		10.0 ± 16.8
CRP, mg/L?		227.2 ± 88.5
WBC,10^{12}/L		13.7 ± 9.0

SOFA sequential organ failure assessment score, *APACHE* acute physiology and chronic health evaluation, *ICU* intensive care unit, *MAP* mean arterial pressure, *PCT* procalcitonin, *WBC* white blood cells, *CRP* c-reactive protein. Data are presented as mean ± SD or percentage (%).

a broader range of MV populations to elucidate potential functional differences. This is particularly relevant given that we observed significant differences in the number, protein content, and cargo between SMVs and TMVs. The inflammatory environment in septic patients is highly complex, involving a combination of pro-inflammatory cytokines associated with the systemic inflammatory response characteristic of sepsis (e.g., IL-1β, IL-6, TNF-α, and interferon-γ). For future experiments, it may be beneficial to use either a defined mix of these cytokines or plasma from patients in the acute phase of sepsis to better replicate the *in vivo* conditions.

Exosomes from patients with septic shock have been described to convey miRNAs and mRNAs related to pathogenic pathways, including inflammatory response, oxidative stress, and cell cycle regulation [15]. Therefore, exosomes may represent a novel mechanism for intercellular communication during sepsis. Since MV could originate from various cells affected by the pathophysiology of sepsis, their origin, activation, and the immunological state of the parent cell most likely influence the content and effects of MV. However, there is currently no clear evidence regarding quantity, cargo, and time course of MV during sepsis progression in patients. Hence, we based the concentrations used in our *in vitro* experiments ($3–10 \times 10^6$ MV/mL) on prior *in vitro* studies that demonstrated functional effects within similar concentration windows.

Additionally, the dynamic nature of intercellular communication mediated by MV warrants consideration. While our experimental setup allowed for the direct exposure of cardiomyocytes to MV, it is possible that the observed effects are transient or context-dependent.

Here, we selected the 6-h and 16-h timepoints based on a combination of practical usability, biological relevance, and protein expression kinetics in hiPSC-CM. Regarding usability and cellular viability, timepoints beyond 24 h were associated with increased cell stress and declining viability in pilot experiments, limiting the interpretability of downstream readouts. The 6–16 h window allowed us to capture early and intermediate cellular responses while preserving cell health and morphology. With respect to protein expression kinetics, our primary endpoints included markers of inflammatory response and functional proteins such as contractile elements and metabolic regulators. Previous studies, as well as our own kinetics profiling, suggest that differential protein expression in hiPSC-CM in response to inflammatory stimuli is detectable between 6- and 16-h post-exposure. The 6-h timepoint captures early signaling events and transcriptional activation, while the 16-h timepoint reflects post-transcriptional and translational outcomes relevant for phenotypic changes. While the dynamics of circulating SMV concentrations in patients vary based on the severity and phase of sepsis, elevated levels are typically sustained over several hours to days during the acute phase. Thus, exposing hiPSC-CM to SMVs for 6 and 16 h reflects clinically plausible exposure durations within this window, allowing us to model both acute-onset and sustained exposure scenarios relevant to septic cardiac dysfunction.

Long-term studies tracking the fate of MV and their effects on cardiomyocyte function over time could provide valuable insights into the temporal dynamics of MV-mediated signaling. A key limitation of this study is the exclusive use of hiPSC-derived cardiomyocytes (hiPSC-CMs), which, despite their relevance as a human-based model, do not fully recapitulate the structural complexity, cellular heterogeneity, and long-term remodeling responses of native cardiac tissue. In particular, the absence of multicellular interactions, vascularization, and tissue-level organization may limit the translational applicability of our findings. Future studies will incorporate more complex model systems such as cardiac organoids, engineered heart tissues, or *in vivo* models to validate and extend these results under more physiologically relevant conditions. In addition, longitudinal studies will be essential to assess the durability and adaptive nature of the observed responses over time.

Our findings that Ang-2 is present in all MV preparations analyzed confirm their endothelial origin. Given the established

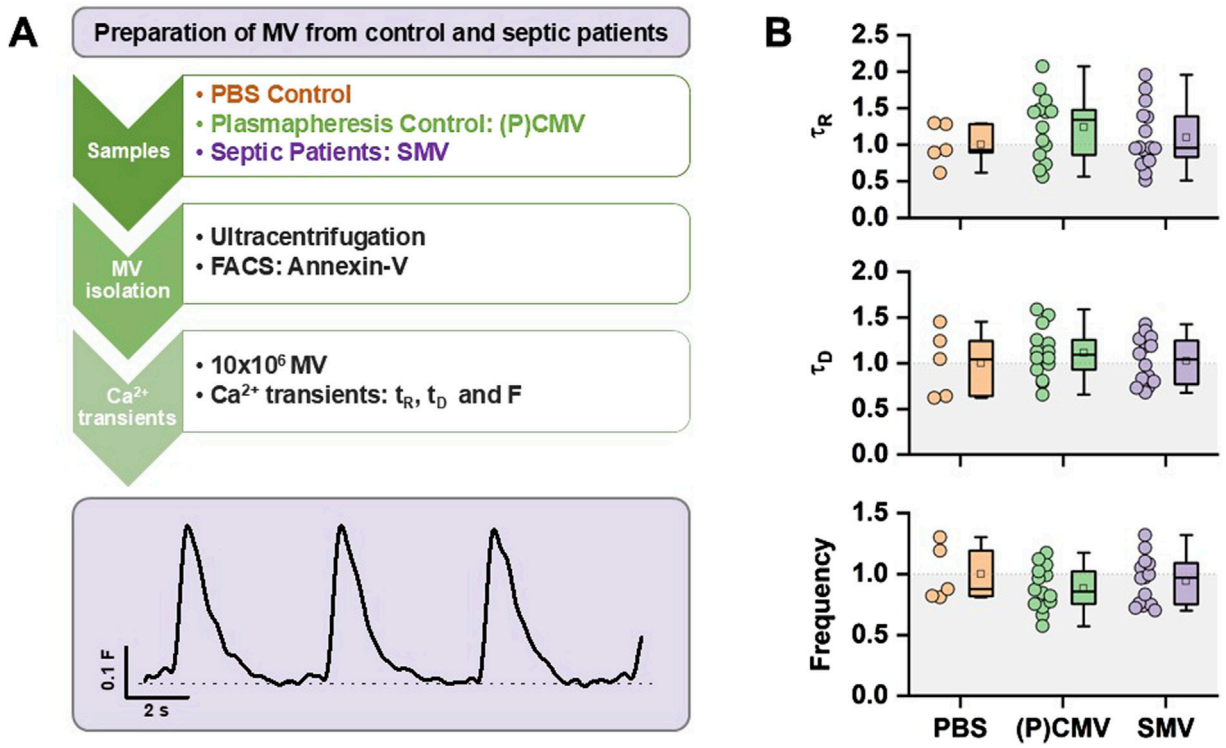

FIGURE 7
Effect of septic MV from patients on hiPSC-CM. **(A)** Strategy of experimental setup. hiPSC-CM were incubated for 16 h with MV before analysis of Ca^{2+} transients. **(B)** Statistical summary of τ_R, τ_D, and *F* from hiPSC-CM Ca^{2+} transients from PBS, (P)CMV, and SMV treatment. Data are normalized to PBS control. Experiments were carried out from one hiPSC passage and differentiation. Each data point summarizes the average of 3 Ca^{2+} transients per cell, with a group size of five (PBS), 14 ((P)CMV)), and 16 (SMV) cells total per group.

role of Ang-2 in endothelial activation and vascular permeability, its presence in MV could contribute to the propagation of endothelial dysfunction in inflammatory or septic conditions. As Ang-2 is known to destabilize endothelial junctions, promote vascular leakage, and amplify inflammation, it may indirectly impair cardiomyocyte oxygenation, survival, and function via endothelial dysfunction. In line with the findings of Chatterjee et al, we also found TNFα to induce the production of MVs that express markers of cell injury or activation in endothelial cells [25]. We would have also expected the MV from septic patients to express ICAM-1 and VCAM-1 as these are typical for proinflammatory signaling, immune cell recruitment, and inflammation. Although ICAM-1 and VCAM-1 are well-known markers of endothelial activation and play central roles in leukocyte adhesion and inflammation, their absence in MV derived from septic patients may reflect a selective packaging mechanism that favors the inclusion of intracellular or membrane-associated proteins involved in vesicle formation, signaling, or stress response—rather than classical surface adhesion molecules.

Additionally, shedding of MV may occur from endothelial regions or cellular compartments where ICAM-1 and VCAM-1 are either not highly expressed or are retained on the parent cell surface to fulfill their adhesion functions. It is also possible that under the conditions of severe systemic inflammation, proteolytic cleavage or internalization of these molecules limits their availability for incorporation into vesicles.

Finally, MV cargo composition may be influenced by disease stage, cytokine milieu, or oxidative stress, leading to altered protein sorting that deprioritizes adhesion molecules in favor of other proinflammatory mediators (e.g., cytokines, danger signals, or coagulation-related proteins).

Further identification of the content and the effect of MV on the heart cells will provide important information for the use of MV for diagnostic and therapeutic purposes. Both the content and the membranes can be engineered independently and thus be used for different purposes and applications [9].

In conclusion, while our study did not reveal any consistent impact of MV on cardiomyocyte contractility under most of the conditions tested, it is essential to recognize the complexity of intercellular communication mediated by MV. Further investigations incorporating refined experimental models, diverse MV populations, and longitudinal analyses are warranted to fully elucidate the role

of MV in modulating cardiac function, especially during sepsis. These efforts will contribute to a deeper understanding of MV biology and may uncover novel therapeutic avenues for septic cardiomyopathy.

Author contributions

DF and NU designed the study protocol. MS, JS, AT, and LT performed data collection and experiments. DF, NU, MS, JS, and AT analyzed the data. DF, NU, SM, JS, AT, CM, SD, NG, MD, AH, TL, and MW interpreted data and drafted the manuscript. All authors contributed to the article and approved the submitted version.

Data availability

The original contributions presented in the study are included in the article/Supplementary Material, further inquiries can be directed to the corresponding author.

Ethics statement

Ethical approval for this study (reference number S-664/2020) was provided by the Ethical Committee of the Medical Faculty of Heidelberg University. The study was registered at the German Clinical Trial Register (DRKS00023301). The studies were conducted in accordance with the local legislation and institutional requirements. The participants provided their written informed consent to participate in this study.

Funding

The author(s) declare that financial support was received for the research and/or publication of this article. This work was supported by departmental resources and by the German Research Foundation (DFG, UL 466/2-1 to NU).

Acknowledgments

We would like to express our sincere gratitude to all the patients who participated in this study. The authors wish to thank M. Höfer for her expertise in stem cell culture and differentiation techniques.

Conflict of interest

The author(s) declared no potential conflicts of interest with respect to the research, authorship, and/or publication of this article.

Generative AI statement

The author(s) declare that no Generative AI was used in the creation of this manuscript.

Supplementary material

The Supplementary Material for this article can be found online at: https://www.ebm-journal.org/articles/10.3389/ebm.2025.10461/full#supplementary-material

References

1. Parker MM, Shelhamer JH, Bacharach SL, Green MV, Natanson C, Frederick TM, et al. Profound but reversible myocardial depression in patients with septic shock. *Ann Intern Med* (1984) **100**(4):483–90. doi:10.7326/0003-4819-100-4-483

2. Ehrman RR, Sullivan AN, Favot MJ, Sherwin RL, Reynolds CA, Abidov A, et al. Pathophysiology, echocardiographic evaluation, biomarker findings, and prognostic implications of septic cardiomyopathy: a review of the literature. *Crit Care* (2018) **22**(1):112. doi:10.1186/s13054-018-2043-8

3. Lin H, Wang W, Lee M, Meng Q, Ren H. Current status of septic cardiomyopathy: basic science and clinical progress. *Front Pharmacol* (2020) **11**: 210. doi:10.3389/fphar.2020.00210

4. Reid VL, Webster NR. Role of microparticles in sepsis. *Br J Anaesth* (2012) **109**(4):503–13. doi:10.1093/bja/aes321

5. Terrasini N, Lionetti V. Exosomes in critical illness. *Crit Care Med* (2017) **45**(6):1054–60. doi:10.1097/ccm.0000000000002328

6. Weber B, Henrich D, Hildebrand F, Marzi I, Leppik L. The roles of extracellular vesicles in sepsis and systemic inflammatory response syndrome. *Shock* (2023) **59**(2):161–72. doi:10.1097/shk.0000000000002010

7. Hashemian SM, Pourhanifeh MH, Fadaei S, Velayati AA, Mirzaei H, Hamblin MR. Non-coding RNAs and exosomes: their role in the pathogenesis of sepsis. *Mol Ther Nucleic Acids* (2020) **21**:51–74. doi:10.1016/j.omtn.2020.05.012

8. Ginini L, Billan S, Fridman E, Gil Z. Insight into extracellular vesicle-cell communication: from cell recognition to intracellular fate. *Cells* (2022) **11**(9):1375. doi:10.3390/cells11091375

9. Kao CY, Papoutsakis ET. Extracellular vesicles: exosomes, microparticles, their parts, and their targets to enable their biomanufacturing and clinical applications. *Curr Opin Biotechnol* (2019) **60**:89–98. doi:10.1016/j.copbio.2019.01.005

10. Azevedo LC, Janiszewski M, Pontieri V, Pedro MA, Bassi E, Tucci PJF, et al. Platelet-derived exosomes from septic shock patients induce myocardial dysfunction. *Crit Care* (2007) **11**(6):R120. doi:10.1186/cc6176

11. Mortaza S, Martinez MC, Baron-Menguy C, Burban M, de la Bourdonnaye M, Fizanne L, et al. Detrimental hemodynamic and inflammatory effects of microparticles originating from septic rats. *Crit Care Med* (2009) **37**(6):2045–50. doi:10.1097/ccm.0b013e3181a00629

12. Zhang Q, Shang M, Zhang M, Wang Y, Chen Y, Wu Y, et al. Microvesicles derived from hypoxia/reoxygenation-treated human umbilical vein endothelial cells promote apoptosis and oxidative stress in H9c2 cardiomyocytes. *BMC Cell Biol* (2016) **17**(1):25. doi:10.1186/s12860-016-0100-1

13. Zhang S, Yin Y, Li C, Zhao Y, Wang Q, Zhang X. PAK4 suppresses TNF-induced release of endothelial microparticles in HUVECs cells. *Aging (Albany NY)* (2020) **12**(13):12740–9. doi:10.18632/aging.103173

14. Liu Y, Zhang R, Qu H, Wu J, Li L, Tang Y. Endothelial microparticles activate endothelial cells to facilitate the inflammatory response. *Mol Med Rep* (2017) **15**(3): 1291–6. doi:10.3892/mmr.2017.6113

15. Real JM, Ferreira LRP, Esteves GH, Koyama FC, Dias MVS, Bezerra-Neto JE, et al. Exosomes from patients with septic shock convey miRNAs related to inflammation and cell cycle regulation: new signaling pathways in sepsis? *Crit Care* (2018) **22**(1):68. doi:10.1186/s13054-018-2003-3

16. Ye R, Lin Q, Xiao W, Mao L, Zhang P, Zhou L, et al. miR-150-5p in neutrophil-derived extracellular vesicles associated with sepsis-induced cardiomyopathy in septic patients. *Cell Death Discov* (2023) **9**(1):19. doi:10.1038/s41420-023-01328-x

17. Rossler U, Hennig AF, Stelzer N, Bose S, Kopp J, Søe K, et al. Efficient generation of osteoclasts from human induced pluripotent stem cells and functional investigations of lethal CLCN7-related osteopetrosis. *J Bone Mineral Res* (2021) **36**(8):1621–35. doi:10.1002/jbmr.4322

18. Zhao M, Tang Y, Zhou Y, Zhang J. Deciphering role of Wnt signalling in cardiac mesoderm and cardiomyocyte differentiation from human iPSCs: four-dimensional control of Wnt pathway for hiPSC-CMs differentiation. *Sci Rep* (2019) **9**(1):19389. doi:10.1038/s41598-019-55620-x

19. Singer M, Deutschman CS, Seymour CW, Shankar-Hari M, Annane D, Bauer M, et al. The third international consensus definitions for sepsis and septic shock (Sepsis-3). *JAMA* (2016) **315**(8):801–10. doi:10.1001/jama.2016.0287

20. Lajqi T, Köstlin-Gille N, Hillmer S, Braun M, Kranig SA, Dietz S, et al. Gut microbiota-derived small extracellular vesicles endorse memory-like inflammatory responses in murine neutrophils. *Biomedicines* (2022) **10**(2):442. doi:10.3390/biomedicines10020442

21. Lee SK, Yang SH, Kwon I, Lee OH, Heo JH. Role of tumour necrosis factor receptor-1 and nuclear factor-κB in production of TNF-α-induced pro-inflammatory microparticles in endothelial cells. *Thromb Haemost* (2014) **112**(3):580–8. doi:10.1160/th13-11-0975

22. Bers DM. Cardiac excitation-contraction coupling. *Nature* (2002) **415**(6868): 198–205. doi:10.1038/415198a

23. Kermani F, Mosqueira M, Peters K, Lemma ED, Rapti K, Grimm D, et al. Membrane remodelling triggers maturation of excitation-contraction coupling in 3D-shaped human-induced pluripotent stem cell-derived cardiomyocytes. *Basic Res Cardiol* (2023) **118**(1):13. doi:10.1007/s00395-023-00984-5

24. Silbernagel N, Körner A, Balitzki J, Jaggy M, Bertels S, Richter B, et al. Shaping the heart: structural and functional maturation of iPSC-cardiomyocytes in 3D-micro-scaffolds. *Biomaterials* (2020) **227**:119551. doi:10.1016/j.biomaterials.2019.119551

25. Chatterjee V, Yang X, Ma Y, Cha B, Meegan JE, Wu M, et al. Endothelial microvesicles carrying Src-rich cargo impair adherens junction integrity and cytoskeleton homeostasis. *Cardiovasc Res* (2020) **116**(8):1525–38. doi:10.1093/cvr/cvz238

EBM Experimental Biology and Medicine

TYPE Original Research
PUBLISHED 22 September 2025
DOI 10.3389/ebm.2025.10489

OPEN ACCESS

*CORRESPONDENCE
Yun Yang,
zazhibinpai01@111.com

RECEIVED 02 January 2025
ACCEPTED 16 June 2025
PUBLISHED 22 September 2025

CITATION
Chen L and Yang Y (2025) Variational autoencoder enhanced analysis of energy metabolism and autophagy in exercising cardiomyocytes.
Exp. Biol. Med. 250:10489.
doi: 10.3389/ebm.2025.10489

Variational autoencoder enhanced analysis of energy metabolism and autophagy in exercising cardiomyocytes

Liquan Chen[1] and Yun Yang[2]*

[1]School of Culture and Tourism, Quzhou College of Technology, Quzhou, Zhejiang, China, [2]College of Physical Education, Henan Normal University, Xinxiang, China

Abstract

Autophagy of myocardial cells involves the interaction of multiple molecular signaling pathways, and regulatory factors, while existing methods are difficult to handle. This study utilized the variational autoencoder (VAE) model to reveal the characteristic distribution of myocardial cell energy autophagy under different exercise conditions. First, this paper is based on mass spectrometry analysis, enzyme-linked immunosorbent assay ELISA (Enzyme-Linked Immunosorbent Assay) to determine the cardiomyocyte metabolite concentration data, and RNA-Seq (Ribonucleic Acid-Sequencing) to collect genes related to cardiomyocyte energy metabolism and autophagy expression data; in the VAE model, this paper utilizes the full connectivity layer to encode the data into potential representations, and reconstructs the numerical data through the numerical data decoder. The loss function is defined as the data reconstruction error and KL (Kullback-Leibler) scatter, and Adam is used to optimize the training process; the features are analyzed and the classification performance is verified under different motion conditions based on RF (Random Forest); the relationship between the features and metabolite concentration and gene expression is analyzed by LASSO (Least Absolute Shrinkage and Selection Operator) regression model to analyze the relationship between features and metabolite concentration and gene expression; the features in the latent space are downscaled using t-SNE (t-distributed Stochastic Neighbor Embedding) to visualize the feature distribution; finally, CRISPR-Cas9 (Clustered Regularly Interspaced Short Palindromic Repeats-Cas9) knockdown experiments to reveal the importance of AMPK, PGC1A, CPT1B, and SIRT1 in cardiomyocyte autophagy and energy metabolism, which provide potential targets for future gene-based therapies.

KEYWORDS

myocardial cell, energy autophagy, variational autoencoder, metabolite concentration, gene expression, feature extraction and analysis

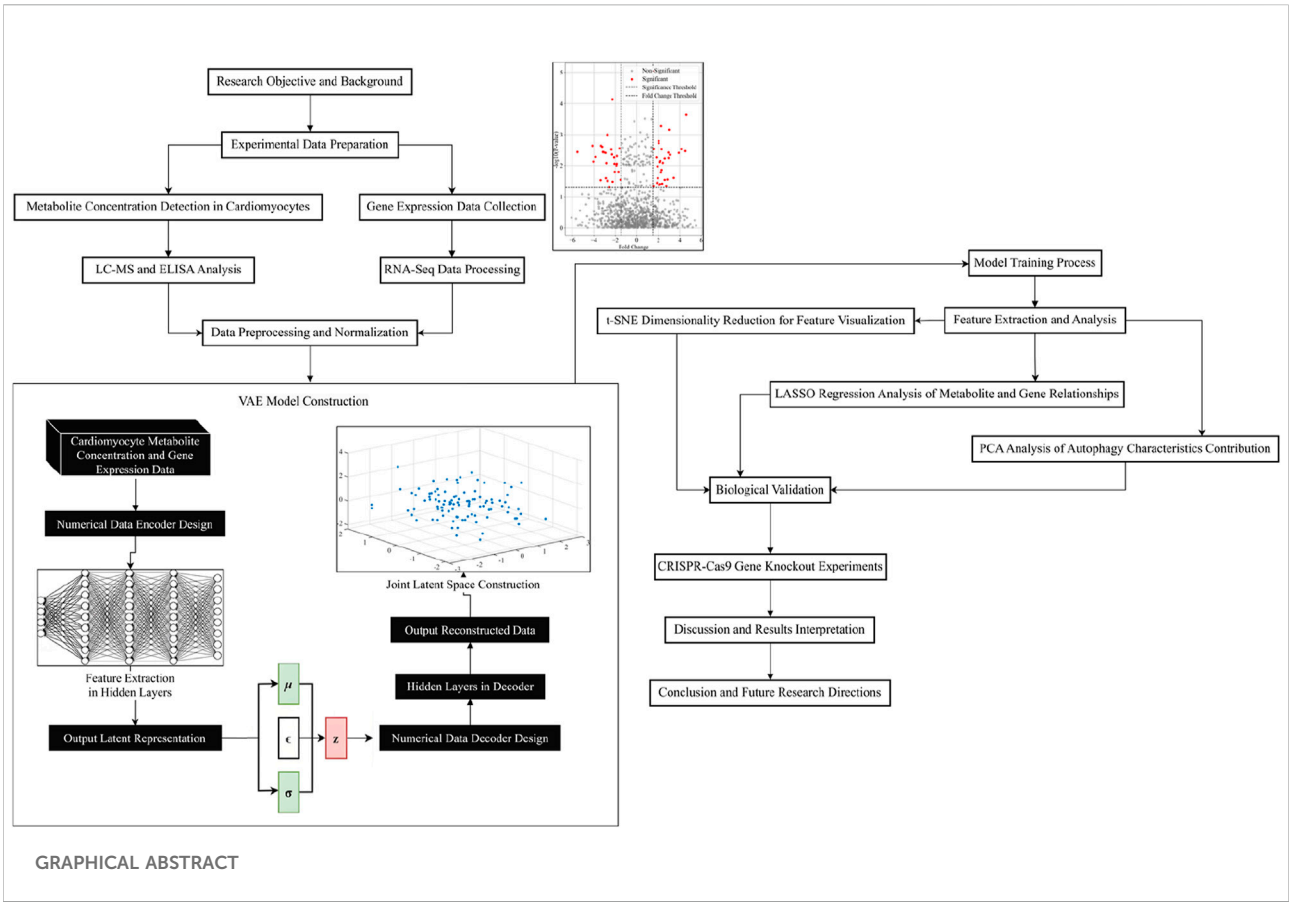

GRAPHICAL ABSTRACT

Impact statement

This study advances our understanding of myocardial cell energy metabolism and autophagy, particularly under different exercise conditions. Using advanced technologies such as RNA sequencing, mass spectrometry, and machine learning models, the research identifies key molecular regulators involved in energy metabolism and autophagy, such as AMPK, PGC1A, CPT1B, and SIRT1. These findings provide new insights into how these factors interact to support cardiac function and reveal the importance of autophagy in maintaining heart cell health. By combining experimental and computational approaches, this work offers a deeper understanding of the regulatory networks that govern heart cell energy balance, which is crucial for developing targeted therapies for heart diseases. The results suggest that manipulating these key regulators could offer new therapeutic strategies for treating cardiovascular conditions, thereby making a significant contribution to the field of cardiovascular research and providing potential pathways for gene-based treatments.

Introduction

Energy autophagy in cardiomyocytes is a complex and important biological process that plays a key role in maintaining cardiomyocyte function and responding to metabolic stress. Energy autophagy ensures normal cellular function by degrading and reusing damaged or excess intracellular components [1, 2]. The process involves the interaction of multiple molecular signaling pathways and regulatory factors [3, 4], and is particularly important in the pathogenesis of several cardiovascular diseases [5, 6]. Due to the high-dimensional complexity of the energy autophagy process, traditional research methods face many challenges in resolving its dynamic features and mechanisms [7, 8]. The development of new methods capable of handling high-dimensional data and revealing complex biological processes is of great research significance and practical value.

Nowadays, there are extensive studies in cardiomyocyte energy autophagy. In 2020, Fan Jiamao [9] et al. investigated the metabolite changes in cardiomyocytes under different metabolic stresses by enzyme-linked immunosorbent assay. However, this approach can only deal with data under a single dimension and cannot fully integrate and parse the complex interactions in multidimensional data [10, 11]. Meanwhile, traditional methods have certain limitations in data processing and feature extraction efficiency [12, 13]: although mass spectrometry analysis can provide detailed metabolite information, it is less efficient in dealing with

complex datasets with large data volume and high dimensionality [14, 15]. In 2022, Wu Xun [16] et al. attempted to introduce SVM (Support Vector Machine) model to analyze metabolic data, and although some progress had been made, it was still deficient in the generalization and accuracy of high-dimensional data. Most of the past studies were limited to single-dimensional data analysis, which could not fully reveal the interactions between multidimensional data during cardiomyocyte energy autophagy, and were obviously insufficient for a comprehensive understanding of the complex mechanisms of the process.

To overcome the challenge of high dimensionality of data, in recent years, researchers have begun to explore the use of deep learning techniques to process and analyze complex biological data. Oriented towards the molecular mechanisms behind basic mitochondrial autophagy, Godtliebsen Gustav [17] et al. demonstrated that OXPHOS (oxidative phosphorylation) induction leaded to an increase in mitochondrial fragmentation through deep learning techniques. Evaluating cardiomyocytes from 289 childhood cancer survivors, Chaix Marie-A [18] et al. developed a risk prediction model incorporating genetic and clinical predictors using RF. Using deep learning for simulation analysis and *in vivo* validation, Iborra-Egea Oriol [19] et al. revealed the mechanism of action of Empagliflozin in Heart Failure with Reduced Ejection Fraction (HFrEF). In 2024, Liu Shuhui [20] et al. successfully extracted and analyzed the metabolic features of cancer cells using the VAE model, demonstrating the powerful ability of VAE in handling high-dimensional data. By encoding high-dimensional data into low-dimensional latent representations [21] and reconstructing the data through a decoder [22], the model effectively captures the main features and complex interactions in the data [23, 24]. The methods are able to discover hidden patterns and structures in the latent space while dealing with high-dimensional data [25, 26], effectively avoiding the complexity of directly dealing with high-dimensional data by means of low-dimensional representations of the latent space in order to capture the main features of the data [27, 28], and have obvious advantages in dealing with the nonlinear relationships and complex structures of the data [29, 30]. However, the application of VAE in cardiomyocyte energy autophagy characterization and analysis is still relatively rare until now, and further research and validation are urgently needed.

The application of VAE in extracting energy-autophagy features of myocardial cells offers unique advantages over PCA, UMAP, or standard autoencoders. One of the core features of VAE is its probabilistic encoding capability, which introduces a probability distribution in the latent space. This allows VAE not only to learn low-dimensional representations of the data but also to capture the uncertainty inherent in the data. Given that biological processes involve highly dynamic and nonlinear molecular interaction networks, the data often contain noise and heterogeneity. Through probabilistic encoding, VAE can generate smooth distributions in the latent space, thereby better reflecting the complex relationships between metabolite concentrations and gene expression.

Compared with traditional dimensionality reduction methods like PCA, VAE is capable of capturing nonlinear relationships, whereas PCA is limited to linear transformations. The energy metabolism and autophagy processes of myocardial cells involve multiple nonlinear regulatory pathways (such as interactions among AMPK, PGC1A, CPT1B, and SIRT1), making VAE more suitable for uncovering these intricate relationships. Unlike UMAP or t-SNE, which focus primarily on visualization, VAE can not only reduce dimensionality but also reconstruct the original data through its decoder, thereby validating the effectiveness of the latent features. While standard autoencoders can also perform nonlinear dimensionality reduction, they lack the probabilistic constraints of VAE, potentially leading to discontinuities in the latent space, which can affect the stability of subsequent analyses.

The aim of this paper is to extract and analyze the energy autophagy characteristics of cardiomyocytes under exercise conditions using the VAE model. Sixty healthy mice were selected and randomly divided into six groups, and the experimental groups were subjected to different types of exercise interventions, including resting condition, low-intensity exercise, moderate-intensity exercise, high-intensity exercise, prolonged low-intensity exercise, and intermittent high-intensity exercise. At the end of the exercise intervention, cardiomyocytes were isolated and extracted, metabolites were detected using LC-MS and ELISA, and gene expression analysis was performed. Cardiomyocyte metabolite concentrations and gene expression data were processed using the VAE model, and features were extracted and mapped to a low-dimensional potential space. The overall features of cardiomyocytes under different exercise intensities were found to be significantly different by t-SNE downscaling analysis. The distribution of features was more concentrated in the resting state and low-intensity exercise, while the features were more dispersed in the moderate- and high-intensity exercise groups, suggesting that high-intensity exercise triggered more metabolic pathways and intracellular state variability. The LASSO regression model further showed a strong relationship between exercise conditions and metabolite concentration and gene expression. The contribution of cardiomyocyte autophagy characteristics was analyzed using PCA (Principal Component Analysis), and gene knockout experiments were performed using CRISPR-Cas9 technology to observe the effect of specific genes on cardiomyocyte energy autophagy.

Materials and methods

Description of experimental data

To obtain cardiomyocyte data in this study, 60 healthy mice, half male and half female, weighing between 20 and 25 g were selected. The mice were randomly divided into 6 groups of

10 mice each and grouped according to exercise conditions as follows A-F:

A. Resting state group: no exercise intervention.
B. Low-intensity exercise group: mice ran on a low-speed rotor for 30 min.
C. Medium intensity exercise group: mice ran on a medium speed rotor for 45 min.
D. High-intensity exercise group: mice are subjected to high-intensity interval training, which consist of alternating short bursts of high-velocity running and resting for 20 min.
E. Prolonged low-intensity exercise group: mice ran continuously for 90 min on a low-speed rotor.
F. Intermittent high-intensity exercise group: mice are subjected to high-intensity interval training, with each cycle consisting of 4 min of high-intensity running and 2 min of low-intensity slow walking, lasting a total of 24 min.

Measurement of cardiomyocyte metabolite concentration data

Immediately after the end of the exercise intervention, the mice were euthanized to ensure tissue sample activity. Mouse hearts were rapidly collected for cardiomyocyte isolation and extraction. Cardiomyocytes were washed with saline to remove blood and other impurities, cell samples were rapidly frozen by liquid nitrogen and stored in a refrigerator at −80°C to ensure that the samples did not degrade. The frozen cardiomyocyte samples were thawed to 4°C, and metabolite extraction was performed by adding a solvent mixture of methanol/water/chloroform (2:2:1), vortexing, centrifuging the supernatant, and collecting the metabolite extracts to avoid interference from cellular debris.

The extracted metabolites were concentrated and dried and redissolved in 50% aqueous methanol solution. The different types of metabolites were detected separately by positive and negative ion mode using Liquid Chromatography-Mass Spectrometry (LC-MS). The mass spectrometry data were acquired into a computer, and peak detection, peak alignment and normalization were performed using the mass spectrometry data processing software MetaboAnalyst to obtain the relative concentration data of the metabolites.

At the same time, pre-treatment and sample preparation based on ELISA were performed: a series of standard samples with different concentrations were prepared for the establishment of concentration standard curves of metabolites, and cardiomyocyte samples and standard samples were loaded into the wells of ELISA plates pre-coated with antigens, respectively. Specific enzyme-labeled antibodies were added to bind to the antigen and washes were performed to remove non-specific binding material. Substrate was added to produce a color reaction and absorbance was measured using an enzyme marker to determine metabolite concentration.

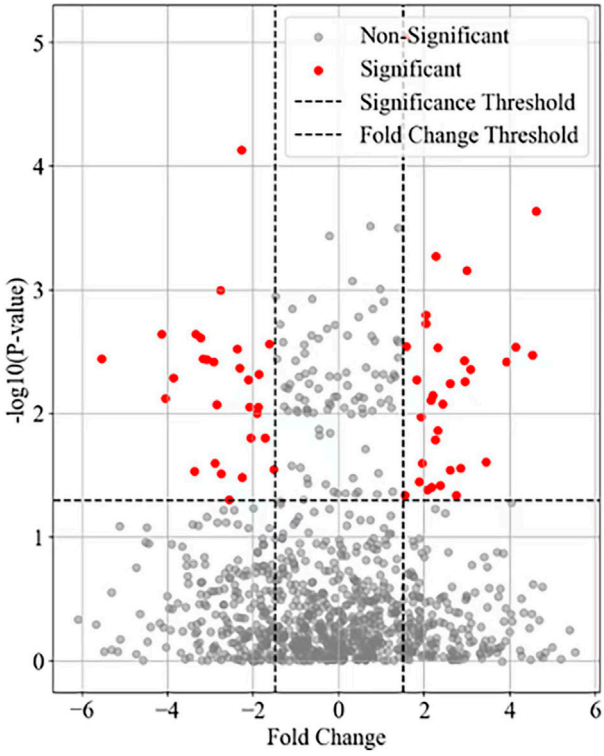

FIGURE 1
Differential expression of autophagy related genes in myocardial cells.

Cardiomyocyte energy metabolism, autophagy-related gene expression data Collection

The same cardiomyocyte samples were collected as those for metabolite analysis, and total RNA was extracted using TRIzol reagent to ensure the integrity and purity of the RNA samples, and the concentration and quality of the RNA were assessed using NanoDrop and Bioanalyzer (RNA Integrity Number >7).

Ribosomal RNA from total RNA was removed using the rRNA (Ribosomal RNA) Removal Kit to obtain mRNA (Messenger RNA). Using the mRNA-Seq (Messenger RNA Sequencing) Library Construction Kit to reverse transcribe the mRNA into cDNA (Complementary DNA), which was fragmented, spliced, and amplified by PCR (Polymerase Chain Reaction) to construct an RNA-Seq sequencing library.

The constructed RNA-Seq library was sent to NovaSeq, a high-throughput sequencing platform, for sequencing. The raw data obtained from sequencing was collected and quality

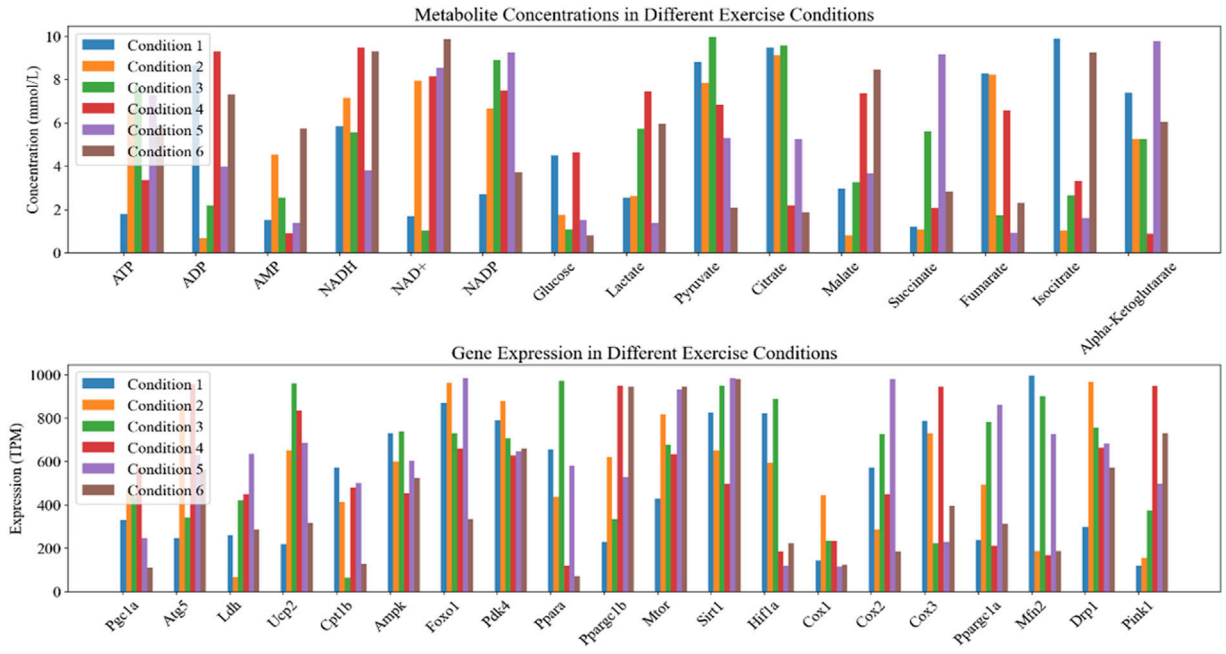

FIGURE 2
Statistics of changes in metabolic product concentration and gene expression in myocardial cells.

controlled using FastQC (Fast Quality Control) to remove low-quality reads and splice contamination.

High-quality sequencing reads were compared to the reference genome based on HISAT2 (Hierarchical Indexing for Spliced Alignment of Transcripts 2), and the results were quantified using FeatureCounts comparisons to get the read counts for each gene, which DESeq2 normalized to normalization to obtain the expression TPM of each gene under different exercise conditions.

The research design divided 60 mice into 6 groups (a resting state group and 5 exercise intervention groups), detected the gene expression data of myocardial cells in each group through RNA-Seq technology, and used a volcano plot to visualize the differentially expressed genes between each experimental group (Groups B-F) and the resting group (Group A). The results of visualizing the gene variance analysis based on the volcano map are shown in Figure 1.

The horizontal axis in Figure 1 represents Fold Change, while the vertical axis represents the negative logarithmic value of statistical significance (- log10 (P-value)). Each data point represents a gene, and the fold-change and significance P-value of the data points are measures of difference. Top20 genes were selected as the focus of the study. The mean values of metabolite concentrations and gene expression changes in mouse cardiomyocytes under the corresponding experimental groups are shown in Figure 2.

In Figure 2, Condition 1-6 corresponds to experimental groups A-F. The upper graph demonstrates the changes of metabolite concentrations under different exercise conditions, the horizontal axis indicates different metabolites, and the vertical axis indicates product concentrations (unit: mmol/L). The lower graph shows the changes of gene expression under different exercise conditions, the horizontal axis indicates different genes, and the vertical axis indicates gene expression (unit: TPM/Transcripts Per Million).

Among them ATP, ADP, AMP are the core molecules of intracellular energy metabolism [31, 32]. NADH, NAD+, NADP are important coenzymes in redox reactions and energy metabolism [33]. Glucose, Lactate, Pyruvate are the key products of glucose metabolism, which are associated with the provision of energy supply by cardiomyocytes [34]. Citrate, Malate, Succinate, Fumarate, Isocitrate, Alpha-Ketoglutarate are key intermediates in the citric acid cycle and are involved in energy production and metabolic pathways [35]. Among the gene expression types, genes such as Pgc1a, Atg5, Ldh, Ucp2, Cpt1b, Ampk, Foxo1, Pdk4, Ppara, Ppargc1b, Mtor, Sirt1, and Hif1a are associated with the processes of energy metabolism, autophagy, and oxidative stress. Cox1, Cox2, Cox3, Mfn2, Drp1, Pink1 and other genes are involved in mitochondrial function, apoptosis and mitochondrial dynamics processes [36, 37].

Genes such as AMPK, PGC1A, CPT1B, and SIRT1 play central regulatory roles in cellular metabolism and autophagy mechanisms. They interact through complex signaling networks

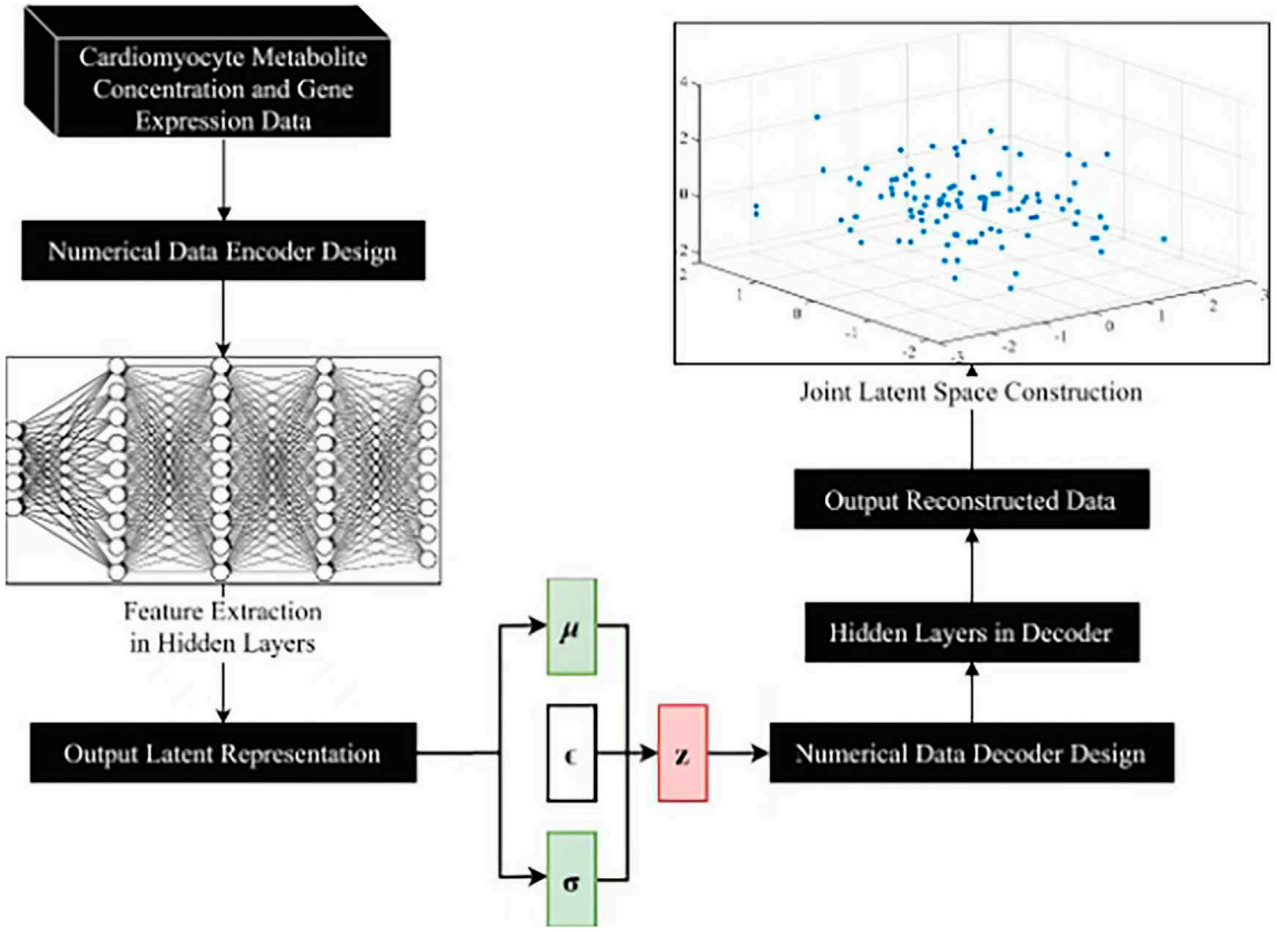

FIGURE 3
VAE model design.

to collectively maintain energy homeostasis and autophagic balance in cardiomyocytes. AMPK acts as a cellular energy sensor, becoming activated when ATP levels decrease. It promotes catabolic pathways (such as fatty acid oxidation and glycolysis) by phosphorylating downstream targets to restore energy supply while inhibiting anabolic processes. Additionally, AMPK can directly or indirectly regulate the expression of autophagy-related genes (e.g., Atg5), thereby enhancing autophagic activity to respond to energy crises. PGC1A is a key regulator of mitochondrial biogenesis and function, working synergistically with various transcription factors (e.g., Ppara and Foxo1) to modulate the expression of genes associated with fatty acid oxidation, the electron transport chain, and oxidative phosphorylation, such as Cox1, Cox2, and Cpt1b, optimizing the energy production efficiency of cardiomyocytes. CPT1B is the rate-limiting enzyme for long-chain fatty acids entering mitochondria for β-oxidation, whose expression is regulated by PGC1A and Ppara, directly influencing the ability of cardiomyocytes to utilize fatty acids. SIRT1 is an NAD+-dependent deacetylase that senses changes in the intracellular NAD+/NADH ratio to regulate downstream target genes closely related to energy metabolism and autophagy (e.g., Pgc1a and Foxo1). Under stress conditions, it enhances autophagy pathway activity through deacetylation modifications. These genes not only play critical roles in their respective functional modules but also form tightly interconnected networks through cross-regulation. For example, AMPK can activate SIRT1 activity, while SIRT1 can reciprocally regulate the AMPK signaling pathway. This bidirectional feedback mechanism ensures the adaptive response capability of cardiomyocytes under different exercise conditions.

VAE model construction

The overall design for the VAE model is shown in Figure 3. The numerical data encoder receives cardiomyocyte metabolite concentration data and gene expression data as input. The

features are gradually extracted through multiple fully connected layers to capture the complex correlations of the data and map the input data into a low-dimensional joint potential space. A symmetric decoder structure is designed to match the encoder to accurately reconstruct the original data, and the decoder parameters are optimized by back propagation algorithm to minimize the reconstruction error.

Before inputting high-dimensional omics data into the VAE model, preprocessing of transcriptomic and metabolomic data was performed to ensure data quality and compatibility for subsequent analyses. In this study, a logarithmic transformation was applied to the metabolite concentration data to mitigate the impact of its skewed distribution, which commonly occurs in metabolomic datasets due to the wide dynamic range of metabolite concentrations. This transformation not only stabilizes the data variance but also reduces the dominance of highly abundant metabolites, resulting in a more balanced representation of the data. For the gene expression data, z-score normalization was used to standardize the expression values across different genes.

To correct for batch effects, the widely used empirical Bayes framework, ComBat was employed. This method adjusts for batch-specific biases while preserving biological variability, thereby enhancing the reliability and reproducibility of downstream analyses. Additionally, statistical methods such as principal component analysis (PCA) and hierarchical clustering were utilized for outlier detection to identify and exclude samples that deviate significantly from the overall data distribution.

Numerical data encoder design

The numerical data encoder adopts a deep neural network structure, and its inputs are cardiomyocyte metabolite concentration data x and expression-based data y, i.e., $x \in \mathbb{R}^{n\times m_x}$, $y \in \mathbb{R}^{n\times m_y}$, where n denotes the number of samples, and m_x and m_y denote the metabolite and gene dimensions, respectively.

The encoder objective is to map the input data to a Gaussian distribution parameter $(\mu, \log\sigma^2)$ in the latent space, where μ and σ are the mean and standard deviation vectors of the latent space, and the encoder structure denoted as show in Equation 1:

$$\mu, \log\sigma^2 = f_{\text{encoder}}(x, y; \theta_{\text{encoder}}) \tag{1}$$

Here, f_{encoder} denotes the mapping function of the encoder and θ_{encoder} denotes the encoder parameters. The encoder uses a multilayer neural network structure, where the output h_i of layer i denoted as show in Equation 2:

$$h_i = \sigma(W_i[h_{i-1}, x, y] + b_i) \tag{2}$$

Among them, W_i and b_i denote the weights and bias parameters of the ith layer respectively, σ denotes the activation function, and $[h_{i-1}, x, y]$ denotes connecting the output of the previous layer with the input data. The final encoder achieves efficient coding of the input data by mapping the input data to the Gaussian distribution parameters in the latent space.

Numerical data decoder design

The numerical data decoder aims to decode the latent representation z into raw data. The goal of the decoder is to generate a conditional probability distribution $p(t|u)$ of the raw data given the latent variable u, where t represents the raw data. To approximate this conditional distribution, the decoder maps latent variables u to reconstructed data $t' = f_{\text{decoder}}(u; \theta_{\text{decoder}})$ in the data space, where f_{decoder} denotes the decoder mapping function and θ_{decoder} denotes the decoder parameters.

The decoder uses a deep neural network structure and the computation of its output t' is represented by Equations 3, 4:

$$H_i = \sigma(W_i h_{i-1} + b_i) \tag{3}$$

$$t' = \text{sigmoid}(W' h_L + b') \tag{4}$$

Here, H_i denotes the hidden state of the decoder, W' and b' denote the weight and bias parameters of the last layer, h_L denotes the hidden state of the last layer of the decoder and sigmoid denotes the activation function.

By optimizing the parameters, the decoder accurately reconstructs the input data.

Joint potential space construction

A shared joint latent space is formed by combining the latent representations of the encoder and decoder for information transfer and exchange. The joint latent variable z is introduced and its conditional distribution is represented in Equation 5:

$$q(z|x, y) = \mathcal{N}(z \,|\, \mu_{\text{encoder}}(x, y), \Sigma_{\text{encoder}}(x, y)) \tag{5}$$

Among them, $\mu_{\text{encoder}}(x, y)$ and $\Sigma_{\text{encoder}}(x, y)$ denote the mean vector and covariance matrix of the latent variables output by the encoder, respectively. To realize the information transfer between the encoder and decoder, the variational inference technique is introduced to decompose the joint latent variable into the output of the encoder and the input of the decoder, i.e., $z = \mu_{\text{encoder}}(x, y) + \epsilon \odot \sigma_{\text{encoder}}(x, y)$, where ϵ denotes a random variable that obeys a standard normal distribution, and $\odot$ denotes an element-by-element multiplication.

The training process is defined by maximizing the variational lower bound, as shown in Equation 6, to optimize the model parameters.

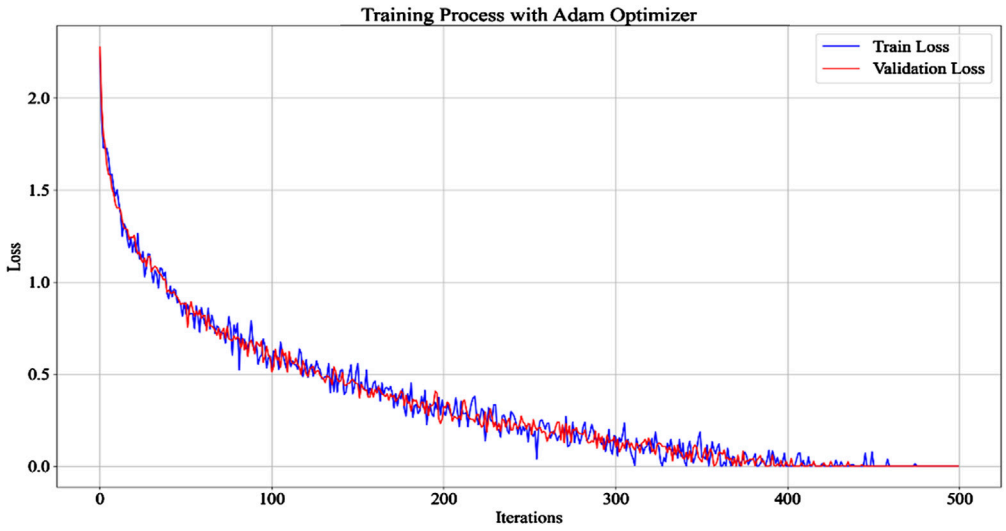

FIGURE 4
Model iteration process.

$$\mathcal{L} = \mathbb{E}_{q(z|x,y)}[\log p(x'|z)] - D_{\mathrm{KL}}[q(z|x,y)\|p(z)] \quad (6)$$

Where, the first term is the reconstruction loss, which measures the difference between the reconstructed data x' and the original data x, and the second term is the KL scatter, which measures the difference between the distribution of latent variables in the output of the encoder $q(z|x,y)$ and the *a priori* distribution $p(z)$.

Effective information transfer and joint potential space construction between the encoder and decoder is achieved by optimizing the variational lower bound for effective representation and reconstruction of the input data.

Model training process

During the model training process, the cardiomyocyte metabolite concentration data and the gene expression data were paired to form a joint dataset so that the encoder and decoder could process both types of data simultaneously. Defining the loss function to supervise the model training process, which consists of 2 components: data reconstruction error and KL scatter.

The Root Mean Square Error (RMSE) measure of reconstruction error is calculated using Equation 7.

$$Reconstruction\ Loss = \sqrt{\frac{1}{n}\sum_{i=1}^{n}(x_i - x_i')^2} \quad (7)$$

Here, n denotes the number of samples, and x_i and x_i' denote the original and reconstructed data of the ith sample, respectively. The KL dispersion is calculated according to Equation 8.

$$D_{\mathrm{KL}}[q(z|x,y)\|p(z)] = \frac{1}{2}\sum_{i=1}^{k}(\sigma_i^2 + \mu_i^2 - \log\sigma_i^2 - 1) \quad (8)$$

Among them, k denotes the dimension of the latent variable, and μ_i and σ_i denote the mean and standard deviation of the latent variable output by the encoder, respectively. During the training process, the model parameters are updated to minimize the loss function using the Adam optimizer, which is an adaptive learning rate optimization algorithm that adaptively adjusts the learning rate according to the parameter gradient to accelerate the model convergence process. The gradient of the loss function with respect to the model parameters is calculated by the back-propagation algorithm, and the Adam optimizer is used to update the model parameters, which makes the loss function decrease gradually, so that the VAE model learns effective data representation and reconstruction laws. The process is shown in Figure 4.

In Figure 4, the VAE model is shown in 500 iterations, with the number of iterations on the x-axis and the loss values on the y-axis. The model converges after 400 iterations and remains constant after 477 iterations. The similarity in the trend of loss values in the training and validation sets indicates that the model has good generalization ability during training. The operational efficiency and complexity of the model's encoding and decoding were further validated, with results shown in Table 1.

Table 1 shows the operational efficiency and complexity of the model's encoding and decoding. It can be seen that the computation time for the numerical data encoder is only 0.85 s per epoch, with 12.5 million parameters and a memory usage of 6.2 GB. The input dimension is (n × m_x + n × m_y), which is

TABLE 1 Model encoding and decoding efficiency.

Index	Numerical data encoder	Numerical data decoder	Joint latent space construction
Computation Time (seconds/epoch)	0.85	1.2	0.45
Number of Parameters (millions)	12.5	15.3	8.7
Memory Usage (GB)	6.2	7.8	4.5
Data Dimensionality (Input → Output)	(n × m_x + n × m_y) → (n × k)	(n × k) → (n × m_x + n × m_y)	(n × k)

TABLE 2 Classification results of energy autophagy characteristics of exercise myocardial cells.

Experimental group	Accuracy	Precision	Recall	F1 score
A	0.85	0.90	0.90	0.90
B	0.94	0.94	0.92	0.93
C	0.89	0.90	0.94	0.92
D	0.96	0.87	0.88	0.87
E	0.90	0.85	0.90	0.87
F	0.88	0.83	0.83	0.83

mapped to a low-dimensional latent space (n × k), demonstrating its high efficiency in handling dimensionality reduction of high-dimensional data. On the other hand, the numerical data decoder, which needs to reconstruct the low-dimensional latent representation (n × k) back into high-dimensional original data (n × m_x + n × m_y), has an increased computation time and memory usage to 1.2 s per epoch and 7.8 GB respectively, with the number of parameters reaching 15.3 million, indicating a higher demand for computational resources during the decoding process. The construction of the joint latent space, however, exhibits higher efficiency, with a computation time of just 0.45 s per epoch, 8.7 million parameters, and a memory usage of 4.5 GB. It also maintains a low-dimensional output (n × k). By integrating and transferring information through a low-dimensional latent space, it effectively reduces complexity and ensures a balanced overall performance of the model.

Feature extraction and analysis

Random Forest classifier is used to analyze the features in different sports conditions by constructing multiple decision trees and synthesizing the results for classification. The accuracy, precision, recall, and F1 score are calculated to quantify the effectiveness of the features for distinguishing different sports conditions, and the results are shown in Table 2.

As can be seen from Table 2, the model reaches high classification performance for different experimental groups (A-F), with all indicators above 0.83, indicating that the energy autophagy features of exercising cardiomyocytes have a high degree of differentiation under different exercise intensities. The features in the potential space of the VAE model are downscaled by the t-SNE algorithm. Setting the perplexity degree to 30, which makes the local structure more prominent, i.e., the clustering between similar samples is better; the number of iterations is 1000, to ensure that the algorithm has enough time to converge to a stable layout. The two-dimensional feature distribution map in potential space was obtained to observe the feature distribution of cardiomyocyte energy autophagy and its change trend under different exercise conditions, as shown in Figure 5.

Figure 5 uses t-SNE, UMAP, and lactate concentration overlay visualization methods to display the energy metabolism and autophagy characteristics of cardiomyocytes under different exercise conditions. The t-SNE results clearly distinguish the distribution patterns of each experimental group, particularly highlighting the significant separation of experimental group F under high-intensity exercise, reflecting its unique metabolic and autophagic state. UMAP further optimizes the presentation of global structure, emphasizing the boundaries between experimental groups, especially showing smoother cluster distributions in moderate-intensity exercise groups (such as B, C, and D). The t-SNE plot with lactate concentration overlay reveals a gradient change in lactate levels as exercise intensity increases, with high-lactate regions concentrated in experimental group F, indicating significantly enhanced anaerobic metabolism during high-intensity exercise.

In this study, the determination of the L1 regularization parameter value of 0.01 was based on the need to balance model

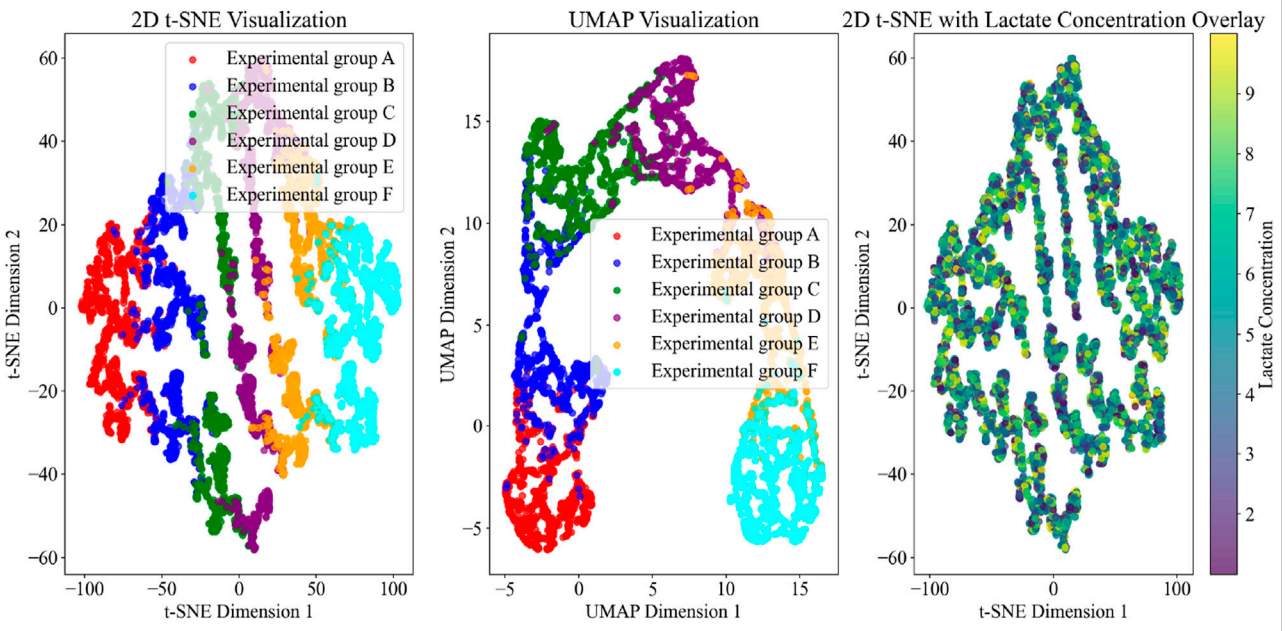

FIGURE 5
Dimensionality reduction and lactate overlay of cardiomyocyte features under exercise conditions.

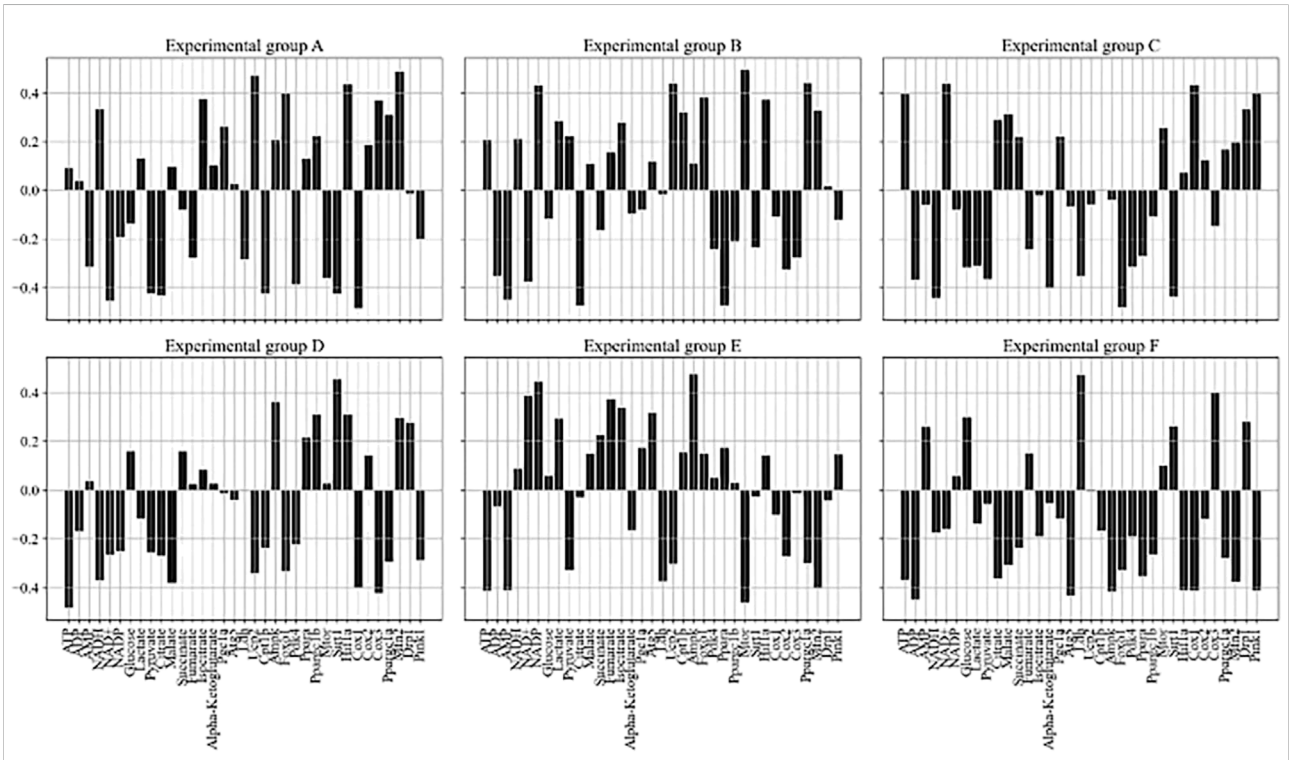

FIGURE 6
Regression coefficients between each exercise condition and metabolite concentration, gene expression. **(A)** Resting state group. **(B)** Low-intensity exercise group. **(C)** Moderate-intensity exercise group. **(D)** High-intensity exercise group. **(E)** Prolonged low-intensity exercise group. **(F)** Intermittent high-intensity exercise group.

performance and sparsity. Multiple experiments were conducted on the training dataset, and cross-validation was used to evaluate the impact of different regularization parameter values (e.g., 0.001, 0.01, 0.1, 1) on model performance. When the regularization parameter value was too small (e.g., 0.001), the model failed to effectively perform feature selection, resulting in the retention of too many irrelevant or redundant features, which increased model complexity and the risk of overfitting. Conversely, when the regularization parameter value was too large (e.g., 0.1 or 1), too many feature coefficients were compressed to zero, oversimplifying critical information and leading to underfitting. After systematic comparison, it was found that when the regularization parameter value was set to 0.01, the model could maintain a high prediction accuracy while selecting features closely related to exercise conditions, metabolite concentrations, and gene expression.

The LASSO regression model was further used to explore the relationship between exercise conditions and changes in metabolite concentrations and gene expression characteristics. Feature selection and model sparsification were achieved by penalizing larger coefficients through the introduction of an L1 regularization term. The regularization parameter was set to 0.01 in the study and the model was fitted using the training dataset. After the fitting was completed, the regression coefficients between each exercise condition and metabolite concentration and gene expression were obtained to reveal the extent and direction of the effect of exercise conditions on the target variables in the experimental group, and the results are shown in Figure 6.

In Figure 6, six subgraphs represent different experimental groups (A-F), with the concentration of each metabolite and gene expression characteristics in the horizontal direction, and the regression coefficients of the model in the vertical direction. ATP, as an important carrier of energy, is closely related to the activation/inhibition of metabolic pathways with the change of its concentration under different exercise conditions. Exercise condition B significantly increased the concentration of ATP (0.26), indicating that this condition increased energy demand and promoted the synthesis of energetic substances. In contrast, exercise condition D showed a significant decrease in ATP concentration (−0.48), reflecting increased energy expenditure and accelerated ATP catabolism due to high-intensity prolonged exercise. Changes in gene expression also provided insight into how exercise affected intracellular homeostasis. Pgc1a showed higher expression levels (0.26) under exercise condition A, which correlated with enhanced mitochondrial function and increased efficiency of energy production, which in turn adapted to the changes in energy demand brought about by exercise.

At the same time, the interactions between metabolites and gene expression do not exist in isolation but constitute a complex network. The concentration of Lactate decreases (−0.31) accompanied by an increase in the expression of Pgc1a (0.22) under exercise condition C, suggesting that the reduction of lactate stimulates mitochondrial biogenesis and increases the efficiency of oxidative phosphorylation in response to the energy demands of the hypoxic conditions. The relatively high expression level of Hif1a (0.14) under exercise condition E, when ATP concentration is low (−0.41), reflects the fact that cells in a hypoxic environment promote adaptive responses including an increase in glycolytic activity by up-regulating Hif1a to meet energy demands. Exercise can remodel metabolic pathways over time by regulating gene expression to adapt to different physiological demands.

The autophagy characteristics of exercising cardiomyocytes from different experimental groups were analyzed using PCA to calculate the feature contribution, and the statistical Top10 results are shown in Figure 7.

Figure 7 demonstrates the effects on the autophagy profile of cardiomyocytes under six different exercise conditions, i.e., from resting to high-intensity interval training, and the top 10 metabolites and gene expression changes contributing most to the autophagy profile were extracted by PCA in each group. In the resting state of group A, the 0.061 contribution of NADH as a key coenzyme in the electron transport chain reveals that energy metabolism in resting cardiomyocytes is dependent on oxidative phosphorylation, whereas the high contributions of Mtor (0.053) and Pgc1a (0.052) imply important regulatory roles for protein synthesis and mitochondrial biogenesis, respectively. With changes in exercise intensity and duration, such as low-intensity exercise in group B and prolonged low-intensity exercise in group E, the significant contributions of Pdk4 (0.058 and 0.054) and Cpt1b (0.056 and 0.054) reflect activation of the fatty acid oxidation pathway, a hallmark of adaptive metabolic regulation. In group C moderate-intensity exercise, the higher contribution of Pyruvate (0.050) reveals the balancing role of glycolysis and pyruvate oxidation in energy supply. In high-intensity exercise in group D and intermittent high-intensity exercise in group F, the high contribution of Sirt1 (0.051) and Pink1 (0.045) demonstrates the close association of exercise-induced autophagy with mitochondrial quality control mechanisms. The high contribution of AMP (0.058) and ADP (0.048) under high-intensity exercise suggests activation of the AMPK signaling pathway during increased energy demand, which is consistent with the physiological effects of exercise in enhancing energy metabolism and promoting autophagy.

Biological validation

Gene knockdown experiments were performed using CRISPR-Cas9 technology to observe the effects of specific genes on energy autophagy in cardiomyocytes. Based on previous studies and comprehensive analysis, several key genes closely related to the regulation of energy autophagy were selected for the experiments, including AMPK, PGC1A, CPT1B, and SIRT1.

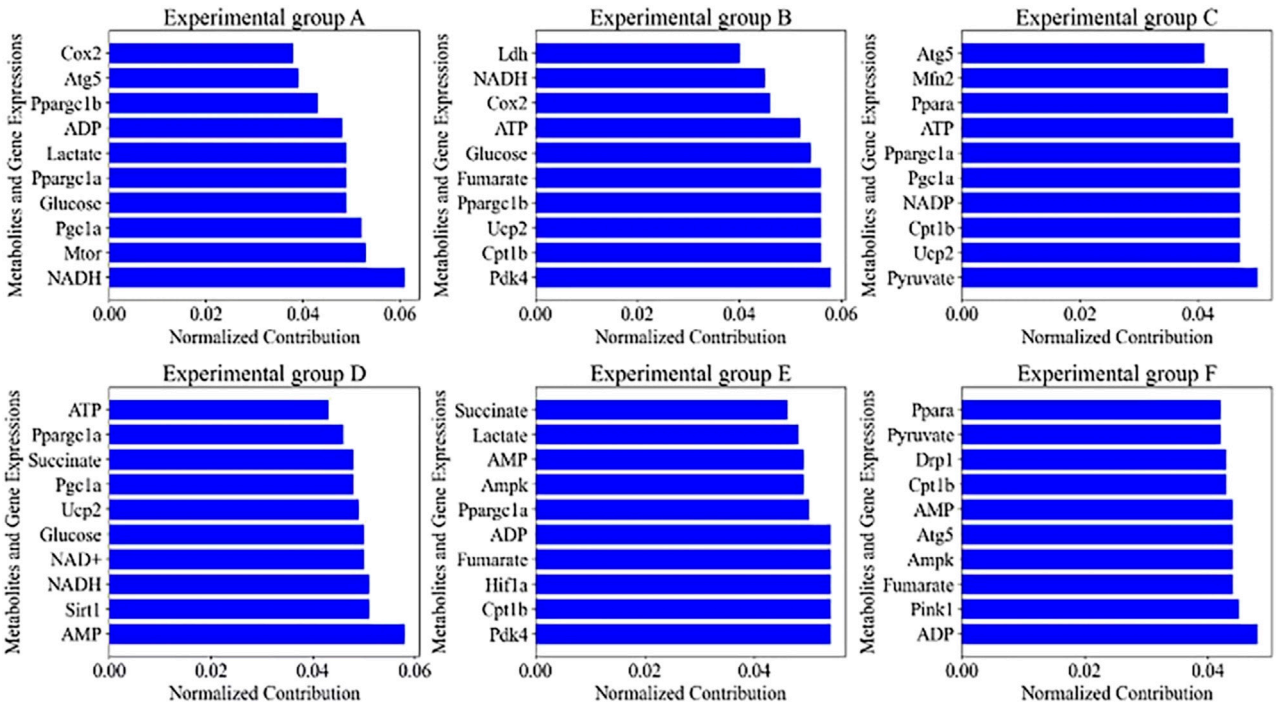

FIGURE 7
Characteristics of the top 10 contributors in the **(A–F)** experimental group.

This study utilized neonatal rat cardiomyocytes as the experimental model due to their wide applicability and biological relevance in energy metabolism and autophagy research. To ensure the efficiency of gene knockdown or knockout, changes in mRNA and protein levels of the target genes were verified using qPCR and Western blot, respectively. Functional experiments, such as measuring the LC3-II/LC3-I ratio and p62 degradation, were further conducted to confirm alterations in autophagic activity. During the CRISPR-Cas9 editing process, strict negative controls (cells not transfected with sgRNA) and positive controls (cells with known loss-of-function gene knockouts) were established to exclude non-specific effects and validate the reliability of the experimental system. Additionally, by optimizing the transfection method, it was ensured that sgRNA and Cas9 protein could efficiently enter the cells and form the CRISPR-Cas9 complex in the nucleus, thereby accurately cleaving the target gene sequence. The confirmation of gene knockout efficiency relied on the significant reduction in target gene expression levels detected by qPCR and Western blot, while also combining the results of functional experiments to verify their impact on autophagy and energy metabolism in cardiomyocytes.

For each selected gene, a gene editing design tool was used to design specific sgRNA sequences to ensure that they accurately recognize and cleave the target gene sequence. Healthy cardiomyocytes were cultured in cell culture medium and divided into different experimental groups. For each gene knockdown experiment, the designed sgRNA was cotransfected with Cas9 protein into cardiomyocytes. The optimized transfection method ensures that sgRNA and Cas9 can effectively enter the cell and form CRISPR-Cas9 complexes in the nucleus. Changes in autophagic activity of exercising cardiomyocytes were assessed by LC3-II/LC3-I ratio and p62 protein expression levels in knockout-positive and control cells, as shown in Table 3. Changes in the concentration of metabolites, including ATP, ADP, AMP, etc., were determined in knockout-positive and control cells. The metabolite levels were compared under different conditions to assess the effect of knockdown on energy metabolism in cardiomyocytes, and the results are shown in Table 4.

Table 3 presents the changes in autophagic activity in knockout-positive cells versus control cells, using the LC3-II/LC3-I ratio and p62 protein expression level as the main assessment indicators. The data show that cardiomyocytes with knockout genes B, C, D, E, and F exhibit significantly different autophagic activities compared to experimental group A. In group B, the LC3-II/LC3-I ratio increases from 0.05 to 0.08, whereas the p62 protein expression level decreases from 0.08 to 0.06. This trend is also seen in groups C, D, and F, where the LC3-II/LC3-I ratios increases to 0.12, 0.15, and 0.14,

TABLE 3 Changes in the autophagy activity of myocardial cells.

Experimental group	LC3-II/LC3-I ratio	p62 protein expression level
A	0.05	0.08
B	0.08	0.06
C	0.12	0.04
D	0.15	0.03
E	0.10	0.05
F	0.14	0.02

TABLE 4 Changes in metabolite concentration.

Experimental group	ATP (μmol/L)	ADP (μmol/L)	AMP (μmol/L)	NADH (μmol/L)	NAD+ (μmol/L)	NADP (μmol/L)
A	20	15	5	25	20	10
B	22	14	6	23	21	11
C	25	12	7	20	22	12
D	27	10	8	18	25	13
E	24	13	6	22	23	11
F	26	11	7	21	24	12

respectively, while the p62 protein expression level decreases to 0.04, 0.03, and 0.02, indicating that deletion of these genes significantly enhances autophagic activity in cardiomyocytes. However, the data for group E are slightly different, with the p62 protein expression level remaining relatively stable at 0.05, despite the elevation of the LC3-II/LC3-I ratio to 0.10.

Table 4 further demonstrates the changes in metabolite concentrations in cardiomyocytes after knockdown, including ATP, ADP, AMP, NADH, NAD+, and NADP. Comparing the different experimental groups, significant differences in metabolite levels are observed, directly reflecting the state of energy metabolism. The concentrations of NADH, NAD+, and NADP show different levels of fluctuations in group A and experimental groups B through F, suggesting changes in redox state and energy conversion efficiency. ATP is present in experimental group A at a concentration of 20 μmol/L, whereas this value fluctuates in the knockout experimental group, with ATP concentrations of 22 μmol/L, 25 μmol/L, 27 μmol/L, 24 μmol/L, and 26 μmol/L in groups B, C, D, E, and F, respectively, suggesting that the gene knockout facilitates energy production. Changes in the concentrations of ADP and AMP reveals adjustments in the balance of energy supply and demand, with the ADP concentration being 15 μmol/L in experimental group A and generally decreasing in the knockout experimental group to 10 μmol/L in group D, reflecting an increase in the efficiency of energy utilization.

In Table 3, this paper evaluates the impact of gene knockout on autophagic activity in cardiomyocytes through changes in the LC3-II/LC3-I ratio and p62 protein expression levels. To determine whether cardiomyocytes with knocked-out genes B, C, D, E, and F exhibit significantly different autophagic activity compared to Group A, a paired t-test was used to compare the mean differences between the two groups and assess their statistical significance. The results are shown in Table 5.

In Table 4, this paper presents changes in metabolite concentrations in cardiomyocytes after gene knockout, including key metabolites such as ATP, ADP, AMP, NADH, NAD+, and NADP. To determine significant differences across all experimental groups, ANOVA was used to comprehensively evaluate the overall significance of differences between different experimental groups, as shown in Table 6.

The paired t-test results in Table 5 show that all experimental groups (B-F) exhibit significant differences compared to Group A in terms of the LC3-II/LC3-I ratio and p62 protein expression levels ($p < 0.05$), indicating that knocking out the genes significantly enhanced autophagic activity in cardiomyocytes. Meanwhile, the ANOVA results in Table 6 reveal that all metabolites (ATP, ADP, AMP, NADH, NAD+, NADP) demonstrate statistically significant concentration changes across different experimental groups ($p < 0.05$), suggesting that gene knockout significantly impacted the energy metabolism state of cardiomyocytes. To further validate the

TABLE 5 Paired t-test results.

Experimental group	LC3-II/LC3-I ratio (experimental group vs. A)	p-value	p62 protein expression level (experimental group vs. A)	p-value
B	0.08 vs. 0.05	0.012	0.06 vs. 0.08	0.015
C	0.12 vs. 0.05	<0.001	0.04 vs. 0.08	<0.001
D	0.15 vs. 0.05	<0.001	0.03 vs. 0.08	<0.001
E	0.10 vs. 0.05	0.008	0.05 vs. 0.08	0.045
F	0.14 vs. 0.05	<0.001	0.02 vs. 0.08	<0.001

TABLE 6 ANOVA results.

Metabolite	Group A	Group B	Group C	Group D	Group E	Group F	F-value	p-value
ATP (μmol/L)	20	22	25	27	24	26	12.87	<0.001
ADP (μmol/L)	15	14	12	10	13	11	9.45	<0.001
AMP (μmol/L)	5	6	7	8	6	7	6.32	0.002
NADH (μmol/L)	25	23	20	18	22	21	8.12	<0.001
NAD+ (μmol/L)	20	21	22	25	23	24	10.76	<0.001
NADP (μmol/L)	10	11	12	13	11	12	5.48	0.004

effects of gene knockout on autophagy activity and energy metabolism in cardiomyocytes, this study incorporated multiple autophagosome flux markers (p62 degradation, ATG expression) and mitochondrial function indicators (OCR, ECAR, and mitochondrial membrane potential). Below are the results comparing the control group A with experimental groups B-F (gene knockout groups):

The data in Table 7 reveal that gene knockout significantly enhances autophagy activity in cardiomyocytes, as evidenced by increased p62 degradation rates and elevated ATG5 expression levels across experimental groups B-F compared to control group A. Notably, group D exhibits the most pronounced effect, with a p62 degradation rate of 54.6% and an ATG5 expression level reaching 1.83, suggesting that the gene knockout in this group may have promoted autophagosome formation by upregulating ATG5 expression. Additionally, OCR values, which reflect mitochondrial oxidative phosphorylation capacity, are significantly higher in groups B-F than in group A, indicating that gene knockout enhances mitochondrial respiratory function. Group D shows the highest OCR value at 247.6 pmol/min, underscoring its substantial impact on mitochondrial performance. Similarly, ECAR values, which indicate glycolytic activity, are elevated in all knockout groups, with group D again showing the most significant increase at 34.7 mpH/min, highlighting a shift toward glycolytic metabolism. The absolute values of mitochondrial membrane potential decrease in groups B-F compared to group A, with group D exhibiting the lowest value at −91.8 mV. This reduction in membrane potential may be linked to enhanced autophagy activity and mitochondrial turnover. Overall, the results in Table 7 demonstrate that gene knockout significantly boosts autophagy activity and improves mitochondrial function, consistent with findings from Tables 3 and 4. These findings further confirm the critical roles of AMPK, PGC1A, CPT1B, and SIRT1 in regulating energy metabolism and autophagy in cardiomyocytes, providing important insights for future gene-based therapeutic strategies.

The dynamic changes of cardiomyocyte metabolism and autophagy at different time points were further analyzed, and the results are shown in Table 8.

The time-series data in Table 8 reveal the dynamic regulatory mechanisms of energy metabolism and autophagy in cardiomyocytes after exercise. High-intensity exercise (Group D) exhibited significant metabolic stress immediately after exercise (0 h), with a 28% decrease in ATP levels, accompanied by activation of autophagy (a 200% increase in the LC3-II/LC3-I ratio), consistent with the highly dispersed feature distribution observed in the VAE model. After 24 h, ATP levels partially recovered (↑14%), and AMPK activity decreased (↓14%), suggesting that cells initiated energy compensation mechanisms. By 72 h, autophagic activity returned to baseline levels (the LC3-II/LC3-I ratio decreased to 1.6 times that of the control group), indicating the completion of short-term adaptive repair. The continuous downregulation of SIRT1 expression (a 30% decrease at 72 h compared to 0 h) may reflect long-term suppression of NAD+-dependent signaling. These results

TABLE 7 Autophagosome flux markers and mitochondrial function test results.

Experimental group	p62 degradation rate (%)	ATG5 expression level (relative value)	OCR (pmol/min)	ECAR (mpH/min)	Mitochondrial membrane potential (mV)
A	9.8	1	148.3	19.6	−121.4
B	24.7	1.28	179.5	24.3	−110.7
C	39.2	1.57	208.9	29.8	−101.2
D	54.6	1.83	247.6	34.7	−91.8
E	29.5	1.39	187.3	27.5	−114.3
F	48.9	1.68	228.4	32.1	−96.5

TABLE 8 Dynamic changes in metabolism and autophagy of cardiomyocytes at different time points.

Time point	Group	ATP (μmol/L)	LC3-II/LC3-I	p62 (ng/mg)	AMPK activity (relative value)	SIRT1 expression (TPM)
Immediately after exercise (0h)	A	20.1 ± 1.2	0.05 ± 0.01	0.08 ± 0.02	0.85 ± 0.05	4.2 ± 0.3
	D	16.3 ± 1.5↓	0.15 ± 0.02↑	0.03 ± 0.01↓	1.42 ± 0.08↑	6.8 ± 0.5↑
24h after exercise	A	19.8 ± 1.0	0.06 ± 0.01	0.07 ± 0.02	0.88 ± 0.04	4.3 ± 0.4
	D	18.7 ± 1.3↑	0.12 ± 0.02↓	0.04 ± 0.01↓	1.21 ± 0.06↓	5.9 ± 0.4↓
72h after exercise	A	20.3 ± 1.1	0.05 ± 0.01	0.08 ± 0.02	0.86 ± 0.05	4.1 ± 0.3
	D	19.5 ± 1.4↑	0.08 ± 0.01↓	0.06 ± 0.02↓	0.98 ± 0.07↓	4.7 ± 0.4↓

Note: ↑ indicates a significant increase compared to the previous time point ($p < 0.05$); ↓ indicates a significant decrease ($p < 0.05$). Group A is the control group, and Group D is the high-intensity exercise group.

support the ability of the VAE model to capture metabolic heterogeneity and provide experimental evidence for optimizing the timing of exercise interventions.

Discussion

By integrating the VAE model with multi-omics and experimental validation, this study advances the understanding of exercise-mediated energy autophagy in cardiomyocytes, bridging gaps in existing research. While prior studies have established autophagy's role in maintaining cardiac homeostasis under stress [38, 39], the dynamic interplay between exercise intensity, metabolic reprogramming, and autophagic regulation remains incompletely characterized. Our findings align with and extend previous observations that exercise modulates autophagy bidirectionally and that mitochondrial quality control is critical for cardiac adaptation. By employing VAE to decode high-dimensional data, we provide a computational framework to dissect complex interactions between metabolites and genes, addressing limitations of traditional reductionist approaches.

The observed stability of metabolic and autophagic features under low-intensity exercise versus the dispersion seen in moderate-to-high intensity conditions underscores the dose-dependent role of exercise in cardiac stress adaptation. This aligns with reports that excessive autophagy may exacerbate cardiac injury, while optimal activation supports energy provision and organelle renewal [40, 41]. Notably, our identification of hypoxia-inducible factor 1α (HIF1α) and lactate dynamics as key metabolic sensors resonates with studies linking exercise preconditioning to ischemia–hypoxia tolerance via autophagy. These findings collectively suggest that exercise-induced metabolic stress primes cardiomyocytes for adaptive responses, a mechanism potentially harnessed in therapeutic strategies.

The LASSO regression analysis revealed tight coupling between PGC1α, ATP levels, and autophagy markers, reinforcing PGC1α's central role in mitochondrial biogenesis and energy homeostasis [13, 42]. The inverse relationship between AMPK/SIRT1 activity and p62 accumulation further validates their regulatory roles in autophagic flux, consistent with their established functions in nutrient sensing and stress resistance. By contrast, the decline in ATP under HIF1α upregulation highlights a trade-off between glycolytic adaptation and oxidative stress—a balance critical for cell survival under metabolic duress [43, 44]. These insights refine existing models of exercise-mediated cardioprotection,

positioning autophagy as both a stress response and a prophylactic mechanism.

CRISPR-Cas9-mediated knockout of AMPK, PGC1α, CPT1B, and SIRT1 confirmed their non-redundant roles in autophagy regulation, corroborating their established functions in preclinical models [45, 46]. The LC3-II/I ratio and p62 dynamics observed here mirror findings from ischemia-reperfusion studies, where autophagy mitigates mitochondrial dysfunction. Notably, our work advances the field by integrating these molecular insights with systemic exercise responses, offering a roadmap for gene-based therapies targeting metabolic disorders. For instance, modulating CPT1B—a key enzyme in fatty acid oxidation—could enhance exercise capacity in heart failure patients, while SIRT1 agonists may bolster stress resistance in aging cardiomyocytes.

Future studies should explore how VAE-derived latent space features correlate with clinical outcomes, leveraging multi-domain modeling to predict individualized exercise regimens. Additionally, cross-validation with extracellular vesicle (EV) profiling could unveil novel paracrine mechanisms linking autophagy to systemic metabolic health. By merging computational and experimental approaches, this work lays a foundation for precision medicine strategies targeting autophagy in cardiovascular disease.

Conclusion

In this paper, we utilized the VAE model to efficiently process high-dimensional metabolite concentration and gene expression data to reveal the dynamic changes of energy metabolism and autophagy process in cardiomyocytes under different exercise conditions. Exercise intensity was found to significantly affect cardiomyocyte energy metabolism and autophagy activity, with high-intensity exercise triggering more extensive metabolic stress and injury, activating more metabolic pathways, and leading to high intracellular state variability. Through LASSO regression modeling, the tight connection between exercise conditions and metabolite concentration and gene expression was clarified, demonstrating how exercise adapted to different physiological demands by regulating autophagic processes. Gene knockdown experiments verified the key roles of AMPK, PGC1A, CPT1B and SIRT1 in autophagy and energy metabolism in cardiomyocytes, which provided a new idea for gene-targeted therapy.

While this study provides valuable findings, limitations such as small sample size and model generalizability remain. Future research will expand the sample size, optimize the model, and explore additional genes associated with energy autophagy in cardiomyocytes. Furthermore, time-course analyses will be incorporated to characterize both transient and sustained effects of exercise on cardiac metabolism and autophagy. These efforts aim to deepen our understanding of the complex mechanisms underlying exercise-mediated cardioprotection and support the development of precision medicine strategies targeting autophagy-related cardiovascular diseases.

Author contributions

CLQ is responsible for designing the research framework, writing, revising paper, and analyzing data, including proofreading. YY is responsible for designing the research framework, writing papers, and analyzing data, and designing research architectures.

Data availability

The original contributions presented in the study are included in the article/supplementary material, further inquiries can be directed to the corresponding author.

Ethics statement

I have confirmed that all methods were performed in accordance with the relevant guidelines and regulations for animal studies by including a statement in the methods section to this effect. All experimental protocols were approved by a named institutional and/or licensing committee. This project was approved by Henan Normal University 23112121. All methods were carried out in accordance with relevant guidelines and regulations, which were taken from the European Commission regulation (2010/63/EU). I have confirmed that all experiments were performed in accordance with the ARRIVE guidelines (PLoS Bio 8(6), e1000412, 2010) and regulations. The images included in this research are original and do not require proper permission and/or credit. Written informed consent was provided by all participants or their authorized proxy. The study was conducted in accordance with the local legislation and institutional requirements.

Funding

The author(s) declare that financial support was received for the research and/or publication of this article. This study was supported by the National Social Science Foundation Project: Study on the Formation Mechanism, Current Situation Evaluation and Realization Path of Low-carbon Development and Utilization of Outdoor Sports Resources in China (No. 24BTY064).

Conflict of interest

The author(s) declared no potential conflicts of interest with respect to the research, authorship, and/or publication of this article.

Generative AI statement

The author(s) declare that no Generative AI was used in the creation of this manuscript.

References

1. Daniels LJ, Varma U, Annandale M, Chan E, Mellor KM, Delbridge LMD. Myocardial energy stress, autophagy induction, and cardiomyocyte functional responses. *Antioxid and Redox Signaling* (2019) **31**(6):472–86. doi:10.1089/ars.2018.7650

2. Wang H, Li J, Xu T, Yao H, Chen G, Hu J. Effects of Sirt3-autophagy and resveratrol activation on myocardial hypertrophy and energy metabolism. *Mol Med Rep* (2020) **22**(2):1342–50. doi:10.3892/mmr.2020.11195

3. Shi B, Ma M, Zheng Y, Pan Y, Lin X. mTOR and Beclin1: two key autophagy-related molecules and their roles in myocardial ischemia/reperfusion injury. *J Cell Physiol* (2019) **234**(8):12562–8. doi:10.1002/jcp.28125

4. Altamimi TR, Chowdhury B, Singh KK, Zhang L, Mahmood MU, Pan Y, et al. A novel role of endothelial autophagy as a regulator of myocardial fatty acid oxidation. *The J Thorac Cardiovasc Surg* (2019) **157**(1):185–93. doi:10.1016/j.jtcvs.2018.07.047

5. Qiu F, Yuan Y, Luo W, Gong Y, Zhang Z, Liu Z, et al. Asiatic acid alleviates ischemic myocardial injury in mice by modulating mitophagy-and glycophagy-based energy metabolism. *Acta Pharmacologica Sinica* (2022) **43**(6):1395–407. doi:10.1038/s41401-021-00763-9

6. Xu C, Cao Y, Liu R, Liu L, Zhang W, Fang X, et al. Mitophagy-regulated mitochondrial health strongly protects the heart against cardiac dysfunction after acute myocardial infarction. *J Cell Mol Med* (2022) **26**(4):1315–26. doi:10.1111/jcmm.17190

7. Liu H, Liu S, Qiu X, Yang X, Bao L, Pu F, et al. Donor MSCs release apoptotic bodies to improve myocardial infarction via autophagy regulation in recipient cells. *Autophagy* (2020) **16**(12):2140–55. doi:10.1080/15548627.2020.1717128

8. Zheng Y, Shi B, Ma M, Wu X, Lin X. The novel relationship between Sirt3 and autophagy in myocardial ischemia–reperfusion. *J Cell Physiol* (2019) **234**(5):5488–95. doi:10.1002/jcp.27329

9. Fan J, Zhu Q, Wu Z, Ding J, Qin S, Liu H, et al. Protective effects of irisin on hypoxia-reoxygenation injury in hyperglycemia-treated cardiomyocytes: role of AMPK pathway and mitochondrial protection. *J Cell Physiol* (2020) **235**(2):1165–74. doi:10.1002/jcp.29030

10. Hekman KE, Koss KM, Ivancic DZ, He C, Wertheim JA. Autophagy enhances longevity of induced pluripotent stem cell-derived endothelium via mTOR-independent ULK1 kinase. *Stem Cells Translational Med* (2022) **11**(11):1151–64. doi:10.1093/stcltm/szac069

11. Shah SJ, Borlaug BA, Kitzman DW, McCulloch AD, Blaxall BC, Agarwal R, et al. Research priorities for heart failure with preserved ejection fraction: national heart, lung, and blood institute working group summary. *Circulation* (2020) **141**(12):1001–26. doi:10.1161/CIRCULATIONAHA.119.041886

12. Ljubojević-Holzer S, Kraler S, Djalinac N, Abdellatif M, Voglhuber J, Schipke J, et al. Loss of autophagy protein ATG5 impairs cardiac capacity in mice and humans through diminishing mitochondrial abundance and disrupting Ca2+ cycling. *Cardiovasc Res* (2022) **118**(6):1492–505. doi:10.1093/cvr/cvab112

13. Huang Q, Su H, Qi B, Wang Y, Yan K, Wang X, et al. A SIRT1 activator, ginsenoside Rc, promotes energy metabolism in cardiomyocytes and neurons. *J Am Chem Soc* (2021) **143**(3):1416–27. doi:10.1021/jacs.0c10836

14. Hu Q, Zhang H, Gutiérrez Cortés N, Wu D, Wang P, Zhang J, et al. Increased Drp1 acetylation by lipid overload induces cardiomyocyte death and heart dysfunction. *Circ Res* (2020) **126**(4):456–70. doi:10.1161/CIRCRESAHA.119.315252

15. Madonna R, Moscato S, Cufaro MC, Pieragostino D, Mattii L, Del Boccio P, et al. Empagliflozin inhibits excessive autophagy through the AMPK/GSK3β signalling pathway in diabetic cardiomyopathy. *Cardiovasc Res* (2023) **119**(5):1175–89. doi:10.1093/cvr/cvad009

16. Wu X, Qin K, Iroegbu CD, Xiang K, Peng J, Guo J, et al. Genetic analysis of potential biomarkers and therapeutic targets in ferroptosis from coronary artery disease. *J Cell Mol Med* (2022) **26**(8):2177–90. doi:10.1111/jcmm.17239

17. Godtliebsen G, Larsen KB, Bhujabal Z, Opstad IS, Nager M, Punnakkal AR, et al. High-resolution visualization and assessment of basal and OXPHOS-induced mitophagy in H9c2 cardiomyoblasts. *Autophagy* (2023) **19**(10):2769–88. doi:10.1080/15548627.2023.2230837

18. Chaix MA, Parmar N, Kinnear C, Lafreniere-Roula M, Akinrinade O, Yao R, et al. Machine learning identifies clinical and genetic factors associated with anthracycline cardiotoxicity in pediatric cancer survivors. *JACC: CardioOncology* (2020) **2**(5):690–706. doi:10.1016/j.jaccao.2020.11.004

19. Iborra-Egea O, Santiago-Vacas E, Yurista SR, Lupón J, Packer M, Heymans S, et al. Unraveling the molecular mechanism of action of empagliflozin in heart failure with reduced ejection fraction with or without diabetes. *JACC: Basic Translational Sci* (2019) **4**(7):831–40. doi:10.1016/j.jacbts.2019.07.010

20. Liu S, Zhang Y, Peng J, Shang X. An improved hierarchical variational autoencoder for cell–cell communication estimation using single-cell RNA-seq data. *Brief Funct Genomics* (2024) **23**(2):118–27. doi:10.1093/bfgp/elac056

21. Rashid S, Shah S, Bar-Joseph Z, Pandya R. Dhaka: variational autoencoder for unmasking tumor heterogeneity from single cell genomic data. *Bioinformatics* (2021) **37**(11):1535–43. doi:10.1093/bioinformatics/btz095

22. Grønbech CH, Vording MF, Timshel PN, Sønderby CK, Pers TH, Winther O. scVAE: variational auto-encoders for single-cell gene expression data. *Bioinformatics* (2020) **36**(16):4415–22. doi:10.1093/bioinformatics/btaa293

23. Trong TN, Mehtonen J, González G, Kramer R, Hautamäki V, Heinäniemi M. Semisupervised generative autoencoder for single-cell data. *J Comput Biol* (2020) **27**(8):1190–203. doi:10.1089/cmb.2019.0337

24. Svensson V, Gayoso A, Yosef N, Pachter L. Interpretable factor models of single-cell RNA-seq via variational autoencoders. *Bioinformatics* (2020) **36**(11):3418–21. doi:10.1093/bioinformatics/btaa169

25. Zilvan V, Ramdan A, Heryana A, Krisnandi D, Suryawati E, Yuwana RS, et al. Convolutional variational autoencoder-based feature learning for automatic tea clone recognition. *J King Saud University-Computer Inf Sci* (2022) **34**(6):3332–42. doi:10.1016/j.jksuci.2021.01.020

26. Heydari AA, Davalos OA, Zhao L, Hoyer KK, Sindi SS. ACTIVA: realistic single-cell RNA-seq generation with automatic cell-type identification using introspective variational autoencoders. *Bioinformatics* (2022) **38**(8):2194–201. doi:10.1093/bioinformatics/btac095

27. He C, Zhu S, Wu X, Zhou J, Chen Y, Qian X, et al. Accurate tumor subtype detection with Raman spectroscopy via variational autoencoder and machine learning. *ACS omega* (2022) **7**(12):10458–68. doi:10.1021/acsomega.1c07263

28. Ai D, Wang Y, Li X, Pan H. Colorectal cancer prediction based on weighted gene co-expression network analysis and variational auto-encoder. *Biomolecules* (2020) **10**(9):1207. doi:10.3390/biom10091207

29. Marino J. Predictive coding, variational autoencoders, and biological connections. *Neural Comput* (2022) **34**(1):1–44. doi:10.1162/neco_a_01458

30. Cohen Kalafut N, Huang X, Wang D. Joint variational autoencoders for multimodal imputation and embedding. *Nat Machine Intelligence* (2023) **5**(6):631–42. doi:10.1038/s42256-023-00663-z

31. Steinberg GR, Hardie DG. New insights into activation and function of the AMPK. *Nat Rev Mol Cel Biol* (2023) **24**(4):255–72. doi:10.1038/s41580-022-00547-x

32. Liu K, Jin X, Zhang X, Lian H, Ye J. The mechanisms of nucleotide actions in insulin resistance. *J Genet Genomics* (2022) **49**(4):299–307. doi:10.1016/j.jgg.2022.01.006

33. Chini CCS, Zeidler JD, Kashyap S, Warner G, Chini EN. Evolving concepts in NAD+ metabolism. *Cell Metab* (2021) **33**(6):1076–87. doi:10.1016/j.cmet.2021.04.003

34. Mohamed TMA, Abouleisa R, Hill BG. Metabolic determinants of cardiomyocyte proliferation. *Stem Cells* (2022) **40**(5):458–67. doi:10.1093/stmcls/sxac016

35. Chopra M, Kumar V, Singh M, Aggarwal NK. An overview about the approaches used in the production of alpha-ketoglutaric acid with their applications. *Phys Sci Rev* (2024) **9**(1):211–25. doi:10.1515/psr-2022-0162

36. Shi W, Tan C, Liu C, Chen D. Mitochondrial fission mediated by Drp1-Fis1 pathway and neurodegenerative diseases. *Rev Neurosciences* (2023) **34**(3):275–94. doi:10.1515/revneuro-2022-0056

37. Kumar R, Harilal S, Parambi DGT, Kanthlal S, Rahman MA, Alexiou A, et al. The role of mitochondrial genes in neurodegenerative disorders. *Curr Neuropharmacology* (2022) **20**(5):824–35. doi:10.2174/1570159x19666210908163839

38. Zhang L, Zhang M, Huang J, Huang J, Zhang Y, Zhang Y, et al. Klf9 is essential for cardiac mitochondrial homeostasis. *Nat Cardiovasc Res* (2024) **3**(11):1318–36. doi:10.1038/s44161-024-00561-6

39. Marzoog BA. Autophagy behavior in post-myocardial infarction injury. *Cardiovasc and Hematological Disorders-Drug Targets* (2023) **23**(1):2–10. doi:10.2174/1871529x23666230503123612

40. Tang Y, Xu W, Liu Y, Zhou J, Cui K, Chen Y. Autophagy protects mitochondrial health in heart failure. *Heart Fail Rev* (2023) **29**(1):113–23. doi:10.1007/s10741-023-10354-x

41. Gatica D, Chiong M, Lavandero S, Klionsky DJ. The role of autophagy in cardiovascular pathology. *Cardiovasc Res* (2022) **118**(4):934–50. doi:10.1093/cvr/cvab158

42. Yin L, Yuan L, Tang Y, Luo Z, Lin X, Wang S, et al. Nucleolin promotes autophagy through PGC-1α in LPS-induced myocardial injury. *Shock* (2023) **60**(2):227–37. doi:10.1097/shk.0000000000002152

43. Taylor CT, Scholz CC. The effect of HIF on metabolism and immunity. *Nat Rev Nephrol* (2022) **18**(9):573–87. doi:10.1038/s41581-022-00587-8

44. Attaway AH, Bellar A, Mishra S, Karthikeyan M, Sekar J, Welch N, et al. Adaptive exhaustion during prolonged intermittent hypoxia causes dysregulated skeletal muscle protein homeostasis. *The J Physiol* (2023) **601**(3):567–606. doi:10.1113/jp283700

45. Gu M, Wei Z, Wang X, Gao Y, Wang D, Liu X, et al. Myostatin knockout affects mitochondrial function by inhibiting the AMPK/SIRT1/PGC1α Pathway in skeletal muscle. *Int J Mol Sci* (2022) **23**(22):13703. doi:10.3390/ijms232213703

46. Zahedi E, Sadr SS, Sanaeierad A, Roghani M. Valproate-induced murine autism spectrum disorder is associated with dysfunction of amygdala parvalbumin interneurons and downregulation of AMPK/SIRT1/PGC1α signaling. *Metab Brain Dis* (2023) **38**(6):2093–103. doi:10.1007/s11011-023-01227-1

EBM Experimental Biology and Medicine

TYPE Original Research
PUBLISHED 18 September 2025
DOI 10.3389/ebm.2025.10710

OPEN ACCESS

*CORRESPONDENCE
Stephania A. Cormier,
stephaniacormier@lsu.edu

RECEIVED 13 June 2025
ACCEPTED 29 August 2025
PUBLISHED 18 September 2025

CITATION
Bakshi A, Baconguis L, Al-Mamun MA, Yu Q, Richmond-Bryant J and Cormier SA (2025) A case study of long-term disease burden in a rural community near an open burn facility. *Exp. Biol. Med.* 250:10710. doi: 10.3389/ebm.2025.10710

A case study of long-term disease burden in a rural community near an open burn facility

Arundhati Bakshi[1], Liana Baconguis[1], Md Abdullah Al-Mamun[2], Qingzhao Yu[2], Jennifer Richmond-Bryant[3] and Stephania A. Cormier[1,4]*

[1]Department of Biological Sciences, Louisiana State University, Baton Rouge, LA, United States, [2]Department of Biostatistics and Data Science, Louisiana State University Health Sciences Center, New Orleans, LA, United States, [3]Department of Forestry and Environmental Resources, North Carolina State University, Raleigh, NC, United States, [4]Pennington Biomedical Research Center, Baton Rouge, LA, United States

Abstract

Open burning and open detonation (OB/OD) of explosive and hazardous wastes creates various toxic waste products, including particulate matter, that is released into the atmosphere and capable of generating significant health impacts upon exposure. The last commercially run OB/OD thermal treatment facility in operation in the United States is located near the rural community of Colfax in central Louisiana. To evaluate the community's concerns about the potential health impacts from air pollution due to the facility's regular open burning of explosive and hazardous wastes, we examined the disease burden in Colfax compared to the surrounding parish and state. In a cross-sectional study, we analyzed hospitalizations and mortality (2000–2018) where a primary or secondary disease code was associated with cardiovascular, respiratory, thyroid and skin disease. After adjusting for age, sex and race, morbidity and mortality due to cardiovascular and respiratory diseases were significantly higher in Colfax compared to the surrounding areas. In addition, comparing age-adjusted rates across geographies, stratified by race and sex, revealed place-based differences within sub-populations. The higher estimated prevalence of disease conditions is consistent with long-term particulate matter exposure and suggests a need for comprehensive exposure studies within the community. Our data further stress the need for enhanced epidemiological studies and tailored statistical methods to address exposures and environmental health impacts in rural populations, with fewer than 2,500 individuals, like Colfax.

KEYWORDS

open burning, hazardous waste, rural communities, environmental health, health impact

Impact Statement

This study investigates the health impacts associated with the last remaining commercial open burning/open detonation (OB/OD) facility in the United States, located in the rural town of Colfax, Louisiana. The facility's ongoing open burning of explosive and hazardous waste has raised significant concern among residents about long-term exposure to particulate matter and other toxic byproducts.We present a cross-sectional analysis of hospitalization and mortality data (2000–2018) for cardiovascular, respiratory, thyroid, and skin diseases in Colfax, comparing these rates to the surrounding parish and the state. This study was driven by residents citing various respiratory, cardiovascular, dermal, and thyroid disorders, in addition to cancers. Our findings demonstrate significantly elevated rates of cardiovascular and respiratory diseases, consistent with long-term exposure to airborne pollutants from OB/OD activities. Importantly, we also highlight disparities within subpopulations when stratifying by race and sex, underscoring the necessity of context-specific public health interventions. This work provides a rare and timely evaluation of pollutant exposure and health outcomes in a rural, underserved community. Moreover, it emphasizes the urgent need for robust epidemiological methods tailored to small populations that often fall outside the scope of traditional environmental health surveillance.We believe our study offers critical insights into the environmental justice implications of hazardous waste disposal practices and the value of integrating community concerns into scientific investigation.

Introduction

Thermal treatment of explosives and other hazardous wastes by open burning and open detonation (OB/OD) results in incomplete combustion of the wastes and the dispersal of residual hazardous constituents into the air. Thus, people may be exposed to hazardous constituents by inhalation of contaminated air, ingestion of contaminated water and food, and/or dermal contact and absorption. While the residual constituents released depend on the compounds processed by the OB/OD facility, studies of military burn pits with explosive waste streams have identified emissions of respirable particulate matter (PM) along with associated environmentally persistent free radicals, which act as precursors to dioxins and furans, polycyclic aromatic hydrocarbons, metals, and volatile organic compounds [1–6]. In addition to irritation of the respiratory tract, eyes, and skin, human exposure to these substances have been associated with increased cancer rates and respiratory, cardiovascular, endocrine, and neurologic diseases [7–10].

Colfax is a rural town in the state of Louisiana and is the seat of Grant Parish (the state's equivalent to counties). According to the U.S. Census Bureau's American Community Survey (2022), it has a population of about 1600 people and a higher percentage of Black residents (66%) than Grant Parish (15%) and Louisiana (32%). A larger percentage of the Colfax population lives below poverty level (38%) compared with Grant Parish (15%) and Louisiana (19%) [11] (Table 1).

A thermal treatment facility operated by Clean Harbors, LLC is located about five miles north of the Colfax town limits (Figure 1). Operational since 1985, it is the only commercially operating OB/OD facility for the thermal treatment of hazardous wastes in the country. Clean Harbors, LLC is one of three sites monitored by the U.S. EPA's Toxic Release Inventory (TRI) program in Grant Parish, and the only one within the Colfax ZIP code (Figure 1). It produced over 99% of TRI-catalogued pollutants released to the land in the parish (shown for 2015 as an example, but relative proportions are similar for other years) (Table 2). Air releases are declared in the TRI to be zero for Clean Harbors Colfax, indicating that declared releases are landfilled after thermal treatment. Its operations include daily OB/OD of munitions from various sources, which has been noted by the community to cause consistent smoke plumes and noise disturbances [12]. The thermal treatment of explosives is known to generate various toxic byproducts [13], including environmentally persistent free radicals, an emerging class of pollutants associated with particulate matter (PM) that can persist for years in the environment [14, 15]. Three air monitoring samples collected by the Louisiana Department of Environmental Quality (LDEQ) in 2016 also showed that acrolein–a common cardio-, neuro-, nephro-, respiro- and hepato-toxin [16] – levels in the area were above the EPA's risk-based screening levels [17]. A subsequent cancer risk assessment report by Louisiana Department of Health (LDH) found a higher incidence of colorectal cancer in the census tract that includes Colfax and respiratory cancers in Grant Parish [18].

The thermal treatment facility is a focus of community concern, with residents citing various respiratory, cardiovascular, dermal, gastric, thyroid, and other disorders, in addition to cancers [12]. However, no current surveillance data are available at the municipal level that can be used to assess the community's health concerns. Here, we have used an innovative method aggregating 19 years of hospitalization data to estimate the disease burden in the Colfax ZIP code relative to other areas in Grant Parish and the state using inpatient discharge and mortality records from LDH. The prevalence of respiratory and cardiovascular diseases was estimated based on the inclusion of specific disease codes associated with all-cause hospitalization and mortality. All data were temporally aggregated over 19 years (2000–2018) to preserve patient confidentiality and improve

TABLE 1 Comparison of American Community Survey 5-year estimates (2022) for Louisiana, Grant Parish, Colfax town, ZIP code 71417 (which includes Colfax and is defined as Colfax for this study), and other ZIP codes in Grant Parish.

Characteristics	Louisiana	Grant Parish	ZIP code 71417 (Colfax)[a]	All other Grant Parish ZIP codes[c]
Total population	4,640,546	22,185	4,943	18,434
% Age <18 years	23%	21%	21%	20%
% Age ≥65 years	16%	15%	18%	15%
% Female	51%	43%	44%	43%
% All non-White races (% Black or African-American alone)	41% (32%)	21% (15%)	32% (31%)	17% (11%)
% Hispanic or Latino	6%	5%	1%	6%
% Below Poverty Level	19%	15%	21%	12%
% Without health insurance[b]	8%	10%	7%	11%
% Covered by Medicaid alone[b]	23%	29%	31%	27%

[a]Data pertain to ZIP Code Tabulation Areas (ZCTAs), which are the closest geographic approximation of ZIP codes. As ZCTAs can cross state and parish boundaries, the sum of the population by ZCTA may not equal to the census population data for the parish.
[b]Data pertain to civilian, non-institutionalized population only.
[c]Includes ZIP codes 71404, 71407, 71423, 71432, 71454, 71467.

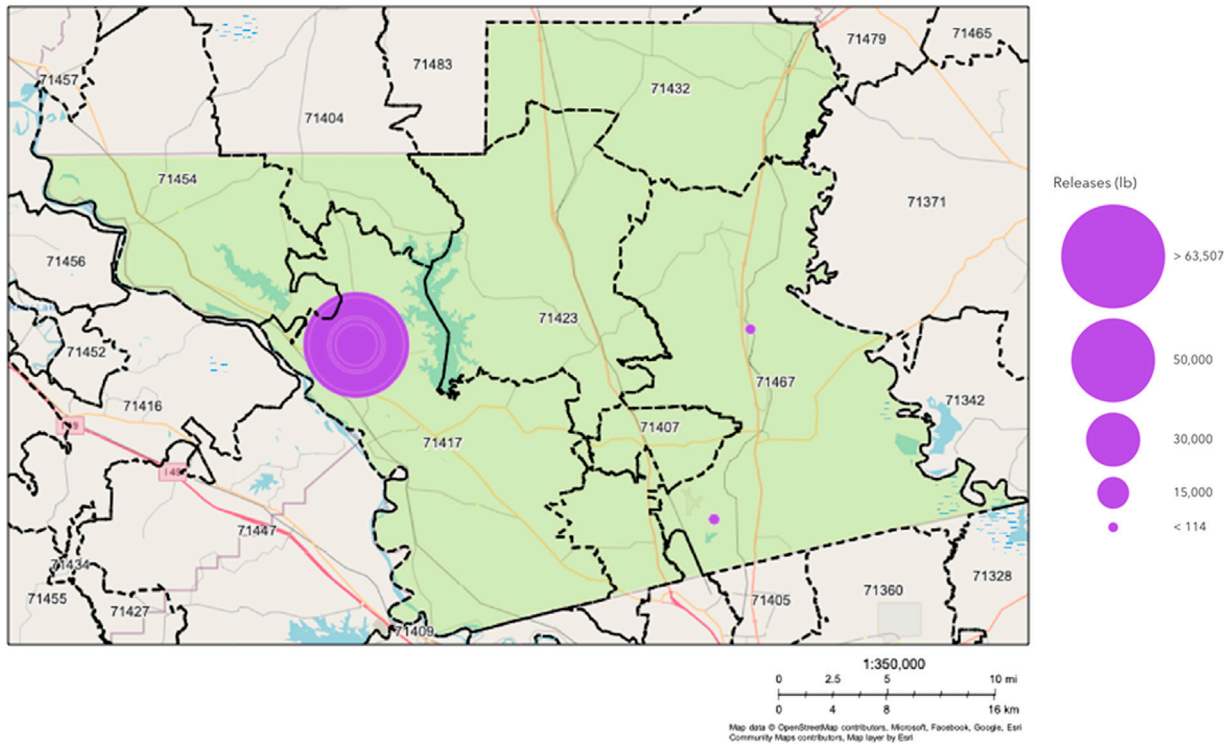

FIGURE 1
Map from EPA's Toxic Release Inventory (TRI) showing the location of the thermal-treatment plant at Clean Harbors Colfax, LLC and two other TRI sites in Grant Parish, LA (shown in green). Purple dots show TRI sites with their relative sizes indicating the relative amount of toxic land release in pounds in 2015. Air release is declared to be 0 pounds at the Clean Harbors Site.

TABLE 2 Toxic Release Inventory (TRI) Land Release data in Colfax (ZIP code 71417) and Grant Parish (2015). Note that Air Release data are listed as 0 in the TRI.

Characteristics	ZIP 71417 (Colfax)	Grant Parish
Number of TRI-reporting facilities within boundaries	1	3
Total chemical release (lb)	63,507.5	64,030.8
Lead and lead compounds (lb)	27,185	27,708
Dioxin and dioxin-like compounds (lb)	0	0.166
Copper and copper compounds (lb)	11,392	11,392
Mercury compounds (lb)	72.5	72.5
Nitroglycerin (lb)	24,858	0

rate stability, considering the small size of the Colfax population. Using these data, we tested the hypothesis that the community of Colfax has a disproportionately high burden of respiratory and cardiovascular diseases compared to the surrounding areas, based on the current literature on the health hazards of exposure to residual hazardous constituents from thermal treatment of explosive and other hazardous wastes.

Materials and methods

Population data

Decennial census data for 2000 and 2010 were obtained from the United States Census Bureau (USCB) for the state of Louisiana, Grant Parish, and Grant Parish's ZIP Code Tabulation Areas (ZCTA; the closest geographic approximation of a ZIP code). As intercensal population estimates are unavailable at the ZCTA-level from USCB for the entire study period, the population for years 2001 through 2018 was extrapolated based on the average annual rate of change in the population for each geography between 2000 and 2010. These individual years of population estimates were then summed for the individual ZCTAs, Grant Parish and the state to create the cumulative population estimate for the 19-year study period.

Inpatient discharge and mortality records

Based on availability of data when the study was conceived, statewide hospital inpatient discharge and mortality data for the years 2000–2018 were obtained from LDH. Inpatient discharge reporting data often lags by a year; thus, data from 2019 onwards could not be included due to disruptions in the regular reporting system in 2020 due to COVID-19. The 19-year study period was selected to maximize the study size given the small population of Colfax (Table 1). SAS Enterprise Guide® 7.1 was used to extract hospitalization and mortality counts from the respective databases using recorded diagnosis/mortality codes from the International Classification of Diseases (ICD). In the United States, the transition from using ninth-edition (ICD9) to tenth-edition (ICD10) diagnosis codes began in the fourth quarter of 2015; therefore, both ICD9 and ICD10 codes were utilized for this study period. The ICD9 codes used were 390–459 for cardiovascular and circulatory diseases; 460–519 for respiratory diseases; 240–246 for thyroid diseases; and 690–698 for skin inflammation. The ICD10 codes used were I00-I99 for cardiovascular and circulatory diseases; J00-J99 for respiratory diseases; E00-E07 for thyroid diseases; and L20-L30 for skin inflammation. Specific diseases considered included asthma, chronic obstructive pulmonary disease (COPD), lung cancer, respiratory tract infection, hypertension, ischemia, and arrhythmia (Supplementary Material S1). Diseases were selected based on the current evidence of health impact associated with PM exposure as well as community concerns [19, 20]. Estimated prevalence for all disease conditions were calculated from the inpatient discharge data by extracting all records where any of the ICD codes of interest were recorded as a primary or secondary diagnosis code, thus identifying current and underlying respiratory, cardiovascular, thyroid and inflammatory skin diseases among all hospitalized patients. A similar protocol was applied to the mortality data; cases were extracted that recorded the disease of interest (cardiovascular and respiratory) as one of the causes of death. Thyroid and inflammatory skin disorders were excluded from the mortality assessments due to low case counts. Each case was then categorized by the diseases they represented and assigned a geography based on the patient's ZIP code of residence.

Crude rates of hospitalization and mortality with the diseases of interest were calculated by dividing the number of cases in each geography by the total population and multiplying by a factor of 10,000. These were then adjusted for age, sex assigned at birth (male/female) and race (Black/White) to the 2000 U.S. Standard Population. Age groups used for age-adjustment included 0–11 months, 1–17 years, 18–59 years, 60–74 years

TABLE 3 Estimated prevalence of cardiovascular, respiratory, thyroid and inflammatory skin diseases among hospitalized residents of Colfax (ZIP code 71417), other ZIP codes in Grant Parish, and Louisiana, adjusted for age, sex and race (2000–2018). Age-adjusted rates also presented stratified by race and sex, except for diseases with <=20 cases in Colfax that yielded unstable estimates due to low number of cases.

Health condition	ZIP code 71417 (Colfax)	Other Grant Parish ZIP codes	Louisiana
Age, sex, race-adjusted rates per 10,000 population			
All Cardiovascular[a,b]	477	434	364
Arrhythmia[b,c]	100	121	92
Ischemia[b]	170	176	120
Hypertension[a,b]	363	343	285
All respiratory[a,b]	254	243	182
Asthma[b]	35	38	27
COPD[b]	78	83	57
Lung Cancer[a,b]	10	7	7
Respiratory Tract Infections[a,b]	114	105	66
Thyroid disorders[b]	84	79	62
Skin inflammation	7	6	6
Age-adjusted rates per 10,000 Black residents			
All cardiovascular[a,b]	546	341	463
Arrhythmia[a,b]	103	87	82
Ischemia[a,b]	177	142	121
Hypertension[a,b]	467	301	392
All respiratory[a,b]	232	200	203
Asthma[a,b]	59	46	41
COPD[c]	46	65	52
Respiratory Tract Infections[a,b]	106	87	72
Thyroid disorders[a,b]	53	31	42
Age-adjusted rates per 10,000 White residents			
All cardiovascular[a,b]	473	434	354
Arrhythmia[c]	102	126	96
Ischemia[b]	174	184	123
Hypertension[b]	350	334	272
All respiratory[a,b]	262	242	181
Asthma[b]	30	34	25
COPD[b]	85	87	59
Respiratory Tract Infections[a,b]	118	107	66
Thyroid disorders[b]	88	81	65
Age-adjusted rates per 10,000 Female residents			
All cardiovascular[a,b]	549	465	400
Arrhythmia[b,c]	102	124	88

(Continued on following page)

TABLE 3 (*Continued*) Estimated prevalence of cardiovascular, respiratory, thyroid and inflammatory skin diseases among hospitalized residents of Colfax (ZIP code 71417), other ZIP codes in Grant Parish, and Louisiana, adjusted for age, sex and race (2000–2018). Age-adjusted rates also presented stratified by race and sex, except for diseases with <=20 cases in Colfax that yielded unstable estimates due to low number of cases.

Health condition	ZIP code 71417 (Colfax)	Other Grant Parish ZIP codes	Louisiana
Ischemia[b]	159	152	104
Hypertension[a,b]	442	367	321
All respiratory[b]	271	269	202
Asthma[a,b]	58	49	42
COPD[b,c]	65	94	58
Respiratory Tract Infections[b]	119	116	71
Thyroid disorders[b,c]	109	120	84
Age-adjusted rates per 10,000 Male residents			
All cardiovascular[a,b]	514	415	426
Arrhythmia	119	128	113
Ischemia[b]	214	219	164
Hypertension[a,b]	389	309	330
All respiratory[a,b]	262	223	202
Asthma	24	24	21
COPD[b]	88	82	64
Respiratory Tract Infections[a,b]	119	101	77
Thyroid disorders[b]	48	42	37

[a]Colfax rate significantly higher than the rate for other ZIP codes in Grant Parish ($P < 0.05$).
[b]Colfax rate significantly higher than the statewide average ($P < 0.05$).
[c]Colfax rate significantly lower than the rate for other ZIP codes in Grant Parish ($P < 0.05$).

and 75 years and older [21]. These age groups were selected based on the differing immunological states of infants, children, young adults and older adults [22, 23]. Other assigned sex and race could not be considered due to very low case counts. Rates were determined for the Colfax ZIP code (71417), Grant Parish excluding the Colfax ZIP code and the state of Louisiana. In order to evaluate differences in cardiovascular and respiratory health outcomes by race and sex, age-adjusted rates were stratified by race (Black and White) and assigned sex (female and male). Certain diseases, including thyroid, skin, asthma and arrhythmia, were excluded from the mortality data analysis due to low case counts. Relative rates were calculated by dividing the Colfax rate by a reference value (i.e., the rate for Grant Parish excluding Colfax or Louisiana). Calculations were conducted using the unconditional maximum likelihood method ('Wald') using the *epitools* package (version 5-10.1) in R (4.3.1). All 95% CI for adjusted and relative disease rates were calculated using normal approximation. Differences in disease rates were considered statistically significant if the 95% confidence intervals (CI) of the groups did not overlap). Relative rates where the 95% CI did not include the value of 1.0 was considered statistically significant.

Results

Estimated prevalence of cardiovascular, respiratory and other diseases among hospitalized Residents of Colfax, LA

The rate for presence of cardiovascular disease among hospitalized Colfax residents (2000–2018), adjusted for age, sex and race, was 1.30 times the state average (95% CI: 1.27–1.35; $p < 0.0001$) and 1.10 times that of Grant Parish excluding Colfax (95% CI: 1.06–1.13; $p < 0.0001$) (Table 3; Figures 2A,B). Of the specific cardiovascular diseases examined, hypertensive and ischemic disorders followed a similar trend, though the estimated prevalence of ischemia was comparable across all ZIP codes of Grant Parish, and only significantly elevated in Colfax relative to the state average. A contrasting trend was observed for arrhythmia, whose estimated prevalence in Colfax was significantly lower compared to surrounding areas of Grant Parish, though slightly elevated relative to Louisiana.

The rates for the presence of respiratory disease among hospitalized Colfax residents (2000–2018) were similarly

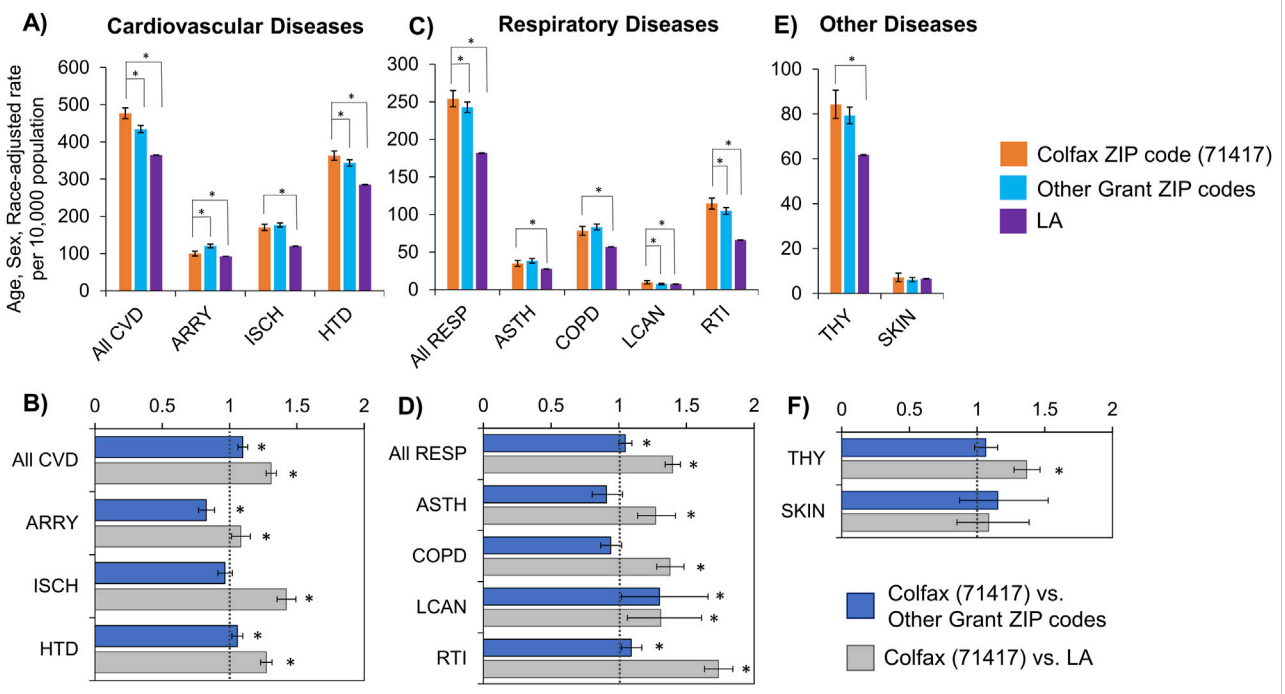

FIGURE 2
Rates **(A,C,E)** and rate ratios **(B,D,F)** for hospitalizations with cardiovascular **(A,B)**, respiratory **(C,D)**, thyroid and skin **(E,F)** diseases, adjusted for age, sex and race. Statistically significant differences between Colfax and a comparing geography at $\alpha = 0.05$ are marked with an asterisk (*). CVD, Cardiovascular diseases; ARRY, Arrhythmias; ISCH, Ischemia; HTD, Hypertensive disorders; RESP, Respiratory diseases; ASTH, Asthma; COPD, Chronic Obstructive Pulmonary Disease; LCAN, Lung cancer; RTI, Respiratory Tract Infections; THY, Thyroid diseases; SKIN, Skin diseases.

elevated compared to surrounding areas, after adjusting for age, sex and race (Table 3; Figures 2C,D). The Colfax rate for the study period was 1.40 times the state rate (95% CI: 1.34–1.45; $p < 0.0001$), and approximately 5% higher than the parish rate excluding Colfax ($p < 0.047$). The four specific respiratory diseases evaluated (asthma, COPD, lung cancer and respiratory tract infections) followed a similar trend where the Colfax rate was 27%–73% higher than the state rate, but similar to the parish rate excluding Colfax.

After adjusting for age, sex and race, rates for thyroid disorders among hospitalized residents of Colfax was slightly but not significantly higher than that of other residents of Grant Parish; however, it was significantly higher than the statewide average by 36% ($P < 0.0001$). No significant difference was noted regarding skin disorders between residents of Colfax and other areas of the parish or the state (Table 3; Figures 2E,F).

Age-adjusted rates for all diseases were also stratified by race and sex to identify disparities among subgroups (Table 3). The burden of cardiovascular and respiratory diseases overall remained higher in Colfax regardless of race or sex (Figure 3). However, when individual disease rates were examined by race, Black residents of Colfax exhibited a higher burden of disease relative to Black population elsewhere in Grant Parish whereas rates were often comparable for White persons across all ZIP codes in Grant Parish (Supplementary Figure S1). Some differences were noted by sex, as well. Differences in overall respiratory disease prevalence between Colfax and other areas of Grant Parish was noted among males but not females (Figure 3). However, a difference in asthma prevalence between Colfax and other areas of Grant Parish was noted among females and not males (Supplementary Figure S1).

Estimated mortality resulting from cardiovascular and respiratory diseases among Residents of Colfax, LA

The cardiovascular mortality rate in Colfax (2000–2018), adjusted for age, sex and race, was 2.44 times the state rate (95% CI: 2.24–2.64; $p < 0.0001$), and 1.17 times the parish rate excluding Colfax (95% CI: 1.07–1.29; $p = 0.0009$) (Table 4, Figures 4A,B). Of the specific cardiovascular diseases examined, mortality rates with hypertension and ischemic events were significantly higher than those of surrounding regions. Deaths in Colfax, where hypertension was recorded as a cause of death, was 1.34 times that of the rest of Grant Parish (95% CI: 1.11–1.62; $p = 0.002$) and 2.34 times that of the state (95%

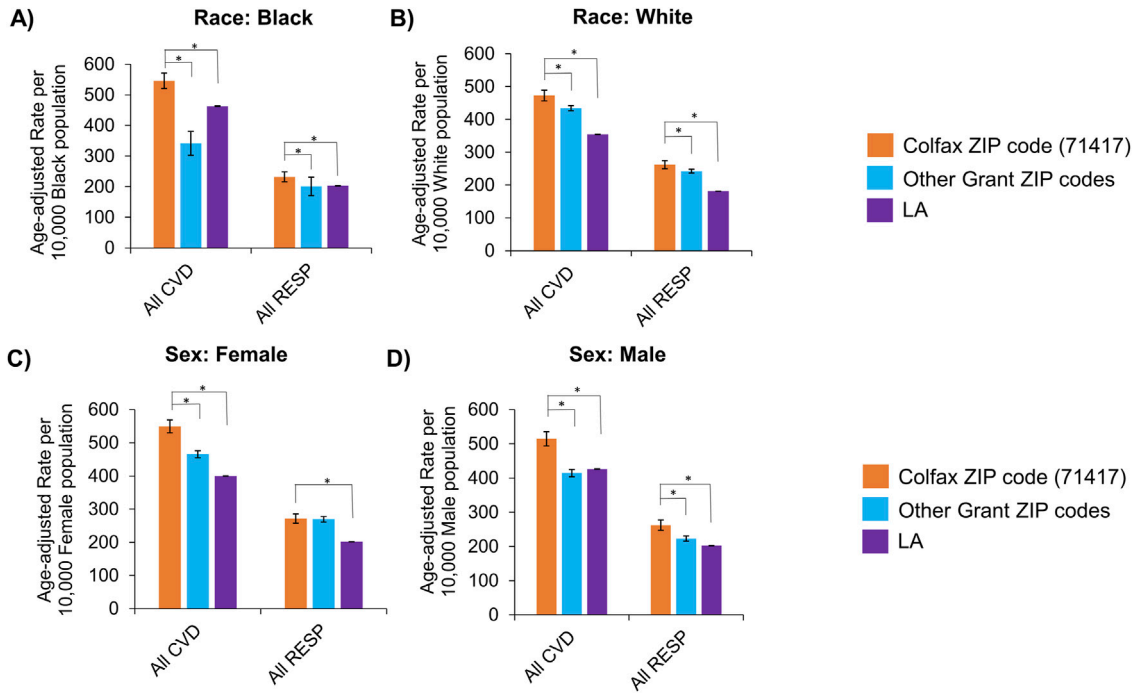

FIGURE 3
Age-adjusted rates of hospitalizations with any cardiovascular (CVD) or respiratory (RESP) disease, stratified by race **(A,B)** and assigned sex **(C,D)**. Race categories shown include Black **(A)** and White **(B)**; other groups could not be examined due to small sample sizes. Sexes apart from female **(C)** and male **(D)** that may have been assigned also could not be assessed for the same reason. Statistically significant differences between Colfax and a comparing geography at $\alpha = 0.05$ are marked with an asterisk (*). Error bars represent the 95% confidence interval.

CI: 1.99–2.75; $p < 0.0001$). Similar trends were observed for ischemia as well.

The mortality rate in Colfax for all respiratory disease conditions was 2.36 times the state rate (95% CI: 2.08–2.68; $p < 0.0001$) (Table 4, Figures 4C,D). This pattern was consistent for the individual respiratory health conditions examined from the mortality records, including COPD, lung cancer and respiratory tract infections. No major differences were observed for Colfax relative to other Grant Parish ZIP codes.

Age-adjusted mortality rates in Colfax were also examined stratified by race, and compared for people of the corresponding race residing in surrounding areas and the state. Among Black Colfax residents (Table 4, Figures 5A,B), the mortality rate with cardiovascular disease was 2.48 times the state rate for Black individuals (95% CI: 2.19–2.80; $p < 0.0001$), and 1.64 times the rate for Grant Parish excluding Colfax (95% CI: 1.35–1.99; $p < 0.0001$). Among White individuals (Table 4, Figures 5C,D), the age-adjusted mortality rate with cardiovascular disease was 2.43 times the state rate for White persons (95% CI: 2.20–2.69; $p < 0.0001$) and 1.22 times the rate for White residents of other areas of Grant Parish (95% CI: 1.003–1.265; $p = 0.0443$). The respective trends for Black and White individuals were noted for hypertension and ischemia when examined specifically as well.

Age-adjusted mortality rate, with respiratory disease as a cause of death, among Black Colfax residents was 2.63 times the state rate for Black individuals (95% CI: 2.15–3.21; $p < 0.0001$) and 1.41 times the rate for Grant Parish excluding Colfax (95% CI: 1.04–1.90; $p = 0.0269$) (Table 4, Figures 5A,B). The mortality rate with respiratory disease for White individuals in Colfax was 2.34 times the state rate for White Louisianans (95% CI: 2.01–2.739; $p < 0.0001$) but not significantly different from White residents of other parts of Grant Parish. The respective trends by race were consistent when examined for the specific respiratory health conditions: COPD, lung cancer, and respiratory tract infections (Table 4, Supplementary Figure S2).

Similar results were observed when stratified by sex as well. Among females, the age-adjusted mortality rate with cardiovascular disease was 2.56 times the statewide rate for females (95% CI: 2.28–2.87; $p < 0.0001$) and 1.20 times the rate for other Grant Parish ZIP codes (95% CI: 1.04–1.37; $p = 0.0093$) (Table 4, Figures 5C,D). The rate ratios for mortality with cardiovascular disease remained comparable in the male population (Table 4, Figures 5C,D). When examined specifically, trends for ischemia were similar to that of

TABLE 4 Estimated mortality adjusted for age, sex and race, where cardiovascular and respiratory diseases were recorded as a cause of death, in Colfax (ZIP code 71417), other ZIP codes in Grant Parish and Louisiana (2000–2018). Age-adjusted rates also presented stratified by race and sex. Diseases with ≤20 cases in Colfax, LA excluded as they yielded unstable estimates due low case counts.

Cause of death	ZIP code 71417 (Colfax)	Other Grant Parish ZIP codes	Louisiana
Age, sex, race-adjusted rates per 10,000 residents			
All Cardiovascular[a,b]	63	54	26
Ischemia[a,b]	28	22	10
Hypertension[a,b]	12	16	7
All respiratory[b]	27	27	11
COPD[b]	11	12	4
Lung Cancer[b]	6	7	3
Respiratory Tract Infections[b]	17	19	7
Age-adjusted rates per 10,000 Black residents			
All cardiovascular[a,b]	81	49	32
All respiratory[a,b]	30	21	11
Age-adjusted rates per 10,000 White residents			
All cardiovascular[a,b]	62	55	25
All respiratory[b]	27	28	12
Age-adjusted rates per 10,000 Female residents			
All cardiovascular[a,b]	61	51	24
Ischemia[a,b]	23	18	8
Hypertension[b]	15	12	7
All respiratory[b]	25	25	10
COPD[b]	9	12	4
Lung Cancer[b]	5	5	2
Respiratory Tract Infections[b]	16	18	6
Age-adjusted rates per 10,000 Male residents			
All cardiovascular[a,b]	75	57	31
Ischemia[a,b]	37	26	13
Hypertension[a,b]	20	12	8
All respiratory[b]	31	30	14
COPD[b]	12	15	5
Lung Cancer[b]	9	10	4
Respiratory Tract Infections[b]	20	23	9

[a]Colfax rate significantly higher than the rate for other ZIP codes in Grant Parish ($P < 0.05$)
[b]Colfax rate significantly higher than the statewide average ($P < 0.05$)

cardiovascular diseases overall. However, mortality due to hypertension was only elevated significantly among male residents of Colfax relative to other male population of Grant Parish; no difference was noted for females (Supplementary Figure S2). Significant difference in mortality due to respiratory diseases were noted only between Colfax and Louisiana for both males and females, where the Colfax rate was about twice the state rate for the corresponding population ($p < 0.0001$). This trend remained consistent for all specific respiratory diseases examined.

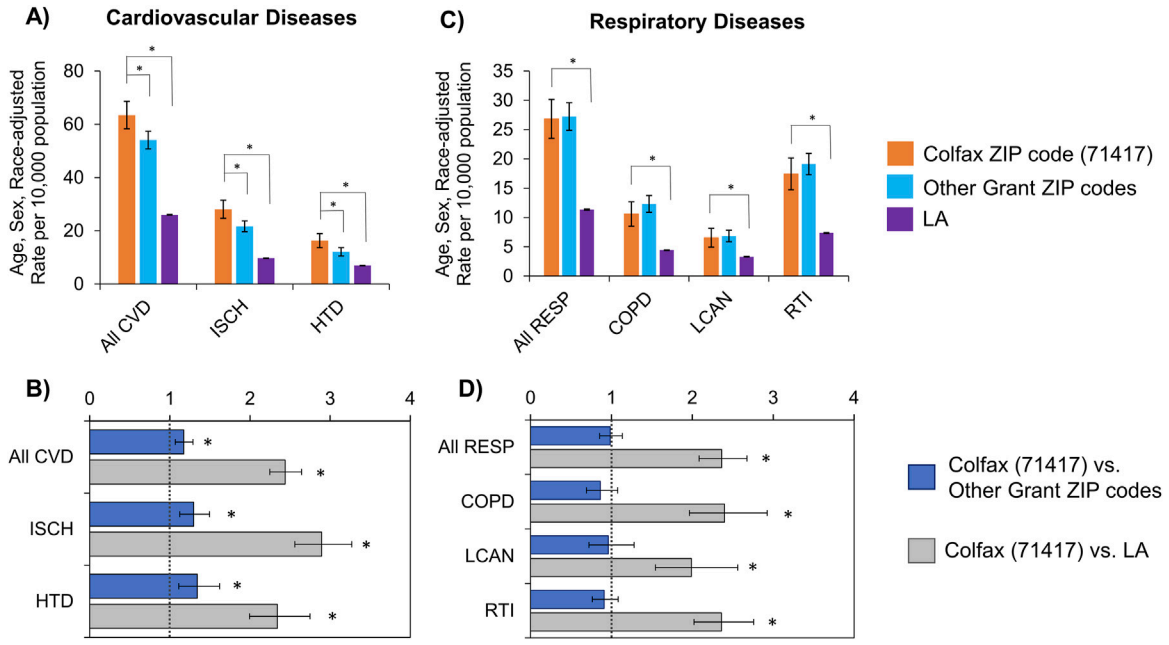

FIGURE 4
Rates **(A,C)** and rate ratios **(B,D)** for mortality, where a cardiovascular **(A,B)** and respiratory disease **(C,D)** was recorded as a cause of death, adjusted for age, sex and race. Statistically significant differences between Colfax and a comparing geography at $\alpha = 0.05$ are marked with an asterisk (*). CVD, Cardiovascular diseases; ISCH, Ischemia; HTD, Hypertensive disorders; RESP, Respiratory diseases; COPD, Chronic Obstructive Pulmonary Disease; LCAN, Lung cancer; RTI, Respiratory Tract Infections. Rates for arrhythmia- and asthma-related mortality were unstable due to small counts; hence not shown.

Discussion

In this study, we evaluated the association between residency near a hazardous waste OB/OD facility and hospitalization for cardiovascular, respiratory, thyroid, or skin disease along with mortality from cardiovascular or respiratory disease. This is the first study to examine the impact of living in the 71417 ZIP code (i.e., the community of Colfax, LA) on specific causes of morbidity and mortality. After adjusting for age, sex and race for the study period (2000–2018), our study found a significant increase in cardiovascular and respiratory diseases as a primary or secondary diagnosis at discharge among hospitalized patients in Colfax, LA compared to residents of other ZIP codes of Grant Parish. In addition, residents of Colfax experienced higher mortality with cardiovascular diseases, including ischemia and hypertension. Residents of Colfax were also more likely to have respiratory diseases, like lung cancer and respiratory tract infections, recorded as a diagnosis code, compared to residents of other ZIP codes of Grant Parish. Mortality rates due to respiratory diseases were higher in Colfax than the statewide rate but were similar across Grant Parish (Figures 2, 4).

Since Colfax has a higher proportion of Black residents compared to surrounding areas in Grant Parish, and it is well known that Black Americans tend to face worse cardiovascular and respiratory health outcomes than White Americans [24–26], we compared health outcomes across geographies normalized by race. This analysis revealed disproportionately higher rates of cardiovascular and respiratory diseases overall among both Black and White Colfax residents who were hospitalized, compared to the corresponding population residing elsewhere in the parish (Figure 3). Mortality resulting from cardiovascular diseases was also elevated among Colfax's Black and White residents compared to residents of the respective race elsewhere in the parish (Figure 5). This indicates that residents of Colfax, regardless of their race, may be affected by environmental factors specific to the area of residence that are not experienced by people living elsewhere in Grant Parish. The data further suggested that Black residents of Colfax experienced greater prevalence and mortality relative to Black people residing elsewhere in Grant Parish, whereas health outcomes were more similar for all White residents across all ZIP codes of Grant Parish (Supplementary Figures S1, S2). Due to the low Black population in other ZIP codes of Grant Parish except Colfax (ZIP code 71417), further investigation is warranted to evaluate potential interactions in place- and race-based disparities for specific disease states in Grant Parish.

Study limitations are balanced by insights gained from our analyses. Hospitalization rates are presented adjusted for age, sex and race at the individual level in an attempt to isolate place-based differences in health outcomes. It is important to

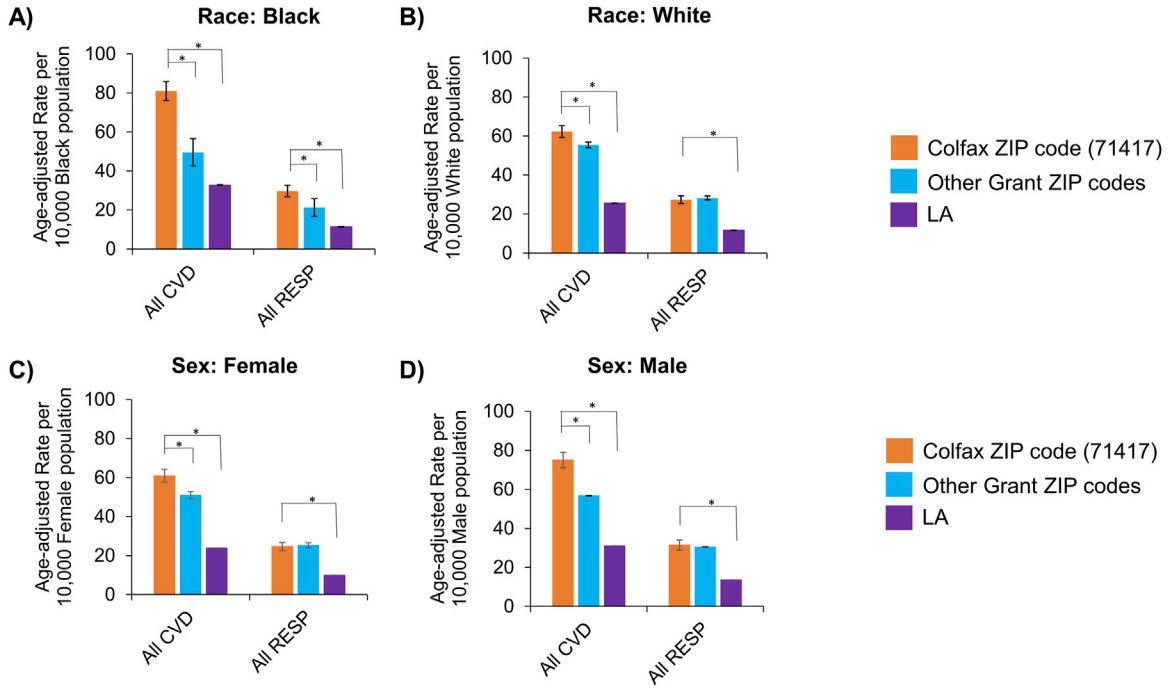

FIGURE 5
Age-adjusted mortality rate due to any cardiovascular (CVD) or respiratory (RESP) disease, stratified by race **(A,B)** and assigned sex **(C,D)**. Race categories shown include Black **(A)** and White **(B)**; other groups could not be examined due to small sample sizes. Sexes apart from female **(C)** and male **(D)** that may have been assigned also could not be assessed for the same reason. Statistically significant differences between Colfax and a comparing geography at $\alpha = 0.05$ are marked with an asterisk (*). Error bars represent the 95% confidence interval.

emphasize that children and older adults represent particularly vulnerable subpopulations in the context of environmental exposures. Due to their developing or aging physiological systems, these groups are more susceptible to the adverse health effects of airborne pollutants and contaminated water, such as those associated with open burning of hazardous wastes [27, 28]. Children inhale more air per body weight and have immature detoxification systems, while older adults often have pre-existing health conditions that can be exacerbated by environmental stressors [29]. Future studies should prioritize evaluating health outcomes in these age groups to better understand and mitigate the long-term impacts of environmental exposures in rural communities like Colfax. Age-adjusted rates are also stratified by race and sex to show differences across geographies within each sub-population. However, we note that hospital discharge data likely underreports the true disease burden, as it only cites data from hospitals within the state and cannot account for either individuals who were not hospitalized at any point during the 19-year study period or those who sought care out-of-state. Our method of estimating disease burden relied on hospital staff recording not just primary but also secondary diagnosis codes for the disease conditions evaluated. Hospital reporting to the state varies annually, potentially causing the database to miss some inpatient encounters. Though many of these limitations (e.g., underreporting and missing data) could result in an underestimation of morbidity and mortality, it is expected that most sources of error would be consistent across the state and therefore the relative difference between geographies would remain unaffected. Even if underreporting were more severe in rural areas, our detection of differences between the Colfax ZIP code and the state would only be an underestimation. In other words, the differences between Colfax and the state of Louisiana would be even larger if urban-rural effects on data quality were removed. This speaks to the strength of our approach to geographic comparison involving rural areas in the absence of having a sufficiently large sample population for estimating exposure-response relationships.

High spatial resolution is essential in environmental health disparities studies to effectively identify correlations between pollution, health outcomes, and demographic characteristics. [30]. The rural nature of Colfax required use of the entire 71417 ZIP code to protect the identity of individuals included in the hospital database. The 71417 ZIP code is 365 km^2 in area, and the OBOD facility is 25 km from the southeast corner of the ZIP code. Moreover, the meteorological characteristics of the area are often stable, with high humidity and calm wind conditions 48% of the time over the study duration. Winds

flow from the south 24% of the time, and winds emanate from all other directions with roughly equal frequency over the remaining 28% of the time [31]. As a retrospective community health study, we did not collect air pollution surface measurements, as attributing spatially resolved exposures to health outcomes among the 71,417 residents would require detailed information on individuals' residential history, occupational exposures, and other relevant factors. Although lack of environmental data and coarse resolution are limitations, comparison with the remainder of Grant Parish and with the remainder of the State of Louisiana allowed for some exploration of the role of source proximity in exposures among different population subgroups. This more coarse resolution was still sufficient to detect a statistically significant effect.

Other study limitations involve the lack of available data surrounding genetic or lifestyle factors (e.g., smoking, exercise), most social determinants of health (e.g., poverty status, housing and food insecurity, and preventative healthcare access), indoor/outdoor environmental exposures arising from industrial or agricultural activities, and length of time lived in the specified area of residence at the time of hospitalization—all of which can affect hospitalization and mortality rates, especially in rural areas [32]. Combined with the retrospective ecological design and lack of contemporaneous local air pollutant data or exposure assessments in the area, no correlation or causal inference studies could be performed between the disease burden and known anthropogenic sources of fine PM pollution in the region (e.g., biomass burning for land management [33]). Despite the limitations, it is apparent that Colfax, LA suffers a disproportionate disease burden compared to the rest of Grant Parish and the state. We speculate that exposure to hazardous air pollutants contributes to the disease burden in Colfax, which is consistent with the previously observed increased cancer rates [18] and acrolein levels reported by LDH [34]. Future studies analyzing long-term longitudinal pollutants present in the area and further investigation into potential underlying causes of the increased cardiovascular and respiratory disease burden would greatly benefit the community.

Further, we emphasize the need to develop rigorous methods for analyzing the effects of localized pollution sources for similarly small and potentially at-risk locations like Colfax, LA. Future studies need to focus on geocoding street addresses to a particular point location, possibly combined with population survey and interview data (i.e., mixed methods approaches), to be able to conduct epidemiological studies at smaller scales in rural places, while protecting patient privacy. Use of newer technology may help to identify places that are comparable to Colfax in terms of socioeconomic and demographic characteristics but dissimilar in terms of its environmental characteristics, which could then help to isolate the attributable fraction of the environment on the observed disease burden. Additional resources should be devoted to designing and implementing prospective cohort studies in the area, in collaboration with the community members. By carefully documenting individual health metrics, exposures, potential confounding factors and tracking health outcomes longitudinally, it is more likely that causal inference can be drawn. In the meantime, greater efforts need to be made to ensure at-risk community members have the resources to manage their underlying health conditions. Finally, use of artificial intelligence and machine learning may help public health and research professionals test possible interventions as simulations conducted on synthetic populations that then help to identify specific interventions that can improve health outcomes in the area.

Conclusion

By calculating the estimated prevalence from the inpatient discharge database, we report a higher burden of cardiovascular and respiratory diseases in the rural community of Colfax, Louisiana (2000–2018), after adjusting for age, sex and race. Mortality associated with these conditions was also significantly higher in Colfax compared to other areas of Grant Parish and Louisiana. These data demonstrate the need for more in-depth studies to understand the differences in rates of hospitalizations and mortality associated with living in the Colfax ZIP code (71417) and to determine if these health impacts are associated with air pollution emitted from the nearby open burning of hazardous wastes. This study also highlights the importance of developing novel methods to estimate disease prevalence in rural regions where low population density leads to data exclusion due to privacy concerns, low statistical power, and data instability, thereby hindering precise prevalence measurements. Further, the lack of infrastructure for consistent, long-term environment and health measurements pose additional challenges specific to addressing environmental health disparities in small, rural populations. Overcoming these challenges will require innovative statistical solutions that help to make "no community. . .invisible" [35].

Author contributions

AB, LB, and SC conceived of the study. AB, MA-M, QY, JR-B, and SC analyzed and interpreted the final data. AB was a major contributor in writing the final manuscript. AB, QY, JR-B, and SC wrote or revised select portions of the manuscript. All authors contributed to the article and approved the submitted version.

Author disclaimer

The content is solely the responsibility of the authors and does not necessarily represent the official views of LDH or NIH.

Data availability

The data analyzed in this study is subject to the following licenses/restrictions: The raw data underlying this study are available from the Louisiana Department of Health (LDH), but restrictions apply due to the need to protect patient confidentiality, and as such, the data are not publicly accessible. Aggregated and deidentified data, with appropriate suppression to safeguard privacy, may be obtained from the authors upon reasonable request and with prior approval from LDH. Requests to access these datasets should be directed to https://ldh.govqa.us/WEBAPP/_rs/(S(b4niape4vnpgud4fb4byeyxi))/SupportHome.aspx?sSessionID=&lp=2.

Ethics statement

The studies involving humans were approved by Louisiana Department of Health and Louisiana State University IRB#4378. The studies were conducted in accordance with the local legislation and institutional requirements. Written informed consent for participation was not required from the participants or the participants' legal guardians/next of kin in accordance with the national legislation and institutional requirements.

Funding

The author(s) declare that financial support was received for the research and/or publication of this article. This work was supported by the National Institute of Environmental Health Sciences (P42 ES013648, R21 ES036500, P30 ES025128), National Cancer Institute (R01 CA275089) and National Institute on Minority Health and Health Disparities (R15 MD012387).

Acknowledgments

This was a collaborative effort between members of Louisiana State University Superfund Research Program.

Conflict of interest

The author(s) declared no potential conflicts of interest with respect to the research, authorship, and/or publication of this article.

Generative AI statement

The author(s) declare that no Generative AI was used in the creation of this manuscript.

Any alternative text (alt text) provided alongside figures in this article has been generated by Frontiers with the support of artificial intelligence and reasonable efforts have been made to ensure accuracy, including review by the authors wherever possible. If you identify any issues, please contact us.

Supplementary material

The Supplementary Material for this article can be found online at: https://www.ebm-journal.org/articles/10.3389/ebm.2025.10710/full#supplementary-material

SUPPLEMENTARY FIGURE 1
Heat map showing rate ratios for age-adjusted hospitalizations, stratified by race (Black, White) and sex (female, male). Values greater than one (orange) and less than one (green) indicate significantly higher and lower rate in Colfax, respectively, relative to the reference geography, for the sub-population as noted ($P < 0.05$). Grey shading indicates no statistically significant difference. Asterisks (*) indicate rate ratios based on unstable rates calculated with counts <=20. CVD, Cardiovascular diseases; ARRY, Arrhythmias; ISCH, Ischemia; HTD, Hypertensive disorders; RESP, Respiratory diseases; ASTH, Asthma; COPD, Chronic Obstructive Pulmonary Disease; LCAN, Lung cancer; RTI, Respiratory Tract Infections; THY, Thyroid diseases; SKIN, Skin diseases.

SUPPLEMENTARY FIGURE 2
Heat map showing rate ratios for age-adjusted mortality, stratified by race (Black, White) and sex (female, male). Values greater than one (orange) and less than one (green) indicate significantly higher and lower rate in Colfax, respectively, relative to the reference geography, for the sub-population as noted ($P < 0.05$). Grey shading indicates no statistically significant difference. Asterisks (*) indicate rate ratios based on unstable rates calculated with counts <=20. CVD, Cardiovascular diseases; ARRY, Arrhythmias; ISCH, Ischemia; HTD, Hypertensive disorders; RESP, Respiratory diseases; ASTH, Asthma; COPD, Chronic Obstructive Pulmonary Disease; LCAN, Lung cancer; RTI, Respiratory Tract Infections; THY, Thyroid diseases; SKIN, Skin diseases.

References

1. DeMarini DM, Warren SH, Lavrich K, Flen A, Aurell J, Mitchell W, et al. Mutagenicity and oxidative damage induced by an organic extract of the particulate emissions from a simulation of the deepwater horizon surface oil burns. *Environ Mol Mutagenesis* (2017) **58**(3):162–71. doi:10.1002/em.22085

2. Gullett BK, Aurell J, Williams R. *Characterization of air emissions from open burning and open detonation of Gun propellants and ammunition*. Washington, DC: United States Environmental Protection Agency (2016).

3. National Academies of Sciences E, and Medicine. *Alternatives for the demilitarization of conventional munitions*. Washington, DC: The National Academies Press (2019).

4. Truong H, Lomnicki S, Dellinger B. Potential for misidentification of environmentally persistent free radicals as molecular pollutants in particulate matter. *Environ Sci Technol* (2010) **44**(6):1933–9. doi:10.1021/es902648t

5. Vejerano EP, Rao G, Khachatryan L, Cormier SA, Lomnicki S. Environmentally persistent free radicals: insights on a new class of pollutants. *Environ Sci Technol* (2018) **52**(5):2468–81. doi:10.1021/acs.est.7b04439

6. Zhang H, Zhu Y, Wang S, Zhao S, Nie Y, Liao X, et al. Contamination characteristics of energetic compounds in soils of two different types of military demolition range in China. *Environ Pollut* (2022) **295**:118654. doi:10.1016/j.envpol.2021.118654

7. BotHoS P, CotL-ThcoEtBPi I. *Long-term health consequences of exposure to burn pits in Iraq and Afghanistan*. Afghanistan: National Academies Press (2011).

8. Savitz DA, Woskie SR, Bello A, Gaither R, Gasper J, Jiang L, et al. Deployment to military bases with open burn pits and respiratory and cardiovascular disease. *JAMA Netw Open* (2024) **7**(4):e247629. doi:10.1001/jamanetworkopen.2024.7629

9. Smoot J, Padilla S, Kim YH, Hunter D, Tennant A, Hill B, et al. Burn pit-related smoke causes developmental and behavioral toxicity in zebrafish: influence of material type and emissions chemistry. *Heliyon* (2024) **10**(8):e29675. doi:10.1016/j.heliyon.2024.e29675

10. Vance SA, Kim YH, George IJ, Dye JA, Williams WC, Schladweiler MJ, et al. Contributions of particulate and gas phases of simulated burn pit smoke exposures to impairment of respiratory function. *Inhalation Toxicol* (2023) **35**(5-6):129–38. doi:10.1080/08958378.2023.2169416

11. ACS Demographic and Housing Estimates. *American community survey, ACS 5-Year estimates data profiles*. Table DP05 U.S. Census Bureau (2022). Available online at: https://data.census.gov/table/ACSDP5Y2022.DP05?q=grantparish,la (Accessed April 15, 2024).

12. Richmond-Bryant J, Odera M, Subra W, Vallee B, Tucker C, Oliver C, et al. A community-integrated geographic information system study of air pollution exposure impacts in colfax, LA. *Local Environ* (2022) **27**(6):728–46. doi:10.1080/13549839.2022.2075840

13. Wilcox JL, Entezam B, Molenaar MJ, Shreeve TR. Characterization of emissions produced by the open burning/open detonation of complex munitions: ANDRULIS RESEARCH CORP ARLINGTON VA (1996).

14. Cormier SA, Lomnicki S, Backes W, Dellinger B. Origin and health impacts of emissions of toxic by-products and fine particles from combustion and thermal treatment of hazardous wastes and materials. *Environ Health Perspect* (2006) **114**(6):810–7. doi:10.1289/ehp.8629

15. Sigmund G, Santín C, Pignitter M, Tepe N, Doerr SH, Hofmann T. Environmentally persistent free radicals are ubiquitous in wildfire charcoals and remain stable for years. *Commun Earth Environ* (2021) **2**(1):68. doi:10.1038/s43247-021-00138-2

16. Moghe A, Ghare S, Lamoreau B, Mohammad M, Barve S, McClain C, et al. Molecular mechanisms of acrolein toxicity: relevance to human disease. *Toxicol Sci* (2015) **143**(2):242–55. doi:10.1093/toxsci/kfu233

17. epa.gov/naaqs. Reviewing national ambient air quality standards (NAAQS): scientific and technical information (2025). Available online at: https://www.epa.gov/naaqs (Accessed April 12, 2024).

18. Cancer Incidence Review of Colfax, LA and Grant Parish. *Bureau of infectious diseases, section of environmental epidemiology and toxicology* (2019). Available online at: https://ldh.la.gov/assets/docs/LegisReports/HR226RS2018b.pdf (Accessed April 24, 2024).

19. Institute for Health Metrics and Evaluation. Air pollution (2024). Available online at: https://www.healthdata.org/research-analysis/health-risks-issues/air-pollution-research-library.2024 (Accessed April 24, 2024).

20. State of Global Air. *Health impacts of PM2.5. fine-particle outdoor air pollution is the largest driver of air pollution's burden of disease worldwide* (2019). p. 2024.

21. Klein RJ, Schoenborn CA. Age adjustment using the 2000 projected U.S. population. In: *PsycEXTRA dataset*. American Psychological Association APA (2001).

22. Simon AK, Hollander GA, McMichael A. Evolution of the immune system in humans from infancy to old age. *Proc R Soc B: Biol Sci* (2015) **282**(1821):20143085. doi:10.1098/rspb.2014.3085

23. Valiathan R, Ashman M, Asthana D. Effects of ageing on the immune system: infants to elderly. *Scand J Immunol* (2016) **83**(4):255–66. doi:10.1111/sji.12413

24. Caldwell JT, Ford CL, Wallace SP, Wang MC, Takahashi LM. Racial and ethnic residential segregation and access to health care in rural areas. *Health and Place* (2017) **43**:104–12. doi:10.1016/j.healthplace.2016.11.015

25. Liu J, Clark LP, Bechle MJ, Hajat A, Kim SY, Robinson AL, et al. Disparities in air pollution exposure in the United States by race/ethnicity and income, 1990-2010. *Environ Health Perspect* (2021) **129**(12):127005. doi:10.1289/EHP8584

26. Sood L, Sood V. Being African American and rural: a double jeopardy from COVID-19. *The J Rural Health* (2021) **37**(1):217–21. doi:10.1111/jrh.12459

27. Esposito S, Fainardi V, Titolo A, Lazzara A, Menzella M, Campana B, et al. How air pollution fuels respiratory infections in children: current insights. *Front Public Health* (2025) **13**:1567206. doi:10.3389/fpubh.2025.1567206

28. Dondi A, Carbone C, Manieri E, Zama D, Del Bono C, Betti L, et al. Outdoor air pollution and childhood respiratory disease: the role of oxidative stress. *Int J Mol Sci* (2023) **24**(5):4345. doi:10.3390/ijms24054345

29. Chanda F, Lin K-x, Chaurembo AI, Huang J, Zhang H, Deng W, et al. PM2.5-mediated cardiovascular disease in aging: cardiometabolic risks, molecular mechanisms and potential interventions. *Sci The Total Environ* (2024) **954**:176255. doi:10.1016/j.scitotenv.2024.176255

30. Gardner-Frolick R, Boyd D, Giang A. Selecting data analytic and modeling methods to support air pollution and environmental justice investigations: a critical review and guidance framework. *Environ Sci Technol* (2022) **56**(5):2843–60. doi:10.1021/acs.est.1c01739

31. National Centers for Environmental Information. *National centers for environmental information*. Alexandria, LA (2025).

32. Long AS, Hanlon AL, Pellegrin KL. Socioeconomic variables explain rural disparities in US mortality rates: implications for rural health research and policy. *SSM - Popul Health* (2018) **6**:72–4. doi:10.1016/j.ssmph.2018.08.009

33. Kaulfus AS, Nair U, Jaffe D, Christopher SA, Goodrick S. Biomass burning smoke climatology of the United States: implications for particulate matter air quality. *Environ Sci Technol* (2017) **51**(20):11731–41. doi:10.1021/acs.est.7b03292

34. Louisiana Department of Health. Health assessment of the Louisiana department of environmental quality's clean Harbor- colfax, LLC facility (2017). Available online at: https://ldh.la.gov/assets/oph/SEET/Clean_Harbors_Air_Assessment_Report_FINAL.pdf (Accessed April 12, 2024).

35. Chen MS. Unprecedented government/community engagement (2024). Available online at: https://obamawhitehouse.archives.gov/blog/2012/05/22/unprecedented-governmentcommunity-engagement (Accessed April 16, 2012).

EBM Experimental Biology and Medicine

TYPE Original Research
PUBLISHED 21 August 2025
DOI 10.3389/ebm.2025.10704

OPEN ACCESS

*CORRESPONDENCE
Honghui Yang,
yanghonghui@zzu.edu.cn

RECEIVED 10 June 2025
ACCEPTED 28 July 2025
PUBLISHED 21 August 2025

CITATION
Yang Y, Tu R, Zhu L, Xu G, Yang T, Li Q, Wang C and Yang H (2025) Association between systemic immune-inflammation index and 10-year risk of cardiovascular disease in the United States (NHANES 1999–2018). *Exp. Biol. Med.* 250:10704. doi: 10.3389/ebm.2025.10704

Association between systemic immune-inflammation index and 10-year risk of cardiovascular disease in the United States (NHANES 1999–2018)

Yapan Yang[1,2], Runqi Tu[3], Lijie Zhu[1,2], Guian Xu[1,2], Tingjie Yang[1,2], Qingman Li[1,2], Che Wang[1,2] and Honghui Yang[1,2]*

[1]Department of Cardiology, Central China Fuwai Hospital, Central China Fuwai Hospital of Zhengzhou University, Henan Provincial People's Hospital Heart Center, Zhengzhou, Henan, China, [2]Department of Cardiology, Henan Provincial People's Hospital, People's Hospital of Zhengzhou University, Zhengzhou, Henan, China, [3]Department of Epidemiology and Biostatistics, College of Public Health, Zhengzhou University, Zhengzhou, Henan, China

Abstract

The relationship between the systemic immune-inflammation index (SII) and the risk of developing cardiovascular disease (CVD) over the next 10 years in the United States is largely unknown. The aim of this study is to assess the association between SII and 10-year CVD risk. This population-based cross-sectional study included 9901 participants aged between 30 and 74 from the National Health and Nutrition Examination Survey (NHANES) 1999–2018. The 10-year CVD risk was calculated using the Framingham cardiovascular risk score (FRS). The Pearson test, generalized linear model (GLM) and restricted cubic splines (RCS) were used to analyze the associations between SII and the FRS. Based on the total population, the Pearson test and GLM revealed that there were positive relationships between Ln-transformed SII (Ln (SII)) and the FRS. After adjusting for confounding factors, the odds ratio (OR) for the FRS was 1.52 (95% confidence interval [CI]: 1.12–2.06) per unit increment in Ln (SII) (P = 0.009). Compared to the lowest quartile (Q1) of Ln (SII), the OR for the FRS in the highest quartile (Q4) was 1.89 (95% CI: 1.20–2.98; P = 0.007). RCS revealed that there was a linear association between Ln (SII) and the FRS (P for non-linearity = 0.972). As Ln (SII) increased, the value of FRS rose gradually (P for overall trend <0.001). However, the relationship between Ln (SII) and FRS showed ethnic heterogeneity. In conclusion, SII exhibits significant associations with 10-year CVD risk as assessed by the FRS. However, this association varies across ethnic groups, necessitating cautious application and further validation.

KEYWORDS

systemic immune inflammation index, cardiovascular disease, framingham cardiovascular risk scores, 10-year cardiovascular disease risk, inflammation

Impact statement

This study investigated the relationship between systemic immune-inflammation index (SII) and cardiovascular disease (CVD) risk. The 10-year CVD risk was calculated by Framingham cardiovascular risk scores (FRS). We found that there was a positive significant association between SII and 10-year CVD risk. Therefore, SII is expected to become an effective metric for identifying the 10-year CVD risk of human, providing well preventive strategies and improving risk stratification.

Introduction

Cardiovascular disease (CVD) is one of the most significant public health problems threatening human life. In recent years, it has remained the leading cause of death and disability worldwide in addition to being the leading cause of disease burden in the United States [1]. A report from the American Heart Association suggested that the prevalence of CVD is 48.6% in adults aged ≥20 years. Moreover, in 2020 the number of cardiovascular deaths worldwide was 19.05 million, which amounted to an increase of nearly one-fifth since 2010 [2]. Dyslipidemia, hypercoagulability, insulin resistance, hypertension, and inflammatory responses are the risk factors for the pathogenesis of CVD [3]. Based on several sex-specific multivariable risk factors, the Framingham Heart Study developed the first CVD risk equations, which were used to quantify risk and guide preventive care [4]. The Framingham Risk Score (FRS) is a widely used predictive tool that can be applied to relatively healthy individuals to estimate their probability of having a fatal or non-fatal cardiovascular event over the next decade [5, 6], and it has been used in several studies [6–8]. In addition, in recent years, inflammatory cytokines have shown promise as diagnostic tools for coronary heart disease, heart failure (HF), and other CVDs [9, 10].

With the in-depth study of chronic systemic inflammation, it has been found that inflammatory responses are connected to many different diseases [11–14]. Several immune cell types and inflammatory mediators have been implicated in the progression and pathogenesis of CVD [15, 16]. Mounting evidence suggests that chronic inflammation substantially contributes to cardiovascular risk. The Systemic Immune-Inflammation Index (SII), which is calculated using platelet, neutrophil, and lymphocyte counts, is a comprehensive biomarker that reflects both local immune responses and systemic inflammation [17]. Mechanistically, SII captures key inflammatory processes across atherogenesis. In the early phase, hemodynamic stress and lipid abnormalities appear to trigger inflammatory activation in endothelial cells, facilitating monocyte recruitment through adhesion molecules [18]. In the advanced phase, macrophage-derived inflammatory mediators promote extracellular matrix degradation via matrix metalloproteinases, increasing plaque vulnerability [19, 20]. Although SII has been established as an independent predictor of cancer, CVD and all-cause mortality [21–26], its association with the FRS — a key CVD risk assessment tool — remains unclear.

Previous studies on SII and CVD risk have several limitations. First, existing analyses have primarily assumed linear relationships, potentially overlooking complex nonlinear associations between SII and CVD outcomes. Second, there has been insufficient consideration of key lifestyle confounders, particularly comprehensive adjustment for physical activity patterns and dietary factors. Third, the integration of SII with established clinical risk prediction tools like the FRS remains unexplored in population-based studies. To address these limitations, our study specifically: (1) employs restricted cubic splines (RCS) to characterize potential non-linear relationships, (2) incorporates enhanced adjustment for objectively measured lifestyle factors including device-based physical activity and dietary intake, and (3) evaluates the relationship between SII and the FRS in a nationally representative sample. This study was based on the National Health and Nutrition Examination Survey (NHANES) to assess the association of SII with the FRS.

Materials and methods

Data and sample source

The NHANES is a cross-sectional survey conducted by the National Center for Health Statistics (NCHS) in the United States. The NCHS and the Centers for Disease Control and Prevention (CDC) conducted the survey. The NCHS' Research Ethics Review Board evaluated and approved the NHANES study protocol. The study protocol was approved by the NCHS Ethics Review Board, and all participants provided informed consent. For further confirmation, please refer to the link to the NCHS ethics approval document for the NHANES data[1]. Briefly, the NHANES uses a stratified and multistage probability approach, which surveys approximately 5,000 participants annually. The data collected includes demographic data, questionnaire data, laboratory data, examination data and limited access data.

There were a total of 101,316 participants included in the NHANES from 1999 to 2018. Of those, we excluded 62,568 participants because their age was younger than 30 or older than 74; 3,676 subjects were excluded due to imponderable total cholesterol (TC); 2 individuals were excluded due to imponderable high-density lipoprotein (HDL); 17,935 were excluded due to missing glucose; 655 participants were excluded due to imponderable blood pressure; and 58 individuals were excluded due to imponderable SII. Of 1,692 participants with CVD,448 were excluded for using NSAIDs and statins; 4,381 subjects with arthritis and thyroid disease were excluded. Finally, 9901 participants were included in this study (Figure 1).

1 www.cdc.gov/nchs/nhanes/irba98.htm

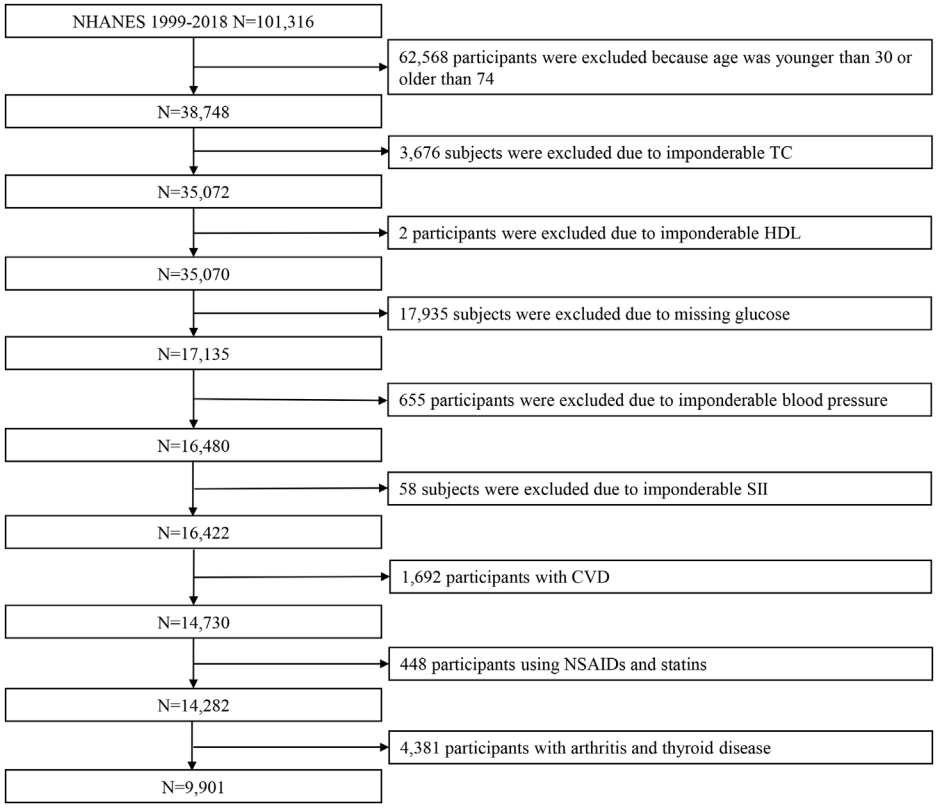

FIGURE 1
Flowchart showing the selection of participants from the NHANES from 1999 to 2018. Abbreviations: NHANES, National Health and Nutrition Examination Survey; TC, total cholesterol; HDL, high-density lipoprotein; SII, systemic immune-inflammation index; CVD, cardiovascular disease.

Systemic immune-inflammation

The SII is based on a complete blood count. Standardized protocols for measuring blood counts (platelets, lymphocytes, and neutrophils) were provided by the NHANES Laboratory Procedures Manual. More details can be found at[2]. In the present study, the following equation was utilized to calculate the SII (SII = platelet count × neutrophil count / lymphocyte count) [17]. The SII data were unevenly distributed and skewed to the right. Natural logarithmic transformation converts absolute differences into proportional changes. For clinical interpretation, Ln-transformed SII (Ln(SII)) values can be back-transformed to the original scale. A one-unit increase in Ln (SII) corresponds to an e-fold (≈2.72-fold) multiplicative change in the original SII values. Based on this, the SII data need to be Ln-transformed. Supplementary Figure S1 shows the distributional characteristics and normality assessment of SII values. (A) The histogram of the raw SII values showed extreme right-skewness. (B) The quantile-quantile plot confirmed severe non-normality (Anderson-Darling A = 617.20, $P < 0.001$). (C) The histogram of Ln (SII) showed substantial improvement, although with residual skewness. (D) The quantile-quantile plot of the transformed values demonstrated a persistent deviation from normality (A = 6.62, $P < 0.001$). The red lines represent theoretical normal distributions.

FRS

The FRS is a general 10-year risk estimate for CVD, which was developed using a Cox model based on the Framingham Heart Study [4]. In the present study, the FRS was calculated using sex, age, TC, HDL, systolic blood pressure (SBP), treatment for hypertension, smoking and diabetes. The FRS was Ln-transformed to reduce the effects of non-normality. To eliminate the potential contribution of neighborhood clustering by age and sex on neighborhood-level variance, the outcome variable used in the analysis was the normalized residual of the Ln-transformed FRS regressed on age and sex.

2 https://www.cdc.gov/nchs/nhanes/biospecimens/serum_plasma_urine.htm

Low 10-year CVD risk was defined as FRS <10%; FRS ≥10% was considered intermediate or high 10-year CVD risk.

Covariates

The baseline characteristics included demographic factors (age, sex (men or women), education (high school or below and college graduate or above), marital status (married/Living with a partner, never married and widowed/divorced/separated), poverty income ratio (PIR) (2, 2-4 and 4) and ethnicity (Mexican American, Other Hispanic, Non-Hispanic White, Non-Hispanic Black, and Other Ethnicity), behavioral factors (smoking, alcohol consumption, physical activity (PA), and energy intake), and low-density lipoprotein (LDL). The metabolic equivalent (MET) represents the rate of oxygen uptake required to maintain the body's basic metabolic processes while at complete rest. In line with World Health Organization (WHO) recommendations, we used MET values of 3.3 for walking, 4 for moderate activities, and 8 for vigorous activities [27]. PA was valued by total MET-minutes/week. Vigorous activity was defined as accumulating at least 3,000 MET-minutes/week, while moderate activity required a minimum of 600 MET-minutes/week. Individuals who met neither criterion were classified into the light activity category. Energy intake was estimated using the dietary intake data from the 24-h period before the interview. Body mass index (BMI) was calculated by dividing weight in kilograms by the square of height in meters. Participants were categorized into four BMI groups according to WHO criteria: underweight (BMI <18.5 kg/m^2), normal weight (BMI 18.5–24.9 kg/m^2), overweight (BMI 25.0–29.9 kg/m^2), and obese (BMI ≥30.0 kg/m^2). The diagnosis of CVD was determined by self-reported physician diagnoses obtained during interviews using a standardized questionnaire. subjects were asked, "Has a doctor or other health expert ever informed you that you have angina/congestive heart failure/coronary heart disease/heart attack (myocardial infarction)/stroke?" If the answer was "yes" to any of the above questions, the subjects were considered to have CVD.

Statistical analysis

Participants were stratified into four groups according to Ln (SII) quartiles. Continuous and categorical baseline characteristics were presented as mean ± standard deviation (SD) and number (percentage), respectively. Differences in the distribution of variables were compared using a weighted one-way analysis of variance (ANOVA) test for continuous data and a weighted chi-square test for categorical data, respectively.

The Pearson test was used to analyze the correlation between Ln (SII) and the FRS. Two models were developed to assess associations of Ln (SII) and the FRS or 10-year CVD risk level by using weighted GLM: the crude model was not adjusted; the adjusted model was adjusted for education, marital status, PIR, ethnicity, alcohol consumption, PA, energy intake, BMI, and LDL. To rigorously assess the robustness of our results, we performed a subgroup analysis to investigate potential modifying effects based on ethnicity.

Furthermore, weighted RCS were used to explore non-linear relationships between Ln (SII) and FRS or 10-year CVD risk level. Knot placement and model specification were implemented using Harrell's rms package. Interior knots were positioned at clinically relevant percentiles of the Ln (SII) distribution following established conventions: the 10th, 50th, and 90th percentiles were used for the optimal 3-knot configuration, which was determined by comparing Akaike Information Criterion (AIC) across 3 to 6 knot models. Boundary knots were automatically anchored at the observed minimum Ln (SII)value of 2.47.

All statistical analyses were performed using R version 4.2.2, with a significance threshold of $P < 0.05$, and all statistical tests were two-sided.

Results

Study population characteristics

A total of 9901 subjects were included in the study, among whom 53.27% were men, and 46.73% were women. The number of participants who were judged as having an intermediate or high 10-year CVD risk was 1,438 (14.52%). The demographic characteristics of the subjects by Ln (SII) quartiles are shown in Table 1. The results suggest statistically significant differences in age, gender, marital status, ethnicity, smoking status, treatment for hypertension, BMI, PA, TC, FRS, and 10-year CVD risk level (all $P < 0.05$). The demographic characteristics of the subjects after weighting are shown in Supplementary Table S1.

Associations of Ln (SII) with the FRS

A Pearson correlation analysis was performed to examine the correlation between Ln (SII) and the FRS, along with other continuous variables. There was a positive relationship found between Ln (SII) and the FRS, with a corresponding correlation coefficient of 0.09 ($P < 0.001$). Except for energy intake and PA, there were positive relationships between the other factors and the FRS. The results of the Pearson correlation coefficient are shown in Figure 2.

Associations of Ln (SII) and Ln (SII) quartiles with the FRS

Table 2 suggests the results of the association between Ln (SII) and Ln (SII) quartiles and the FRS in the crude model and adjusted

10.3389/ebm.2025.10704

TABLE 1 Demographic characteristics of subjects (n = 9901) in the NHANES 1999–2018.

Variables	Q1 (N = 2,476)	Q2 (N = 2,475)	Q3 (N = 2,475)	Q4 (N = 2,475)	Total (N = 9901)	*P*
Age (year) (mean ± SD)	48.02 ± 12.10	47.55 ± 12.22	46.99 ± 11.69	46.82 ± 12.15	47.34 ± 12.05	0.002
Gender (%)						<0.001
Men	1,500 (60.58)	1,404 (56.73)	1,275 (51.52)	1,095 (44.24)	5,274 (53.27)	
Women	976 (39.42)	1,071 (43.27)	1,200 (48.48)	1,380 (55.76)	4,627 (46.73)	
Education (%)						0.940
High school or below	1,190 (48.06)	1,181 (47.72)	1,170 (47.27)	1,183 (47.80)	4,724 (47.71)	
College graduate or above	1,285 (51.90)	1,291 (52.16)	1,303 (52.65)	1,291 (52.16)	5,170 (52.22)	
Marital status (%)						0.002
Married/Living with partner	1710 (69.06)	1726 (69.74)	1714 (69.25)	1,605 (64.85)	6,755 (68.23)	
Never married	423 (17.08)	444 (17.94)	431 (17.41)	526 (21.25)	1824 (18.42)	
Widowed/Divorced/Separated	322 (13.00)	275 (11.11)	303 (12.24)	315 (12.73)	1,215 (12.27)	
PIR (%)						0.569
<2	982 (39.66)	943 (38.10)	941 (38.02)	958 (38.71)	3,824 (38.62)	
2–4	635 (25.65)	602 (24.32)	623 (25.17)	636 (25.70)	2,496 (25.21)	
≥4	646 (26.09)	722 (29.17)	706 (28.53)	673 (27.19)	2,747 (27.74)	
Ethnicity (%)						<0.001
Mexican American	459 (18.54)	542 (21.9)	528 (21.33)	489 (19.76)	2018 (20.38)	
Other Hispanic	213 (8.60)	242 (9.78)	243 (9.82)	230 (9.29)	928 (9.37)	
Non-Hispanic White	690 (27.87)	952 (38.46)	1,062 (42.91)	1,178 (47.60)	3,882 (39.21)	
Non-Hispanic Black	778 (31.42)	465 (18.79)	403 (16.28)	373 (15.07)	2019 (20.39)	
Other Ethnicity	336 (13.57)	274 (11.07)	239 (9.66)	205 (8.28)	1,054 (10.65)	
Smoke (%)						<0.001
No	1,459 (58.93)	1,427 (57.66)	1,397 (56.44)	1,256 (50.75)	5,539 (55.94)	
Yes	1,017 (41.07)	1,048 (42.34)	1,078 (43.56)	1,219 (49.25)	4,362 (44.06)	
Alcohol consumption (%)						0.567
No	1709 (69.02)	1730 (69.90)	1734 (70.06)	1710 (69.09)	6,883 (69.52)	
Yes	568 (22.94)	566 (22.87)	574 (23.19)	595 (24.04)	2,303 (23.26)	
Treatment for hypertension (%)						0.034
No	2060 (83.20)	2033 (82.14)	2082 (84.12)	2009 (81.17)	8,184 (82.66)	
Yes	416 (16.80)	442 (17.86)	393 (15.88)	466 (18.83)	1717 (17.34)	
T2DM (%)						0.356
No	1,232 (49.76)	1,244 (50.26)	1,250 (50.51)	1,291 (52.16)	5,017 (50.67)	
Yes	1,244 (50.24)	1,231 (49.74)	1,225 (49.49)	1,184 (47.84)	4,884 (49.33)	

(Continued on following page)

TABLE 1 (*Continued*) Demographic characteristics of subjects (n = 9901) in the NHANES 1999–2018.

Variables	Q1 (N = 2,476)	Q2 (N = 2,475)	Q3 (N = 2,475)	Q4 (N = 2,475)	Total (N = 9901)	*P*
BMI (kg/m2) (mean ± SD)	27.98 ± 5.67	28.28 ± 5.79	28.78 ± 6.19	29.07 ± 6.80	28.53 ± 6.14	<0.001
Underweight	34 (1.37)	36 (1.45)	28 (1.13)	39 (1.58)	137 (1.38)	<0.001
Normal weight	742 (29.97)	714 (28.85)	677 (27.35)	671 (27.11)	2,804 (28.32)	
Overweight	612 (24.72)	570 (23.03)	559 (22.59)	526 (21.25)	2,267 (22.90)	
Obese	1,068 (43.13)	1,147 (46.34)	1,195 (48.28)	1,209 (48.85)	4,619 (46.65)	
Energy intake (kcal) (mean ± SD)	2,154.30 ± 945.14	2,152.5 ± 860.88	2,137.35 ± 924.32	2,137.03 ± 898.14	2,145.27 ± 907.38	0.859
PA (MET-minutes/week) (mean ± SD)	4,286.55 ± 8,987.26	3,658.71 ± 6,222.36	3,848.23 ± 15,673.21	2,993.56 ± 8,034.72	3,700.21 ± 10,367.76	0.001
Vigorous	625 (25.24)	673 (27.19)	731 (29.54)	799 (32.28)	2,828 (28.56)	<0.001
Moderate	742 (29.97)	750 (30.30)	719 (29.05)	700 (28.28)	2,911 (29.40)	
Light	666 (26.90)	606 (24.48)	561 (22.67)	490 (19.80)	2,323 (23.46)	
TC (mg/dL) (mean ± SD)	198.76 ± 40.91	199.81 ± 40.89	200.95 ± 39.55	201.96 ± 41.91	200.37 ± 40.84	0.035
HDL (mg/dL) (mean ± SD)	53.79 ± 16.46	52.97 ± 16.01	53.18 ± 16.24	53.64 ± 16.24	53.40 ± 16.24	0.249
LDL (mg/dL) (mean ± SD)	119.43 ± 35.18	120.31 ± 35.86	120.32 ± 33.9	120.32 ± 35.24	120.09 ± 35.05	0.779
SBP (mm Hg) (mean ± SD)	123.09 ± 18	122.61 ± 17.71	122.53 ± 17.87	122.68 ± 18.23	122.73 ± 17.95	0.695
Ln (SII) (mean ± SD)	5.46 ± 0.32	5.96 ± 0.09	6.28 ± 0.10	6.78 ± 0.28	6.12 ± 0.53	<0.001
FRS (mean ± SD)	5.04 ± 8.12	5.21 ± 7.89	5.29 ± 8.26	5.78 ± 8.61	5.33 ± 8.23	0.011
Low 10-year CVD risk	2,136 (86.27)	2,118 (85.58)	2,136 (86.30)	2073 (83.76)	8,463 (85.48)	0.032
Intermediate and high 10-year CVD risk	340 (13.73)	357 (14.42)	339 (13.70)	402 (16.24)	1,438 (14.52)	

Abbreviations: SD, standard deviation; PIR, poverty income ratio; SBP, systolic blood pressure; T2DM, type 2 diabetes mellitus; BMI, body mass index; PA, physical activity; MET, metabolic equivalent; TC, total cholesterol; HDL, high-density lipoprotein; LDL, low-density lipoprotein; Ln (SII), Ln-transformed SII; SII, systemic immune-inflammation index; FRS, framingham cardiovascular risk score; CVD, cardiovascular disease.

Published by Frontiers
Society for Experimental Biology and Medicine
10.3389/ebm.2025.10704

FIGURE 2
Correlation analysis. Pearson correlation coefficients between Ln (SII) with the FRS and the factors that were computed for the FRS. The correlation coefficients are shown as numbers and colors. Blue indicates a positive correlation and red indicates a negative correlation. A flatter circle represents a stronger correlation. *indicates $p < 0.05$; **indicates $p < 0.01$; ***indicates $p < 0.001$. Abbreviations: BMI, body mass index; PA, physical activity; TC, total cholesterol; HDL, high-density lipoprotein; LDL, low-density lipoprotein; SBP, systolic blood pressure; Ln (SII), Ln-transformed SII; SII, systemic immune-inflammation index; FRS, Framingham cardiovascular risk score.

model. In the crude model, Ln (SII) was analyzed as a continuous variable. The odds ratio (OR) for FRS was 2.18 [95% confidence interval (CI): 1.57–3.02] per unit increment in Ln (SII). Compared to the lowest quartile (Q1) of Ln (SII), the OR (95% CI) for Q2, Q3, and Q4 were 1.22 (0.76-1.96), 1.86 (1.15–3.01), and 3.06 (1.90–4.93), respectively (P for trend <0.001). In the adjusted model, the OR (95% CI) for FRS was 1.52 (1.12–2.06) for a per-unit increment in Ln (SII). Compared to the Q1 of Ln (SII), the OR (95% CI) for Q2, Q3, and Q4 were 1.19 (0.73–1.92), 1.49 (0.95–2.35), and 1.89 (1.20–2.98), respectively (P for trend = 0.004).

The non-linear association between Ln (SII) and the FRS

A non-linear relationship was explored between Ln (SII) and the FRS by RCS. Figure 3 shows that a linear association was found between Ln (SII) and the FRS (P for non-linearity = 0.972). As Ln (SII) increased, so did the value of FRS (P for overall trend <0.001).

The relationship between Ln (SII) and 10-year CVD risk

Supplementary Table S2 shows the results of the association between Ln (SII) and Ln (SII) quartiles and 10-year CVD risk in the crude model and adjusted model. After adjusting for the potential confounders, all associations became non-significant (OR range: 1.03–1.13, $P > 0.05$ for all comparisons). Supplementary Figure S2 shows a linear association between Ln (SII) and 10-year CVD risk (P for non-linearity = 0.541). With the Ln (SII) increasing, 10-year CVD risk gradually increased (P for overall trend <0.001).

TABLE 2 Associations of Ln (SII) and Ln (SII) quartiles with the FRS, as estimated by weighted generalized linear models.

Factor	Crude model			Adjusted model		
	OR	95%CI	*P* value	OR	95%CI	*P* value
Ln (SII)	2.18	1.57–3.02	<0.001	1.52	1.12–2.06	0.009
Stratified by Ln (SII) quartiles	1.47	1.26–1.71	<0.001	1.24	1.07–1.43	0.004
Q1	Ref			Ref		
Q2	1.22	0.76–1.96	0.417	1.19	0.73–1.92	0.488
Q3	1.86	1.15–3.01	0.013	1.49	0.95–2.35	0.086
Q4	3.06	1.90–4.93	<0.001	1.89	1.20–2.98	0.007

The crude model was not adjusted;
The adjusted model was adjusted for education, marital status, PIR, ethnicity, alcohol consumption, PA, energy intake, BMI, and LDL.
Abbreviations: Ln (SII), Ln-transformed SII; SII, systemic immune-inflammation index; FRS, framingham cardiovascular risk score; OR, odds ratio; Ref, reference; PIR, poverty income ratio; PA, physical activity; BMI, body mass index; LDL, low-density lipoprotein.

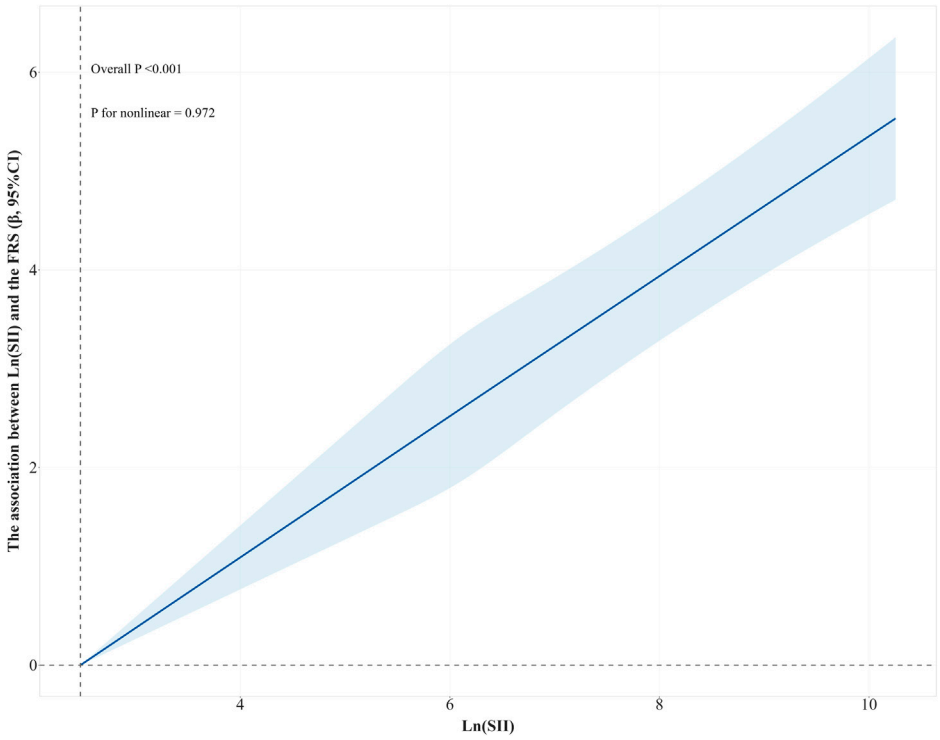

FIGURE 3
RCS curve of the association between Ln(SII) and the FRS. The results were adjusted for education, marital status, PIR, ethnicity, alcohol consumption, PA, energy intake, BMI, and LDL. Abbreviations: RCS, restricted cubic splines; Ln (SII), Ln-transformed SII; SII, systemic immune-inflammation index; FRS, Framingham cardiovascular risk score; PIR, poverty income ratio; PA, physical activity; BMI, body mass index; LDL, low-density lipoprotein.

Subgroup analysis

Supplementary Tables S3-S12 present ethnicity-stratified analyses of the association between Ln (SII) (as both continuous and quartile variables) and the FRS and 10-year CVD risk level. After fully adjusting for education, marital status, PIR, alcohol consumption, physical activity, energy intake, BMI, and LDL, we observed distinct ethnicity-associated patterns: No significant associations were found among Mexican American patients (OR range: 0.84–1.75, all

$P > 0.05$), Other Hispanic subjects (OR range: 0.34-1.39, all $P > 0.05$), or Non-Hispanic Black subjects (OR range: 0.98–2.34, all $P > 0.05$). In the Non-Hispanic White group, higher Ln (SII) was associated with an increased FRS (per-unit OR = 1.72, 95% CI: 1.13–2.60; Q4 vs. Q1 OR = 2.30, 95% CI: 1.27–4.16; P for trend = 0.007), but it was not associated with 10-year CVD risk (OR range: 1.05–1.18). Conversely, the Other Ethnicity group exhibited an inverse 10-year CVD risk association (per-unit OR = 0.46, 95% CI: 0.27–0.79; Q3 vs. Q1 OR = 0.41, 95% CI: 0.19–0.90), whereas no significant association was observed for the FRS (OR range: 0.48–0.86).

Discussion

It is increasingly recognized that systemic inflammation initiates and exacerbates the pathological processes of chronic diseases. Many inflammatory predictors associated with CVD risk have been identified [28]. The present study showed that the FRS increased with the increase of SII. Both the Pearson correlation analysis and RCS revealed a significant positive association between Ln (SII) and the FRS. Therefore, SII may serve as a useful biomarker for assessing 10-year CVD risk in the general population. SII could be used to quickly identify high-risk subjects with a 10-year risk of CVD at a relatively low cost.

Several studies have supported the finding of a positive relationship between SII and the CVD risk [24, 25, 29]. Another study suggested that an elevation of SII level would be obvious in almost all subtypes of CVD, including ischemic stroke, hemorrhagic stroke, myocardial infarction, and peripheral arterial disease [30]. Furthermore, SII was found to be associated with poor short-term prognosis in atrial fibrillation patients with ischemic stroke [31]. Meanwhile, SII levels were also elevated in patients with ST-segment elevation myocardial infarction [32, 33]. Based on these, a close relationship was found to exist between SII and CVD risk. These results also provide sufficient evidence that chronic inflammation in the healthy population greatly increases the risk of developing CVD.

The underlying mechanisms of SII relating to the FRS can be attributed to several factors. First, chronic systemic inflammation can cause abnormal platelet aggregation, allowing them to adhere to the surface of endothelial cells, causing hypoxia, ischemia and microthrombus formation, leading to local tissue death [34, 35]. Second, long-term aberrant decrease of lymphocyte counts indicates excessive lymphocyte death in the human body, leading to reduced immune system capacity and immune dysfunction. Subsequently, lymphocyte death could further lead to endothelial dysfunction, abnormal aggregation of platelets, and thrombosis after platelet activation [24]. Third, monocytes and neutrophils can also promote abnormal coronary plaque status by activating and generating inflammatory responses, inducing atherosclerotic plaque rupture and thrombosis, thereby increasing the risk of adverse cardiovascular events [36]. As a complex inflammatory index, SII could effectively and comprehensively reflect the inflammatory state and immune system state of the body. The cumulative effect of the interaction between the three different cell lines synergistically enhances the association between systemic inflammation and the 10-year CVD risk assessed by the FRS. Therefore, the interaction between platelets, neutrophils, and lymphocytes may represent a potential therapeutic target for chronic inflammation in patients with high FRS.

Subgroup analyses revealed complex heterogeneity in the relationship between Ln (SII) and the FRS: significant positive associations were observed in Non-Hispanic Whites, whereas null effects were found in the Mexican American, Other Hispanic, and Non-Hispanic Black groups. In contrast, the Other Ethnicity group exhibited a negative relationship between Ln (SII) and 10-year CVD risk. These differential patterns likely reflect the interplay between ethnicity, SII and CVD. The findings in the Mexican American/Hispanic/Other Ethnicity groups may reflect the "health paradox" phenomenon [37, 38]. The reason for the different relationships between different ethnic groups likely originates from three interconnected mechanisms: First, racism generates population health disparities through the propagation of beliefs, attitudes, and treatment of group members by both individuals and institutions [39]. Second, some research suggests that Black individuals in the United States experience premature death from a variety of causes, including multiple diseases [40, 41]. Second, the immigrant health advantage has always played a critical role in this situation. Several studies have shown lower mortality rates [42], and fewer chronic conditions [43] in immigrants than in US-born subjects. Third, current ethnic classifications inadequately capture heterogeneity, while undifferentiated pan-ethnic labels mask critical variations in nativity and phenotype [44].

It is important to emphasize the limitations of the present study. First, the NHANES had a cross-sectional design, which limits its ability to establish causality. Specifically, simultaneous SII and FRS measurements prevent determining whether inflammation precedes or results from subclinical CVD; influencing factors (e.g., occult infections, undiagnosed autoimmune disorders) may independently influence both SII and CVD risk. Furthermore, single-time-point in front sampling cannot capture how the relationship between SII and CVD risk evolves over time. Considering the large sample size of the NHANES and its complex, multi-stage, probabilistic sampling design, the results still indicated stability in the relationship between SII and 10-year CVD risk. Second, due to missing information in the data set, excluded participants with incomplete data may introduce bias into the analysis. Third, hematological parameters were assessed at a single time point (a limitation inherent to the NHANES protocol), while the substantial sample size provides sufficient statistical power to detect meaningful population-level associations. Large-scale epidemiological investigations have consistently demonstrated that single measurements of inflammatory biomarkers retain significant predictive value for long-term cardiovascular risk stratification in adult populations. In addition, utilizing the NHANES database

inevitably introduces the possibility of imprecise data capture and recall bias.

Conclusion

The results demonstrate a significant positive association between SII and the FRS, supporting the potential of SII as an effective biomarker for identifying 10-year CVD risk. Nonetheless, variations in the relationship between SII and the FRS among different ethnic groups underscore the importance of careful application. Further studies with larger and more diverse cohorts are required for comprehensive validation.

Author contributions

All authors participated in the design, interpretation of the study and analysis of the data and review of the manuscript. YY designed this study. RT, LZ, GX, and TY analyzed the data. YY, QL, and CW wrote the manuscript, and HY reviewed the manuscript. All authors contributed to the article and approved the submitted version.

Data availability

The datasets presented in this study can be found in online repositories. The names of the repository/repositories and accession number(s) can be found in the article/Supplementary Material.

Ethics statement

The studies involving humans were approved by the National Center for Health Statistics' Research Ethics Assessment Board. The studies were conducted in accordance with the local legislation and institutional requirements. The participants provided their written informed consent to participate in this study. Written informed consent was obtained from the individual(s) for the publication of any potentially identifiable images or data included in this article.

Funding

The author(s) declare that no financial support was received for the research and/or publication of this article.

Acknowledgments

The authors thank all NHANES staff and participants for their contributions, including data collection and sharing.

Conflict of interest

The author(s) declared no potential conflicts of interest with respect to the research, authorship, and/or publication of this article.

Generative AI statement

The author(s) declare that no Generative AI was used in the creation of this manuscript.

Supplementary material

The Supplementary Material for this article can be found online at: https://www.ebm-journal.org/articles/10.3389/ebm.2025.10704/full#supplementary-material

References

1. Ahmad FB, Anderson RN. The leading causes of death in the US for 2020. *Jama* (2021) **325**:1829–30. doi:10.1001/jama.2021.5469

2. Tsao CW, Aday AW, Almarzooq ZI, Anderson CAM, Arora P, Avery CL, et al. Heart disease and stroke statistics-2023 update: a report from the American heart association. *Circulation* (2023) **147**:e93–e621. doi:10.1161/cir.0000000000001123

3. Ndumele CE, Neeland IJ, Tuttle KR, Chow SL, Mathew RO, Khan SS, et al. A synopsis of the evidence for the science and clinical management of cardiovascular-kidney-metabolic (CKM) syndrome: a scientific statement from the American heart association. *Circulation* (2023) **148**:1636–64. doi:10.1161/CIR.0000000000001186

4. D'Agostino RB, Sr, Vasan RS, Pencina MJ, Wolf PA, Cobain M, Massaro JM, et al. General cardiovascular risk profile for use in primary care: the Framingham Heart Study. *Circulation* (2008) **117**:743–53. doi:10.1161/circulationaha.107.699579

5. Nyirenda M. Assessment of cardiovascular disease risks using Framingham risk scores (FRS) in HIV-positive and HIV-negative older adults in South Africa. *Prev Med Rep* (2021) **22**:101352. doi:10.1016/j.pmedr.2021.101352

6. Gale CR, Cooper C, Sayer AA. Framingham cardiovascular disease risk scores and incident frailty: the English longitudinal study of ageing. *Age (Dordrecht, Netherlands)* (2014) **36**:9692. doi:10.1007/s11357-014-9692-6

7. Kwobah E, Koen N, Mwangi A, Atwoli L, Stein DJ. Prevalence of lifestyle cardiovascular risk factors and estimated framingham 10-year risk scores of adults with psychotic disorders compared to controls at a referral hospital in Eldoret, Kenya. *BMC psychiatry* (2023) **23**:909. doi:10.1186/s12888-023-05409-0

8. Birhanu MM, Evans RG, Zengin A, Riddell M, Kalyanram K, Kartik K, et al. Absolute cardiovascular risk scores and medication use in rural India: a cross-sectional study. *BMJ open* (2022) **12**:e054617. doi:10.1136/bmjopen-2021-054617

9. Adamo L, Rocha-Resende C, Prabhu SD, Mann DL. Reappraising the role of inflammation in heart failure. *Nat Rev Cardiol* (2020) **17**:269–85. doi:10.1038/s41569-019-0315-x

10. Kaptoge S, Seshasai SR, Gao P, Freitag DF, Butterworth AS, Borglykke A, et al. Inflammatory cytokines and risk of coronary heart disease: new prospective study

and updated meta-analysis. *Eur Heart J* (2014) **35**:578–89. doi:10.1093/eurheartj/eht367

11. Ruparelia N, Chai JT, Fisher EA, Choudhury RP. Inflammatory processes in cardiovascular disease: a route to targeted therapies. *Nat Rev Cardiol* (2017) **14**:133–44. doi:10.1038/nrcardio.2016.185

12. Zheng H, Yin Z, Luo X, Zhou Y, Zhang F, Guo Z. Associations between systemic immunity-inflammation index and heart failure: evidence from the NHANES 1999-2018. *Int J Cardiol* (2024) **395**:131400. doi:10.1016/j.ijcard.2023.131400

13. Yoshihara F. Systemic inflammation is a key factor for mortality risk stratification in chronic kidney disease patients with coronary Artery Calcification. *Circ J* (2016) **80**:1537–8. doi:10.1253/circj.CJ-16-0506

14. Li X, Cui L, Xu H. Association between systemic inflammation response index and chronic kidney disease: a population-based study. *Front Endocrinol* (2024) **15**:1329256. doi:10.3389/fendo.2024.1329256

15. Carrillo-Salinas FJ, Ngwenyama N, Anastasiou M, Kaur K, Alcaide P. Heart inflammation: immune cell roles and Roads to the heart. *The Am J Pathol* (2019) **189**:1482–94. doi:10.1016/j.ajpath.2019.04.009

16. Strassheim D, Dempsey EC, Gerasimovskaya E, Stenmark K, Karoor V. Role of inflammatory cell subtypes in heart failure. *J Immunol Res* (2019) **2019**:1–9. doi:10.1155/2019/2164017

17. Hu B, Yang XR, Xu Y, Sun YF, Sun C, Guo W, et al. Systemic immune-inflammation index predicts prognosis of patients after curative resection for hepatocellular carcinoma. *Clin Cancer Res* (2014) **20**:6212–22. doi:10.1158/1078-0432.Ccr-14-0442

18. Tabas I, García-Cardeña G, Owens GK. Recent insights into the cellular biology of atherosclerosis. *The J Cel Biol* (2015) **209**:13–22. doi:10.1083/jcb.201412052

19. Tiwari RL, Singh V, Barthwal MK. Macrophages: an elusive yet emerging therapeutic target of atherosclerosis. *Med Res Rev* (2008) **28**:483–544. doi:10.1002/med.20118

20. Libby P. Current concepts of the pathogenesis of the acute coronary syndromes. *Circulation* (2001) **104**:365–72. doi:10.1161/01.cir.104.3.365

21. Tan Y, Hu B, Li Q, Cao W. Prognostic value and clinicopathological significance of pre-and post-treatment systemic immune-inflammation index in colorectal cancer patients: a meta-analysis. *World J Surg Oncol* (2025) **23**:11. doi:10.1186/s12957-025-03662-z

22. Wang BL, Tian L, Gao XH, Ma XL, Wu J, Zhang CY, et al. Dynamic change of the systemic immune inflammation index predicts the prognosis of patients with hepatocellular carcinoma after curative resection. *Clin Chem Lab Med (Cclm)* (2016) **54**:1963–9. doi:10.1515/cclm-2015-1191

23. Dong M, Shi Y, Yang J, Zhou Q, Lian Y, Wang D, et al. Prognostic and clinicopathological significance of systemic immune-inflammation index in colorectal cancer: a meta-analysis. *Ther Adv Med Oncol* (2020) **12**:1758835920937425. doi:10.1177/1758835920937425

24. Xia Y, Xia C, Wu L, Li Z, Li H, Zhang J. Systemic immune inflammation index (SII), system inflammation response index (SIRI) and risk of all-cause mortality and cardiovascular mortality: a 20-year Follow-Up cohort study of 42,875 US adults. *J Clin Med* (2023) **12**:1128. doi:10.3390/jcm12031128

25. Jin Z, Wu Q, Chen S, Gao J, Li X, Zhang X, et al. The associations of two novel inflammation Indexes, SII and SIRI with the risks for cardiovascular diseases and all-cause mortality: a ten-year follow-up study in 85,154 individuals. *J Inflamm Res* (2021) **14**:131–40. doi:10.2147/jir.S283835

26. Li J, He D, Yu J, Chen S, Wu Q, Cheng Z, et al. Dynamic status of SII and SIRI Alters the risk of cardiovascular diseases: evidence from Kailuan cohort study. *J Inflamm Res* (2022) **15**:5945–57. doi:10.2147/jir.S378309

27. Diao X, Ling Y, Zeng Y, Wu Y, Guo C, Jin Y, et al. Physical activity and cancer risk: a dose-response analysis for the Global Burden of Disease Study 2019. *Cancer Commun (London, England)* (2023) **43**:1229–43. doi:10.1002/cac2.12488

28. Azambuja MI. Inflammation as the cause of coronary heart disease. *The Lancet Infect Dis* (2010) **10**:142–3. doi:10.1016/s1473-3099(10)70029-3

29. Xu M, Chen R, Liu L, Liu X, Hou J, Liao J, et al. Systemic immune-inflammation index and incident cardiovascular diseases among middle-aged and elderly Chinese adults: the Dongfeng-Tongji cohort study. *Atherosclerosis* (2021) **323**:20–9. doi:10.1016/j.atherosclerosis.2021.02.012

30. Ye Z, Hu T, Wang J, Xiao R, Liao X, Liu M, et al. Systemic immune-inflammation index as a potential biomarker of cardiovascular diseases: a systematic review and meta-analysis. *Front Cardiovasc Med* (2022) **9**:933913. doi:10.3389/fcvm.2022.933913

31. Lin KB, Fan FH, Cai MQ, Yu Y, Fu CL, Ding LY, et al. Systemic immune inflammation index and system inflammation response index are potential biomarkers of atrial fibrillation among the patients presenting with ischemic stroke. *Eur J Med Res* (2022) **27**:106. doi:10.1186/s40001-022-00733-9

32. Esenboğa K, Kurtul A, Yamantürk YY, Tan TS, Tutar DE. Systemic immune-inflammation index predicts no-reflow phenomenon after primary percutaneous coronary intervention. *Acta Cardiol* (2022) **77**:59–65. doi:10.1080/00015385.2021.1884786

33. Huang J, Zhang Q, Wang R, Ji H, Chen Y, Quan X, et al. Systemic immune-inflammatory index predicts clinical outcomes for elderly patients with acute myocardial infarction receiving percutaneous coronary intervention. *Med Sci Monitor* (2019) **25**:9690–701. doi:10.12659/msm.919802

34. Banka AL, Guevara MV, Brannon ER, Nguyen NQ, Song S, Cady G, et al. Cargo-free particles divert neutrophil-platelet aggregates to reduce thromboinflammation. *Nat Commun* (2023) **14**:2462. doi:10.1038/s41467-023-37990-z

35. von Ungern-Sternberg SNI, Vogel S, Walker-Allgaier B, Geue S, Maurer A, Wild AM, et al. Extracellular Cyclophilin A Augments platelet-Dependent thrombosis and thromboinflammation. *Thromb Haemost* (2017) **117**:2063–78. doi:10.1160/th17-01-0067

36. Ankeny RF, Hinds MT, Nerem RM. Dynamic shear stress regulation of inflammatory and thrombotic pathways in baboon endothelial outgrowth cells. *Tissue Eng A* (2013) **19**:1573–82. doi:10.1089/ten.TEA.2012.0300

37. Arias E, Eschbach K, Schauman WS, Backlund EL, Sorlie PD. The Hispanic mortality advantage and ethnic misclassification on US death certificates. *Am J Public Health* (2010) **100**(Suppl. 1):S171–7. doi:10.2105/ajph.2008.135863

38. Boen CE, Hummer RA. Longer-but harder-lives? The hispanic health paradox and the social determinants of racial, ethnic, and immigrant-native health disparities from midlife through late life. *J Health Soc Behav* (2019) **60**:434–52. doi:10.1177/0022146519884538

39. Gee GC, Walsemann KM, Brondolo E. A life course perspective on how racism may be related to health inequities. *Am J Public Health* (2012) **102**:967–74. doi:10.2105/ajph.2012.300666

40. Dwyer-Lindgren L, Kendrick P, Kelly YO, Sylte DO, Schmidt C, Blacker BF, et al. Life expectancy by county, race, and ethnicity in the USA, 2000-19: a systematic analysis of health disparities. *The Lancet* (2022) **400**:25–38. doi:10.1016/s0140-6736(22)00876-5

41. Gupta R, Agrawal R, Bukhari Z, Jabbar A, Wang D, Diks J, et al. Higher comorbidities and early death in hospitalized African-American patients with Covid-19. *BMC Infect Dis* (2021) **21**:78. doi:10.1186/s12879-021-05782-9

42. Dupre ME, Gu D, Vaupel JW. Survival differences among native-born and foreign-born older adults in the United States. *PloS one* (2012) **7**:e37177. doi:10.1371/journal.pone.0037177

43. Gorman BK, Read JG, Krueger PM. Gender, acculturation, and health among Mexican Americans. *J Health Soc Behav* (2010) **51**:440–57. doi:10.1177/0022146510386792

44. Chinn JJ, Hummer RA. Racial disparities in Functional limitations among Hispanic women in the United States. *Res Aging* (2016) **38**:399–423. doi:10.1177/0164027515620244

EBM Experimental Biology and Medicine

EBM is the official journal of the Society for Experimental Biology and Medicine

Experimental Biology and Medicine (EBM) is a global, peer-reviewed journal dedicated to the publication of multidisciplinary and interdisciplinary research in the biomedical sciences.

Discover more of our Special Issues

See more →

Contact

development@ebm-journal.org

See more

ebm-journal.org

publishingpartnerships.frontiersin.org/our-partners